E0 Measurements in ^{154}Sm Using SAGE

An Investigation of Collectivity in Rare-Earth Nuclei

James Smallcombe

A thesis submitted for the degree of

Doctor of Philosophy

University of York

Department of Physics

September 2013

Abstract

Using the Silicon And GErmanium array (SAGE) at the University of Jyväskylä (JYFL), $E0$ transition strengths in ^{154}Sm were measured as a test case for further measurements in the rare-earth region. A large degree of collectivity is expected in nuclear excitations of even-even rare-earth nuclei and the nature of excited 0^+ states in these nuclei is of particular interest. SAGE was employed to measure the $E0$ transition strength of the $0_2^+ \rightarrow 0_1^+$ and $2_2^+ \rightarrow 2_1^+$ transitions in ^{154}Sm. Such transition strengths provide a key observable to differentiate between nuclear models. To facilitate this measurement, peak-fitting techniques were developed to improve the analysis of the particular peak shapes observed in electron spectra from SAGE. A method of background subtraction was developed to remove time-random coincidences using the timing information available from the JYFL Total Data Readout (TDR) system.

An isotopically enriched samarium target was bombarded by a 65 MeV beam of ^{16}O, populating states of interest via Coulomb excitation (CoulEx), after which de-excitation via internal conversion and γ-ray emission were observed. The $0_2^+ \rightarrow 0_1^+$ $E0$ transition could not be measured in this work due to the background found in the current experimental setup. The equally important $2_2^+ \rightarrow 2_1^+$ $E0$ transition strength could be studied by implementation of background subtraction to remove false-coincidences. The experiment was normalised by measurement of conversion coefficients for known transitions in ^{154}Sm and in the contaminants ^{152}Sm, ^{166}Yb and ^{167}Yb.

An electron peak associated with the $2_2^+ \rightarrow 2_1^+$ transition in ^{154}Sm was not observable, but a stringent upper-limit was placed on the $E0$ transition strength. The measurement was compared to the Interacting Boson Approximation (IBA) and Bohr and Mottleson collective models and was found to be smaller than predicted by both collective interpretations. The usefulness of SAGE and this measurement technique was proved and the direction for future research in this area is discussed.

Contents

List of Figures

List of Tables

Acknowledgements

I'd like to say a big thanks to my supervisor *Dr Charles J. Barton III* for all his help and support and for everything he's taught me, some of which relates to Nuclear Physics. His quality advice, quality chocolate and quality drink were always gratefully received and the frequency with which he bestowed all three was more than any graduate student could hope for. I really learnt a lot from Charles through this work and the other projects we worked on together. He even convinced me I understand some nuclear theory.

This work wouldn't have been possible without the *Jyväskylä Group*, so thanks to them for the use of their facility and their help during the experiment and analysis. Thanks also to the *Liverpool Group* for the use of their detector and the SAGE advice provided by their members.

I'd also like to thank *The Drunken Vicar* for being my moral compass for the last four years, for giving me sage advice, for driving me mad and for keeping me sane.
Thanks to *The Green Fingered Coloradan* for making York such a welcoming place for me and for getting me settled in the academic world by providing perspective and support.
Thanks also to *The Belligerent Yorkshireman* for always putting me in my place and imparting to me the wisdom of his many many years.
Thanks to *The Baker Stuck with a Physicist's Brain* and *The Lock Who Can Read* for their help in ensuring that this thesis contains fewer errors than it started with.
Thanks to *The Great Dane* for being a fountain of knowledge and provoking thoughts, who occasionally left me with fewer questions than I had initially.
Thanks to *The Angry Scrum Half*, *Mrs Hudson* and *The Mensa Magpie* for many good pub chats, some of which even related to physics.
Thanks to *The Prolific Professor* for sparking my interest in to nuclear structure.
Many thanks to *The Captain* and *The Captain's Wife* without whom none of my achievements would have been possible, thank you for giving me the good start I needed in my education and for continued support through the years.
Thanks to the *Operations Director of the Quality of Life Division* for inspiring me to enter the physics community.
And finally thanks to *The Woman*.

Declaration

This thesis has been submitted for the degree of Doctor of Philosophy, in accordance with the regulations of the University of York. I declare that the work presented in this thesis is based on my own research, and has not been submitted previously for a degree at this or another research institution. All materials from other sources are referenced where present.

1 Introduction

The atomic nucleus represents one of the most varied and complex quantum system available to scientists. Nuclear physics aims to understand how the many-bodied nuclear force acts in this environment and to explain how it governs the behaviour of the nucleons involved. Doing so requires a wealth of experimental data, combined with a multifaceted theoretical knowledge-base. A plethora of phenomena have been uncovered, from the spin-orbit and pairing interactions, which dominate shell theory, to the giant dipole resonance in ^{197}Au and the halo nucleus ^{11}Be. However, scientific understanding is far from complete and complementary development of experimental knowledge and theoretical models remains paramount.

Starting from the classically-based liquid-drop model, the lowest energy state of a nucleus would always be expected to be spherical. However the occurrence of deformed ground states in nuclei are well-documented and widespread throughout the nuclear chart. The pairing interaction makes it energetically favourable for pairs of nucleons to be coupled to zero angular momentum and even parity. The strength of the pairing interaction and coupling result in a 0^+ ground state of all even-even nuclei. As a result of pairing, the ground state and low energy structure is not dominated by behaviour of single nucleons in such nuclei. In even-even nuclei, deformation is largest in the mid-region between major shell closures; a return to sphericity is observed at closed shells. Figure 1.1 shows ground state quadrupole deformation in even-even nuclei across the nuclear landscape. As atomic number, Z, or neutron number, N, approaches a shell closure, the Pauli exclusion principle prevents excitation without expending a large about of energy to promote nucleons across the shell gap to create particle-hole excitations. This requires either the energy to excite a pair of nucleons or to separate a coupled pair. Whereas, in the mid-shell region valence nucleons are free to interact and recouple. Thus it seems that the many interactions between the two types of valence nucleon drive deformation and lead to a lower energy state than would be expected if nucleons minimised energy by simply filling, in order, the lowest energy single particle states. It is observed experimentally that nuclei are typically quadrupole-prolate deformed but there are also quadrupole-oblate deformed nuclei (^{74}Kr) and even octupole-deformed pear-shaped nuclei (^{224}Ra).

As well as deformed ground states, excitations are also observed in nuclei attributed to rotations and vibrations of deformed shapes. These collective excitations are found to dominate the low energy spectrum of medium- to high-mass nuclei ($A \gtrsim 50$). Microscopic models, such as the shell model or *ab initio* models, which attempt to describe the nucleus from effective nucleon-nucleon interactions, struggle to function due to the large valence spaces required to describe these collective excitations. The Bohr and Mottelson collective

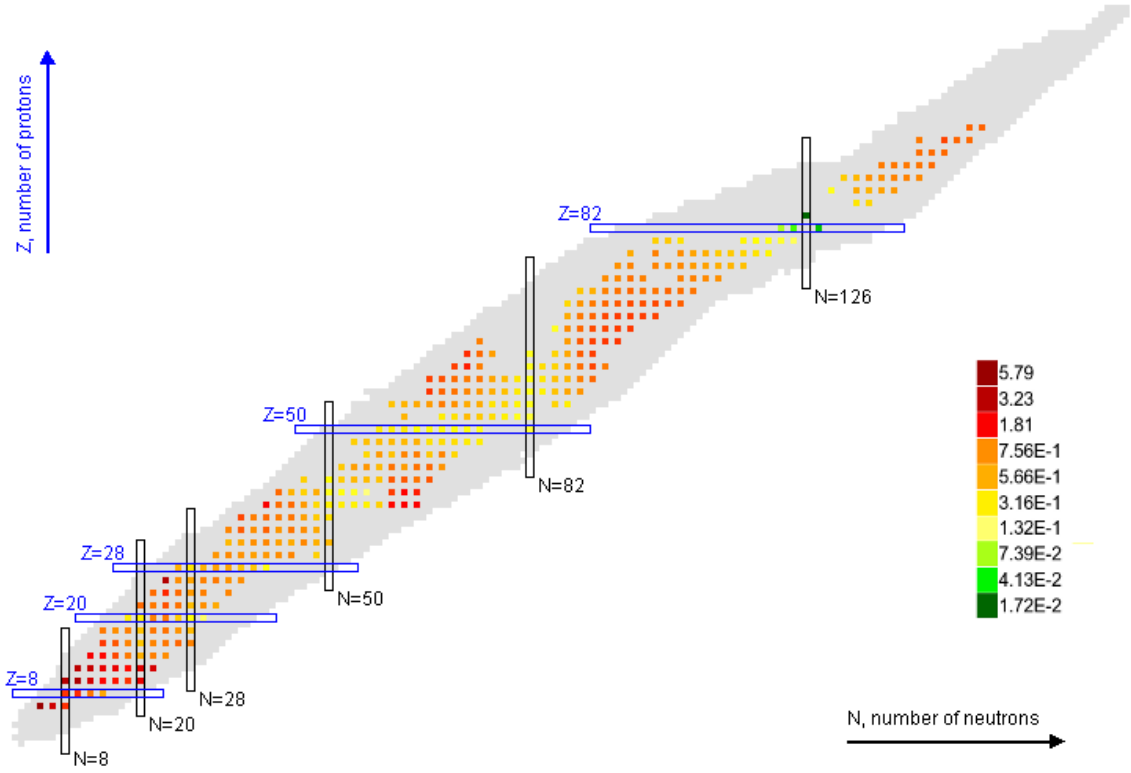

Figure 1.1: Absolute value of the quadrupole deformation parameter β_2 for even-even nuclei across the nuclear chart, calculated from $B(E2)$ measurements. The major shell gaps seen for protons and neutrons near stability are highlighted.

model, and developments upon it, remains one of the best ways to describe the excitations of medium- to high-mass nuclei. Continued work is needed to amend the model and understand where the approximations made are inadequate. In doing so we will advance the knowledge of the collective behaviour of nuclear matter.

1.1 Nuclear Experimentation

The technique of γ-ray spectroscopy has become the mainstay of nuclear structure physics. As the emission of a γ ray is the most common mode of de-excitation between nuclear states, their detection is an ideal tool to observe and measure the properties of excited states in nuclei. The measurement of the emitted quantum of a transition gives information about the difference between the two linked states. By linking back to the ground state, or another known state, of the nucleus, the properties of the states can be inferred. Hence, a level scheme showing the ground state, excited states and the linking transitions can be produced from the observation of emitted γ rays. The energy of a γ ray gives the energy difference between two states, and from the angular distribution and polarization of the emitted γ rays spin and parity changes can be deduced. The rate at which a given transition occurs, which is related to the observed half-life, can give direct insight into the nuclear wavefunctions of the two states. Owing to a complete understanding of the electromagnetic force that governs the interaction, all energy and angular momentum dependence can accounted for in the calculations and an experimentally-measured value

related directly to the nuclear structure dependence. The nuclear structure dependence here is realised as the quantum mechanical nuclear matrix element of transition, $\langle \Psi_f | \hat{T} | \Psi_i \rangle$, which is the expectation value of the operator for the transition between the initial and final state wavefunctions. The term 'matrix elements' refers to the complete set of all possible eigenstate pairs, represented as a symmetric matrix.

The lowest order electromagnetic transitions, $E0$ transitions, cannot proceed by simple γ-ray emission. $E0$ transitions provide crucial insight into nuclear charge radii, which is a key observable for nuclear shape deformation. For excited 0^+ states in even-even nuclei, the $E0$ transitions from the excited state to the ground 0^+ state can yield crucial information on the nature of the excitation. The nature of such 0^+ states is of continued interest as different kinds of 0^+ states are predicted in collective and microscopic models. Thus $E0$ transition strengths represent a fundamental piece of nuclear structure information which would be lost without ancillary detectors in γ-ray experiments. One such detector is the Silicon And GErmanium array (SAGE) system at the University of Jyväskylä (JYFL). This detector system, shown in Figure 1.2, is a purpose-built electron spectrometer for the measurement of electrons from internal conversion. This is the main decay mode by which an $E0$ type nuclear transition may proceed. A solenoidal magnet is utilised for electron transport, such that electrons over a broad range of energies can be detected in a single setup. SAGE is designed to operate alongside the JUROGAMII γ-ray detector array so that both electron emission and γ-ray emission associated with nuclear transitions can be detected in a single experiment, allowing coincident events to be identified. By simultaneous study of transition strengths of $0_i^+ \rightarrow 0_f^+$ $E0$ transitions, alongside competing γ-ray branches, great insight can be gained into the collective nature of nuclei.

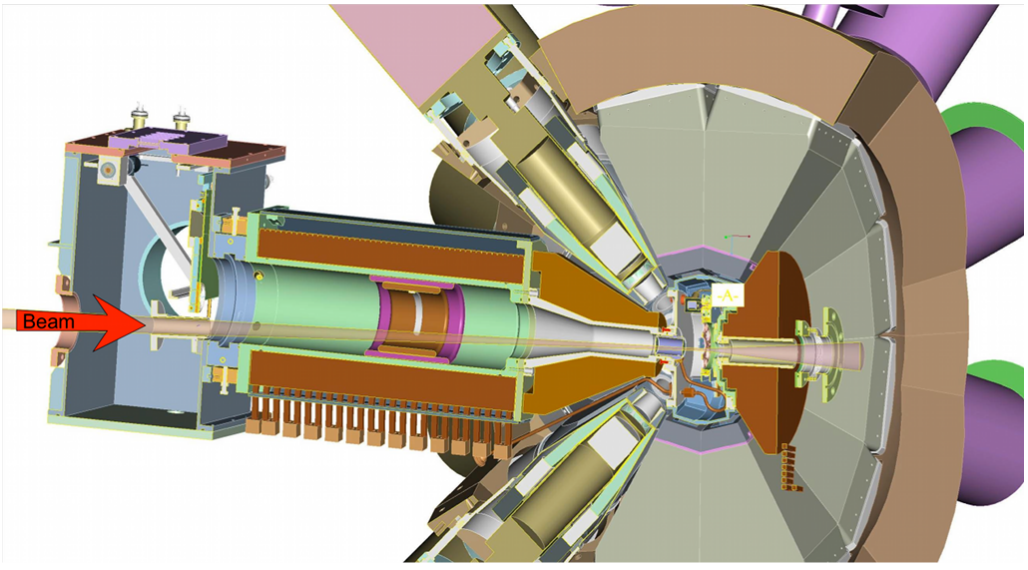

Figure 1.2: Cut-through of the SAGE electron spectrometer (left) and JUROGAMII γ-ray detector array (right). The ion beam enters from the left and passes through the SAGE solenoid (shown in brown) and is focused onto a target at the focus of JUROGAMII.

1.2 Thesis Overview

In this work the SAGE spectrometer is used to measure $E0$ transition strengths in ^{154}Sm. This is done as a test of collective interpretations of the 0_2^+ band in ^{154}Sm, from which strong $E0$ transitions to the ground state band are predict. The measurement is performed by means of Coulomb excitation (CoulEx) of a samarium target and recording subsequently emitted conversion electrons and γ rays. Gating on coincident γ-rays transitions is used to cleanly identify experimental transitions of interest. Relative intensities of transition modes are then used to determine the transition strengths. Considerable effort is given to understanding of the SAGE system, including development of electron peak fitting and time-based background subtraction techniques, in order to facilitate the measurement.

In Chapter 2 an overview of theory relevant to the subsequent work is presented. Firstly, the link between experimental observables for electromagnetic transitions and the associated nuclear matrix elements is discussed. The focus is on single γ rays and conversion electrons. Secondly, a brief overview of relevant nuclear models is given. In each case the interpretation of $E0$ matrix elements within the model is given.

Chapter 3 and Chapter 4 provides a guide to equipment and data processing with the SAGE setup. A discussion of all the equipment associated with SAGE is presented, as well as descriptions of the peak fitting and background subtraction techniques developed for use in this work.

In Chapter 5 the scientific motivation for exploration of $E0$ transitions in the rare-earth nuclei is presented. Subsequently, the test case experiment of ^{154}Sm is presented, details of the experiment are given and the preliminary results are shown.

Chapter 6 contains discussion of the analysis for the test case experiment. An upper limit result for an $E0$ transition in ^{154}Sm is given and discussion of the measured value in relation to competing theoretical models is presented.

Chapter 7 concludes the work with a discussion of the success of the test case experiment and suggestions for improvement and future work.

2

Theory

The nucleus is a many-bodied quantum mechanical system, which must exist in one of a series of orthogonal energy and angular momentum eigenstates. The lowest energy state is known as the ground state. A nucleus in any other state than the ground state will transition towards lower energy states, due to energetic favourability, wherever a physically allowed mode of transition exists. Study of the properties of transitions between two states yields information on the states involved, their spin, energy, parity and more detailed structure. In order to extract more detailed structural information, it is convenient to study transitions in which it is possible to separate the unknown nuclear state dependence from the force governing the transition.

2.1 Electromagnetic Transitions

A nucleus in an excited state may decay to a lower energy state in the nucleus via an electromagnetic transition. During such a transition, the angular momentum and the energy difference between the two states is transferred away from the nucleus by an emitted quanta. In this work, a discussion of single γ-ray emission and single electron emission is presented. Because the electromagnetic force is well understood these transition modes are particularly useful for extracting the nuclear dependence of the transition between states.

Electromagnetic interactions in the nucleus are categorised as *electric multipole* or *magnetic multipole* transitions of order l, m, where l and m are the angular momentum and projection of the transfer respectively. The parity of the transition is defined as [1]:

$$\text{Parity of electric multipole } l, m = (-1)^l \tag{2.1}$$

$$\text{Parity of magnetic multipole } l, m = -(-1)^l \tag{2.2}$$

Standard angular momentum selection rules apply; for a transition between a state ψ_A with angular momentum J_A and projection M_A and a state ψ_B with angular momentum J_B and projection M_B, only transitions of multipole order which obey

$$|J_A - J_B| \leq l \leq J_A + J_B \tag{2.3}$$

$$M_A - M_B = m \tag{2.4}$$

are allowed.

In general, the lowest-order multipole will be strongest. However, magnetic type transitions are generally weaker and an $l = 2$ electric transition may dominate over an $l = 1$ magnetic transition, for example [1].

2.1.1 Gamma-Ray Transitions

The most common form of electromagnetic transition is decay by emission of a γ-ray photon. The change with time of charges and currents in the nucleus during a transition between two states can create a radiating electromagnetic field, which can take away energy and angular momentum from the nucleus in the form of a photon.

Multipole Radiation Fields

The electric, $\varepsilon(r)$, and magnetic, $\mathcal{H}(r)$, multipole radiation fields produced by a system of charges and currents can be expanded, outside the source of the radiation, as [1]:

$$\varepsilon(r) = \sum_{l=1}^{\infty} \sum_{m=-l}^{l} a_E(lm)\varepsilon_E(lm;r) + a_M(lm)\varepsilon_M(lm;r) \tag{2.5}$$

$$\mathcal{H}(r) = \sum_{l=1}^{\infty} \sum_{m=-l}^{l} a_E(lm)\mathcal{H}_E(lm;r) + a_M(lm)\mathcal{H}_M(lm;r)\,, \tag{2.6}$$

where $\varepsilon_E(lm;r)$ is the electric field and $\mathcal{H}_E(lm;r)$ is the magnetic field for electric multipole radiation of order l, m. Similarly $\varepsilon_M(lm;r)$ and $\mathcal{H}_M(lm;r)$ are the fields for magnetic multipole radiation of order l, m. These functions are defined in Reference [1]. All $\varepsilon(lm)$ and $\mathcal{H}(lm)$ go to zero for $l = 0$, hence $L = 0$ transitions are strictly forbidden. The coefficients $a(lm)$ determine the amplitude of the corresponding multipole radiation and depend on the source of the radiation. In the case of γ-ray emission they depend on the nuclear transition. The coefficients, defined in Reference [1], are given by:

$$a_\sigma(lm) = -\frac{4\pi}{(2l+1)!!}\left(\frac{l+1}{l}\right)^{1/2} k^{l+2} X_{\sigma lm} \tag{2.7}$$

where $k = E_\gamma/\hbar c$ and $X_{\sigma lm}$ is the multipole moment of order l, m of the transition. The symbol σ denotes the multipole type, E or M. This result is correct in the long wavelength approximation, in which the radiating charges are constrained to a volume much smaller than the wavelength of the emitted radiation. Given a typical nuclear radius of $R_0 = 1.2A^{1/3}\,\mathrm{fm}$ and the relation $\lambda_\gamma E_\gamma \approx 1240\,\mathrm{fm\,MeV}$ the long wavelength approximation is valid in the energy range of most nuclear transitions.

$X_{\sigma lm}$, which is denoted Q_{lm} for an electric multipole moment and M_{lm} for a magnetic multipole moment, contains all the nuclear information regarding the transition and is equivalent to the nuclear matrix element:

$$X_{lm} = \langle \psi_B | \hat{\mathfrak{M}}(lm) | \psi_A \rangle\,, \tag{2.8}$$

where $\hat{\mathfrak{M}}(lm)$ is the electric or magnetic multipole moment operator.

Transition Probability

The probability for transition via the emission of a γ ray of a given multipole field can be considered in terms of the energy carried by the field. The Poynting vector giving the rate of flow of energy in a light wave is given by

$$S = \varepsilon \times \mathcal{H} \,. \tag{2.9}$$

For a pure multipole field, the rate of energy being radiated away from the source into a given solid angle, $d\Omega$, is obtained as [1]:

$$U_\sigma(lm;\Omega) = \frac{c}{2\pi k^2} Z_{lm}(\theta,\phi)|a_\sigma(lm)|^2 \,, \tag{2.10}$$

where $Z_{lm}(\theta,\phi)$ is the angular distribution of the emitted energy. Z is a function of l, m and the spherical harmonics $Y_{lm}(\theta,\phi)$, but independent of the electric or magnetic type of the multipole field. As a result the angular distribution of emitted radiation can only yield information on the order of the multipole. The type of the multipole can be determined from the polarisation of ε and $\mathcal{H}$ which differs everywhere by 90° between the two types.

Integrating $U_\sigma(lm;\Omega)$ over all space gives the energy that would be radiated out of the system per second by the pure multipole field. Dividing this by the transition energy, E_γ, gives the transition probability for the pure multipole γ-ray transition, $W_\gamma(\sigma lm)$, in units of s^{-1}. The full integral over all space of $Z_{lm}(\theta,\phi) = 1$, the transition probability can be written by the combination of Equations (2.7) and (2.10) as

$$W_\gamma(\sigma lm) = \frac{8\pi(l+1)}{l[(2l+1)!!]^2} \frac{k^{2l+1}}{\hbar} |X_{\sigma lm}|^2 \,. \tag{2.11}$$

The partial mean lifetime of the state, with respect to decay by the given multipole γ-ray transition, is then given by

$$\tau_\gamma(\sigma lm) = \frac{1}{W_\gamma(\sigma lm)} \,. \tag{2.12}$$

Experimental Forms

For an experimentally measured transition between two states, the total γ-transition rate will be a sum of all the possible decay modes,

$$\tau_\gamma(\psi_A \to \psi_B) = \frac{1}{\sum\limits_{\sigma,l,m} W_\gamma(\sigma lm;\psi_A \to \psi_B)} \,. \tag{2.13}$$

It is convenient to define "reduced transition probability" between two states, $B(\sigma l)$, which depends only on the angular momentum transferred, l, and the transition multipole type[1] [2]. The value of $B(\sigma l)$ is defined as

$$B(\sigma l;\psi_A \to \psi_B) = \frac{1}{2J_A+1} |\langle \psi_B || \hat{\mathfrak{M}}(\sigma l) || \psi_A \rangle|^2 \,. \tag{2.14}$$

[1] Clearly the multipole type and l are related by the parity of the transition, as defined in Equations (2.1) and (2.2).

where the double line denotes that this is the "reduced matrix element" and is independent of m, M_A and M_B. Hence, one can write the equivalent relationship to Equation (2.11), for the γ-ray transition probability between two states independent of initial polarisation M_A or transfer m,

$$W_\gamma(\sigma l; \psi_A \to \psi_B) = \frac{8\pi(l+1)}{l[(2l+1)!!]^2}\frac{k^{2l+1}}{\hbar}B(\sigma l; \psi_A \to \psi_B)\,. \tag{2.15}$$

The value of $B(\sigma l)$ may be considered as the square of the individual transition matrix elements (Equation (2.8)) averaged over the initial sub-states, M_A, and summed over the final sub-states, M_B [2]. It is common to make use of the Wigner-Eckart theorem for a spherical tensor operator [2, 3], such that the individual matrix elements may be written as

$$\langle \psi_B|\hat{\mathfrak{M}}(\sigma lm)|\psi_A\rangle = \langle J_A M_A lm|J_B M_B\rangle \frac{\langle \psi_B||\hat{\mathfrak{M}}(\sigma l)||\psi_A\rangle}{\sqrt{2J_B+1}}\,. \tag{2.16}$$

The first term is a Clebsch-Gordan coefficient, containing all m dependence, and the second term is the "reduced matrix element".[2,3].

Weisskopf Units

The native units for a reduced transition probability $B(El)$ are e^2fm^{2l} and those for $B(Ml)$ are $\mu_N^2 fm^{2l-2}$ (both may also be expressed in e^2b^l), but it is common to make use of the Weisskopf single particle estimates to express each in units which provide quantitative physical insight [5]. The Weisskopf single particle estimates solve the reduced matrix element of the multipole moment operator assuming a single nucleon in a spherical potential-well moving from a $J = \frac{1}{2}$ to a $J = \frac{1}{2}+l$ orbital. If the radius of the potential well is taken to be $1.2A^{1/3}\,fm$ then single-particle estimates for reduced transition probability are given by

$$B(El)_{sp} = \frac{1}{4\pi}\left(\frac{3}{l+3}\right)^2 (1.2A^{1/3})^{2l} \quad \text{in units of } e^2fm^{2l} \tag{2.17}$$

and

$$B(Ml)_{sp} = \frac{10}{\pi}\left(\frac{3}{l+2}\right)^2 (1.2A^{1/3})^{2l-2} \quad \text{in units of } \mu_N^2 fm^{2l-2}\,. \tag{2.18}$$

These single-particle estimates form the Weisskopf Units (W.u.) which are different for each nuclear mass and transition multipole moment. It is usual to quote the reduced transition probability for measured de-excitation in W.u. This gives a very rough estimate of how like a single-particle transition a measurement is. A value of 1,000 W.u., for example, appears very collective.

[2] In a basic model the reduced matrix element may be given implicitly by $\langle \psi_B||\hat{\mathfrak{M}}(\sigma l)||\psi_A\rangle = \sum_{M_A}\sum_{M_B}\langle \psi_B|\hat{\mathfrak{M}}(\sigma lm)|\psi_A\rangle$ [4].

[3] The factor of $1/\sqrt{2J_B+1}$ may be absorbed into the definition of the reduced matrix element, depending on the formalism used [2].

2.1.2 Internal Conversion Electrons

As well as emission of a photon, an excited nucleus may alternatively decay to a lower energy state by electromagnetic interaction with a bound atomic electron. In this process, energy is transmitted directly to the electron causing it to transition to an unbound state. The process is known as internal conversion. When first discovered, the process was wrongly described as an internal photon effect, in which a photon emitted by the nucleus, is absorbed by an atomic electron [6]. While governed by the exchange of virtual photons which mediate the Coulomb force, no actual photons take part in the transition and the process occurs independently of their emission [7, 3]. As a result, internal conversion is a competing process to the emission of γ rays and the total transition probability is a sum of both processes [8].

The kinetic energy of the emitted electron, T_e, depends on the binding energy of the electron, B_e. Neglecting nuclear recoil, this is given by [5]

$$T_e = E_\gamma - B_e \,. \tag{2.19}$$

As B_e depends on the shell (and sub-shell) from which an electron is emitted, the conversion electrons are labelled according to their origin shell e.g. K, $L_{1,2,3}$, $M_{1,2,3,4,5}$. Each will have a different transition probability. Internal conversion is a threshold process, decay by emission of the most bound electrons may not be possible for low-energy transitions.

Conversion electron spectra show discrete peaks for the different energy electrons from different shells. Furthermore, characteristic energy X-rays are also observed in coincidence with internal conversion. These correspond to the atomic transition of a valence electron moving to fill the core vacancies left by internal conversion. Hence, the X-ray energy depends on the shell of the converted electron electrons.

Transition Probability

For a given electron shell, the probability that a nuclear de-excitation proceeds via emission of an electron from that shell, by an electric type interaction, is proportional to the following matrix element [1]:

$$W_e(E) \propto \langle \psi_B | \langle \varphi_{e,f} | \Phi | \varphi_{e,i} \rangle | \psi_A \rangle \,, \tag{2.20}$$

where Φ is the electric scalar potential, between the electron and nucleus, in the electromagnetic field of the transition. The wavefunctions ψ_A and ψ_B are the nuclear states and $\psi_{e,i}$ and $\psi_{e,f}$ are the initial and final states of the electron. For a K-shell electron, the initial bound wavefunctions, $\varphi_{e,i}$, is given by [1, 3]

$$\varphi_{e,i} = (\pi a^3) \exp\left(\frac{-r}{a}\right) \tag{2.21}$$

where $r = |\vec{r}|$, $\vec{r}$ is the position vector of the electron, $a = a_0/Z$ and a_0 is the Bohr radius of the hydrogen atom. The final free wavefunctions of the electron, $\varphi_{e,f}$, can be given in

the plane wave approximation, when $T_e >> B_e$, as [1]

$$\varphi_{e,f} \propto \exp(i\vec{k} \cdot \vec{r}) \,, \tag{2.22}$$

where $\vec{k}$ is the wave vector of the outgoing electron.

Equation (2.20) may be expanded as [3, 9]

$$W_e(E) \propto \frac{Z}{4\pi\epsilon_0} \int \psi_B^*(\vec{R}) \varphi_{e,f}^*(\vec{r}) \frac{e^2}{|\vec{r} - \vec{R}|} \varphi_{e,i}(\vec{r}) \psi_A(\vec{R}) \; d^3R \; d^3r \,, \tag{2.23}$$

where the integral is over all space for both coordinates.

One can make use of the following expansions, which separate out the multipole dependence of the interaction [1, 9]:

$$\frac{1}{|\vec{r} - \vec{R}|} = \begin{cases} \dfrac{1}{r} \displaystyle\sum_l \sum_m \left(\frac{R}{r}\right)^l \frac{4\pi}{2l+1} Y_{lm}^*(\vec{r}) Y_{lm}(\vec{R}), & \text{for } R < r \\ \dfrac{1}{R} \displaystyle\sum_l \sum_m \left(\frac{r}{R}\right)^l \frac{4\pi}{2l+1} Y_{lm}^*(\vec{r}) Y_{lm}(\vec{R}), & \text{for } R > r \,. \end{cases} \tag{2.24}$$

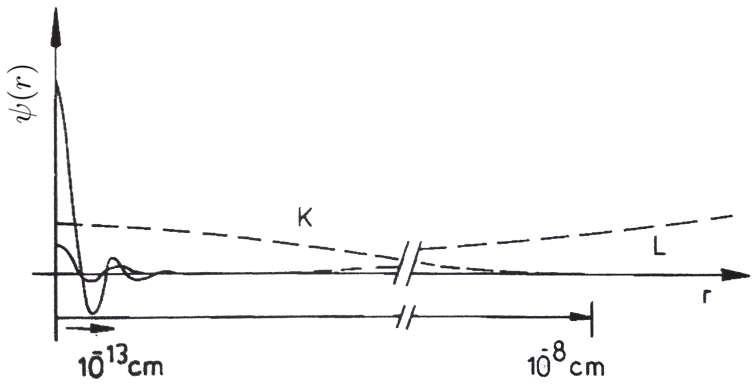

Figure 2.1: Pictorial representation of the different length scales of nuclear (solid lines) and electronic (dashed lines) wavefunctions [3]. The K electron shell has the most overlap with the nucleus of any atomic electron, but its radial extent is much larger and the majority of its probability distribution lies outside the nucleus. The L electron wavefunction has a radial extent which is larger still, its wavefunction drops as r approaches 0, makings its overlap with nucleus minimal.

From Figure 2.1, which shows the overlap of nuclear and bound electron wavefunctions, it can be seen that the radial limit, at which $\varphi_{e,i}(\vec{r})$ tends to zero, is much larger than that of $\psi_A(\vec{R})$. As a result, the main contribution to the integration comes from the region $r > R$. Hence, by combining the $r > R$ relation of Equation (2.24) with Equation (2.23) and the relation [1]

$$Q_{lm} = e \int R^l Y_{lm}(\vec{R}) \psi_B^*(\vec{R}) \psi_A(\vec{R}) \; d^3R \,, \tag{2.25}$$

it can be shown that [4]

$$W_e(Elm) \propto Q_{lm}\,. \tag{2.26}$$

It is possible to separate all the nuclear dependence of an electron conversion, for a given electron shell and multipole order, into a single nuclear matrix element, upon which the equivalent γ-ray transition of the same multipolarity also depends.

Conversion Coefficients

As both internal conversion and γ-ray transitions depend on the same nuclear matrix element, it is common experimentally to refer to the ratio of their intensities, α. The ratio α is called the conversion coefficient and is a measure of which transition mode is preferred [1]. It is defined as

$$\alpha_i(\psi_A \rightarrow \psi_B) = \frac{W_{e,i}}{W_\gamma}\,, \tag{2.27}$$

where the subscript i denotes one or a sum of electron shells. The total conversion coefficient, α, for a transition is the sum of all of the individual shell conversion coefficients, α_i. It is also useful to note the relationship between the total lifetime, τ, for the transition and the partial lifetimes with respect to γ-emission, τ_γ,

$$\tau_\gamma(1+\alpha) = \tau\,. \tag{2.28}$$

For a given multipole transition, $\alpha_i(\sigma l)$ is independent of the nuclear properties of the transition and depends only on a series of atomic and electromagnetic properties deemed calculable. A non-relativistic calculation, assuming a point-like nucleus, gives the following approximate electric and magnetic multipole conversion coefficients [5]

$$\alpha(El) \cong \frac{Z^3}{n^3}\left(\frac{l}{l+1}\right)\left(\frac{e^2}{4\pi\epsilon_0\hbar c}\right)^4\left(\frac{2m_ec^2}{E_\gamma}\right)^{(l+5)/2} \tag{2.29}$$

$$\alpha(Ml) \cong \frac{Z^3}{n^3}\left(\frac{e^2}{4\pi\epsilon_0\hbar c}\right)^4\left(\frac{2m_ec^2}{E_\gamma}\right)^{(l+3)/2}\,, \tag{2.30}$$

where n is the principal quantum number for the bound electron wavefunction, n_K=1, n_L=2, n_M=3 and so on. These results are an oversimplification, as for transitions of energy $\gtrsim$ 0.5 MeV, the emitted electrons are no longer in the classical limit $T_e << m_ec^2$, and therefore must be treated relativistically. Additionally these results do not account for the effects produced as the electron wavefuction penetrates the nucleus, i.e. the nucleus cannot be treated as point like. They serve to illustrate the important features of electron conversion, which are consistent for more thorough calculations and can provide rough-value estimates.

From Equations (2.29) and (2.30), it can be seen that internal conversion becomes an increasingly important process in nuclei with large Z. For a 100 keV $E2$ transition in neon (Z=10), internal conversion is almost negligible as $\alpha_K \approx$0.006, but for the same

[4] A full derivation, including both the electric scalar and magnetic vector potentials of the transition, yields results for both electric and magnetic multipoles [9].

type of transition in samarium (Z=62) internal conversion is the dominant process, with $\alpha_K \approx$1.5. Conversion coefficients also decrease rapidly with increasing transition energy; this is partly a feature of the increase of W_γ, as shown in Equation (2.11). High-order multipole transitions of both types favour electron conversion. For example, a 200 keV $E2$ transition in samarium yields $\alpha_K \approx$0.13 but for a 200 keV $E4$ transition, $\alpha_K \approx$0.83. This effect can be considered in terms of the higher degrees of forbiddeness for a photon to carry angular momentum $L > 1$, whereas the large radial extent of the initial electron wavefunction allows for enhanced angular momentum transfer. The multipole dependence of conversion coefficients can be used to great effect in experimental nuclear physics. For a mixed multipole transition, the measured conversion coefficient can be used to determine the fraction of each multipole in the transition. Furthermore, for a transition of unknown multipolarity, the measurement of characteristic conversion coefficients can provide an identification of both the multipole order and type, σl, of the transition. This is an advantage over γ-ray angular distributions, which can only determine l and not the parity. Finally it should be noted α_i decreases for higher atomic shells. This follows from the simple observation that the higher-shell electrons have the majority of their bound probability distribution further from the nucleus and hence the electromagnetic interaction is weaker.

Realistic definitions for internal conversion coefficients can be in found in Reference [10], which uses the relativistic Hartree-Fock-Slater method to correct for the previously omitted relativistic behaviour of electrons. Further work in Reference [9], using the Dirac-Fock calculations, aim to account for the interaction when the electron is inside the nucleus. A comparison of calculations to measured values is performed in Reference [11]. The most accurate conversion coefficients are available from the BRICC conversion coefficient calculator [12].

2.1.3 E0 Transitions

Electric monopole transitions are valid under angular momentum selection rules between any states with matching spin, J, and parity, π. However, they are most important in transitions between states with 0 angular momentum, where no other transition modes are available.

Electric monopole γ-ray emission is strictly forbidden as photons have one unit of intrinsic angular momentum. Furthermore, the transition process is one where the Coloumb field is acting and photons are only exchanged 'vertically' [3]. This is a purely radial motion, or pulsation of the charges, which does not alter the electric fields at any point external to the charge volume [5]. Thus, monopole transitions do not produce any electromagnetic field outside of the system of charges, there is no radiative field. Energy transfer must take place inside the volume of the nucleus [1].

A small part of the atomic electron wavefunction does overlap with the nucleus, as shown in Figure 2.1. As a result, $E0$ transitions by internal conversion are possible. As single γ-ray emission is forbidden for $E0$ transitions, a conversion coefficient cannot be defined. The electron transition probability can be approximated from Equation (2.23) using expansion in Equation (2.24). In the region $R < r$, the expansion for $l = 0$ yields

$1/r$ and hence the contribution to $W_e(E0)$ is zero,

$$\int \psi_B^*(\vec{R})\psi_A(\vec{R})\, d^3R = \delta_{AB}\,. \tag{2.31}$$

In the region $R > r$, the expansion for $l = 0$ yields $1/R$ and hence

$$W_e(E0) \propto \int \psi_B^*(\vec{R})\varphi_{e,f}^*(\vec{r})\frac{1}{R}\varphi_{e,i}(\vec{r})\psi_A(\vec{R})\, d^3R\, d^3r\,. \tag{2.32}$$

The integral over the electron coordinate from 0 to R yields the result

$$W_e(E0) \propto \langle\psi_B|R^2|\psi_B\rangle\,. \tag{2.33}$$

More generally, monopole transition strengths are proportional to the nuclear matrix elements of the $E0$ operator, $\hat{T}(E0)$.

The dimensionless monopole transition strength, $\rho(E0)$, is introduced as

$$\rho(E0) = \frac{\langle\psi_B|\hat{T}(E0)|\psi_B\rangle}{er_0^2A^{2/3}}\,, \tag{2.34}$$

which contains all of the nuclear structure information [13]. The monopole transition probability for an allowed process, i, is then related by

$$W_i(E0) = \rho^2(E0)\Omega_i \tag{2.35}$$

where Ω_i is the calculated electronic factor for the process i, which is independent of the nuclear properties of the transition. For internal conversion, the electronic factors for conversion of different electron shells are calculable with the BRICC conversion coefficient calculator [12]. In cases where it is energetically allowed, the K electron shell dominates $E0$ electron conversion due to its large overlap with the nucleus.

Other allowed process for $E0$ decays include pair-production and double γ-ray emission. These processes are both of higher order than electron conversion and will not be discussed in this work.

2.2 E0 Transitions in Nuclear Models

In Section 2.1 the means of extracting nuclear matrix elements between two states for given transition operators by the study of electromagnetic transition rates was discussed. Direct interpretation of these nuclear matrix elements is not possible due to the absence of a unified understanding of the nucleus. The nucleus is a complex many-body system made up of protons and neutrons, collectively called nucleons, which are themselves composite particles of quarks. A single nuclear state is the result of interactions between all of the individual nucleons; a product of two body forces, three body forces and higher order forces, for which there exists no complete analytical solution. There exist many different nuclear models which match experimental data. Some are microscopic, describing the behaviour of individual nucleons, and some are macroscopic, describing the bulk behaviour of nuclear matter which result from the sum of the internal interactions. This section briefly introduces some important nuclear models and discusses the interpretation of $E0$ matrix elements in each.

2.2.1 Shell Model

The shell model is a microscopic model which attempts to describe the nucleus in terms of the individual nucleon wavefucntions and two-body nucleon-nucleon interactions. The nucleus wavefunction is given as [14]

$$|\Psi\rangle = |\varphi_1\varphi_2\varphi_3...\varphi_A\rangle\,, \tag{2.36}$$

where the the multiplicative sum is in fact a Slater determinant, which is required as nucleons are fermions and the wavefunction must be anti-symmetrised under particle exchange.

A full solution would require the Hamiltonian

$$H = T + \sum_{i\neq j} V_{ij}\,, \tag{2.37}$$

where T is the sum kinetic energy and V_{ij} is the potential due to interaction between the i^{th} and j^{th} nucleons.

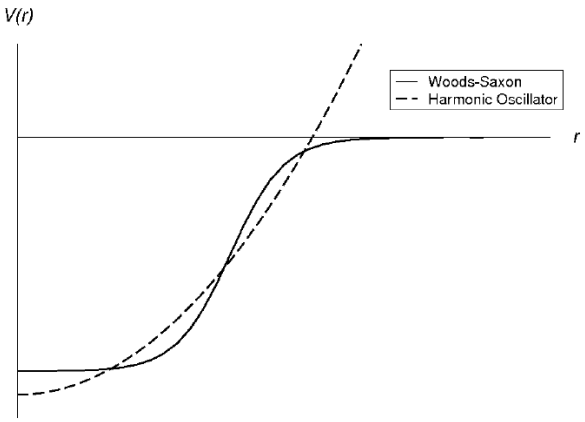

Figure 2.2: Schematic comparison of simple harmonic oscillator and Wood-Saxon potentials. The Wood-Saxon is a more realistic finite potential, with a diffuse edge and flat interior, which mirror well the short range of the nuclear force and incompressibility of nuclear matter.

The shell model makes the assumption that the nucleus can be described by non-interacting nucleons in a simplified mean-field with the addition of a small residual interaction.

$$H = H_0 + H_{res}\,, \tag{2.38}$$

where the residual interaction H_{res} has the form $\sum_{i\neq j} V_{ij}$. H_0 is usually constructed from a kinetic energy term, a Wood-Saxon potential and a spin-orbit term. The Wood-Saxon potential is shown in Figure 2.2 and is used as a more realistic mean-field potential than the harmonic oscillator potential [2]. The spin-orbit term is added to account for the strong spin-orbit coupling, which favours parallel alignment of angular momentum so that particles with $j = |l| + |s|$ are more bound (lower energy states). The individual nucleon wavefunctions φ_i are then taken as the solutions to H_0.[5] The φ_i form an orthonormal basis set with quantum numbers n, l, j and m_j. Their single particle energies, given by $\langle\varphi_i(nlj)|H_0|\varphi_i(nlj)\rangle$, are $2j+1$ degenerate and form the level scheme for the non-interacting nucleon shells shown in Figure 2.3. The most notable feature, is the correct recreation of the major shell gaps, or "magic numbers", which are observed in stable nuclei [3].

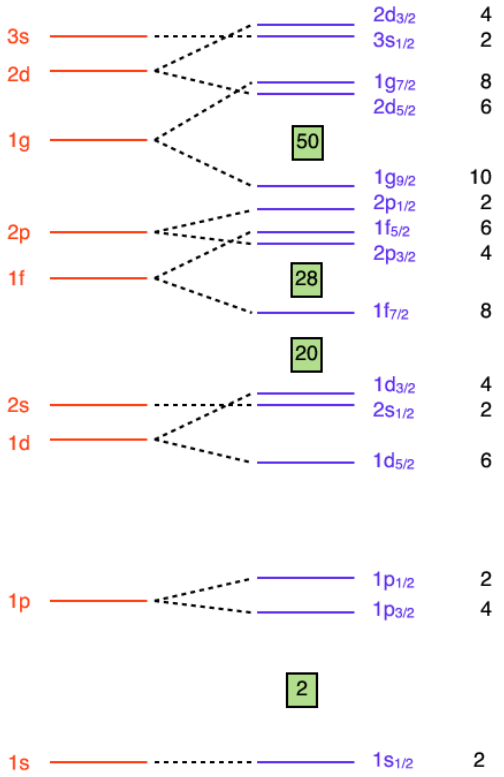

Figure 2.3: Illustration of the energy spacings of the single particle orbitals produced by the shell model. States of nl before the inclusion of spin-orbit coupling are shown on the left and states of nl_j with coupling on the right. The orbital occupancy $2j+1$ is labelled on the far right and the major shell gaps 2,8,20,28 and 50 are indicated.

A complete set of orthonormal basis states can be constructed for the nucleus in terms of the non-interacting H_0. These basis states are defined in terms of the occupied orbitals and total spin and parity J^π.[6] The energies of the basis states depend only on the nucleon occupancy and are energy degenerate with respect to J^π [14]. This degeneracy is broken by

[5] The individual nucleon wavefunctions φ_i are usually constructed from a linear sum of oscillator wavefunctions, in which one dominates [15].

[6] The basis state wavefunctions may be constructed from a sum of Slater determinants of single particle $\varphi(nljm_j)$.

the introduction of the residual interaction H_{res}, the largest term in which is the pairing interaction which strongly couples m_j^+ nucleons to m_j^- nucleons in the same orbital to form 0^+ pairs.

To a good approximation, the shell model can be solved by only considering valence nucleons, that is the nucleons outside of a filled shell when all nucleons are in their lowest energy configuration. The nucleons inside the closed shell are treated as an inert core of total $J^+ = 0^+$ to which the valence nucleons couple.

State Mixing

State mixing can occur in any situation in which an additional perturbative interaction is added to an established system. If one considers a complete set of orthonormal basis states, Ψ_1, Ψ_2, Ψ_3, for an initial Hamiltonian H_0, one may expand the Hamiltonian matrix elements as

$$\langle_j \Psi | H_0 | \Psi_i \rangle = \begin{bmatrix} E_{11} & 0 & 0 \\ 0 & E_{11} & 0 \\ 0 & 0 & E_{22} \end{bmatrix} . \tag{2.39}$$

The addition of a new interaction to the model space can produce off-diagonal matrix elements, such as

$$\langle \Psi_j | H | \Psi_i \rangle = \begin{bmatrix} E_{11} + V_{11} & V_{12} & 0 \\ V_{12} & E_{11} + V_{22} & 0 \\ 0 & 0 & E_{22} \end{bmatrix} . \tag{2.40}$$

Here V_{ij} gives the energy of the perturbative interaction between two basis states. In the shell model, the addition of interactions between nucleons in different shells will not only change the energy of basis states containing nucleons of both shells but also create interactions between basis states of different configurations. The new Hamiltonian must be diagonalised to determine the eigenstates that will be observed in the new system. The new set of states consist of admixtures of the original basis states in the form

$$|\tilde{\Psi}\rangle = \sum_i a_i |\Psi_i\rangle \, . \tag{2.41}$$

where $\sum |a_i|^2 = 1$.

Microscopic $E0$ Operations

The monopole operator can be expressed in terms of single-nucleon degrees of freedom as

$$\hat{T}(E0) = \sum_k e_k r_k^2 \, , \tag{2.42}$$

where the sum is over all nucleons, e_k is the effective charge of the k^{th} nucleon and r_k is its position with respect to the centre of mass. Diagonal matrix elements of the operator yield the mean-squared charge radius of a given state. The off-diagonal matrix elements

yield the monopole transition strength between states, given as

$$\rho^2_{fi}(E0) = |\langle\tilde{\Psi}_f|\hat{T}(E0)|\tilde{\Psi}_i\rangle|^2 \frac{1}{e^2 r_0^4 A^{4/3}} \tag{2.43}$$

Between initial state $|\tilde{\Psi}_i\rangle$ and final state $|\tilde{\Psi}_f\rangle$, which are composite states in the form of Equation (2.41), the $E0$ matrix element can be expanded in terms of basis states as [15]

$$\langle\tilde{\Psi}_f|\hat{T}(E0)|\tilde{\Psi}_i\rangle = \sum_h \sum_j a_h^i a_j^{f*} \langle\Psi_j| \sum_k e_k r_k^2 |\Psi_h\rangle \,. \tag{2.44}$$

Due to the scalar nature of r_k^2 and the orthogonality of the basis states, $\langle\Psi_j|\Psi_h\rangle = \delta_{hj}$, only $h = j$ terms contribute to the sum.

$$T_{fi} = \sum_j a_j^i a_j^{f*} \sum_k e_k \langle\Psi_j|r_k^2|\Psi_j\rangle \,. \tag{2.45}$$

If one were to consider states constructed from nucleons confined to a single harmonic oscillator shell, r_k is the same for all nucleons and independent of $|\Psi_j\rangle$, hence

$$T_{fi} = Zr^2 \sum_j a_j^i a_j^{f*}. \tag{2.46}$$

As orthogonality of initial and final state requires $\sum_j a_j^i a_j^{f*} = 0$, the result is vanishing $E0$ transition strength for states of nucleons confined to a single oscillator shell. Realistic single nucleon wavefunctions include multiple harmonic oscillator shells and basis state configurations may include several nucleon shells. Considering the situation restricted to simple two-state mixing, giving the states

$$|\tilde{\Psi}_i\rangle = a|\Psi_1\rangle \; + b|\Psi_2\rangle \tag{2.47}$$

$$|\tilde{\Psi}_f\rangle = -b|\Psi_1\rangle \; + a|\Psi_2\rangle \,, \tag{2.48}$$

Equation (2.45) can be written explicitly as

$$T_{fi} = \sum_k ab \left(\langle\Psi_2|e_k r_k^2|\Psi_2\rangle - \langle\Psi_1|e_k r_k^2|\Psi_1\rangle\right) . \tag{2.49}$$

If Ψ_1 and Ψ_2 differ in configuration only by a pair of protons moving between shells c and d then

$$T_{fi} = 2e_p ab \left(\langle r_c^2\rangle - \langle r_d^2\rangle\right) . \tag{2.50}$$

Real transitions involve more complex sums of many basis states, but these examples serve to demonstrate the importance of mixing of different radii within state wavefunctions, to achieve non-vanishing $E0$ transitions. The phenomenon of intruder orbitals, in which additional interactions lower the energy of higher n shells, causing greater shell mixing, is clearly important for $E0$ transitions. Such intruder orbitals can be seen in Figure 2.3, where the addition of the spin-orbit interaction dramatically lowers some shell energies. If Equation (2.50) is solved assuming maximal mixing ($a = b = 1/\sqrt{2}$) and radii

corresponding to adjacent harmonic oscillator shells, expected ρ^2 values are given by [15]

$$\rho^2(E0)_{fi} = 0.5A^{-2/3}\,. \tag{2.51}$$

This gives $\rho^2 \times 10^3$ values of 43 and 15 for A=40 and 200, respectively. However, the following observation should be considered. The orbital radius of a particle bound in a potential well, such as that shown in Figure 2.2, will decrease as the particle becomes more bound. As such, the effect of intruder orbitals may not be as extreme as indicated in Equation (2.51). However, this example still serves to show approximate values of ρ^2 for single particle transitions and the expected scaling with respect to A.

2.2.2 Bohr and Mottleson Collective Model

When the behaviour of the nucleus is dominated by a large sum of many small interactions, over a large number of nucleons, microscopic models can become limited. Instead these nuclei may be described in macroscopic models, which consider the bulk behaviour of the nucleus as a volume, with some corrections for individual nucleon behaviour such as pairing.

The Bohr and Mottleson collective model builds on the liquid drop model [5] and describes excitations in terms of surface vibrations and bulk rotation of nuclei. The starting assumption is that the nucleus has a well defined surface, which can be described by an expansion of spherical harmonics as

$$R(\theta,\phi,t) = R_0\left(1 + \sum_{\lambda\geq 1}\sum_{\mu=-\lambda}^{+\lambda}\alpha_{\lambda\mu}(t)Y_{\lambda\mu}(\theta,\phi)\right)\,, \tag{2.52}$$

where $\alpha_{\lambda\mu}$ are the time dependent amplitudes of the relevant harmonic and form the full set of degrees of freedom of the system.

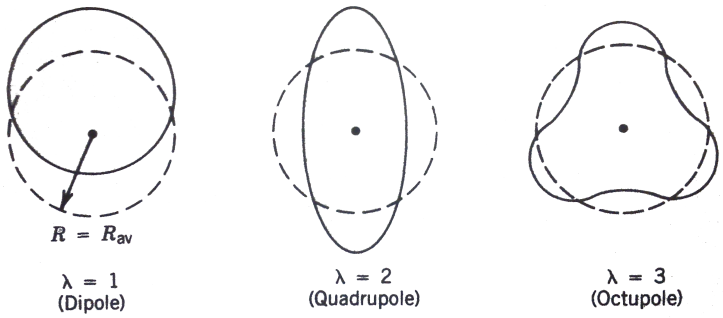

Figure 2.4: Illustration of the lowest 3 orders of deformation, shown as a slice through the nucleus for one possible projection.

The lowest-order deformations are shown in Figure 2.4, where the order λ defines the type of shape. The degrees of freedom with $\lambda = 1$, labelled dipole, correspond to a shift of the centre of mass and may generally be neglected. Degrees of freedom with $\lambda = 2$ (quadrupole), which correspond to ellipsoid deformation, are the most important terms of the expansion to consider, and will be considered exclusively in the remainder of this

section. The $\lambda = 3$ (octupole) degrees of freedom break reflection symmetry and are important for negative parity excitations.

Quadrupole Vibration

The energy associated with quadrupole degrees of freedom, about a spherical equilibrium, may be described by the general harmonic Hamiltonian [16]

$$H = T + V = \sum_{\mu=-2}^{2} \left\{ -\frac{\hbar^2}{2B}\frac{\mathrm{d}^2}{\mathrm{d}\alpha_\mu^2} + \frac{C}{2}|\alpha_\mu|^2 \right\} , \tag{2.53}$$

where B is the mass parameter and C is the restoring force constant, or "nuclear stiffness". The eigenenergies associated with each degree of freedom are then [4]

$$E_{\alpha_\mu} = \hbar\omega(n_{\alpha_\mu} + \tfrac{1}{2}) \tag{2.54}$$

where $\omega = \sqrt{C/B}$ and $n_{\alpha_\mu} = 0, 1, 2...$ is the number of quanta associated with the excitation mode.

It is common to refer to excited states in terms of the quanta of the normal modes of excitation [17]. For purely vibrational modes of excitation, the quanta are referred to as phonons. Bohr states [17] that a vibrational mode is characterised by the property that it can be repeated a large number of times. The n^{th} excited state of a specified mode can this be viewed as consisting of n individual quanta. The dynamic variables associated with the degrees of freedom may be defined in terms of quanta creation and annihilation operators. In the case of quadrupole vibration, one writes

$$\alpha_\mu = \sqrt{\frac{\hbar}{2B\omega}}(b_\mu + (-)^\mu b^\dagger_{-\mu}) \tag{2.55}$$

where $b^\dagger_\mu$ and b_μ are the operators that create and destroy an α_μ quanta of excitation, which is referred as a quadrupole phonon with projection μ [16]. Acting $b^\dagger_\mu$ on the spherical ground state creates the first excited α_μ state with $n_{\alpha_\mu} = 1$:

$$|n_{\alpha_\mu} = 1\rangle = b^\dagger_\mu|0\rangle \, . \tag{2.56}$$

This introduces a $Y_{2\mu}$ dependence to the wavefunction, equating to two units of angular momentum with a projection μ. Subsequently, it is said that the quadrupole phonon associated with the excitation carries two units of angular momentum.

In the above description for a spherical equilibrium, the energies of the different α_μ quanta are degenerate. As such it is normal to refer only to the total number of quadrupole phonons, n. Coupling to a 0^+ ground state the degenerate $n = 1$ state clearly has spin and parity 2^+. For $n = 2$ three possible states 0^+, 2^+ and 4^+ emerge from angular momentum coupling. There are no $n = 2, J = 1$ or $n = 2, J = 3$ states, as only certain n_μ combinations are allowed due to symmetry requirements of the wavefunction [5].

Quadrupole Deformation

It is convenient to make a transformation of coordinates $\{\alpha_{\lambda\mu}\} \rightarrow \{a_{\lambda\mu}\}$, such that the principal axes of deformation are aligned with the axes of the spherical harmonics. For $\lambda = 2$, one finds for the set $\{a_\mu\}$ that $a_1 = a_{-1} = 0$ and $a_2 = a_{-2}$. Following the transform, the five coordinates $\{\alpha_{2\mu}\}$ are replaced by the new set $\{a_0, a_2, \theta_1, \theta_2, \theta_3\}$, in which $\theta_1, \theta_2, \theta_3$ are the three Euler angles describing the orientation of the nucleus in space and a_0, a_2 describe the ellipsoid surface by

$$R(\theta', \phi') = R_0 \left(1 + a_0 Y_{20}(\theta', \phi') + a_2[Y_{22}(\theta', \phi') + Y_{2-2}(\theta', \phi')]\right) . \tag{2.57}$$

For pure quadrupole deformation one may express a_0, a_2 in terms of the Hill-Wheeler coordinates β, γ giving

$$a_0 = \beta \cos(\gamma) , \tag{2.58}$$

$$a_2 = (\beta/\sqrt{2}) \sin(\gamma) . \tag{2.59}$$

The parameter β is a measure of total degree of deformation where $\sum |a_\mu|^2 = \beta^2$, with $\beta = 0$ presenting a sphere and $\beta \neq 0$ an ellipsoid . The angle γ describes the deviation from axial symmetry; for $\gamma = n\pi/3$ the system is symmetric about one of the three principal axes else the ellipsoid is triaxial. The coordinates β, γ are shown in Figure 2.5.

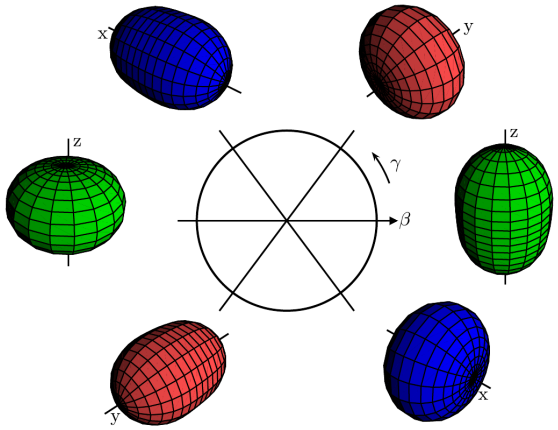

Figure 2.5: Hill-Wheeler coordinates β and γ. Parameter β extends radially from the spherical value 0 and may be negative. The angle γ rotates the deformation through triaxial to axially symmetric along different axes. The axial symmetric shapes for $\beta = 0.4$ are shown at each of the $\gamma = n\pi/3$ vertices [18].

In this system excitations are considered in terms of the Bohr-Mottleson Hamiltonian which is given in the general form [7]

$$H = T_{rot} + T_{vib} + V . \tag{2.60}$$

In this form T_{rot} refers to the energy of rotation of the fixed shape body, T_{vib} is the energy for vibration of the body fixed in space and V is the restoring potential for the shape parameters [18].

Quadrupole Deformed Rotor

For a nucleus with a fixed quadrupole deformation given by $\beta = \beta_0 \neq 0$ and $\gamma = \gamma_0$, the rotational energy may be expanded as a sum of rotation about the three principal axes k

[7] In this more general discussion the more complex vibration-rotation term has been omitted.

as [3]

$$T_{rot} = \frac{\hbar}{2} \sum_{k=1}^{3} \frac{R_k^2}{\mathcal{J}_k} \tag{2.61}$$

Here $\mathcal{J}_k$ is the moment of inertia about the body-fixed axis k and R_k is the component of rotational angular momentum R relative to the body-fixed axis. Moment of inertia $\mathcal{J}_k$ can be given as

$$\mathcal{J}_k = 4B\beta^2 \sin^2(\gamma - \tfrac{2}{3}\pi k)\,. \tag{2.62}$$

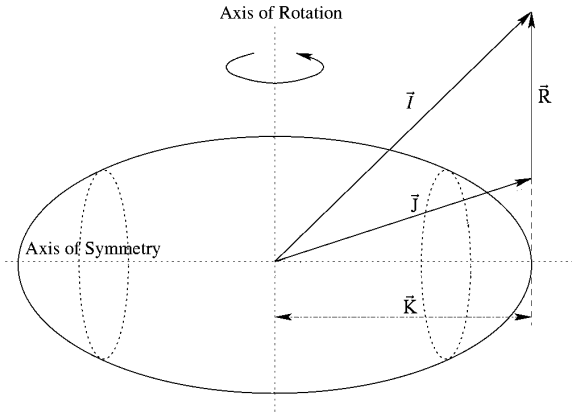

Figure 2.6: Angular momentum projections on an axially-symmetric quadrupole deformation nucleus.

The total angular momentum I is the sum of the rotational angular momentum R and intrinsic angular momentum J of the body-fixed system.

$$\vec{I} = \vec{R} + \vec{J} \tag{2.63}$$

For an axially-symmetric quadrupole deformation ($\gamma = 0$, $\beta \neq 0$), it is impossible to distinguish rotations about the symmetry axis, defined as the $k = 3$ axis. As a result $R_3 \equiv 0$ and $\mathcal{J}_1 = \mathcal{J}_2 = \mathcal{J}$ and only the sum of rotations perpendicular the symmetry axis need be considered. The projection of total angular momentum onto the symmetry axis $I_3 = K$ must therefore be conserved with change of rotation R in a rotational band. The relationship between the different angular momentum vectors is shown in Figure 2.6. In the adiabatic approximation the intrinsic structure is assumed to be rigid and the energy for rotations is given by [2]

$$T_{rot} = \frac{\hbar^2}{2} \left[\frac{I(I+1) - K^2}{\mathcal{J}} \right]. \tag{2.64}$$

As a consequence of reflection symmetry in $k = 1, 2$ plane, the $|K, IM\rangle$ and $|-K, IM\rangle$ states appear in a linear combination (where M is the projection J_z in the lab frame). If the intrinsic wavefunction is symmetric under a π rotation about the $k = 1$ or 2 axis, then the linear combination is given by [3]

$$\frac{1}{\sqrt{2}}[|K, IM\rangle + (-1)^{I+K}|-K, IM\rangle]\,. \tag{2.65}$$

For a $K = 0$ band, the two parts cancel for odd values of I and one observes the spin sequence $I = 0, 2, 4...$. For a $K \neq 0$ band, one observes the spin sequence $I = |K|, |K| + 1, |K| + 2...$ where the smallest possible value of I is naturally the projection K.

Rotational-Vibrational Spectra

In the case of a quadrupole-deformed equilibrium shape, the potential associated with vibrations is different to that of Equation (2.53), as the minimum of the potential is at a non-zero value of the shape parameters. For an axially-symmetric equilibrium shape ($\gamma = 0$), the surface shape coordinates a_0 and a_2 can be written as

$$a_0 = \beta_0 + \xi \tag{2.66}$$

$$a_2 = 0 + \eta\,, \tag{2.67}$$

where β_0 is the magnitude of the static deformation ξ and η are the new dynamic degrees of freedom. The magnitude of ξ and η is assumed to be small compared to β_0:

$$\left|\frac{\xi}{\beta_0}\right| \ll 1 \text{ and } \left|\frac{\eta}{\beta_0}\right| \ll 1\,. \tag{2.68}$$

Various parametrisations exist for the V terms of the Bohr Hamiltonian, which attempt to separate β-and γ-dependence [18]. In terms of ξ and η, the potential is given as

$$V(\xi, \eta) = \tfrac{1}{2}C_0\xi^2 + C_2\eta^2 \tag{2.69}$$

where the restoring force constants C_0 and C_2 are not equal and have different associated oscillation frequencies $\omega_\beta = \sqrt{C_0/B}$ and $\omega_\gamma = \sqrt{C_2/B}$ [19].

Neglecting the rotation vibration interaction, the wavefunction can be separated into a rotational part and parts dependent on ξ and η [4].

$$\Psi(\xi, \eta, \theta) = \varphi(\theta)g(\xi)\chi(\eta)\,. \tag{2.70}$$

As a result, the expected spectrum can be separated into two parts. Firstly, there will be a series of states relating to excitation modes of ξ and η, in the body-fixed frame. And secondly, a rotational band built on each of these states will be observed, with the rotational sequence dependent on the intrinsic properties of the band head state, as described in the previous section. Under the assumption of Equation (2.68), the energy spacing of all the associated rotational bands should approximately follow Equation (2.64), giving

$$T_{rot} = \frac{\hbar^2}{2}\left[\frac{I(I+1) - K^2}{3B\beta_0^2}\right]\,. \tag{2.71}$$

Excitations corresponding to ξ are termed "β-vibrations" and those corresponding to η are termed "γ-vibrations". This nomenclature can be some what of a misnomer as β and γ are not entirely separate as can be seen from Equations (2.58) and (2.59). The precise labelling of quanta for the two modes of excitation, especially the use of term γ-phonon,

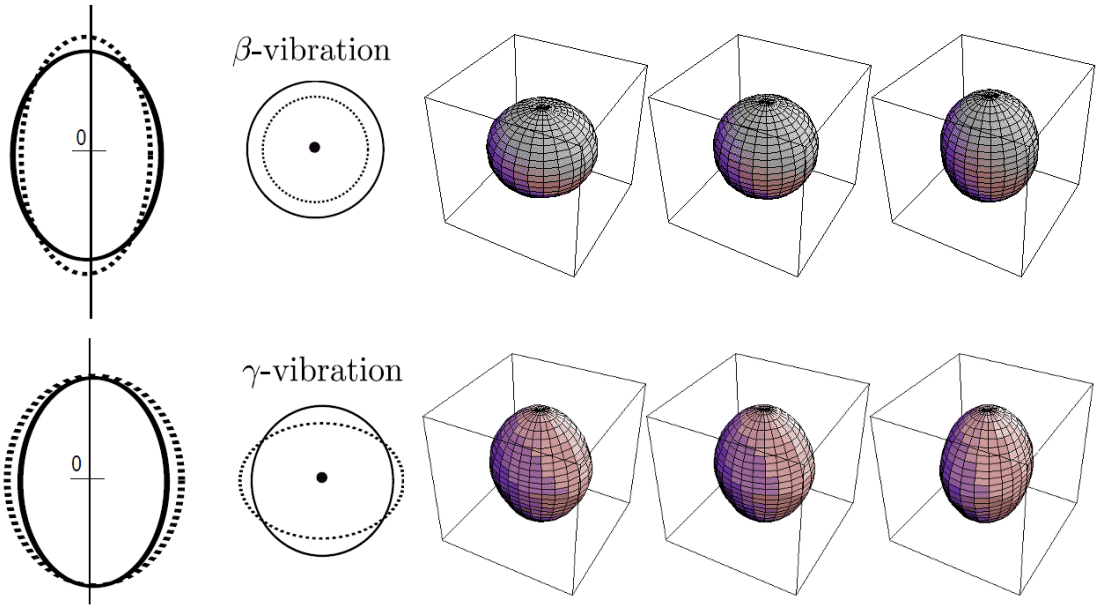

Figure 2.7: Schematic illustration of "β-vibrations" (top) and "γ-vibrations" (bottom). The diagrams to the left show side-on projection and cut-through of the $k = 3$ symmetry axis. The models on the right show snapshots sequential in time.

differs in literature [3, 4, 17]. The nuclear surface in the system is described by

$$R(\theta, \phi) = R_0 \{1 + (\beta_0 + \xi)Y_{20} + \eta[Y_{22} + Y_{2-2}]\} \,. \tag{2.72}$$

Figure 2.7 shows the surface motion associated with the two excitation modes and Figure 2.8 shows the expected level scheme, for a symmetric quadrupole-deformed nucleus.

The β-vibrations (excitations in ξ) involve the motion of matter along the $k = 3$ axis, stretching the nucleus but preserving axial symmetry. The excitation quanta has no angular momentum associated with it and produces series of 0^+ states, each with rotational bands I =0,2,4... [8].

The γ-vibrations (excitations in η) involve the motion of matter between the $k = 1$ and $k = 2$ axes. This breaks the axial symmetry, creating a small degree of triaxiality, and allowing dynamic rotations about the $k = 3$ axis which are intimately coupled with the dynamic shape change [4]. The excitation quanta has two units of angular momentum associated with it and has a projection $K = +2$ or $K = -2$. The first excitation is thus a 2^+ state with rotational band I =2,3,4... . A second excitation may create either a 4^+ state with I =4,5,6... band or a 0^+ state band I =0,2,4... .

Collective $E0$ Transitions

The general definition of the monopole moment is given as [17]

$$m(E0) = \int \rho(r) r^2 dr \,. \tag{2.73}$$

[8] A 0^+ ground state is assumed as these collective behaviours are most important in even-even nuclei.

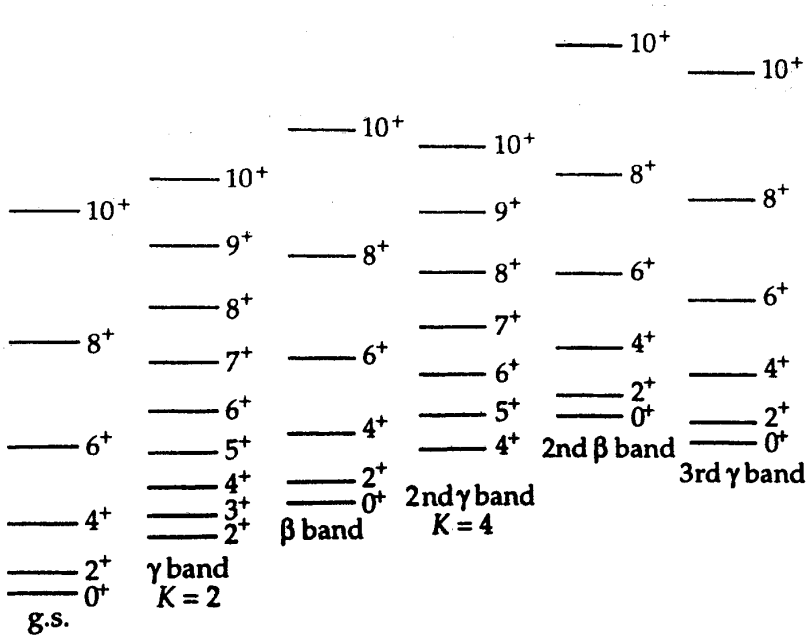

Figure 2.8: Theoretically predicted rotational-vibrational level scheme for a symmetric quadrupole deformed nucleus [4]. A second γ quanta can couple in two ways, producing $K = 0$ and $K = 4$ bands.

If a uniform charge distribution is assumed over the volume of the nucleus described by Equation (2.52) then the collective $E0$ operator is given by [15]

$$\hat{T}(E0) = \frac{3}{5} Z e R_0^2 \left(1 + \frac{5}{4\pi} \sum_{\mu} |\alpha_\mu|^2 \right) , \tag{2.74}$$

in which, only the latter term will produce $E0$ transitions.

Spherical Vibrator. For the spherical vibrator, $E0$ transitions are only possible between states with $\Delta N = 2$ or 0 change in vibration. This follows from angular momentum selection rules and from Equation (2.55) which defines α_μ in terms of creation and annihilation operators. [The $|\alpha_\mu|^2$ dependence of $\hat{T}(E0)$ means it depends on a sum of $b^\dagger b^\dagger$, $bb^\dagger$ and bb terms, and can only couple $\Delta N = 2$ or 0 states.] The resultant matrix elements are given by [15]

$$\langle N, J | \hat{T}(E0) | N, J \rangle = \left(N + \frac{5}{2} \right) \frac{3}{4\pi} Z e R_0^2 \frac{\hbar\omega}{C} \tag{2.75}$$

and

$$\begin{aligned} \langle N, J | \hat{T}(E0) | N-2, J \rangle = & \sum_{J'} \langle N, J || b^\dagger || N-1, J' \rangle \langle N-1, J' || b^\dagger || N-2, J \rangle \\ & \times (-1)^{J+J'} \left\{ N + \frac{1}{2\sqrt{2J+1}} \right\} \frac{3}{4\pi} Z e R_0^2 \frac{\hbar\omega}{C} . \end{aligned} \tag{2.76}$$

The C and ω dependence can be removed by presenting the transition strength in terms of experimental observables, such as $E2$ transitions, which also depend on the constants. Doing this avoids using model-calculated values of the constants, which are generally found

not to reproduce data. Thus, for a spherical vibrator, the $E0$ transition strength between the 0^+ ground state and the 0^+ state with $N = 2$ can be given as

$$\rho^2(E0; 0_2^+ \to 0_1^+) = \frac{2}{5} \frac{|B(E2; 0_1^+ \to 2_1^+)|^2}{\left(\frac{3}{4\pi}\right)^2 Z^2 r_0^8 A^{8/3}} \,. \tag{2.77}$$

Rigid Rotor. For transitions between states in a rotor band, which have increasing values of I, $E0$ transitions are forbidden by angular momentum coupling. Additionally, no part of the $\hat{T}(E0)$ operator affects the rotational part of the wavefunction to couple different rotationally excited states.

Transitions between states of the same I, in different rotational bands, may be considered. When the intrinsic states, upon which the rotational bands are built, cannot be coupled by the $\hat{T}(E0)$ operation, monopole transitions may still occur if there is mixing between bands. From the discussion of two state mixing in Section 2.2.1, the monopole transition strength between states $|I_i\rangle$ and $|I_f\rangle$, which are superposition of the basis states $|I_1\rangle$ and $|I_2\rangle$, can be given as

$$\rho_{fi}(E0) = \frac{1}{eR^2} \left[ab \left(\langle I_1|\hat{T}(E0)|I_1\rangle - \langle I_2|\hat{T}(E0)|I_2\rangle \right) + (a^2 - b^2)\langle I_2|\hat{T}(E0)|I_1\rangle \right] \,, \tag{2.78}$$

where a and b are the mixing coefficients with $a^2 + b^2 = 1$. If the degree of mixing is large, or when $\langle I_2|\hat{T}(E0)|I_1\rangle = 0$, the last term disappears. From the definition $\beta^2 = \sum |a_\mu|^2$ the diagonal matrix elements may be solved explicitly and the monopole transition strength subsequently given as

$$\rho_{fi}^2(E0) = (ab)^2 \left(\frac{3}{4\pi}\right)^2 Z^2 (\beta_1^2 - \beta_2^2)^2 \,. \tag{2.79}$$

The result is very similar to the shell model case. Strong $E0$ transitions can be interpreted as mixing between different deformations. Figure 2.9 shows the variation of strength $E0$ as a function of one of the two basis state deformations.

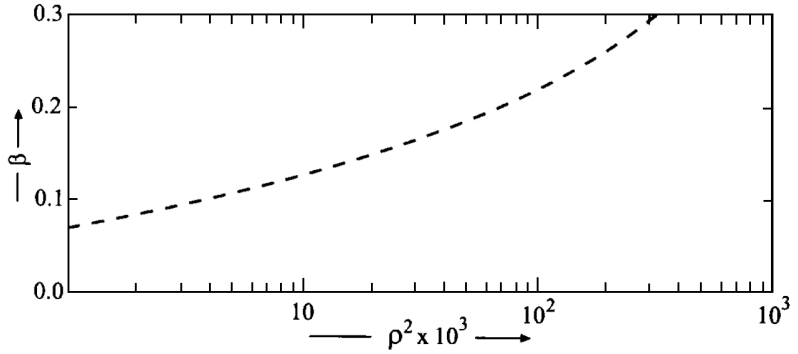

Figure 2.9: Expected monopole transition for Z=55 between two heavily mixed states, one state near spherical and the other with deformation β. The β range shown is typical for defomation observed in the $A = 110 - 120$ mass region [15].

Vibrating Rotor. For the vibrating rotor, the monopole operator can be expanded, using Equations (2.66) and (2.67), in terms of the dynamic variables, ξ and η, as

$$\hat{T}(E0) = \frac{3ZeR_0^2}{4\pi}\left(\beta_0^2 + 2\xi\beta_0 + \xi^2 + \eta^2\right) . \tag{2.80}$$

The β_0^2 term corresponds to the equilibrium shape and will dominate static monopole moment but will not contribute to transitions. Neglecting higher order terms,Equation (2.80) reduces to

$$\hat{T}(E0) = \frac{3ZeR_0^2}{2\pi}\xi\beta_0 , \tag{2.81}$$

which allows transitions to the "β-vibration" states, but results in vanishing "γ-band" transitions. This immediately shows that $E0$ transition from the ground to β band are significantly stronger than those to the γ band. This follows logically from the behaviour of the two excitation modes. The β-excitation mode corresponds to purely radial motion of nuclear matter and the 0 order multipole acts purely radially. Whereas, the first γ mode excitation has a rotational component and thus a transition of several excitation quanta are needed to reach a state of pure radial motion.

Due to the separable nature of the wavefunction, the ground-band to β-band $E0$ matrix element can be solved and the transition strength given as [20]

$$\rho^2(E0; n_\beta = 1 \to n_\beta = 0) = \frac{1}{2}\left(\frac{3}{2\pi}\right)^2 Z^2\beta_0^2\frac{\hbar\omega_\beta}{C_0} . \tag{2.82}$$

As with the spherical vibrator case, dependence on the constants C and ω may be removed by giving the transition strength in terms of other experimental observables that depend on them, giving

$$\begin{aligned}\rho^2(E0; n_\beta = 1 \to n_\beta = 0) &= \frac{9}{8\pi^2}Z^2\beta_0^4\frac{E(2_1^+)}{E(0_\beta^+)} \\ &= \frac{B(E2; 0_1^+ \to 2_\beta^+)4\beta_0^2}{e^2r_0^4A^{4/3}} .\end{aligned} \tag{2.83}$$

It should be noted that the transition strength given here is independent of angular momentum, following from the assumption the rotational wavefunction is separable. As a consequence, ρ^2 is expected to be the same for $0_\beta^+ \to 0_1^+$, $2_\beta^+ \to 2_1^+$, $4_\beta^+ \to 4_1^+$ etc.

2.2.3 The Interacting Boson Model

The Interacting Boson Approximation (IBA) is an algebraic model which can be used to bridge the gap between shell model and collective models in medium and heavy even-mass nuclei. The model, which was first proposed by Arima and Iachello [21], describes low-level nuclear structure in terms of valence nucleons coupled to boson pairs. In the IBA-1 no distinction is made between protons and neutrons. The total boson number N_B is given by half the number of valance protons and neutrons, each relative to nearest closed shell, using the traditional magic numbers 50, 82 and 126.[9] Boson number, N_B, is

[9] This is to the nearest shell above or below, the bosons can be hole-like.

a conserved quantity for all states of a given nucleus. Low-lying collective excitations are then described by excitations of the bosonic pairs, that may either be s bosons ($L = 0$) or d bosons ($L = 2$), where d bosons drive quadrupole deformation. The s boson has one magnetic substate and the d bosons has five possible magnetic substates, hence the sd-space of the IBA is a six-dimensional space, or a U(6) algebraic group. The model may be extended to include g bosons, which are needed to describe high-order deformation, but this is generally not required. The reasoning for the concentrating on s and d bosons is born of generalised seniority arguments of shell-model predictions and empirical observations of near-closed-shell nuclei, in which 0^+ and 2^+ states lie considerably lower in energy than higher angular momentum states [22].

In this model space, bosons can be created with the respective s and d boson creation operators, $s^\dagger$ and $d^\dagger$, and can be destroyed by the respective annihilation operators, $\tilde{s}$ and $\tilde{d}$. Transition operators in the model are defined in terms of these creation and annihilation operators. The total boson number, N_B, must be conserved throughout and can be given in terms of the s and d boson number operators as

$$N_B = \hat{n}_s + \hat{n}_d = s^\dagger \tilde{s} + d^\dagger \tilde{d}\,. \tag{2.84}$$

The nuclear basis states are each defined by the number of d bosons, n_d, total angular momentum, L, and by the number of pairs and triplets of d bosons coupled to spin 0, respectively n_β and n_Δ.[10] The IBA Hamiltonian must then be solved to calculate the energies and composition of predicted eigenstates. Transition probabilities between states, for different transition modes, can then be calculated from the matrix element between the eigenstates with the IBA form of relevant operator. The full IBA Hamiltonian contains many terms and adjustable parameters and it is usual to use a truncated form. The most commonly used is that of the "Consistent Q Formalism", so named because the quadrupole operator, $\hat{Q}^\chi$, is used in both the Hamiltonian and the $E2$ transition operator [23]. The Hamiltonian is thus given as

$$H(\zeta) = c\left[(1-\zeta)\hat{n}_d + \frac{\zeta}{4N_B}\hat{Q}^\chi \cdot \hat{Q}^\chi\right], \tag{2.85}$$

where the quadrupole operator, $\hat{Q}^\chi$, is given by

$$\hat{Q}^\chi = (s^\dagger \tilde{d} + d^\dagger \tilde{s}) + \chi(d^\dagger \tilde{d})^{(2)}. \tag{2.86}$$

The factor c is an energy scaling factor, which scales the entire model, and is usually set to normalise predictions to the experimentally measured 2_1^+ energy. Observables in the IBA are predominately given as ratios, making them mostly insensitive to this value. The parameters ζ and χ are the IBA control parameters, which dictate the behaviour of the Hamiltonian and hence the eigenstates that will be calculated. The power of the IBA in describing low-lying collective structure hinges on use of these parameters.

[10] Different sets of quantum numbers can be used to define the d-boson coupling. The differences are not important to this discussion.

Symmetries of the IBM

For any given Hamiltonian, an upper bound for the energy of the ground state can be given in terms of classical shape parameters, by application of the "Intrinsic-State Formalism", detailed in References [24, 25]. Hence, for a Hamiltonian defined by Equation (2.85) and fixed values of the control parameters ζ and χ, the ground-state energy may be expressed in terms of the geometric parameters, β and γ, of the Bohr and Mottelson collective model [26]. This gives a potential energy surface as a function of β and γ, which is equivalent to the nuclear potential for the Hamiltonian of ζ and χ. By this method, direct analogues can be drawn between the algebraic IBA and geometric Bohr and Mottelson model.

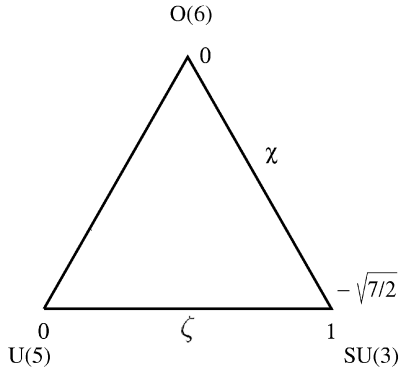

Figure 2.10: IBM dynamic symmetry triangle, which maps the control parameters ζ and χ as coordinates between the limiting cases.

Within the symmetry group of the IBA-1 *sd*-space, there are three separate subgroups, U(5), SU(3) and O(6). Each group is a dynamic symmetry of the model in which a symmetry is broken, which in turn lifts a degeneracy. This introduces new quantum numbers in each of subgroups and hence new selection rules and behaviours of both transitions and state construction.

The control parameters ζ and χ effectively control what part of the model space is accessible, with the terminal values selecting single subgroups. The "position" in the space defined by ζ and χ can be tracked on the IBA dynamic symmetry triangle, as shown in Figure 2.10. The parameter ζ ranges between the values 0 and 1, which correspond to the U(5) limit and the SU(3)+O(6) limit. The parameter χ ranges between the values $-\sqrt{7/2}$ and 0, which correspond to the SU(3) limit and the O(6) limit.[11] The β and γ potential energy surface for the three subgroup limits are shown in Figure 2.11. The U(5) limit is analogous to the collective harmonic vibrator and the SU(3) limit is analogous to the prolate rigid rotor. The O(6) limit is analogous to a γ-soft rotor, which describes a nucleus with definite $\beta \neq 0$ deformation but poorly defined γ.

The power of the IBA lies in allowing ζ and χ to move away from the single group limits. Because the control parameters may take *any* values in range, it is possible to study transitional collective behaviour between the idealised cases of the Bohr and Mottelson geometric interpretation.

[11] In a full parameter space χ ranges from $-\sqrt{7/2}$ to $+\sqrt{7/2}$ and the symmetry triangle is reflected in the U(5)-O(6) vertex, with the reflected half corresponding to oblate deformation.

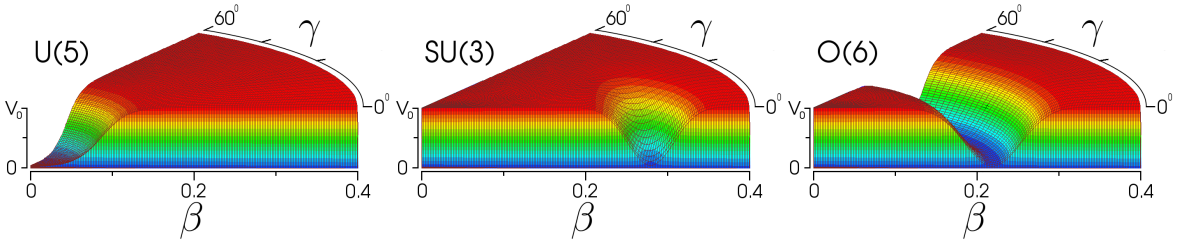

Figure 2.11: Idealised β and γ potential energy surface for the three limits: U(5) (harmonic vibrator), SU(3) (rigid rotor) and O(6) (γ-soft rotor).

IBM $E0$ Transitions

Starting from the general definition of the $E0$ operator,

$$\hat{T}(E0) = \sum_{k=1}^{A} e_k r_k^2 \,, \tag{2.87}$$

it may be assumed that the operator can be given in terms of the mean-squared charge radius operator, $\hat{T}(r^2)$, as [27]

$$\hat{T}(E0) = (e_z Z + e_n N)\hat{T}(r^2) \,, \tag{2.88}$$

where e_z and e_n are the effective charges for protons and neutrons. In the IBA-1, where no distinction is made between neutrons and protons, the charge radius operator is given by

$$\hat{T}(r^2) = \langle r^2 \rangle_c + \alpha N_B + \eta \frac{\hat{n}_d}{N_B} \,, \tag{2.89}$$

where $\langle r^2 \rangle_c$ is the radius of the core nucleus and α and η are model parameters with units of length squared. The second term accounts for the increase in radius of charge from the addition of two nucleons, which has been approximated to linear in this term. The third term gives the contribution to the charge radius caused by deformation. The addition of a $1/N_B$ dependence, introduced in Reference [27], is performed because it is the fraction $\langle \hat{n}_d \rangle / N_B$ which can be equated to the measure of geometric deformation β^2, and not $\langle \hat{n}_d \rangle$ itself. For $E0$ transition between states, $\langle r^2 \rangle_c$ is a constant and does not contribute. The second term does not contribute either as N_B is a conserved quantity across all states. Hence $E0$ transition strength can be given as

$$\rho^2(E0; i \to f) = \frac{(e_z Z + e_n N)^2}{e^2 R_0^4} \left| \eta \frac{\langle f | \hat{n}_d | i \rangle}{N_B} \right|^2 \,, \tag{2.90}$$

where all state dependence is condensed to the d boson matrix element $\langle f | \hat{n}_d | i \rangle$.

A general comment can be made on $E0$ transitions for the three dynamical symmetry limits. In the U(5) limit n_d is a good quantum number, hence $\hat{n}_d$ and subsequently $\hat{T}(E0)$ are diagonal and $E0$ transitions are forbidden. In the SU(3) and O(6) limits, n_d is not a good quantum number and $E0$ transitions are allowed.

It was shown by Brentano [28] that, while some d-boson amplitude is clearly needed in state wavefunction for deformation and $E0$ transitions, large $\rho^2(E0)$ are not simply a

consequence of large $\langle \hat{n}_d \rangle$ values. It was shown that $E0$ strength depends on the fluctuation, or "spreading", of n_d values in the wavefunctions. Brentano says *"It is the **specific d-boson coherence** in the wave functions that control the resultant ρ values."* This is analogous to the observations made for previous model $E0$ transitions, that it is not just the differing radii in wavefunctions that cause strong $E0$ transitions, but crucially the mixing of these radii between the two levels of a transition.

3

Equipment

The experiment discussed in this thesis was performed at the JYFL. The experiment was concerned with the detection of coincident internal conversion electrons and γ rays. In this chapter an overview of the detectors used, the SAGE setup and equipment surrounding it will be presented.

3.1 Experimental Overview

A beam of stable ions from the JYFL K130 cyclotron was focused to a beam spot of a ~ 4 millimetres diameter on thin metal targets mounted on a rotating target ladder. The target is situated at the focal point of the a germanium array, JUROGAMII, and a conversion electron detector system, SAGE. Following the interaction of the beam and target nuclei, different reaction product nuclei may be produced at the target position in excited states, moving with typical speeds of $\beta = \frac{v}{c} \sim 0.02$. These product nuclei will decay to their ground or metastable state primarily by means of γ decay and internal conversion. Those transitions occurring within a nanoseconds correspond to γ rays and conversion electrons being produced < 1 centimetres downstream of the target, which may then be detected in JUROGAMII and SAGE respectively. Downstream of the SAGE target chamber, product nuclei and unreacted beam nuclei, as well as scattered target nuclei, pass into the Recoil Ion Transport Unit (RITU). Reaction products pass through RITU and are implanted in the Gamma Recoil Electron Alpha Tagging focal plane spectrometer (GREAT), where the subsequent decay of radioactive nuclei or long lived isomer states may be detected. An overview of the equipment layout is shown in Figure 3.1.

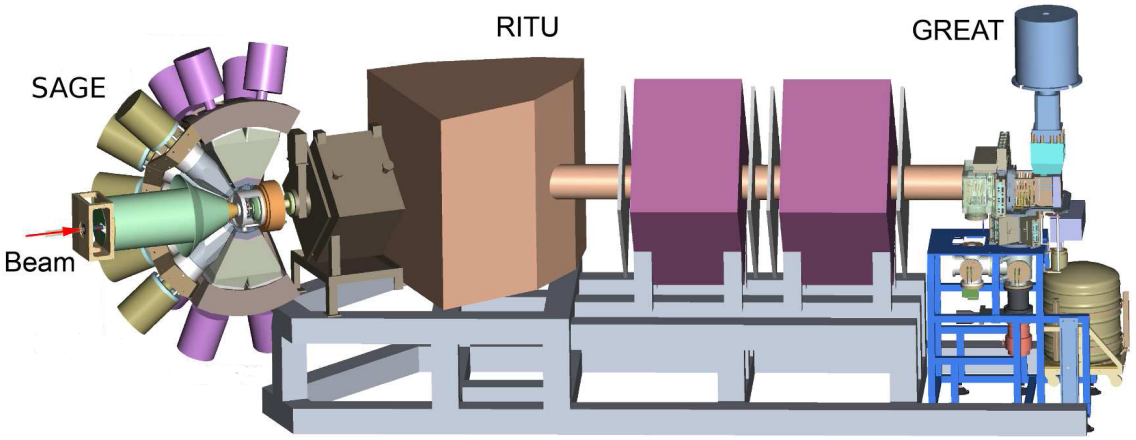

Figure 3.1: The SAGE spectrometer coupled with the RITU gas-filled separator and the GREAT focal plane spectrometer [29].

3.1.1 SAGE

The SAGE spectrometer is an in-beam electron detector, which utilises a water-cooled solenoid and a high-voltage electric field barrier, to measure conversion electrons over a range of energies. The experimental geometry is shown in Figure 3.2. SAGE has two solenoid coils, one before and one after the target, to produce a magnetic field which constrains emitted electrons to helical path, with a radius r defined by Equation (3.1),

$$r = \frac{p_\perp}{eB}\,, \tag{3.1}$$

where B is the magnetic field strength, e the electric charge and $p_\perp$ is the momentum of the electron perpendicular to the magnetic field. The perpendicular momentum $p_\perp$ is related to the electrons kinetic energy, T, by

$$p_\perp = \cos\theta\sqrt{\frac{T^2}{c^2} + 2Tm_e} \tag{3.2}$$

where θ is the angle of the electron trajectory with respect to the magnetic field axis and m_e its rest mass. These coils direct electrons to a silicon detector upstream from the target chamber.

Magnetic Field

The magnetic field produces a force given by $\vec{F} = e\vec{v} \times \vec{B}$, which is perpendicular to the movement of the electron. The field changes the trajectory of the electron, but the kinetic energy that is to be measured remained unchanged. The magnetic field produced by the solenoids of SAGE is shown in Figure 3.3. The coils of SAGE are arranged to provide maximum access for the JUROGAMII detectors while still constraining the electrons. Figure 3.3 shows that the magnetic field is weak at the target position, allowing electrons to make wide, helical trajectories within the target chamber. However, the field increases towards the SAGE detector, constraining electrons more tightly where they must pass through the narrow parts of the equipment. The sharp change in field strength moving

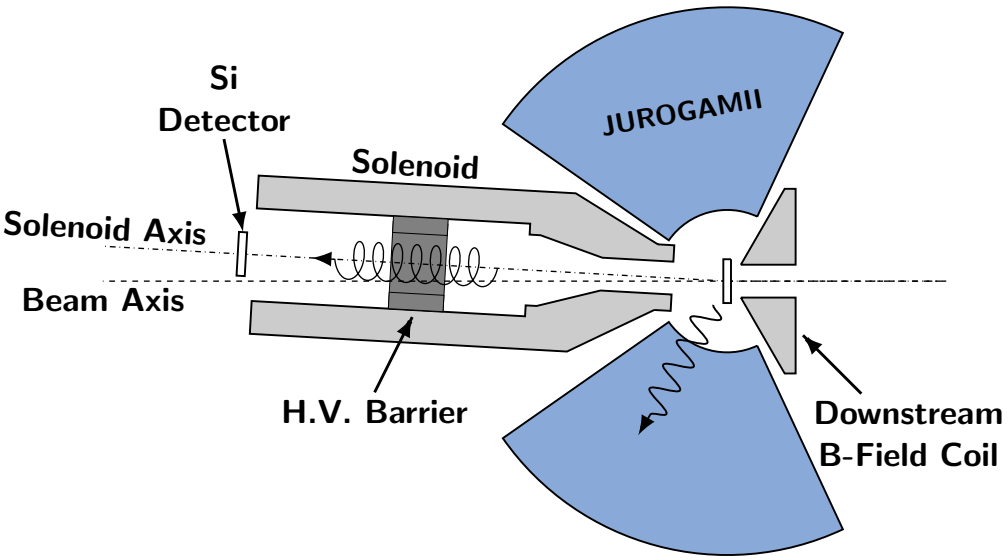

Figure 3.2: Cut-through illustration of the experimental geometry showing the relative locations of JUROGAMII and the silicon detector that comprise the SAGE spectrometer. The target is situated at the focal-point of JUROGAMII. Solenoid coils downstream and upstream of the target create the magnetic field that transports electrons to the SAGE silicon detector. The axis of the upstream solenoid is 3.2° from the beam axis to permit passage of the beam beside the detector. A high-voltage potential barrier within the upstream solenoid suppresses δ-electrons.

downstream of the target, towards RITU, or upstream, towards the SAGE detector, should be noted. This produces a magnetic mirror effect resulting in some electrons without sufficient transverse momentum being reflected back towards the target. See Section 3.2.1 for futher details of this behaviour in SAGE.

Electric Barrier

Delta electrons (or delta rays) are a major hindrance to electron spectroscopy and other nuclear physics techniques, particularly for low statistics observations in high radiation flux areas, such as solar laboratories [30] and some drift-tube counters [31]. Delta electrons are atomic electrons knocked free by the impulse of the passing beam nucleus in a target material. It is this interaction between atomic electrons and the beam nucleus which accounts for the majority of the stopping power of a material, and not nuclear interactions. At very close distances of approach the beam may impart many keV of energy to these delta electrons up to a maximum [32], given by Equation (3.3),

$$E(\delta)_{max} = 4\left(\sqrt{\frac{m_e}{m_\alpha}E_K E_\alpha} + \frac{m_e}{m_\alpha}E_\alpha\right), \tag{3.3}$$

where m_α and E_α are the mass and energy of the beam and E_k is the atomic binding energy of the target K-electron. For example, a beam of mass A=40 and energy 100 MeV impinging on a Z=60 target may impart a maximum of 36 keV to a delta electron. Delta electrons are produced over the range of energies up to this maximum, where the pro-

duction cross-section $\sigma(E_e) \propto 1/E_e$ [33][34]. From an experimentalist point of view the crucial conclusion is that there are many delta electrons of sufficient energy to trigger a detector system for every one conversion electron event of interest. If all of these delta electrons are allowed to reach the detector the count rate/dead time of the system would be untenable.

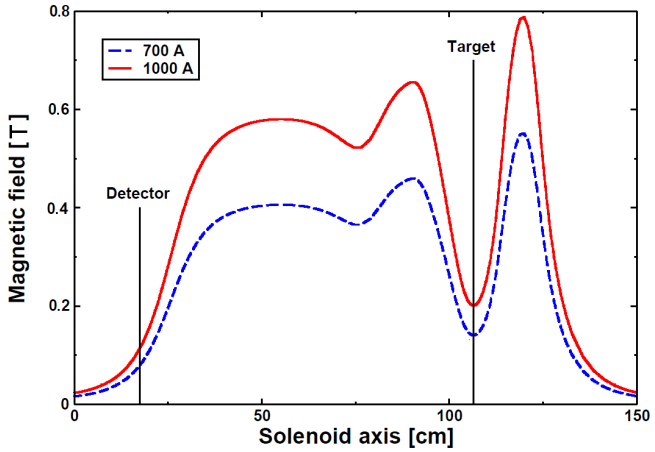

Figure 3.3: Magnetic field strength along the solenoid axis of SAGE for two typical solenoid coil current settings [35]. Note the minimum at the target position leading to the reflection effect refereed to in the text.

SAGE boasts a high voltage electric field barrier midway between target and detector within the solenoid. This electric barrier retards the motion of electrons along the solenoid axis so that only electrons with transverse kinetic energy greater than the height of the barrier potential can pass through. High-energy electrons will pass through the centre of the barrier and regain their kinetic energy as they move away from the potential on the other side. Low-energy electrons, or those that make a large angle with magnetic field axis, are reflected back towards the target and will eventually stop in some inert part of the equipment, playing no further part in the event. The overall effect of this barrier is to repel the majority of the delta electrons, thereby keeping the number of electrons reaching the detector to an acceptable rate, while allowing conversion electrons through to the detector with their energy unchanged. A typical barrier height used in experiment would be 20 kV, sufficient to repel the majority of delta electrons and low enough that most conversion electrons are unhindered.

Detector

SAGE utilises a 1 mm thick, single sided, annular silicon strip detector. Semiconductor detectors are discussed in Section 3.1.2, and more details can be found in Reference [36]. The circular projection of the electron's helical path on to the detector will have a radius dependent on E_e and emission angle θ. The position on the detector will be dependent on emission angle ϕ but always making a tangent with the centre point, resulting in higher rates towards the centre of the detector. The detector diameter is 48 mm and there is a weaker magnetic field ($\sim$0.1 T) at the detector position. For an electron moving perpendicular to the B field, the energy must be below $E_e = 114$ keV in order for the circular projection of the electron's helical path to fall completely within the detector radius.

To improve the incident particle rate under which the detector can operate, the inner section of the detector is more segmented, as all electrons can reach the centre of the detector but only high-energy electrons reach the outer portions. Furthermore delta electrons, electron scattering and the inverse energy dependence of electron conversion all result in a far higher rate of incident electrons with low energies, which are constrained by the magnetic field towards the centre of the detector, as described in Section 3.2.2.

The 90 element segmentation of the detector is shown in Figure 3.4. The inner region of the detector is segmented into 58 pads with 1 mm pitch. Two semi-circular pads occupy the very centre of the detector, whilst the remaining 56 pads have an annular width of $\frac{\pi}{4}$. The outer region of the detector is segmented into 32 pads with 2 mm pitch and annular width $\frac{\pi}{2}$. The 90 elements are instrumented by preamps mounted around the edge of the detector The detector and preamps are mounted on a cooled plate, refrigerated with ethanol, to provide resolution of a few keV even at high rates.

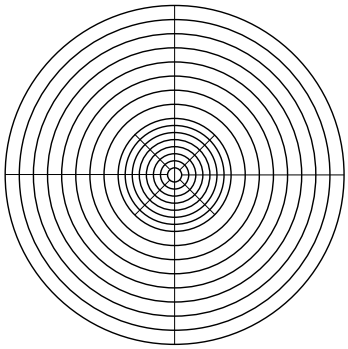

Figure 3.4: Illustration of the segmentation of the SAGE silicon detector, as described in the text.

3.1.2 JUROGAMII

JUROGAMII is a Compton-suppressed High Purity Germanium (HPGe) detector array. Consisting of 24 Clover detectors [37] and 15 Phase-I detectors [38] (detailed below) JUROGAMII is the upgrade to JUROGAM (2003-2008). Prior to this the detectors were part of EUROBALL (1997-2003).

Germanium Detectors

HPGe detectors consist of a germanium semi-conductor crystal inside a liquid nitrogen cryostat with a high voltage ($\sim$ 1 kV) applied across the crystal to fully deplete the detector. Incident γ rays liberate electrons from the crystal lattice by Compton scattering and finally photoelectric absorption. These freed electrons move through the crystal exciting electrons into the conduction band. The number of electrons excited before the freed electrons come to rest is linearly proportional to energy imparted by the incident γ rays i.e. collected charge $\propto E_\gamma$ [36]. Because germanium has a very small band gap (0.7eV) it produces more electrons than other materials, resulting in superior energy resolution, as the statistical counting error $\delta(E) \propto \sqrt{N}$, where N is the number of charge carriers. However, the small band gap means germanium crystals must be cooled with liquid nitrogen

to prevent electrons being thermally excited into the conduction band, resulting in noise from the detector.

Compton Suppression

When a γ ray interacts with matter the interaction mode depends upon the γ ray energy, an example of the variation is shown in Figure 3.5. The most likely interactions for $E_\gamma \leq 4\,\text{MeV}$ are Compton scattering on atomic electrons or photoelectric absorption. When Compton scattering occurs inside a germanium detector crystal, the resultant photon may scatter out of the crystal and the detector will record only the fraction of the γ-ray energy deposited in the scattering event. The result of this effect is a Compton background of incomplete energy measurement in the final spectrum, ranging from 0 to the maximum energy $E_{\text{Compton Edge}}$, given by

$$E_{\text{Compton Edge}} = \frac{2E_\gamma^2}{m_e c^2 + 2E_\gamma}\,, \tag{3.4}$$

where E_γ is the initial energy of the γ ray, m_e is the rest mass of an electron and c is the speed of light. This is a typical effect seen in γ-ray spectra. An illustration of this effect and further details can be seen in Ref [36]. This effect is undesirable as the lower energy range of spectra acquire very large backgrounds from the built up Compton continua of higher-energy γ rays. This can make the identification of low-intensity γ rays difficult, especially when a peak area is statistically insignificant compared to the background which the peak is on top of. Furthermore, when preforming γ-coincidence measurements, these Compton background events contribute heavily to false coincidences. In Compton-suppressed detectors a high absorption (high Z) detector material is placed around the primary crystal and is used to detect such events. In JUROGAMII, Bismuth Germanium Oxide (BGO) scintillator detectors ($\sim 2\,\text{cm}$ thickness) are placed around the sides of the HPGe detectors ($\sim 10\,\text{cm}$ thickness). Due to its high density and Z of the material, the mean free path of a given photon in BGO is significantly shorter than in HPGe and so higher detection efficiencies are achieved with relatively small crystals, but the energy resolution is an order of magnitude worse than HPGe. The BGOs are tapered to allow close packing of the HPGe detectors around the target chamber, thus improving geometric efficiency. If a γ ray is detected in the BGO cowl of a given HPGe in coincidence with a γ ray in that detector, a Compton scatter and escape is assumed to have occurred and the event is discarded.

The Array

When used with SAGE, JUROGAMII consists of 24 Clover detectors and 10 Phase-I detectors. Here a Clover detector comprises 4 individually instrumented HPGe crystals in a single cryostat. This saves on wasted volume taken up by thermal shielding between detectors. Compton scatters between crystals can be added together offline to recover the full γ-ray energy. A Phase-I detector is an individual tapered crystal detector; they are used to fill the narrow region close to the beam pipe at θ =133.57°. A group of 12 Clover detectors form a 2π ring in ϕ at θ =75.5°, the other 12 form a ring at θ =104.5°and the 10

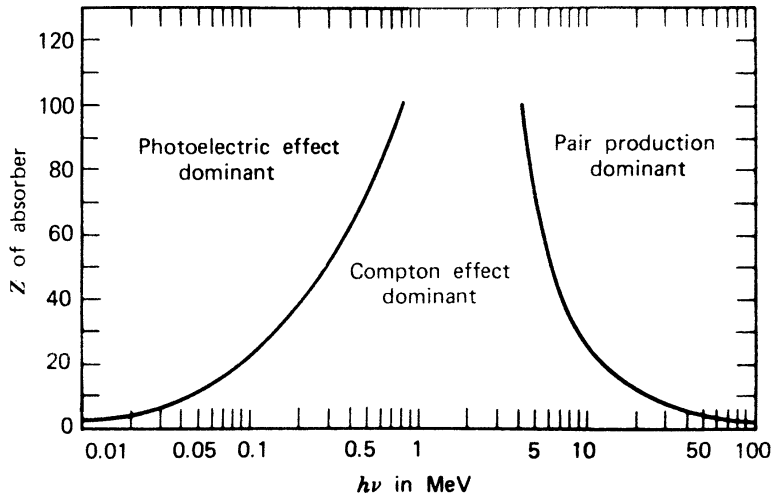

Figure 3.5: The relative importance of the three major types of γ-ray interaction with matter. Lines show the values of $h\nu$ and Z for which neighbouring effects are equal [39].

tapered Phase-I detectors are mounted at θ =133.57°. Further details are in Appendix A. A further ring of 5 Phase-I detectors at θ =157.6°is not compatible with SAGE because of the space taken up by the solenoid.

3.1.3 RITU

The need for recoil separators is evident in considering all possible reactions in any given experimental setup. When the centre of mass energy of the beam and target nuclei is greater than their Coulomb barrier then Coulomb, direct (inelastic scattering, transfer) and compound nucleus reactions all compete; for ^{16}O(^{154}Sm,X) this is 5.2 MeV/u. Centre of mass Coulomb barrier height in MeV can be calculated by Equation (3.5) [40],

$$E_{barrier} \approx 1.44\frac{Z_1 Z_2}{R_1 + R_2} \approx 1.2\frac{Z_1 Z_2}{(A_1^{1/3} + A_2^{1/3})}\,, \tag{3.5}$$

where $R_{1,2}$, $Z_{1,2}$ and $A_{1,2}$ are respective nuclear radii in femtometres (fm) and proton and mass numbers for the recoil and target nuclei and the two numerical constants are 1.44 MeV fm and 1.2 MeV. Dependent on the exact energy regime one reaction may dominate, but there may still be multiple channels of that reaction type available. For example, a fusion evaporation (compound nucleus) reaction may have a dozen available channels; each channel likelihood will be affected by many factors including energetic favourablity (often making 2n, 2p, α evaporation channels more likely) and level density within the daughter nucleus [1]. The reaction product of interest to the experiment might only be accessible, due to beam and target limitations, in situations where it is orders of magnitude less likely than other reaction channels. In these situations a separator can be used to disperse the reactants and trigger or gate on the product of interest.

Rigidity and Gas-Filled Separators

In magnetic separators, dipoles magnets are used to divide incoming particles based on the different curved trajectories they make in a magnetic field. For this purpose it is useful to define the magnetic rigidity, Equation (3.6) [41], where it is common practice to denote the radius of curvature ρ. Transmission through a separator will only occur for a given range of ρ and so B must be set to select a certain magnetic rigidity, $B\rho$ in units of Teslametres (Tm),

$$B\rho = \frac{m\nu}{q}\,, \tag{3.6}$$

for a particle of mass m, charge q and velocity ν. It is clear to see that different particles may have the same rigidity, but when the difference in E is small compared to the difference in A or Z (where q$\propto$Z) then different particles will be separated by a physical distance through the separator. At the energies used with RITU it is unlikely that an ion will be fully stripped of electrons following a nuclear reaction inside a target material. Instead, for any given species, a range of charge states of q<Z will be produced [42]. Transmission through a separator can only be tuned for one of these charge states (dependent on separator size) and so a considerable fraction of desired products will be lost. Gas-filled separators offer improved transmission efficiency at the cost of reduced resolution [43]. By filling the magnet cavity with a low-pressure gas ($\sim$1 mbar) a passing ion will change its charge through atomic collisions (100-1000 permetre) following a trajectory independent of initial charge state [44]. This is illustrated in Figure 3.6. Optimum pressure for the filling gas is determined by the trade-off between charge focusing and multiple scattering in the filling gas [41]. If the ion velocity is in the range $\nu_0 < \nu < \nu_0 Z^{2/3}$ [41], where ν_0 is the Bohr velocity ($2.19 \cdot 10^6 m/s$), then the mean charge is given by Equation 3.7. This is an approximation given by the Thomas-Fermi model of the atom [45]:

$$\bar{q} \approx \frac{\nu}{\nu_0} Z^{1/3}\,. \tag{3.7}$$

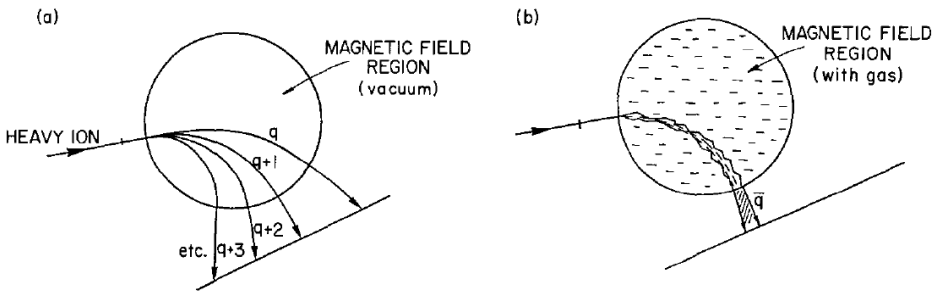

Figure 3.6: Schematic of heavy ion trajectories in a) vacuum b) gas-filled separators [46].

This velocity requirement can be more usefully written as $0.007 < \beta < 0.007 Z^{2/3}$. By using this averaging effect, not only is the collection efficiency enhanced but the rigidity for a given species becomes approximately energy independent, as seen in Equation 3.8

[41]:

$$B\rho \approx 0.0227 \frac{A}{Z^{1/3}} \,. \tag{3.8}$$

As this rigidity depends only on A and Z, Equation (3.8) can be easily manipulated to give the limit of isobaric and isotopic separation in terms of a separator's resolution $\frac{\Delta B\rho}{B\rho}$, which typically lies in the range $1-5\%$ [43][47].

$$\frac{\Delta Z}{Z} \geq \left(\frac{\Delta B\rho}{B\rho} + 1\right)^3 - 1 \text{ Isobaric, and} \tag{3.9}$$

$$\frac{\Delta A}{A} \geq \frac{\Delta B\rho}{B\rho} \text{ Isotopic.} \tag{3.10}$$

RITU

RITU is a helium-filled gas separator of the QDQQ configuration, designed for use with heavy elements produced in fusion reactions. This means there is an initial vertical focusing quadrupole Q (improving the total acceptance) followed by a horizontal-separating dipole D, and then a quadrupole doublet to focus ions onto the focal plane detectors [48], this layout is show in Figure 3.7.

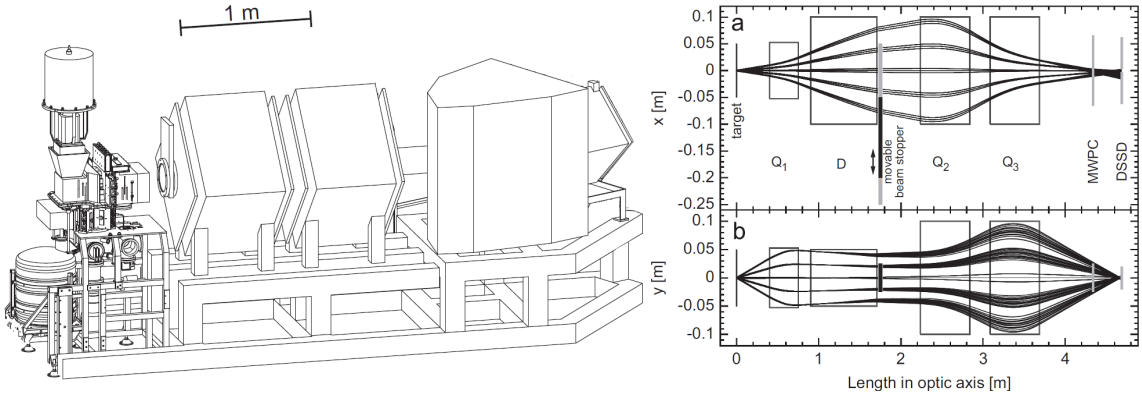

Figure 3.7: RITU gas-filled separator and GREAT focal plane spectrometer. Schematic of the separator optics are included for interest (right) where it can be seen the limit of transmission in the horizontal direction x (shown in subfigure a) is the acceptance of the Q2 quadrupole and the limit in vertical direction y (shown in subfigure b) is Q1. [49]. Focal plane detectors are also marked, see text for details.

RITU is operated with 1 mbar helium gas and its 1.85 m radius dipole can bend a maximum rigidity 2.2 Tm [49]. Using Equation (3.8) it is clear that this rigidity is sufficient for even the heaviest elements. Two $40\,\mu g/cm^2$ carbon foils upstream of the target chamber and a differential pumping system isolate the beam line from the gas volume [50]. Placing the foils upstream of the targets avoids the situation where product nuclei may scatter in the foil before the separator, reducing the overall resolving power. RITU has a mass-resolving power $\Delta A/A$ of 4-5% [43], which is sufficient to remove unreacted and inelastically scattered beam, but isotopic contaminants will still compete with fusion-evaporation channels of interest. When combined with additional techniques, RITU can provide isolation of minor reaction channels with impressively high transmission-efficiency.

3.1.4 GREAT

The GREAT spectrometer includes many detectors for the identification of recoils transported by RITU, including germanium Clovers detector and Si PIN diodes for the detection of electrons [51]. Most important use with SAGE are the Multi Wire Proportional Counter (MWPC) for ion identification and Double Sided Silicon Strip Detector (DSSSD) for implantation and decay tagging.

MWPC

A MWPC is a gas-filled transmission detector [52][53][54], where the gas in this case is isobutane. Passing recoils leave in their wake a path of ionised gas and electrons, and by placing high voltage anode and cathode grids at either end of the gas volume, these charges can be separated and collected as a signal. The energy loss of an ion in matter can be approximately calculated from the Bethe-Bloch formula, Equation 3.11,

$$\frac{dE}{dx} = \frac{4\pi e^4 Z_i^2}{m_e \nu^2} N_t Z_t ln\left(\frac{2m_e\nu^2}{I}\right), \tag{3.11}$$

where Z_i and ν are the atomic number and velocity of the ion; Z_t, I and N_t are the atomic number, mean excitation potential and number density of the target [36]. This can be easily related to number of charge pairs created per unit length of a track. MWPCs operate in a gas pressure regime where the initial ionisation would produce poor signals. However, narrow $\sim 50\mu$m wires are used to form the anode grid in such detectors. The strong resultant electrical field close to the surface of the wires, proportional to 1/r, causes acceleration of the electrons and large secondary ionization [55]. The advantage of operating in this regime is very fast electron movement and hence particularly good timing resolution, of the order of 1 ns [56][57].

Implantation Decay Tagging

In experiments where the products of interest undergo radioactive decay with short half-lives the process of recoil implantation decay tagging can be utilised to purge the data of unwanted events [58][59]. The half-life of the product should be at least as long as the transport time to the implantation medium plus the dead time of the decay detector (if the same detector records the implantation), or else the decay events may be lost. The maximum half-life usable is dependent on the implantation rate and the sensitivity of decay detection.

Energy loss of heavy ions in a medium can be given by Equation 3.11 and some examples of stopping ranges for various heavy products are given in Table 3.1. The values in the table serve to illustrate that such products can be stopped in thin foils or solid state detectors, and that characteristic stopping ranges can be used to help in the identification of the products [60].

Following implantation, emission of charged particles (α, β, p^+, or γ rays) from decay to or by the daughter nucleus can be detected and used to identify the implanted ion as the species of interest. This can be done by implanting the ion into a detector as is done in

Species	β	Energy /MeV	Range in Si /μm
^{204}Rn	0.05	240	21.8
^{204}Rn	0.02	38	6.5
^{163}Ta	0.05	194	20.2
^{163}Ta	0.02	30	3.5
^{46}V	0.05	54	20.2
^{46}V	0.02	8	6.5
α	0.07	10	69.7
α	0.05	5	24.4

Table 3.1: Stopping ranges for various heavy ions in silicon as given by the program SRIM [61].

GREAT or by using detectors neighbouring the implantation medium [62]. In the case of low implantation rate, the linking of decay and implantation event can be achieved simply with timing coincidence. For higher rates, the decay detector should should be segmented to facilitate geometric coincidence.

In GREAT the incoming beam from RITU passes through the MWPC and is spread over two adjacent 300μm thick DSSSDs, which are 240mm downstream of the MWPC. GREAT has the capability of detecting electron and γ rays but the focus of this discussion will be on the detection of α particles.

The two DSSSDs are segmented in to 1 mm strips, 40 on the front and 60 on the back, giving a total 4,800 pixels. Table 3.1 also shows ranges for α particles in the energy range for decay. In 300μm-thick silicon, even from a heavy ion that is implanted very close to the surface, the majority of the solid angle for α particle emission will result in the full E_α being deposited in the detector. It is worth noting here that E_α measured will be $\sim$50 keV higher than the true value when using a calibration performed with an external source, due to an absence of 'dead layer' energy loss [36]. Recoil implantation and α-decay events are distinguished by the MWPC, which produces a signal only for implantation events. When an α decay event occurs, E_α is measured alongside the DSSSD pixel in which the decay occurred. If E_α corresponds to the decay of the chosen nucleus the 'history' of the pixel is retrieved from the buffer. Here 'history' refers to the implantation events immediately preceding the decay for which the implantation of the recoil was recorded in the corresponding pixel. One can then take the SAGE and JUROGAMII data from these historic events as decay gated events and populate spectra free of contaminants. If one assumes the most recent implantation correctly corresponds to the decay and assume that recoils are distributed evenly over the DSSSD pixels, then it is clear to see that ideally the total implantation rate should be $\ll 4{,}800/t_{\frac{1}{2}}$. This technique can produce exceptionally clean spectra, however if efficiency is more desirable it may be advantageous to identify recoils using the Time of Flight (ToF) and ΔE/E methods.

Time of Flight and Energy Loss Recoil Identification

In GREAT using the MWPC and DSSSD, the techniques of ToF and Energy Loss (ΔE/E) ion identification can be used to separate out the nuclei that make it through RITU. This

can be useful in situations where decay tagging is not possible or not desired, and as an aid to this technique. For example, if one requires that these ion identification parameters fall within set values, in order to be considered a valid implantation, then events for which the implantation could not correspond to a given decay may be discarded. This increases the effectiveness of the recoil tagging and increases the possible implantation rate. Events in which an implanted pixel is struck by an invalid implantation ion before the subsequent decay of the first implantation are hence recoverable.

ToF identification relies on the simple mass dependence of the relation between velocity and energy. A timing signal is recorded for a passing ion at two points in the setup giving a velocity; the ion is subsequently stopped in a detector recording its total energy [63]. Using this information, different mass nuclei may be distinguished with a precision dependent on energy and timing resolution [64]. In GREAT the MWPC acts as the start timer and the DSSSD acts as the stop timer, and also provides E_{total} measurement. Assuming velocities are in the classical limit one can write a time-mass resolution relation for particles of matching energy as:

$$\left(\frac{t+\Delta t}{t}\right)^2 = \frac{\Delta A}{A} + 1\,. \tag{3.12}$$

Assuming Δt is limited by detector timing resolutions of about 1 ns for $\beta = 0.02$ this gives a mass resolution $\frac{\Delta A}{A}$ of 6%. This value is insufficient to separate neighbouring heavy nuclei but sufficient to further suppress beam or spurious reaction products that do make it through the separator.

Identification is also provided by the difference in energy loss $\frac{dE}{dx}$ through a medium for different ions. From Equation (3.11), it can be seen $\frac{dE}{dx}$ or 'stopping power' depends on Z and ν of an ion, i.e. for any given energy of a traversing ion, the stopping power is characteristic of the species. If one can measure this rate of energy loss and the total energy of the ion it can provide a unique tag. In Bragg detectors $\frac{dE}{dx}$ is measured across the full energy range as the ion is stopped in a gas [65], however similar results can be obtained using a simple E-ΔE telescope [66]. Such a telescope comprises a thin transmission detector and a thick stopping detector. The transmission detector absorbs a small fraction of the ion's energy, ΔE, as a measure of the stopping power and the thick detector gives the E_{total} to which that stopping power corresponds. Identification of species by such means is often achieved using a 2-dimensional plot such as is shown in Figure 3.8. In such measurements the ΔE detector need not be calibrated in terms of MeV as it serves as a comparative measurement.

In GREAT, E-ΔE is provided by the E measurement in the DSSSD verses ΔE given by the MWPC signal size. As with ToF measurement, E-ΔE in GREAT does not provide unambiguous identification of reaction products and for the best results should be combined with the other measured, species-dependent, quantities.

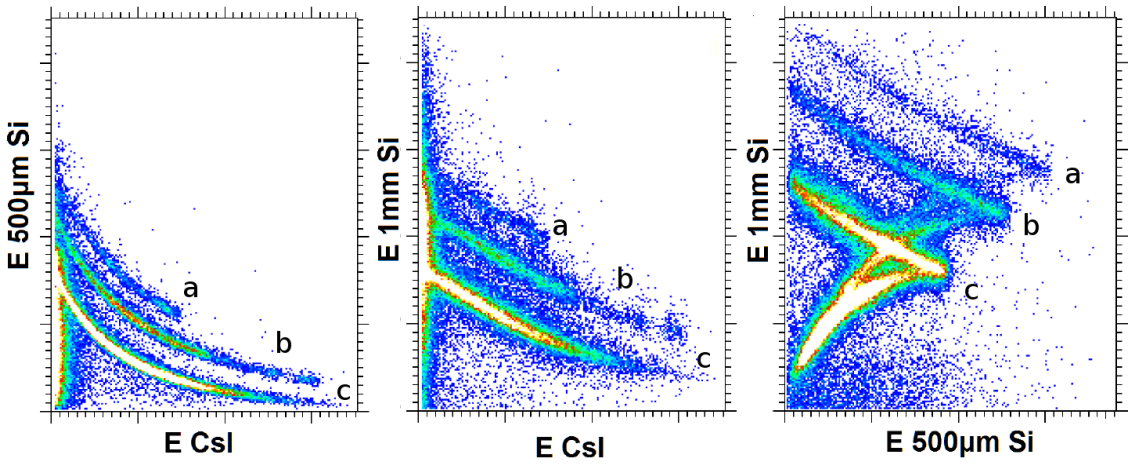

Figure 3.8: Spectrum from a silicon-silicon-caesium iodide ΔE-ΔE-E triple telescope (arbitrary units). Seen are characteristic shapes from (a) ^{3}t, (b) ^{2}d and (v) ^{1}p. The typical back bend seen in the far right panel occurs as particle energy becomes high enough to allow penetration of both silicon detectors. This figure is taken from the my masters work [67] using the ^{11}B(^{3}He,X) reaction and is included as an ideal example of ΔE-E identification.

3.2 Electron Detection Efficiency

Energies of conversion electrons can be measured in the SAGE silicon detector to within a few keV, however to make these measurements have any physical meaning they must be looked at not individually but as an ensemble. Rarely in nuclear physics are experiments such that one can ask meaningful questions of a single nucleus or event. Instead one may ask what fraction of a certain interaction produce a certain result. For example, one may ask for a given nuclear transition what is the conversation coefficient, what is the probability is that the transition proceed by γ ray emission or by internal conversion. To answer such a question one must measure how many of each decay mode occur. The crux of the matter here is that the number of γ rays and conversion electrons is greater than the number that will detect be detected. In order to determine meaningful physical quantities one must establish, of all emitted particles, what fraction do the detected particles constitute.

3.2.1 Efficiency Effects

SAGE is a unique detector and as such the various competing effects on efficiency are worth discussing. In this context the word 'efficiency' is concerned with the following question: what is the probability that an electron emitted at the target position reaches the detector with its full emission energy and that the full energy is measured? The probability is a function of emission angle and energy. An isotropic distribution is assumed and as such the detection efficiency is given by the probability distribution $P(E_e)$.

Orbital Radius

The helical path an electron follows was discussed in depth in Section 3.1.1. The diameter of this path is directly dependent on energy and is a major contributing factor to electrons failing to reach the detector. Between the target volume and the main solenoid volume are two carbon foils to separate the RITU ^{4}He filling gas from the high voltage barrier. This is the narrowest point along the path of an electron, with a radius of 15 mm [68]. The field at this point drops off rapidly, as seen in Figure 3.3, to approximately 0.1 T. Recall that the helical path makes a tangent with the solenoid axis, where the orientation around the axis is dependent on emission angle ϕ and the helical radius depends on emission angle θ and magnetic field strength. The narrowest point is most problematic as θ approaches 90°(electrons perpendicular to the field) and radius is maximum. In this limiting case electrons with energy above 50 keV would strike the foil frame. Of course the majority of electrons will not be emitted perpendicular to the field, and higher energies than this may pass through the bottle neck. The net result is that at higher electron energies, fewer emission angles result in electrons reaching the detector and hence there is a reduced transmission efficiency. Similarly, at the detector position the field is approximately 0.1 T, resulting in higher energy electrons having $d_{helix} > r_{detector}$. For example, if one takes the circular projection on to the detector of helical paths for $E_{e\perp}$ =200 keV only 48 % fall within the circumference of the detector. If energy is increased to $E_{e\perp}$ =500 keV the fraction of the path overlapping with the detector drops to only 27%.

Field Reflections

Another effect in transmission efficiency is the so called 'magnetic mirror' effect that can occur in regions with magnetic field gradients. For a charged particle moving through a field with a helical path, as described by Equation (3.1) the orbital period is given by Equation 3.13,

$$t_{period} = \frac{2\pi m_0 \gamma'}{Bq} = \frac{2\pi m_0}{Bq\sqrt{1-\frac{v_\perp^2}{c^2}}} = \frac{2\pi P_\perp}{Bqv_\perp}\,, \tag{3.13}$$

where γ' is the Lorentz factor for motion perpendicular to the field. If the field varies slowly in space or time relative to this orbital period (adiabatically), it can be shown [69] that the flux linked by the orbit is a conserved quantity.

One result of this conservation has been used to describe the helical trajectories of electrons and is explicitly stated as follows: if an electron is emitted from a point along the axis of an axially-symmetric magnetic field, such as in SAGE, it will move with an orbit that remains tangential to the symmetry axis if the field varies adiabatically, although its outer extent will vary.

Furthermore, the adiabatic conservation can be expressed as conservation of the quantity $P_\perp/B$. It can clearly be seen that if B increases then $P_\perp$ will increase, and hence $P_\parallel$ will decrease. This can be qualitatively considered by noting that if B(Z) is increasing along the symmetry axis Z the field must have a radial component, the force from which will act to change $P_\perp$ and $P_\parallel$. For a sufficiently high field gradient, a particle may be

reflected entirely. This is illustrated in Figure 3.9 and the criterion for reflection is given by Equation 3.14 [69], given in terms of the initial/minimum field B_0 and the momentum at that point P_0,

$$\left|\frac{P_{\|0}}{P_{\perp 0}}\right| < \left(\frac{B_{max}}{B_0} - 1\right)^{1/2} . \tag{3.14}$$

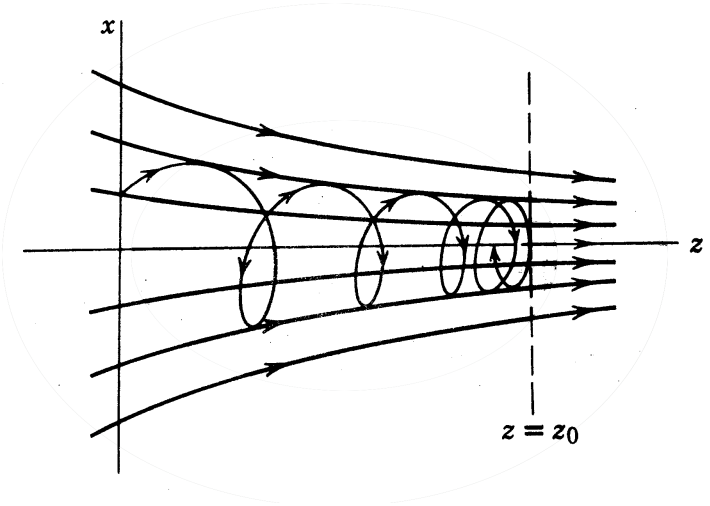

Figure 3.9: Reflection of a charged particle out of a region of high field strength [69].

Referring to Figure 3.3, a very steep magnetic field gradient is observed either side of the target position in SAGE. Using Equation 3.14 any electrons emitted at angles greater than ∼55° from the field axis would be expected to be reflected by the field. Such electrons would be trapped in the target region and never reach the detector accounting for a sizeable transmission efficiency loss. However, if a 500 keV electron is emitted at such an angle, in the weak field at the target position, this constitutes an orbital period of 0.41 ns, during which time the electron would move a longitudinal direction of 8.6 cm. Over such a distance the field increases by ∼40 % illustrating that the field gradient in SAGE is sufficiently steep it may not constitute an adiabatic change. As such the electron's motion may differ from the idealised case presented here, with the effect being greater at higher energy.

In addition to the possibility of reflection by the magnetic field gradient it must also be noted that electrons may also be reflected by the electric potential of SAGE's electric barrier. The electric potential gradient of the barrier is perpendicular to the magnetic field axis, and so it is simple to see that the energy associated with the longitudinal motion of an electron must be greater than the height of the barrier in order for the electron to pass. Using Equation 3.2 one can formulate the maximum emission angle θ for a given kinetic energy T and potential $V_{barrier}$:

$$\theta(T) < cos^{-1}\left(\sqrt{\frac{(eV_{bar})^2 + 2eV_{bar}m_ec^2}{T^2 + 2Tm_ec^2}}\right) . \tag{3.15}$$

Clearly this should have a greater effect on the transmission efficiency at lower energies, and

for T< $V_{barrier}$ no electrons should be detected. An example of the competing transmission efficiency effects is given in Figure 3.10 where the cut-off fraction imposed by each effect is shown. Effectively each effect imposes a $\theta_{max}(E_e)$ cut off for electron transmission and the smallest angle determines the cut off at that energy.

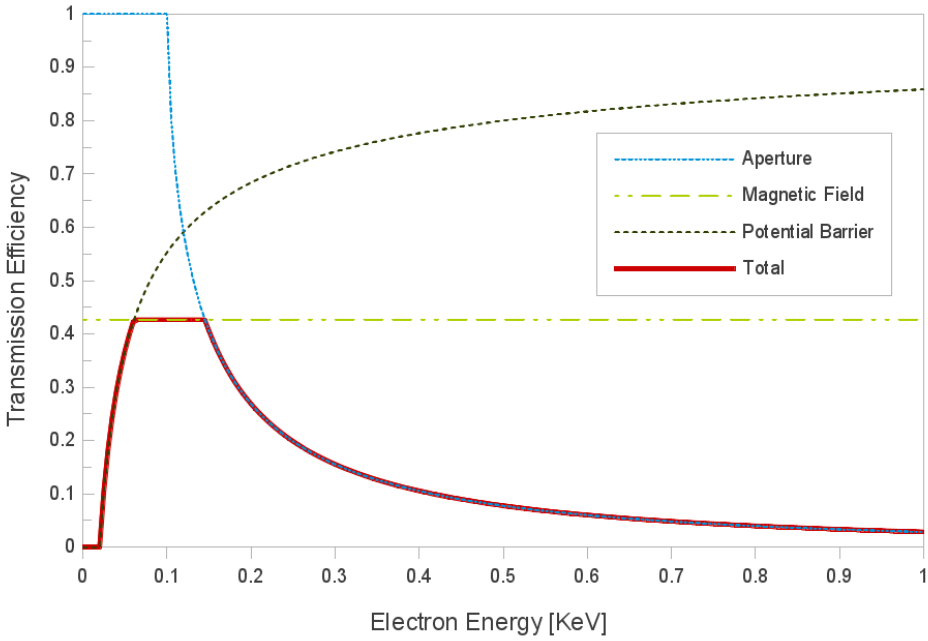

Figure 3.10: Example calculations of the competing transmission efficiency effects for electrons in SAGE, normalised for solid angle as each effect imposes a cut off in emission angle θ. The total effect of the three restrictions combined is shown in red.

Energy Loss

Now following the consideration of transmission efficiency, the interactions of electrons with matter must be considered. These interactions may contribute to transmission losses or affect the full energy detection. Within the SAGE detector system we must consider both the electron interaction with the silicon detector and any matter an electron may interact with between the emitting nucleus and detector.

The targets used are typically thin foils of only a few mg/cm^2 (a few μm) thickness. In a thin target experiment, energy loss of the beam nucleus as it passes through the target material is sufficiently small that the reaction cross section can be considered constant throughout the target. Hence a reaction may happen at any depth through the target with equal probability and so electrons emitted by recoiling nuclei will have to pass through varying amounts of the target, ranging from near zero to the full target thickness. Due to the helical trajectory of the electron, the effective thickness of the target seen by the electrons will be greater than the linear dimension.

Figure 3.11 shows the fraction of an electron's kinetic energy lost per mg/cm^2 of material traversed. This figure shows that for a 100 keV electron 2 % of the total energy is lost in passing through the whole of a 1 mg/cm^2 samarium or erbium target. For energies below this a significant fraction of electrons will either reach the detector with far less than

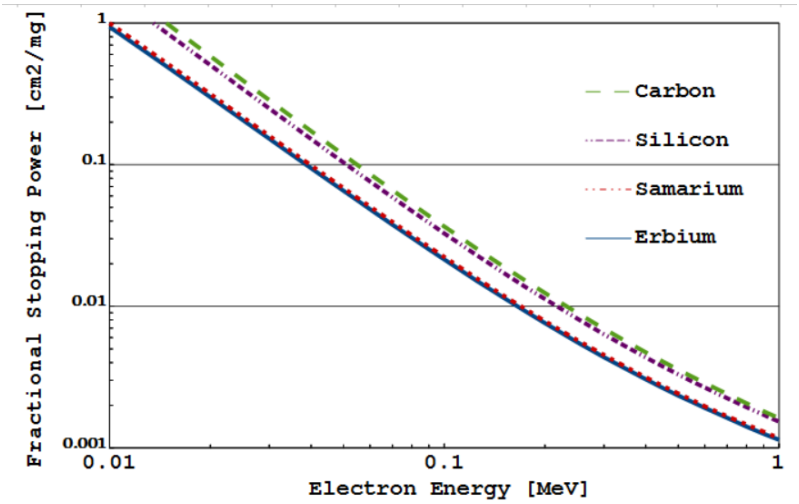

Figure 3.11: Fractional stopping powers for various materials. The fraction of total kinetic energy lost by an electron per mg/cm^2 of 4 different Z target materials. Data from National Institute of Standards and Technology's estar program [70].

their emission energy or never exit the target. Conversely, electrons with energies higher than this will reach the detector with their energy intact, to within the resolution of the detector, independent of emission position. The small energy loss need only be considered if high-precision energy measurements are to be made from the electrons.

Recall that following emission from the target, electrons must also pass through two 40μg/cm^2 carbon foils on the path to the detector. These foils are sufficiently thin that an electron with energy as low as 30 keV may pass through both and only lose 2 % of its energy. All electrons must pass through both foils independent of emission position. These foils will only affect very low-energy electrons which are of little experimental use.

Electrons that impact the carbon foil mounts or target ladder may be assumed to be lost as these aluminium pieces are too thick for even a high-energy electron to penetrate. However, due to their low mass, electrons are easily scattered and there is a small probability they may scatter out of these parts and reach the detector with a reduced energy, especially at low impact angles. The importance of scattering is discussed in Section 3.2.2.

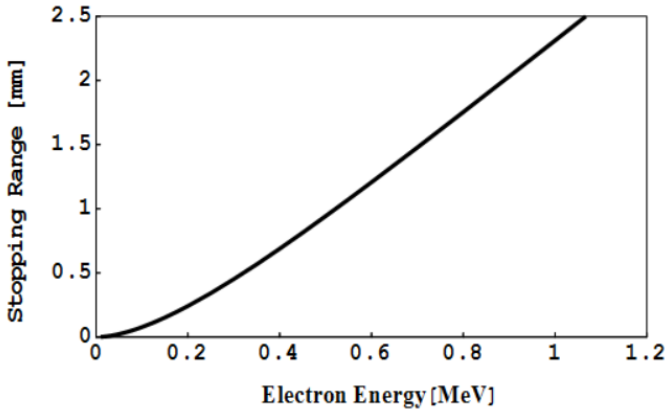

Figure 3.12: Electron stopping ranges in crystalline silicon. Data from National Institute of Standards and Technology's estar program [70]

3.2.2 Scattering and Addback

The range of an electron in silicon as a function of energy is shown in Figure 3.12. A 1 MeV electron has a range of 2.3 mm, as seen in this figure. The silicon detector in SAGE is only 1 mm thick and the smallest elements have an area of 1.178mm^2. For higher-energy electrons the probability for complete energy deposition within the detector will be heavily dependant on scattering effects.

Figure 3.13 shows a Monte-Carlo simulation of 50 electrons scattering in aluminium, using the resources found in Reference [71]. Despite having sufficient energy to punch through the target, this simulation shows the nearly half of the electrons stop within the medium due to the a circuitous route they follow as a result of scattering. About a fifth of the electrons are shown to backscatter out of the medium. This is important because this loss mechanism is present even when electrons do not have sufficient energy to punch through the silicon detector. The probability for electron scattering reduces with increasing energy, so as electron energy increases the probability of backscatter decreases and the probability of punch through increases.

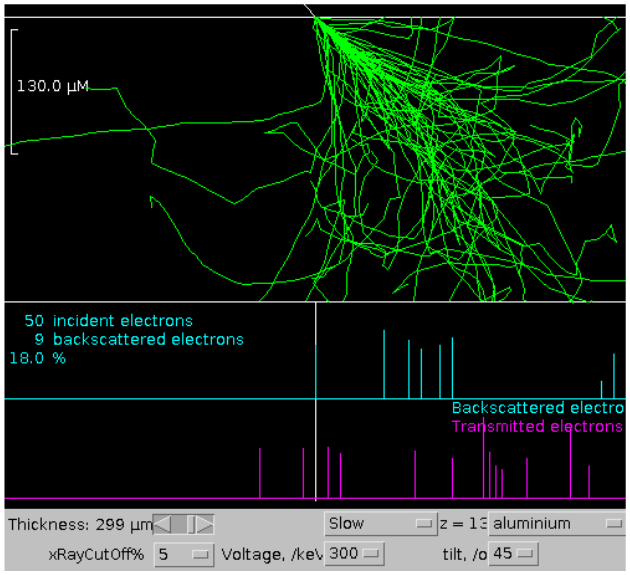

Figure 3.13: Basic Monte-Carlo simulation of 300 keV electrons, with an incident angle of 45°, scattering through 0.3 mm of aluminium [71].

A SAGE spectrum from a ^{207}Bi calibration source is shown in Figure 3.14. Clearly shown in Figure 3.14 is a raised plateau extending at lower energies below each full-energy peak. These distributions of electrons are the result of electrons depositing only part of their full energy in the detector before scattering out of the detection medium and being lost. This figure shows only singles events, those where a single detector element triggered, and so it can be assumed that the electron scatters out of the detector (or scatters before reaching the detector). Similarly, an electron may scatter between elements of the detector resulting in multiple recorded signals, but with no one signal having the full energy. The calibration source was of a sufficiently low activity, and ^{207}Bi has a low branching ratio for the emission of multiple electrons, that it can be assumed that the majority of multiple-hit events from this source are from such scatter events.

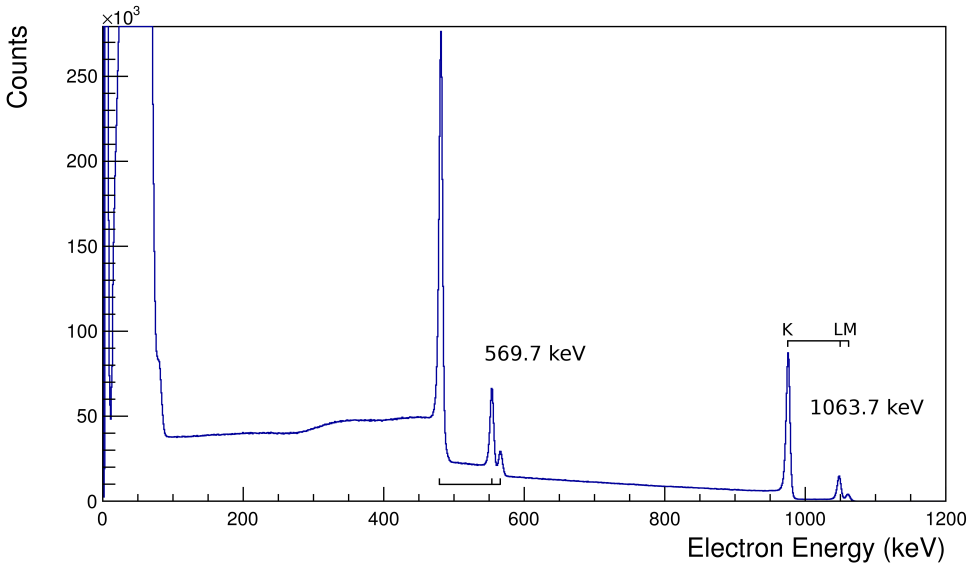

Figure 3.14: Energy calibrated SAGE electron singles spectrum for a ^{207}Bi calibration source, 1 keV/bin. Note the step in background plateau across each peak due additional scattering contributions.

The range of electrons with energies approaching 1 MeV is greater than the detector thickness and the width of many elements. Figure 3.14 shows that there are events where such high-energy electrons deposit their full energy in one element. However, the detection efficiencies could be improved at these energies if the events where the full energy is deposited but over multiple elements could be recovered, hence an addback algorithm was added to the sort code. Initially this code checked all electron hits in multiple-hit events for pairs in neighbouring elements and when such a pair was found their energies were summed. The results are shown in Figure 3.15.

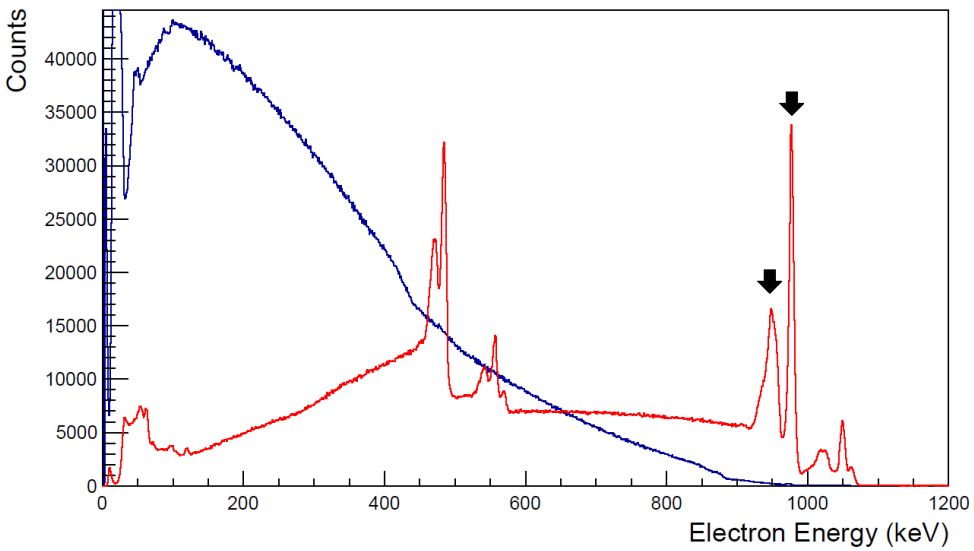

Figure 3.15: SAGE electron spectrum from ^{207}Bi calibration source. Shown in blue are electrons which the algorithm identifies as neighbouring hits in multiplicity > 1 events . Shown in red is spectrum produced when these neighbouring pairs are summed together. Correctly and incorrectly reconstruct 976 keV K electron peaks are indicated.

Initially the algorithm appears to be quite successful: many full-energy electron peaks are correctly reconstructed. However, approximately 30 keV below each correct full-energy peak a smaller, incorrectly-reconstructed peak appears. As this peak is not present in the singles spectrum, it can be assumed it is not caused by anything outside of the detector. The effect is only present in events where electrons have scattered between multiple elements and the energy difference is discrete. Logically it is an effect of the detector and not of the scatter, perhaps due to a dead region between certain elements. To investigate this hypothesis hit pattern maps of the SAGE detector segments for the correctly and incorrectly constructed multiple hits were produced. Figure 3.16 shows these maps gated on the K electron peaks at 976 keV. There is a clear pattern between which detector elements produce a correctly reconstructed energy and which do not, though it is not easily explained. One explanation of the pattern would be that the small energy deficit is caused by loss between different rings of detector elements. This would highlight areas of the detector where there were fewer neighbouring elements of the same radius, due to disabled elements, potentially matching the pattern. When only pairs of the same radius are used in reconstructions the satellite peak is suppressed, but the majority of the correctly reconstructed peak is also lost.

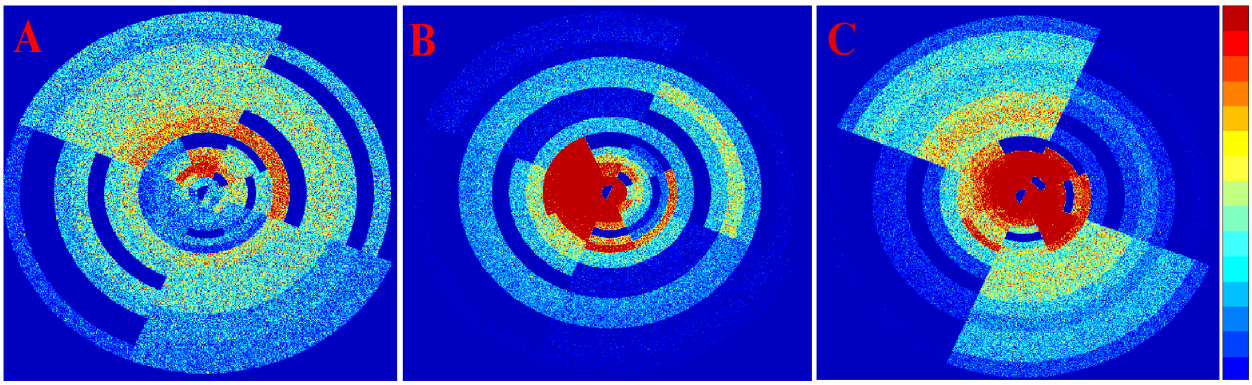

Figure 3.16: SAGE hit pattern map gated on ^{207}Bi 976 keV electron. Red indicates high intensity, empty dark blue areas of the image denote elements which have been disabled because of preamp problems. A) Shows hit pattern when gated on 976 keV peak in raw singles data, demonstrating the normal distribution one might expect B) Shows hit pattern when gated on correctly reconstructed 976 keV peak in the addback spectrum shown in Figure 3.15 C) Shows hit pattern when gated on poorly reconstructed peak at ∼950 keV of the same spectrum

It was concluded that resolution of this error would require more detailed investigation of the detector itself and cannot be solved offline. Hence it is not possible to cleanly produce such addback events at this time. Scattering events can be identified with this procedure in order to remove them from otherwise contributing to background. The rejection of all multiple-electron events, in order to avoid spectra contamination, was decided against as in-beam events are of higher multiplicity. Delta electrons are produced in abundance and, despite the potential barrier in SAGE to suppress the delta electrons, any conversion electron is quite likely to arrive in coincidence with one or more delta electrons. Furthermore, the calibration isotope ^{207}Bi may have a low branching ratio for multiple emission of electrons in its decay, but a highly-excited product in a nuclear reaction may

emit many electrons during its decay to the ground state. Efforts were redirected from constructing addback events to correctly identifying scattering events for exclusion. A balance must be reached in removing as many of the noise-contributing addback events as possible without losing total energy peak events that occur in coincidence with another electron.

The SAGE silicon detector was designed to optimise rate and is single sided, not a DSSSD, as such the 'Front vs Back' method cannot be implemented. In such a method energy measured in perpendicular front and back strips are compared to correctly identify multiple-hit events, as detailed in Reference [72].

In addition to requiring the elements to be adjacent the investigation revealed several other requirements that could be applied in order to optimise the selection.

Firstly a minimum energy threshold was imposed on detector elements, so that no energy under 15 keV would be considered. The potential barrier prevents the lowest energy electrons reaching the detector. As such one might assume low-energy signals result from scattering. However in events where the total energy of the electron is recorded in one detector element a small amount of charge may be induced on neighbouring elements during the charge collection process, appearing as a small neighbouring energy measurement [36]. Secondly it was required energy be evenly distributed between elements (neither should have more than 80% of the total). Thirdly a timing gate was used to further avoid false identification scattering. In a true scattering event the charges are produced in the elements simultaneously, and so a 70 ns maximum time difference was implemented. See Section 3.3.3 for details on removing electronic timing differences.

In multiple-element events all possible combinations of pairs are checked against these conditions and then removed from the event. Figure 3.17 demonstrates the effectiveness of this method in removing background counts while leaving full-energy peaks intact.

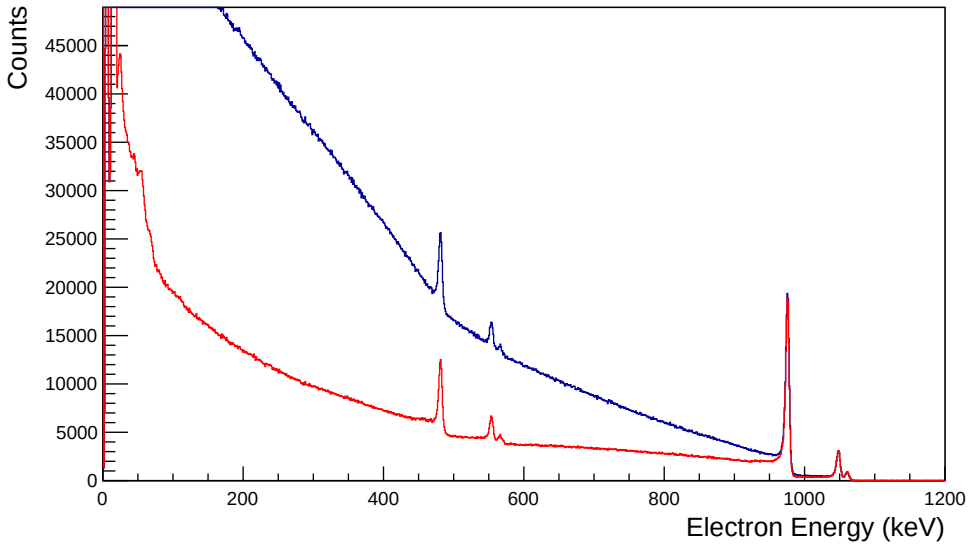

Figure 3.17: Electron energy spectrum obtained from SAGE using the multiple electron events from a ^{207}Bi source. The lower (red) line shows the result of removing identified scattering pair events using the conditions described in the text. Note that the full-energy peaks are unaffected.

Following this a small further subtraction can be made. As discussed in Sections 3.1.1 and 3.2.1 the energy of an electron will determine the path of the electron in SAGE and the region on the detector that it may reach. Events in which an electron scatters before it enters the detector, scatters out of the detector, or scatters within an inactive area of the detector may then be identified. If the measured energy is lower than the minimum needed to reach a given point on the detector the event can be vetoed. This subtraction provides a minimal effect and only acts for $E_e \leq$130 keV. The formulation of this subtraction is detailed in Appendix B, but it was not used. Due to the discrete radii of the detector elements the subtraction introduces discontinuities into the initially continuous background, further complicating analysis.

3.3 Data Acquisition

3.3.1 Total Data Readout

At JYFL a Total Data Readout (TDR) system is implemented for the collection of data [73]. The fundamental aspect of the TDR system is that detector elements are individually instrumented and recorded without a common trigger. Conventional systems, which use a signal in a pre-defined detector to trigger the Data Acquisition system (DAQ) to record the event, suffer from large system dead-time losses. In recoil-decay tagging, where wide common gates are used, these dead-time losses can be particularly large. An event gate as wide as 1 ms would limit the data rate of all detectors to a maximum of 1 kHz. This can be particularly problematic if the channel of interest is only a small fraction of the implantation rate. The TDR system was developed to counter this effect, as well as providing additional flexibility for offline analysis. A flowchart is provided in Figure 3.18 to illustrate the JYFL TDR system described below.

Each detector element, is individually instrumented. This corresponds to each element of the silicon detector in SAGE, and each germanium core and each BGO shield, in the case of JUROGAMII. It is worth noting here that the BGO Compton suppression is not performed online. Hits in coupled germanium and BGO detectors are recorded separately to disk, even when a vetoing event has occurred. Following pre-amplification, detectors are fed into individual channel digitisers. All the digitisers are connected to a 100 MHz clock which provides a time stamp of 10 ns precision throughout the system. Each channel has its own adjustable threshold; if the input signal crosses this threshold level then the channel triggers and the time stamp and other channel data are collected to the system buffer.

The buffered data are passed through TDR Event Builder (TDREB) software which may optionally filter the data before passing the data to disk for storage and Grain analysis package for online analysis. TDREB may be used to filter out events of low multiplicity, i.e. one can require that only data from the buffer in which at least 2 channels cross threshold within a 100 ns window is kept. Such a filter may be used when performing a γ-ray γ-ray coincidence study in which single γ-ray events are of little use. This allows collection of data at a higher rate before disk write-speeds cause limitations. This filter

forms the only system-wide online trigger, beyond this point data passed to Grain either directly from TDREB online or from the disk offline are identical. The notation $\gamma\gamma$ will be used to refer to an event in which two signals were recorded in JUROGAMII and $e^{-}\gamma$ will refer to an event in which a signal was recorded in both JUROGAMII and the SAGE silicon detector.

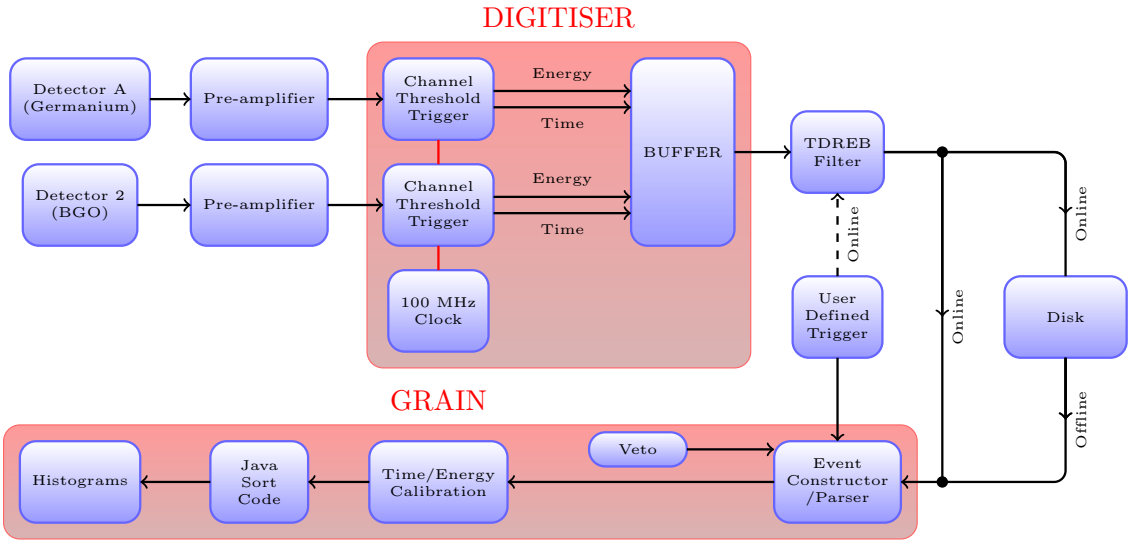

Figure 3.18: Flow chart illustrating the Jyväskylä Total Data Readout data acquisition system and Grain analysis package. A full description of the various stages of the system is given in the text.

3.3.2 Grain

The Grain software package is used to construct events from stored TDR data and to sort those events into histograms for further analysis. Grain also provides the facility for post-sort gating of two-dimensional histograms and contains some basic fitting tools.

The user must first provide Grain with a trigger file. This file tells Grain which digitiser channels should form part of the sort trigger, what multiplicity should be required, what time extent to give the event and which detectors the channels correspond to. Data are loaded to a buffer from disk chronologically based on the time stamp associated with each detector entry. When a trigger detector entry is found in the data stream, Grain begins event construction. The event parser searches backwards through the buffer as far as the specified trigger delay time before the triggering entry. All entries are collected forward in time from this point until the specified event width has passed. The entries form one event. This system for event construction is demonstrated in Figure 3.19. At this point the detectors to which each entry correspond are included, and any BGO vetoes are optionally applied. Following this the user-defined time and energy calibrations are applied to the elements and an event is then passed to the sorter as a collection of Java object arrays for the various detector types. Recoil-decay tagging may then be implemented within the Java sort code. Events identified as implantation events may be added to the 'tagger' and stored in memory in order to be paired with later events identified as decay events.

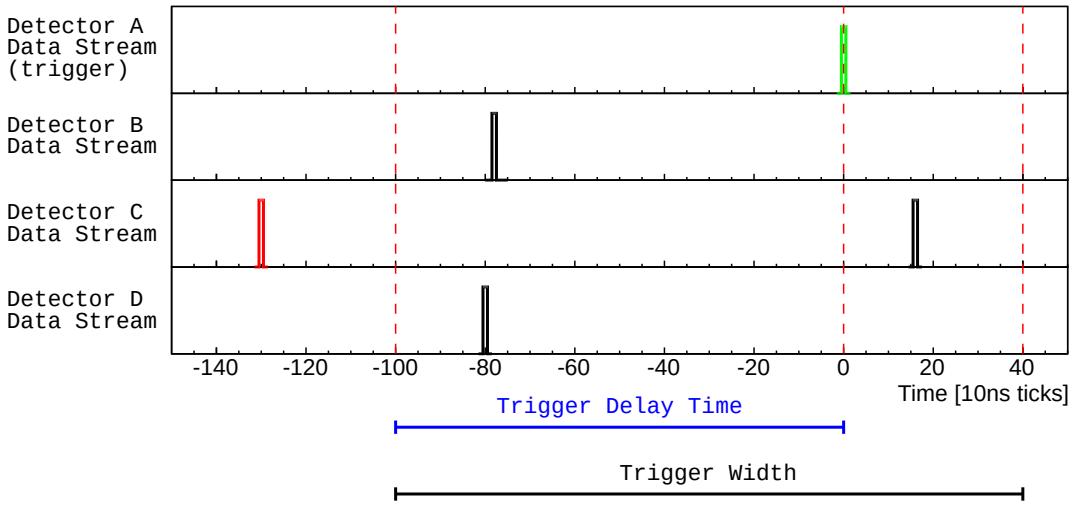

Figure 3.19: An example of trigger and event construction in the Grain event parser. Here a Detector A is selected as the trigger with a delay time of 1μs and and event width of 1.4μs. The entries that occur significantly before the trigger for Detectors B and D are included in the event along with the entry in Detector A that produced the trigger and the later event in detector B.

3.3.3 Time Alignment

In addition to a standard energy calibration, in such a system it is important to perform adequate time calibration. The 100 MHz clock disseminates global time throughout the system but this does not guarantee that simultaneous events will be recorded with the same time stamp in the data stream. Significant variation in cable length (3 ns delay permetre), difference in element threshold levels and variation in hardware response to a signal all contribute to time variation. It is important to eradicate these external time differences in the data. The physical time difference between between say, a γ ray reaching JUROGAMII and a conversion electron from the same nuclear cascade reaching SAGE, should be preserved. Such a physical time difference may differ depending on the physical process involved and may be used to analyse the data.

The signals from the individual elements of SAGE, however, should be aligned in time with each other, and the detectors of JUROGAMII likewise. This is done my using a known physical process, either from calibration or beam data, and construct events triggered on a single detector outside of the array which is coincident with the selected process. Next, histograms are produced for the timing of each array element relative to the single trigger. The histogram for each array element has a clear peak for genuine coincident events, the peak is approximately Gaussian with a width given by a combination of the timing resolution of the detector, electronics and physical process. The centroid of the timing peak for each array element is then recorded and a mean calculated. The timing calibration is then defined by setting a time offset for each array element equivalent to the difference between the elements time centroid and the mean. For the sorting of subsequent data, the offset for an array element is added to the time value recorded for that element in each event to give the calibrated time value. Following timing calibration, a sum of data across the entire array may produce a total timing histogram with a coincidence peak of

comparable resolution to that of an individual element.

The effect is small, only a few 10s of nanoseconds, but any improvement in timing resolution improves time gating, which is very important for background suppression. Figure 3.20 shows electron times relative to a GREAT focal plane trigger, taken from an experiment in which RITU was used. It can be seen that the trigger must be extended backwards in time as the electrons are detected 80 ns before the recoil nucleus is detected at the focal plane at t=0. However, if all the electrons in this event are accepted as part of the event, the spectrum would be dominated by background. Instead, a further time gate is taken within the sample time of the triggered event and it is here that improved time alignment will be vital. The nature of time background and its suppression will be discussed in Section 4.4.4.

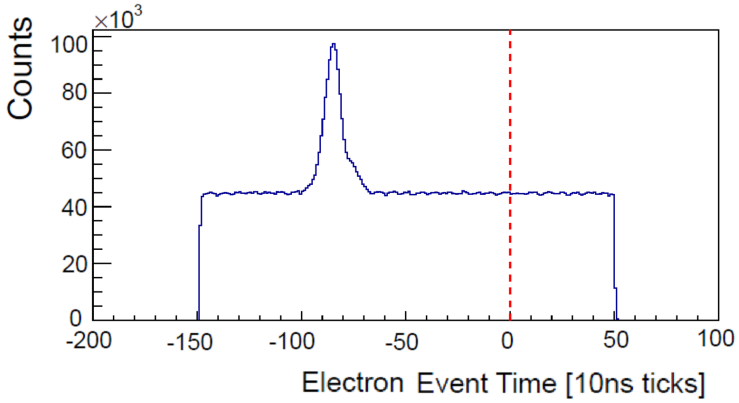

Figure 3.20: Spectrum showing the relative time of recoil-gated electrons in the SAGE detector elements for events triggered on the GREAT focal plane gas detector taken from an experiment in which RITU was used. A peak is seen at -80 ticks corresponding to genuine coincidence events. An asymmetry in the peak indicated two genuine coincidence processes with different timings. The peak sits on a large random background filling the whole of the event window. Small perturbations in the background can be observed corresponding to cyclotron pulses. The event window shown here is long due to the transit time in RITU, timing spectra in Chapter 5 are shorted as RITU was not used.

4

Analysis Techniques

Several of the analysis challenges faced and techniques developed in this work are, including the peak fitting and random background subtraction, are general to a range of experiments. In this chapter an review of the techniques implemented to move between experimental data and meaningful physical results is presented.

4.1 Peak Fitting

For both the efficiency calibration and later experimental measurement an accurate method of determining peak area is needed. In an idealised situation the area of an isolated peak would be found by removing the background and then simply integrating over the remaining peak. An algorithm which estimates the background by iteratively smoothing under peaks can be used to achieve this, giving the area of the peak to the first order. When more precise area measurements are required we must consider the nature of the peak more carefully.

Simple background removal may provide consistent and accurate experimental results for isolated peaks, however when peaks overlap, a full fit is required in order to de-convolute their areas. If an arbitrary background removal is used across multiple peaks, subsequent peak fitting is still required. Following an arbitrary background subtraction, that is not physical in nature, the remainder may consist of irregular peaks. It is advantageous to use a physical background calculation, where peaks are fitted simultaneously and the background contribution of each peak can be directly related to its size and included in the fit. This difference between the two approaches is illustrated in Figure 4.1

4.1.1 Background Step

In both electron and γ spectra, a step in background is seen across each full-energy peak, as small scatters from the full-energy peak in question begin to contribute to background at energies below the peak. For γ rays, this contribution is made up of small angle Compton scatters *into* the detector as well as the escape of photo-electrons from the detector medium. In SAGE, this background step is associated with electrons that have scattered out of the detector or detector elements, or electrons that have had small-angle collisions with part of the apparatus and have continued to reach the detector. These contributions extend from the full peak energy down to zero and will have some distribution shape depending on the various processes included and detector geometries. In electron, spectra this contribution is significant and so the assumption of a simple background is

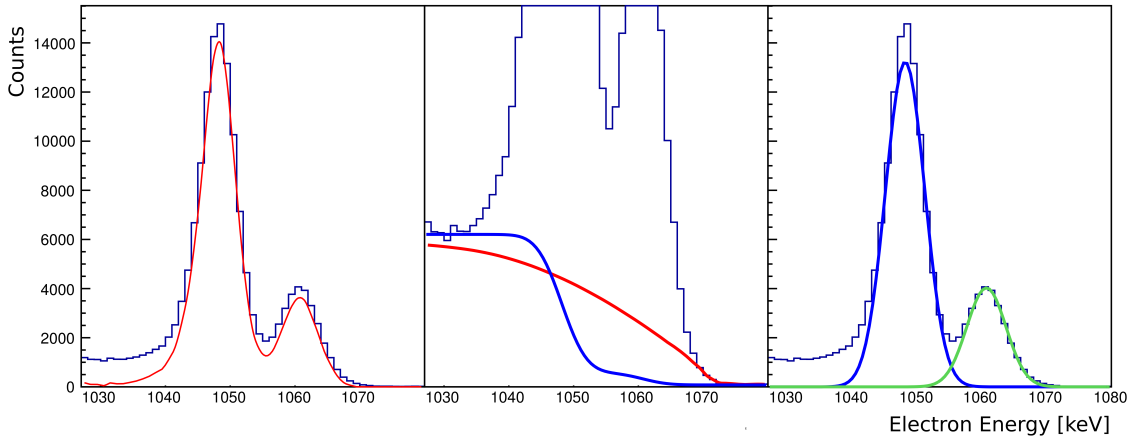

Figure 4.1: For peaks with overlap the subtraction of an interpolated background (left) is insufficient. A simultaneous fit of both peaks and background (right) should be used. The centre panel shows the different backgrounds used, the interpolated background from a smoothing algorithm is shown in red and the physical background from the simultaneous fit is shown in blue.

not appropriate.

The 'background' counts originate from the same physical transition in the nucleus as the full-energy peak and could be considered legitimate counts. Indeed, in an ideal situation the full scattering distribution and the full-energy peak would be accumulated, but in realistic spectral analysis, only the region of a full-energy peak can be clearly identified.

It is important to remain consistent in what is defined as a peak area, i.e. whichever method of area calculation is used must be consistently applied to both calibration and experimental data. In this work only the area of the full-energy peak will was used. This was done by defining the background step in terms of the full-energy peak parameters and fitting them together as a convolved function. Figure 4.2 shows a typical electron peak with three defined areas: full-energy peak P, uncorrelated background B and peak background contribution BP.

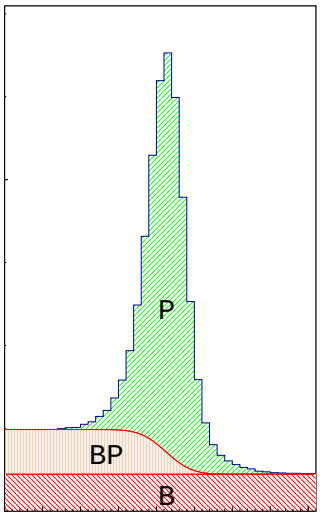

Figure 4.2: Peak background contributions. See text for details.

The full-energy peak is characterised by a distribution, nominally a Gaussian, due to the dominance of random statistical effects in detection involving noise and charge collection. The scattered events that constitute the background step are also subject to these effects. Hence every point in the scattering background between E_{peak} down to zero will have the same distribution. Alternatively one may think of this as each point, within a statistically broadened full-energy peak, contributing to the background below that point. The result of this is that the shape of the background step is expected to be given by the reverse Cumulative Distribution Function (CDF) of the full energy peak distribution. For a Gaussian peak

this is:

$$(1 - \mathrm{CDF}) = \frac{1}{\sqrt{2\pi}} \int_x^\infty \mathrm{e}^{-\left(\frac{t-x_0}{\sigma\sqrt{2}}\right)^2} \mathrm{d}t = \frac{1}{2}\left[1 - \mathrm{erf}\left(\frac{x - x_0}{\sigma\sqrt{2}}\right)\right] \tag{4.1}$$

where x_0 is the peak centroid, σ its width and erf denotes the error function. This forms a more physically accurate definition of the background step that is used throughout this work. Subsequent peak fitting is performed using a peak function + a scaled reverse CDF of the peak function + a linear background. An illustration of the improved background is given in Figure 4.3. Note that when fitting real electron calibration data, allowing the denominator of the error function in Equation (4.1) to vary freely resulted in the minimiser returning a value equal to $\sigma\sqrt{2}$, as it should, supporting the physics behind this definition.

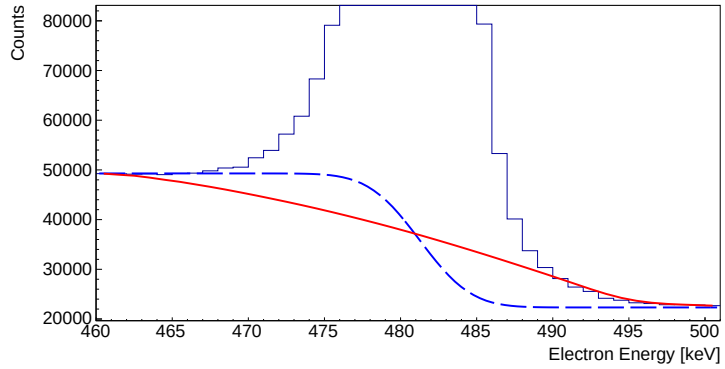

Figure 4.3: Electron calibration peak showing two different background fits. Smoothed interpolated background (solid red) and function fit background (dashed blue). For an isolated peak the difference in calculated peak area is minimal, but establishing a physical fit function is important for consistency when peaks overlap.

4.1.2 Peak Functions

A pure Gaussian peak (4 free parameters including a background step) fits the SAGE electron data reasonably well, but underestimates the peak maximum and the tails on both high-energy and low-energy sides of the peak, indicating that the peak is slightly non-Gaussian. The combination of a sharper peak and long tails is indicative of a Lorentzian contribution. An observed peak in nuclear spectroscopy will always have contributions from the Lorentzian shape of the nuclear state width and a Gaussian broadening from the many statistical effects involved in measurement and counting. The latter Gaussian broadening often dominates and would be expected to do so in these data. As such the non-Gaussian shape must be the result of another effect.

The SAGE spectra to which fits are performed are made up of the sum of data from the individual detector elements. Each detector element is instrumented and calibrated separately. The SAGE energy calibration was repeated to ensure misalignment of elements was not the cause of the peak shape.

The sum of many Gaussian peaks distributed around a mean trend towards another, broader, Gaussian. For a finite number of detector elements, each with their own Gaussian signal, non-standard patterns become possible. A numerical code was written to show the effect of combining a finite number of Gaussian peaks distributed around a set of mean

values. From this it was found that a sum of Gaussian peaks with identical centroids but varying widths resulted in the observed peak shape. Hence it was deduced that the observed peak shape results from varied resolution across different SAGE elements or pre-amplifiers. There are insufficient statistics to consider using the elements individually and as such must select a peak function that fits the sum of all SAGE elements.

Given the Lorentzian characteristics previously observed, a convolution of Lorentzian and Gaussian peaks would seem an appropriate trial function. A true convolution is given by the Voigt profile, a simpler sum of the two functions produces a suitable approximation [74]. The selected trial function consisted of a linear sum of Lorentzian and Gaussian peaks with a joint centroid, normalised to matching FWHM :

$$y = h \cdot \left(\mathrm{e}^{-\left(\frac{x-x_0}{\sigma\sqrt{2}}\right)^2} \cdot \eta + \frac{\sigma^2 2\ln 2}{(x_0 - x)^2 + \sigma^2 2\ln 2} \cdot (1-\eta) \right) , \tag{4.2}$$

where h is the total peak height and η is the mixing ratio limited to the range 0 to 1. This function minimises the number of free parameters (5 parameters including a step), while optimising the fit to the physical shape of the data, so it offers significant improvement over the single Gaussian (4 parameters).

An additional function was trialled, consisting of a sum of two Gaussians with matching centroids (6 parameters) given by :

$$y = h \cdot \left(\mathrm{e}^{-\left(\frac{x-x_0}{\sigma_1\sqrt{2}}\right)^2} \cdot \eta + \mathrm{e}^{-\left(\frac{x-x_0}{\sigma_2\sqrt{2}}\right)^2} \cdot (1-\eta) \right) , \tag{4.3}$$

where the mixing ratio η is again limited to the range 0 to 1, and the two different widths σ_1 and σ_2 are such that one is narrower than the mean width ($\sigma_1 < \bar{\sigma}$) and the other broader ($\sigma_2 > \bar{\sigma}$). Having deduced that the data are the sum of many different width Gaussian peaks, this function offers obvious benefits, and the logical extension is to proceed to a sum of N Gaussians.

For both of these functions, the background step across the peak is determined from the reverse CDF of the peak function as defined previously. A comparison of the trial functions is shown in Figure 4.4 and a deconvolution of their component peaks is shown in Figure 4.5.

For the fitting of overlapping peaks, the values of width σ and mixing η are fixed between neighbouring peaks, as both are dominated by detector behaviour at a given energy and expected not to vary appreciably over the short range of overlapped peaks. Additionally the ratio between each peak area and each background step is fixed across such a fit, as this would be expected to depend on energy alone. For two overlapping spectral peaks, this leaves 7 free parameters for the Voigt fit and 8 free parameters for double Gaussian fit.

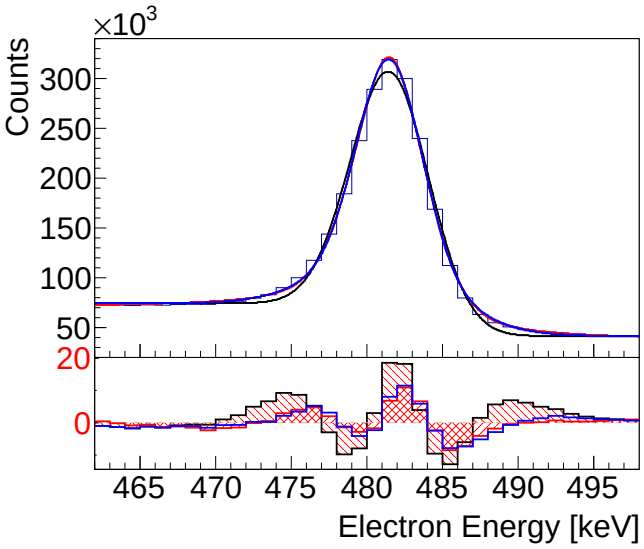

Figure 4.4: Three peak function fits to data. Single Gaussian (black), double Gaussian (blue) and Gaussian + Lorentzian (red). The latter functions have sufficient agreement that they are difficult to resolve. The lower part of the figure shows the residuals from subtraction of each function, highlighting the fit improvement over the single Gaussian.

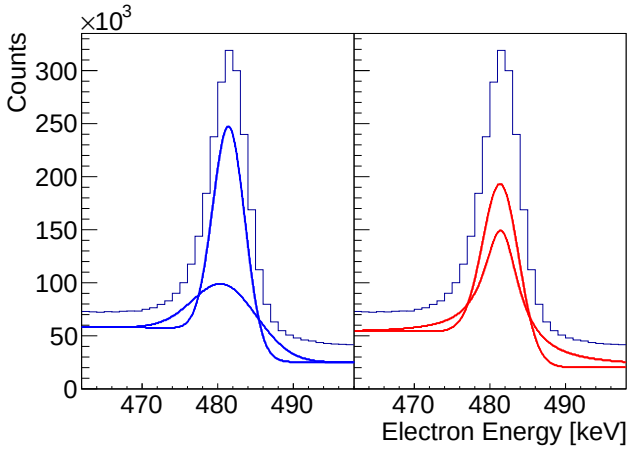

Figure 4.5: Separation of the two peaks making up each fitting function are shown for Double Gaussian (left) and Gaussian + Lorentzian (right).

4.1.3 Peak Area and Error

Fitting was performed using the χ^2 minimization routine "TMinuit" [75] taking a $\sqrt{N}$ counting error on each individual histogram bin.

Following fitting, the area of the defined peak can be determined from the fit parameters. For the Voigt approximation the area is given by:

$$A = h\left(\sigma\sqrt{2\pi}\eta + \pi\sigma\sqrt{2\ln 2}(1-\eta)\right) = h\sigma\sqrt{2\pi}\left(\eta\left(1-\sqrt{\pi\ln 2}\right) + \sqrt{\pi\ln 2}\right) \tag{4.4}$$

and for the double Gaussian, it is simply :

$$A = h\sqrt{2\pi}\left(\sigma_1\eta + \sigma_2(1-\eta)\right) \tag{4.5}$$

The error on the calculated peak area $\sigma(A)$ is then calculated by application of the error formula:

$$V(f) = \sum_j \left(\frac{\partial f}{\partial x_j}\right)^2 V(x_j) + \sum_j \sum_{k\neq j} \left(\frac{\partial f}{\partial x_j}\right)\left(\frac{\partial f}{\partial x_k}\right)\mathrm{cov}(x_j, x_k)\,, \tag{4.6}$$

given here in its general form for a function f and a set of parameters x. For a quantity X,

the variance $V(X) = \sigma(X)^2$. The uncertainty $\sigma(X)$ on a quantity X should not be confused with the distribution parameter σ in this context. The variances (and covariances) of the parameters are determined from the fit minimisation.

As an example, application of the error function to the Voigt approximation function yields the simple but rather cumbersome:

$$\begin{aligned} V(A) = &\left(\frac{A}{h}\right)^2 V(h) + \left(\frac{A}{\sigma}\right)^2 V(\sigma) \\ &+ (h\sigma\beta)^2 V(\eta) \\ &+ 2\left(\frac{A^2}{h\sigma}\right)\mathrm{cov}(h,\sigma) \\ &+ 2\,(A\sigma\beta)\,\mathrm{cov}(h,\eta) \\ &+ 2\,(Ah\beta)\,\mathrm{cov}(\eta,\sigma)\,, \end{aligned} \tag{4.7}$$

where β is the numerical constant $\sqrt{2\pi}\left(1-\sqrt{\pi \ln 2}\right)$ and V and cov are the variances and covariance elements from the covariance matrix of the minimiser. This $\sigma_{fit}(A)$ comprises both the uncertainty in the fit and statistical counting error, accounted for by the choice of minimisation and histogram bin errors. The uncertainty in the area is only dependent on the covariances between parameters on which it directly depends. Other parameter pairs, such as peak height and step height, will have very strong correlations which may indirectly affect the uncertainty in the area in the form of larger individual parameter uncertainties.

It should be clarified that this uncertainty does not reflect how well the chosen function describes the data, but the uncertainty that each parameter of the *chosen function* is optimised to achieve the best fit to data. A sensible choice of fit function must be made in order for the error on calculated quantities (such as area) to be meaningful. Hence there is an intrinsic systematic error associated with choice of function not represented by this value. This systematic error is most clearly seen in the χ^2 value or the residuals as shown in Figure 4.4, for which the trial function offers a factor of five improvement for the electron data over a pure Gaussian.

It is crucial, in minimising the effect of such systematic errors, to remain consistent in peak fitting, especially between calibration and experiment, so that the systematic errors cancel. The double Gaussian fit was selected as the primary peak function to be used as it offered the optimum physical fit to data with only 2 additional parameters over the single Gaussian. Investigations showed the Voigt approximation resulted in underestimation of background beneath the peak and the background step in some fits, thus its rejection.

4.1.4 Asymmetric Peaks

For the very lowest energy electrons, a departure from the standard fitting method is required. In Section 3.2.1 energy loss of electrons was discussed, in Figure 3.11 it is shown that as energy decreases below 1 MeV the fraction of energy lost passing through a material increases logarithmically. The result of this is notable energy loss during transmission through the foils for the low-energy electrons, resulting in an exponential tail on the low-

energy side of the full-energy peak. This is notable only in the lowest energy peak at 45.0 keV in the ^{133}Ba calibration source; the next peak at 75.3 keV is fit suitably by the double Gaussian peak, as shown in Figure 4.6. In experimental data, the tail is significant in peaks below 200 keV. This difference is caused by the addition of the target foil the electrons must pass through between emission and the SAGE detector.

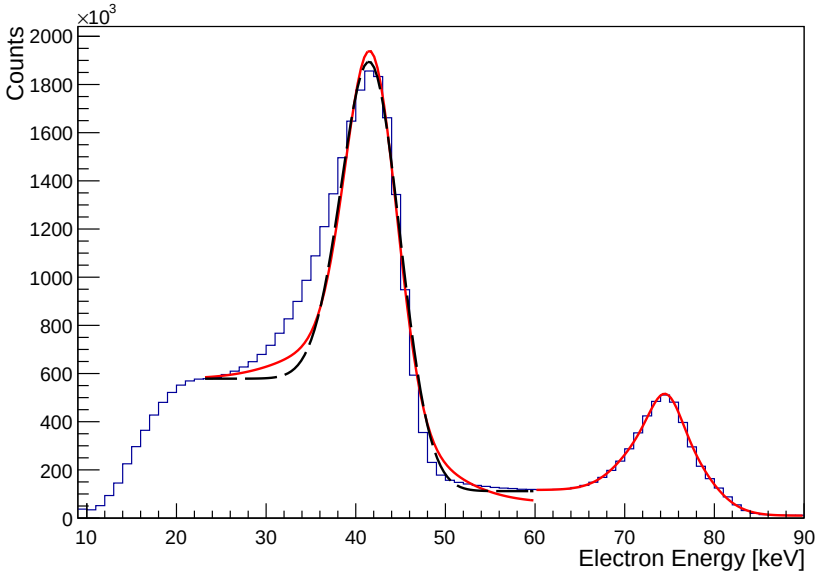

Figure 4.6: Lowest energy ^{133}Ba electron calibration peaks showing double Gaussian (solid red) and single Gaussian (dashed black) peak fits.

Consistency with the peak definitions remains paramount. As every full-energy peak electron must pass through the foils, this is not a random contribution and the energy-loss tail is defined as part of the full-energy peak. It is not included in the processes that contribute to the random scatter background step. As before, the background step is defined by the reverse CDF of the full energy peak function.

An initial trial function was taken from Reference [76], the "Crystal Ball" function for high energy physics. This is a two-part function consisting of a Gaussian peak above a cut off and a power-law tail below the cut. The tail is intended to account for "lossy" processes [76]. This function has previously been suggested as suitable for SAGE data [77]. It is given by :

$$y = h \cdot \begin{cases} e^{-\left(\frac{x-x_0}{\sigma\sqrt{2}}\right)^2}, & \text{for } \frac{x-x_0}{\sigma} > -\alpha \\ \left(\frac{n}{|\alpha|}\right)^n \cdot \mathrm{e}^{-\left(\frac{|\alpha|^2}{2}\right)} \cdot \left(\left[\frac{n}{|\alpha|} - |\alpha|\right] - \frac{x-x_0}{\sigma}\right)^{-n}, & \text{for } \frac{x-x_0}{\sigma} \leq -\alpha \end{cases} \tag{4.8}$$

where α marks the transition to the power-law tail and n is the order of the tail. The function and its first derivative are both continuous.

Figure 4.7 shows the improvement of the Crystal Ball function over a basic Gaussian fit. The fit is still imperfect as it overestimates the peak and lower end of the tail. Additionally, due to the nature of the tail part of the peak function the background step can be absorbed into the full energy peak if the background step size is left as a free

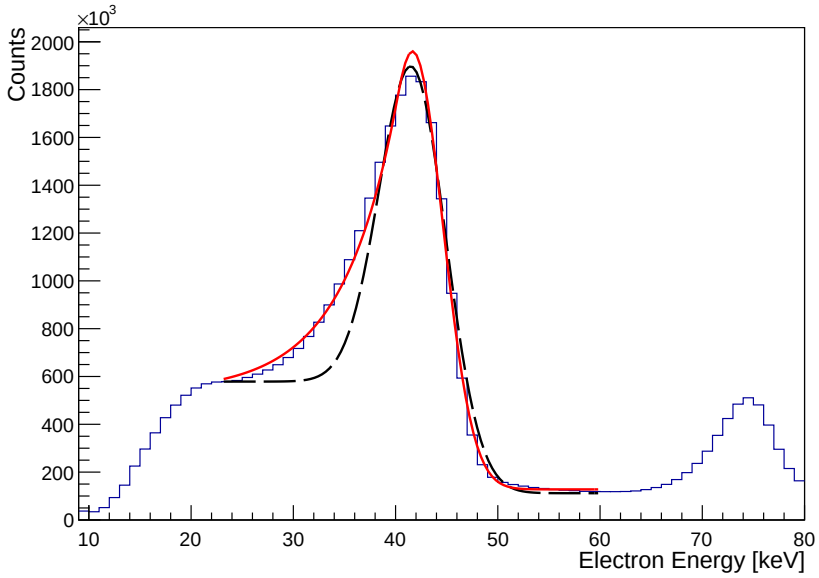

Figure 4.7: Lowest energy ^{133}Ba electron calibration peak showing 'Crystal Ball' (solid red) and Gaussian (dashed black) peak fits.

parameter. The background step height can be fixed to a physically acceptable value, thus preventing this problem. Doing so yields a fit in keeping with the chosen peak definition, but manually fixing the parameter is not ideal as this is not always possible.

A further trial function was taken from Reference [78]. The Radware peak consists of a sum of a regular Gaussian peak and an exponential convolved with a Gaussian broadening. This function is designed for fitting the small tails caused by charge trapping in germanium detectors but can be utilised for this purpose. The peak function is given by:

$$y = h \cdot \left(\mathrm{e}^{-\left(\frac{x-x_0}{\sigma\sqrt{2}}\right)^2} \cdot \eta + \mathrm{e}^{\left(\frac{x-x_0}{\beta}\right)} \cdot \mathrm{erfc}\left[\frac{x-x_0}{\sigma\sqrt{2}} + \frac{\sigma}{\beta\sqrt{2}}\right] \cdot (1-\eta) \right) \tag{4.9}$$

where the complementary error function erfc(x)=1-erf(x) and β controls the length of the tail. The background step used in Reference [78] is the simple one-Gaussian step as given in Equation 4.1. This is a reasonable approximation where the Gaussian term dominates as it does in γ-ray fitting, however for application to the low energy electron peaks from SAGE the second term dominates ($\eta \approx 0$). Hence the function is improved by setting the background step as the reverse CDF per our formalism. For the Radware peak this leads to the following equation :

$$(1 - \mathrm{CDF}) = 1 - \frac{1}{2}\left[\mathrm{erfc}\left(\frac{x_0 - x}{\sigma\sqrt{2}}\right) + \mathrm{e}^{\left(\frac{x-x_0}{\beta} + \frac{\sigma^2}{2\beta^2}\right)} \cdot \mathrm{erfc}\left(\frac{\beta(x-x_0)+\sigma^2}{\beta\sigma\sqrt{2}}\right) \cdot (1-\eta)\right] \tag{4.10}$$

The difference of the new background and the effectiveness of the improved Radware peak is shown in Figure 4.8. This produces a significantly improved fit to the data over the Crystal Ball function and minimises to a physical background without constraint. Using

this improved Radware fit the electron peak area is then give by:

$$A = h \cdot \left[\sigma\sqrt{2\pi} \cdot \eta + 2\beta \mathrm{e}^{\left(-\frac{\sigma^2}{2\beta^2}\right)} \cdot (1-\eta) \right] \tag{4.11}$$

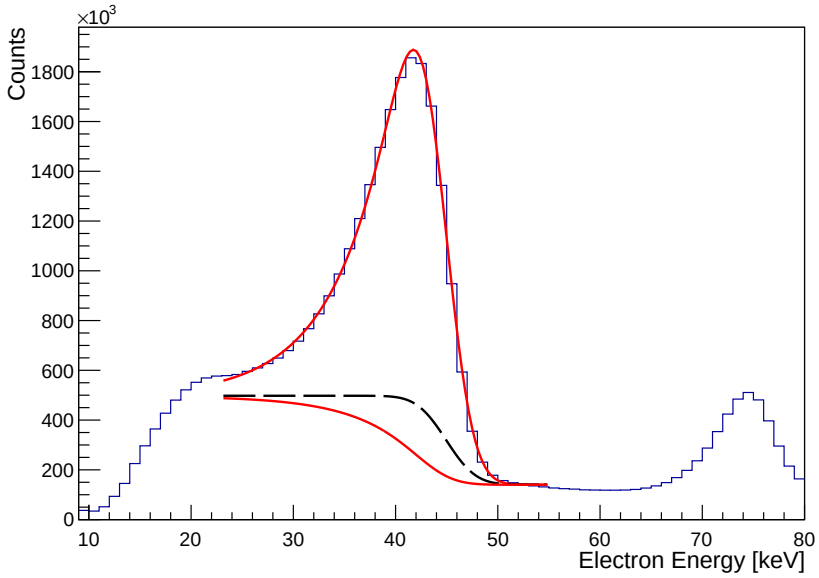

Figure 4.8: Lowest energy ^{133}Ba electron calibration peak showing Radware peak fit with improved background (solid red) and original background (dashed black) for comparison.

As both the low-energy tail and the multiple resolution summing effect are present to some degree at all energies, further improvements were achieved by combining the improved Radware peak with the double Gaussian to create a function that fits the electron peaks in all regions. However, as shown in Figure 4.6, the low-energy tail changes from negligible to dominant over a very short energy range, and as such the benefits from such a combination would be minimal for a large additional complication in fitting. The Radware peak (Equation 4.9) is applied to electron peaks with E_e $\leq$200 keV and the double Gaussian (Equation 4.3) is applied to electron peaks with E_e >200 keV.

4.2 Calibration

In order to measure electron conversion coefficients, α, with SAGE a known absolute detection efficiency for electrons in SAGE, ε_e, and an absolute detection efficiency for γ rays, ε_γ, in JUROGAMII are required in order to relate the measured counts of a quanta to the total number emitted. Both efficiencies are functions of the energy of the quanta being detected, $\varepsilon_\gamma(E_\gamma)$ and $\varepsilon_e(E_e)$. The function must be determined for each of the two detectors. In order to achieve this, a calibration source of known intensity is placed at the target position. During energy calibration the fields of SAGE may be adjusted to ensure all detector elements receive sufficient energy distribution of calibration electrons. For efficiency calibration the source must be at the target position with the SAGE field set to their experiment values in order to get the correct electron transport efficiency in

SAGE, and to get the correct γ-ray attenuation and geometric effects for the calibration of JUROGAMII.

The DAQ must be operated in singles mode and the sort code and detector selection should match that used for the experimental data. Using the known intensity and branching ratios of the calibration source, and an accurate run time measurement (provided by the system's 100 MHz clock), the expected full energy peak intensities can be calculated. The measured peak intensity for each transition can then be used to calculate the absolute efficiency at the peak energy $\varepsilon(E_{peak})$.

This method of efficiency calibration gives the absolute peak efficiency, $\varepsilon_{abs}(E)$, for the emission of an isotropic distribution centred at the target position. Geometric effects, electron transport, intrinsic detector efficiency and the effects of other interactions such as Compton scattering are all folded into this efficiency.

The largest sources of error are the counting error of fitted peaks and the intensity of the calibration sources. In some circumstances a particular source, such as ^{152}Eu for γ rays, might be used to produce a relative efficiency curve across the complete experimental energy range, which relies only on knowledge of branching ratios and removes the source intensity from the calculation. Following this, a different source can be used to scale the relative efficiency curve to an absolute efficiency curve.

The efficiency calibration of JUROGAMII and SAGE can be performed simultaneously from the same source. This is ideal as, strictly speaking, only a relative efficiency between the two is required to calculate α, and any systematic errors from uncertainty in source intensity will cancel. In these experiments calibrations were performed using an open ^{133}Ba source for energies below 0.5 MeV and ^{207}Bi for energies up to 1 MeV.

4.2.1 Gamma-Ray Efficiency Curve

For HPGe γ-ray detectors, the efficiency effects are well understood and have been heavily studied and parametrised. At high energies the peak detection efficiency is affected by an increase in Compton scattering and pair production γ-ray interactions that may result in incomplete energy deposition, as shown in Figure 3.5. The peak detection efficiency is also affected by attenuation length, which is the probability that a γ ray will interact with the matter of the crystal without passing though it. At low energies, the efficiency becomes dominated by attenuation in the cryostat surrounding the detection crystal. Geometric coverage of the detectors affects the efficiency as an energy independent scaling. Using the formalism of D. Radford *et al.* [79], at low energies the efficiency ε_γ is given by :

$$\log_{10}(\varepsilon_\gamma) = A + B \cdot \log_{10}\left(\frac{E_\gamma}{E_1}\right) = \alpha \tag{4.12}$$

and at high energies by :

$$\log_{10}(\varepsilon_\gamma) = D + E \cdot \log_{10}\left(\frac{E_\gamma}{E_2}\right) + F \cdot \log_{10}\left(\frac{E_\gamma}{E_2}\right)^2 = \beta\,, \tag{4.13}$$

where the constants E_1 and E_2 are 100 keV and 1 MeV respectively and A to F are constants to be determined. The complete function is given by :

$$\log_{10}(\varepsilon_\gamma) = \frac{1}{\sqrt[G]{\frac{1}{\alpha^G} + \frac{1}{\beta^G}}} \,. \tag{4.14}$$

G is an interaction parameter between the two regions. G should be positive, hence whichever of α or β is smallest at a given energy will dominate, this is shown in Figure 4.9.[1].

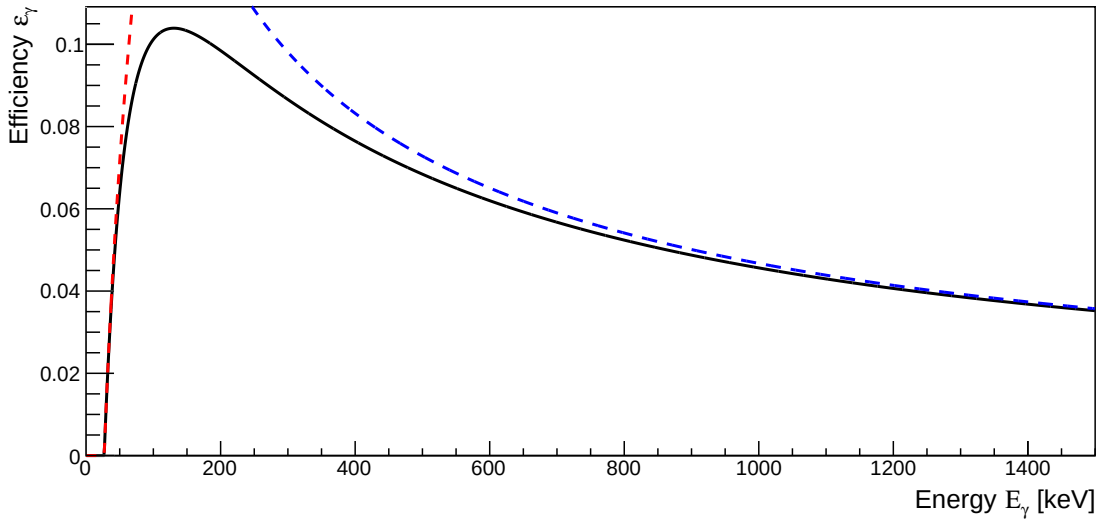

Figure 4.9: A typical efficiency curve for a HPGe γ-ray detector. The low-energy and high-energy components α and β have been separated and overlain as dashed lines.

The uncertainty from the efficiency curve can be determined from the covariance matrix of the parameters, returned by the fit minimiser, in a similar way to the peak fit error. For the increased number of parameters it is helpful to use the matrix form of Equation 4.6,

$$V_f = G V_x G^\top \,, \tag{4.15}$$

where V_x is the covariance matrix with comprised of the element $\mathrm{cov}(x_i, x_j)$ for the set of parameters x. V_f is a matrix of the variances for a set of functions f of the parameters x. The 'G matrix' is a matrix comprised of the elements $\dfrac{\partial f_k}{\partial x_i}$. Expanding Equation 4.15 to show the elements of the matrices gives :

$$\begin{bmatrix} V(f_1) & V(f_2) \end{bmatrix} = \begin{bmatrix} \frac{\partial f_1}{\partial x_1} & \frac{\partial f_1}{\partial x_2} & \dots \\ \frac{\partial f_2}{\partial x_1} & \frac{\partial f_2}{\partial x_2} & \dots \end{bmatrix} \begin{bmatrix} V(x_1) & \mathrm{cov}(x_1, x_2) & \dots \\ \mathrm{cov}(x_2, x_1) & V(x_2) & \dots \\ \dots & \dots & \dots \end{bmatrix} \begin{bmatrix} \frac{\partial f_1}{\partial x_1} & \frac{\partial f_2}{\partial x_2} \\ \frac{\partial f_1}{\partial x_1} & \frac{\partial f_2}{\partial x_2} \\ \dots & \dots \end{bmatrix} \tag{4.16}$$

[1] For an absolute efficiency $\log_{10}(\varepsilon)$ lies in the range $-\infty$ to 0 which causes G to become negative and Equation (4.14) to become complex. So instead Equation (4.14) is solved for $\log_{10}(\varepsilon + 1)$, which lies in the range 0 to $\log_{10}(2)$, with a restricted minimum value of 0.

$$V(f) = \begin{bmatrix} \frac{\partial f}{\partial x_1} & \frac{\partial f}{\partial x_2} & ... \end{bmatrix} \begin{bmatrix} V(x_1) & \text{cov}(x_1, x_2) & ... \\ \text{cov}(x_2, x_1) & V(x_2) & ... \\ ... & ... & ... \end{bmatrix} \begin{bmatrix} \frac{\partial f_1}{\partial x_1} \\ \frac{\partial f_1}{\partial x_1} \\ ... \end{bmatrix} \tag{4.17}$$

For the efficiency function Equation (4.14), the $\frac{\partial f}{\partial x_i}$ components are non-trivial to derive and so the elements of the G matrix are solved numerically.

4.2.2 Electron Efficiency Curve

The various effects involved in the efficiency of SAGE have been discussed in detail. In Figure 3.10 an approximate parametrisation of the different efficiency effects was shown. The functions used there do not account for the complex effects cause by reflection of downstream electrons by the B field of SAGE, or by electrons with high energy or increasingly perpendicular emission angles for which approximations made are no longer valid.

For SAGE the most detailed parametrisation of the efficiency curve comes from Geant4 simulations performed by researchers at JYFL and Liverpool's Oliver Lodge Laboratory [68][77][80]. Simulated data are shown alongside calibration points in Figure 4.10.

In the simulations shown, 50,000 electrons were emitted isotropically for each energy data point. Discrepancies between simulation and data at higher energies are explained by differences in the way in which full-energy peak electrons are defined in the simulations and in the experimentally obtained full-energy peak fitting.

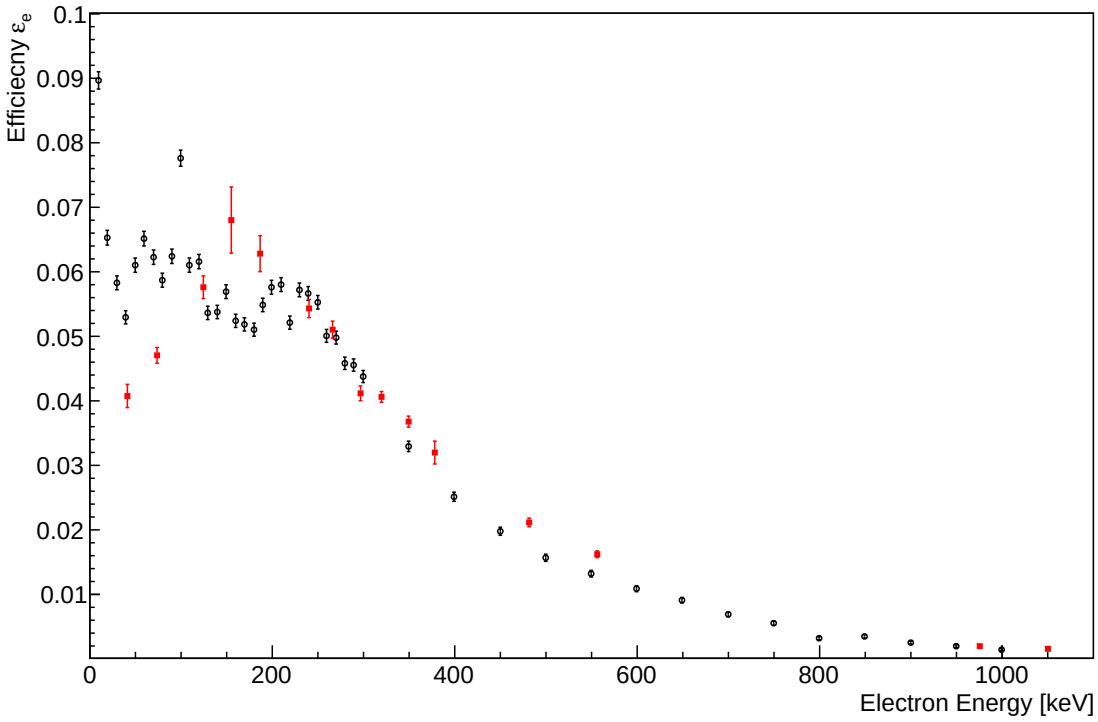

Figure 4.10: SAGE efficiency calibration data (red squares), from ^{133}Ba and ^{207}Bi conversion electron sources, alongside simulation (black circles), without scaling applied to either data set. Both calibration and simulation are with 800 A coil current and no HV.

Above 300 keV, efficiency is dominated by orbital radius limitations imposed by the apparatus. In this region, both the data and the simulation show a smooth exponential trend. This region is fit with the same function used for high energy γ-ray photopeak efficiency, Equation (4.13), which allows for perturbations away from a pure exponential due to higher-order effects.

Below 300 keV, complex field reflection effects are anticipated to dominate the shape of the efficiency curve. However, there is a large deviation from the simulation in this region. Particularly, a downwards trend appears below 200 keV. As discussed in Reference [80], this is mostly likely due to limitations of the electronics used in SAGE in addition to noise which is not being fully accounted for in simulations. Hence in this work the small-order perturbations shown in the simulation will not be included in the efficiency determination. A simplified smooth fit to the experimental data was used instead. Hence the same functional form used for γ-ray detection efficiency curve, Equation 4.14, will be used for the full electron energy range. This is reasonable as there are two main regions of behaviour for electron efficiency, between which a smooth transition must be assumed. There are insufficient data to determine any other conclusion. The fit result is shown in Figure 4.11; a large uncertainty is seen at low energy where there are insufficient data points to constrain the function around the turning point.

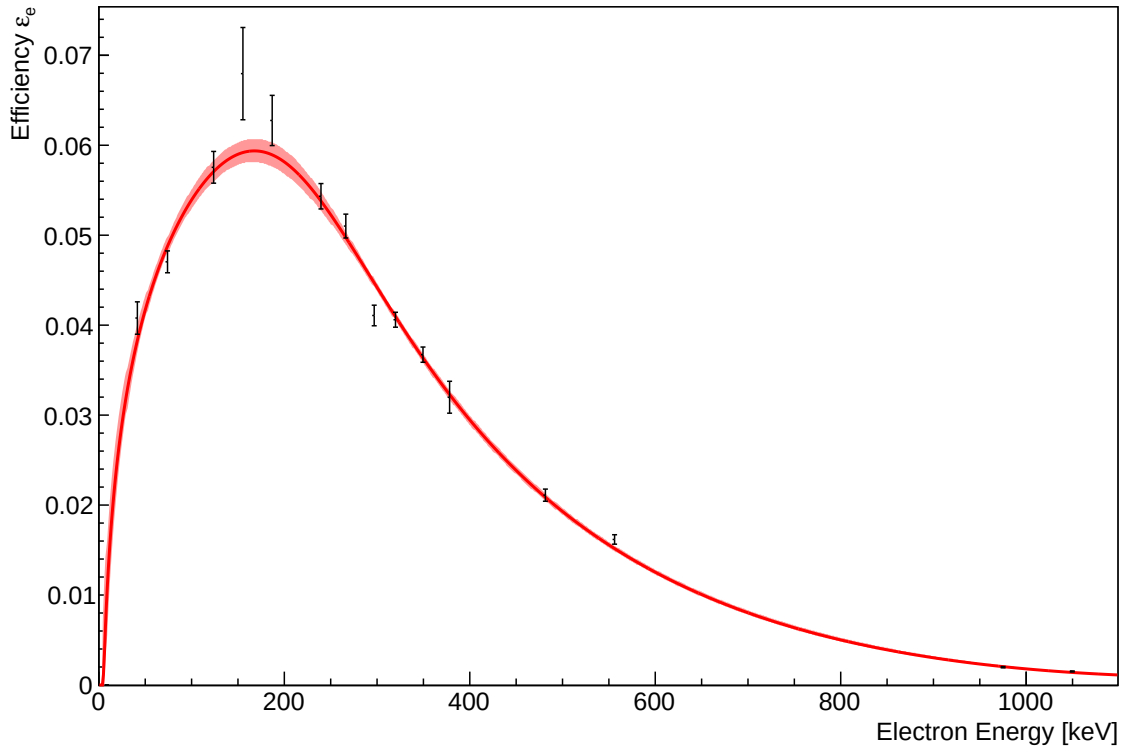

Figure 4.11: Electron full-energy peak efficiency curve as a function of electron energy, with error band. Data are from ^{133}Ba and ^{207}Bi calibration sources.

4.3 Kinematic Correction

Electrons and γ rays emitted by recoiling nuclei and detected in the laboratory frame will be recorded with a different energy to the nuclear frame due to the Lorentz boost. The Lorentz transformation for an emitted particle between the lab (E, p) and nuclear(E', p') frame is given by:

$$\begin{bmatrix} E+m_0 \\ p_1 \\ p_2 \\ p_3 \end{bmatrix} \begin{bmatrix} \gamma & -\beta\gamma & 0 & 0 \\ -\beta\gamma & \gamma & 0 & 0 \\ 0 & 0 & 1 & 0 \\ 0 & 0 & 0 & 1 \end{bmatrix} = \begin{bmatrix} E'+m_0 \\ p'_1 \\ p'_2 \\ p'_3 \end{bmatrix}, \tag{4.18}$$

where the recoiling nucleus is moving in a direction aligned along the axis of p_1 with a velocity of $v = \beta c$ and where $\gamma = \dfrac{1}{\sqrt{1-\beta^2}}$. If the angle between the recoil and emitted particle trajectories is θ, giving $p\cos\theta = p_1$, then by application of $p^2 = E^2 + 2m_0E$ the following relation can be defined :

$$E' = \frac{E + m_0 - \beta\cos\theta\sqrt{E^2 + 2m_0E}}{\sqrt{1-\beta^2}} - m_0\,. \tag{4.19}$$

Hence only knowledge of θ and β is required to correct the measured energy. The effect is smallest when θ =90°, and negligible when β is small.

4.3.1 Gamma-Ray Correction

For γ rays the formula collapses to the compact Doppler correction formula,

$$E' = \frac{E(1-\beta\cos\theta)}{\sqrt{1-\beta^2}}\,. \tag{4.20}$$

When recoils are detected in RITU they have both a clearly defined β and direction along the beam axis. The angle θ can then defined from the JUROGAMII detector polar angles in order to apply a Doppler correction. However, due to the angular acceptance of both the JUROGAMII crystals and RITU, only an average correction can be made and a Doppler broadening effect will be seen in Doppler-corrected energy spectra. As an example: if a 500 keV γ ray is measured in a crystal with a central polar angle of 71° emitted from a nucleus moving with $\beta = 0.03$, a mean Doppler correction of -4.9 keV is calculated. Due to the combined angular acceptance of RITU and JUROGAMII, the maximum and minimum accepted θ are 80.4° and 61.6° and the difference between the Doppler correction for these two angles is 4.6 keV.

4.3.2 Electron Correction

In SAGE, angular information is extremely limited. Due to the helical nature of electron trajectories, the pixel of detection cannot be uniquely correlated with angle of emission. For low-energy electrons, a limitation can be placed on those electrons detected in outer

pixels. This applies to a small fraction of possible events. Furthermore, the SAGE axis and the beam axis differ by 3.2° therefore such limitations poorly constrain the lorentz correction angle θ. As a result all that can be stated is the angular acceptance as a function of electron energy. Figure 4.12 shows a plot of transmission efficiency through SAGE versus emission angle and electron energy. From this, a normalisation for solid angle can be performed and hence the average emission angle θ is established for kinematic correction. As a result, the entire spectrum can be stretched in such a way as to correct centroid energies but a large peak broadening cannot be avoided.

Table 4.1 gives the calculated average emission angle for electrons that will be transported through SAGE at 10 energies and the subsequent kinematic correction calculated for a recoiling nucleus of $\beta = 0.03$. The average θ does not change simply with energy due to the different competing angular limitations on electron transmission, as discussed in Section 3.2.1. It can be seen in Figure 4.13 that despite the complex behaviour of average θ the kinematic correction factor is near linear with respect to energy. A linear function fit to these data can be used to correct experimentally measured energies to within 1 keV.

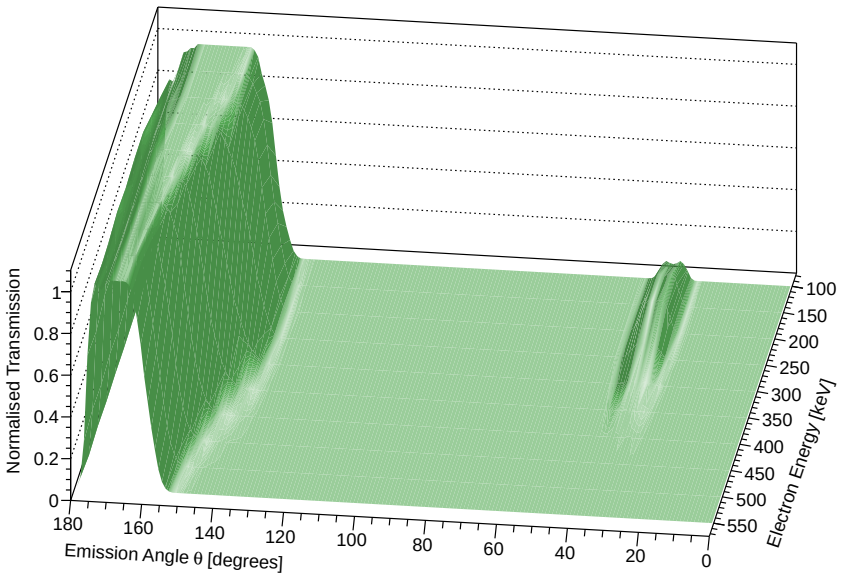

Figure 4.12: SAGE angular transmission fraction as a function of emission angle θ from beam axis and electron energy. Calculated from efficiency simulation data [68].

Lab Energy [keV]	Average θ [degrees]	kinematic Correction [keV]
100	159.2	9.7
150	148.7	11.1
200	147.2	12.8
250	157.1	15.9
300	161.1	18.2
350	163.2	20.3
400	164.9	22.3
450	166.1	24.1
500	167.1	26.0
550	168.1	27.8

Table 4.1: Calculated average emission angle θ and kinematic correction factor for electrons detected in SAGE at 10 energies, assuming a recoiling nucleus of $\beta = 0.03$.

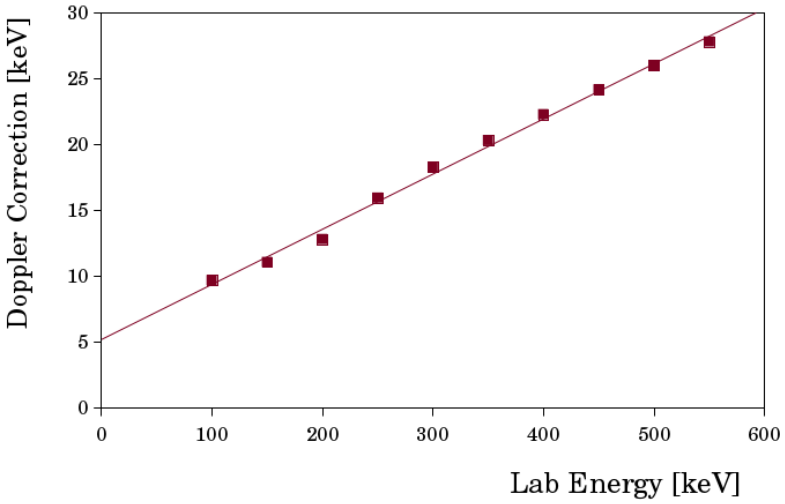

Figure 4.13: Kinematic correction factor for electrons detected in SAGE assuming a recoiling nucleus of $\beta = 0.03$. A linear fit is shown.

4.4 Background Suppression

4.4.1 Formalism

In any experimental measurement one must discern the signal from the noise. When dealing with a set of discrete events, one must contend with background events, which are any events that are not directly related to the measurement of interest and obscure data which is. These can be events from a different physical process producing radiation in the detectors that is detected identically to events of interest. Hence, without an additional data handle, these are inseparable in the ensemble of data from the detector. Background events may also be events from the desired physical process in which a problem arose in the detection process, such as particles scattering in detectors depositing only part of their full energy as discussed in Section 3.2.2.

The aim when dealing with background is to suppress or remove it to a level at which the measurement of interest can be resolved. For instance, the RITU separator can be used as a trigger so that events from reaction channels with cross-sections that may be

many orders of magnitude greater than the channel of interest are rejected and do not swamp the resulting data. BGO Compton suppressions shields in JUROGAMII reduce the number of scattered γ rays recorded in the data, increasing the peak-to-background ratio, so the low intensity γ-ray peaks can be resolved, as shown in Figure 4.14.

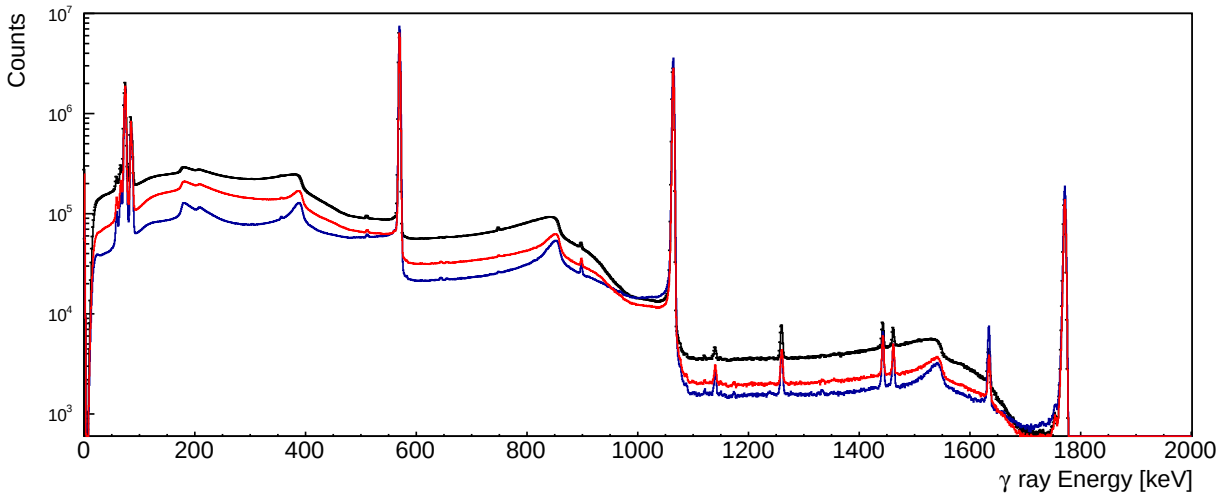

Figure 4.14: Data from ^{207}Bi calibration source in JUROGAMII showing raw data (top, black), data with BGO suppression (middle, red) and data with BGO suppression and clover addback (bottom, blue).

Beyond these suppression techniques one may require a coincidence between multiple detectors and, in addition, gate on a known peak in one or more detectors. Such selection methods will always allow some fraction of the unwanted background events through. The subtraction of these events from the spectra is defined as such:

$$S_p(j) = S_t(j) + B(j)\,, \tag{4.21}$$

where $S_t(j)$ is the j^{th} bin of the histogram containing the selected data, $S_p(j)$ is the j^{th} bin of the resulting spectrum and $B(j)$ the j^{th} bin of the scaled background spectrum. $B(j)$ is then defined as

$$B(j) = S_b(j) \cdot \frac{N_t b_g}{N_b}\,, \tag{4.22}$$

where S_b is the background spectrum (to be determined), N_t is the total number of counts in the spectrum S_t, N_b is the total number of counts in spectrum S_b and b_g is the fraction of background events in spectrum S_t (also to be determined) [81]. Subtraction is performed with histograms at their initial binning from the raw data to avoid loss of information, appropriate re-binning can then be performed afterwards.[2]

The final spectrum S_p will have individual bin errors inherited from a combination of the bin errors $\sqrt{S_b(j)}$ and $\sqrt{S_t(j)}$ and errors in the scaling factor $\frac{N_t b_g}{N_b}$ given by $\sqrt{N_b}$, $\sqrt{N_t}$ and $\sigma(b_g)$. Very large values for the scaling factor will result in a large uncertainty in the background spectrum subtraction and so a sufficiently large sample is needed to determine S_b.

[2]Selection of a suitable initial binning is dependent on joint resolution of detector and electronics. For SAGE an initial binning of 1 keV per bin was used and for JUROGAMII 0.5 keV per bin was used.

It is common to select S_b in such a way that the scaling factor is equal to 1 and can be neglected.

Specific S_b will be discussed in Section 6.1, but in general S_b may be determined by the reverse of the requirements used to select S_t.

4.4.2 Gamma Gating

Clean electron and γ spectra are produced in this work by γ-gating and background subtraction on $e^-\gamma$ and $\gamma\gamma$ matrices.

The primary spectrum S_t is produced from a gate on a coincident γ-ray transition, γ_A. Such a gate also accepts coincidences from background events that fall within the gate. For another γ ray, γ_B, where $E_A < E_B$ the peak of γ_A will appear on top of the Compton continuum from γ_B. Consequently a gate on the peak of γ_A will return events coincident with γ_A and γ_B. When the background beneath a peak is uncorrelated and linear, the same size gate may be taken to the right (higher-energy side) of the peak on a smooth region of the spectrum, and the resultant spectrum defined as $S_b \equiv B$ [82]. Such Compton coincidence and the effect of such background subtraction is demonstrated in Figure 4.15.

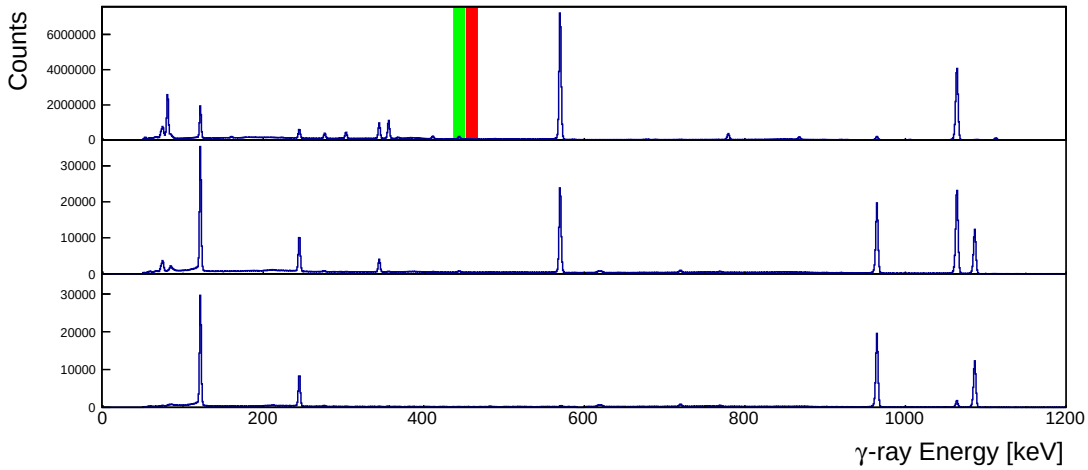

Figure 4.15: Background subtraction is demonstrated here with $\gamma\gamma$ data from ^{133}Ba, ^{152}Eu and ^{207}Bi calibration sources. Spectra shown are the total projection with coincidence gate marked in green and background gate marked in red (top), gated spectrum (middle) and background subtracted spectrum (bottom).

This simple subtraction has the disadvantage that it requires a subjective choice of the smooth background region. For this work a more generalised definition of S_b is used for γ-gating.

A common simplification is to assume the spectrum in coincidence with the background is approximately the same for the background at all energies, and can be well represented by the total matrix projection [83][81].

This simplification may be appropriate when the background coincidence is dominated by false coincidences rather than Compton, and when there are no abnormally intense coincident transitions. However, in this work false coincidences are removed by time gated

subtraction and a few exceptionally intense peaks are present at low energies. The result is over-subtraction if the full projection is taken as S_b. S_b is defined as the projection of the matrix for all $E_\gamma > E_{gate}$.

The background fraction, b_g, is determined by fitting the peak on which the gate was placed in the matrix projection. Fitting used for spectral peaks were discussed in Section 4.1.2. The background fraction b_g is given by

$$b_g = 1 - \frac{A_{gated}}{A_{sum}}, \tag{4.23}$$

where A_{gated} is the peak area within the gate and A_{sum} the total counts within the gate and where $A_{sum} \equiv N_t$. The area A_{gated} is not the full peak area as the gate width does not extend to infinity, indeed it is often beneficial to use a narrow gate which will reduce statistics but minimise b_g [84]. For a Gaussian peak a gate width of only $\pm 2\sigma$ will accept 95.4 % of coincidences, increasing this the gate width to $\pm 3\sigma$ will accept 99.7% of coincidences but b_g will be 1.4 times larger. Figure 4.16 demonstrates such a gate selection. For a Gaussian distribution $\alpha(x)$:

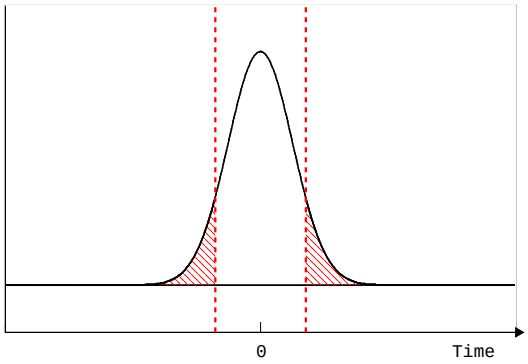

Figure 4.16: Illustration of peak gating fraction showing a gate of width $\pm 1.5\sigma$ on a Gaussian shaped timing peak (arbitrary units).

$$\int_{x_1}^{x_2} \alpha(x)dx = \sigma_\alpha h_\alpha \sqrt{\frac{\pi}{2}} \left[\mathrm{erf}\left(\frac{x - X_\alpha}{\sigma_\alpha \sqrt{2}} \right) \right]_{x_1}^{x_2}. \tag{4.24}$$

By setting x_1 and x_2 to the upper and lower bounds of the gate A_{gated} and its uncertainty can be used to calculated from fit parameters of the gating transition peak. Subsequently b_g and $\sigma(b_g)$ can be calculated from Equation 4.23.

For improved precision in calculation of b_g, one should consider not only the peak area within the gate, but also the small fraction of background contributed by scattering from the full energy peak. Directly under a γ peak this fraction is very small, but represents genuine coincidence counts This is not part of P_b, and thus these counts should not be wrongly assigned as background in this context. In Section 4.1.2 it was discussed that such contributions manifest in the data as a step underneath the full-energy peak. The step was defined such that its function can be written as

$$f(x) = S\frac{1}{2}\left(1 + \mathrm{erf}\left(\frac{x_0 - x}{\sigma\sqrt{2}}\right)\right) \tag{4.25}$$

where the constant S is the total height of the step, which may be defined as a fraction of the total peak height. Hence the contribution of the step to the genuine coincidence in the gate may be written as

$$\begin{aligned} A_{stepgate} &= \int_{x_1}^{x_2} f(x)dx \\ &= S\frac{1}{2}\left((x_2 - x_1) - \left[(x_0 - x)\mathrm{erf}\left(\frac{x_0 - x}{\sigma\sqrt{2}}\right) + \frac{\sqrt{2}\sigma}{\sqrt{\pi}}\mathrm{e}^{-\left(\frac{x_0 - x}{\sigma\sqrt{2}}\right)^2}\right]_{x_1}^{x_2}\right) \end{aligned} \tag{4.26}$$

and

$$b_g = 1 - \frac{A_{gated} + A_{stepgate}}{A_{sum}}\,. \tag{4.27}$$

This addition is only small for γ-gating and reduces b_g by less than its uncertainty. It is presented here for completeness as the additional term is significantly more important if one were to perform electron gating on such a matrix.

4.4.3 Coincidence Timing

When performing coincident measurements between multiple detectors, such as $e^-\gamma$ between SAGE and JUROGAMII, $\gamma\gamma$ between two detectors in JUROGAMII or $recoil \cdot \gamma$ between JUROGAMII and GREAT, additional subtraction can be performed. Here $e^-\gamma$ coincidences will be discussed, but the principle is the same for the other examples.

By fully understanding the timing spectra between detectors, one can not only more precisely constrain the event window to cut out random events, but also remove these random events from within the window. The coincidence time is defined as the time difference between the time stamp of the two detectors $t_{co} = T_{e^-} - T_\gamma$. For beam experimental data the t_{co} spectra can be deconvolved into several components. Each aspect of the spectra is explained in the following list along side an illustration:

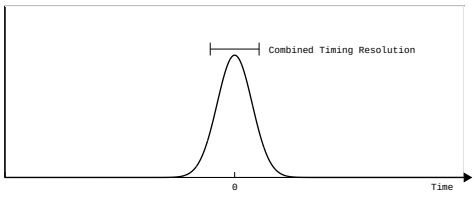

Genuine Coincidence: If both the e^- and γ ray are from the same nuclear cascade, following a beam interaction or target decay, a prompt timing peak will be observed. The peak will be centred around $\overline{t_{co}}$ with a Gaussian distribution of width given by the combined timing resolution of both detectors.

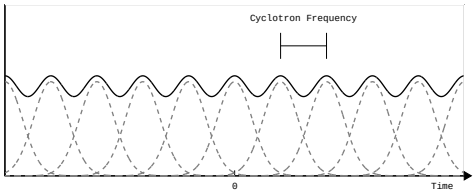

Prompt False: If the e^- and γ ray are both from prompt beam events, but have no other correlation, a series of such peaks will be observed (dashed line). Each peak is separated by the cyclotron beam pulse period, corresponding to the e^- being from an interaction in one beam pulse and the γ ray being from an interaction in a later, or previous pulse. Every combination of beam pulses within the width of a single event are equally likely. The resultant spectrum from summation appears a continuous ripple (solid line).

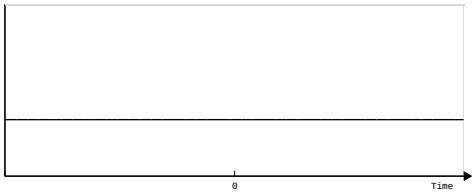

Random False: If either, but only one, of the e^- or γ ray are from a decay event the timing spectrum will be featureless as the decay is equally likely for all t_{co}.

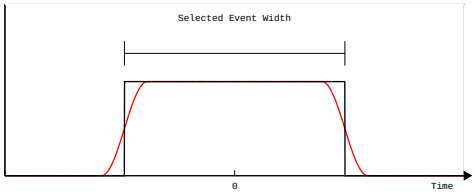

Event Shaping: Events are defined by a timing window which specifies a t_{coMax} and t_{coMin} which imposes step function cut off on timing spectra (black). Timing alignment occurs after event selection and so the step function is blurred as a result of the individual detector elements timing differences (red).

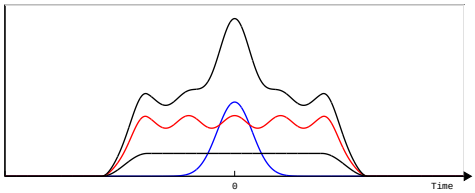

Total Spectrum: The total timing spectrum (upper curve) will be the sum of the genuine and false components all scaled by the blurred event step function.

An example of experimental data fit with a function defined from the deconvolved components is shown in Figure 4.17. The figure features a small genuine coincident peak the extent of which would not be apparent by simple inspection, as the background is both significantly larger and oscillating on the same scale.

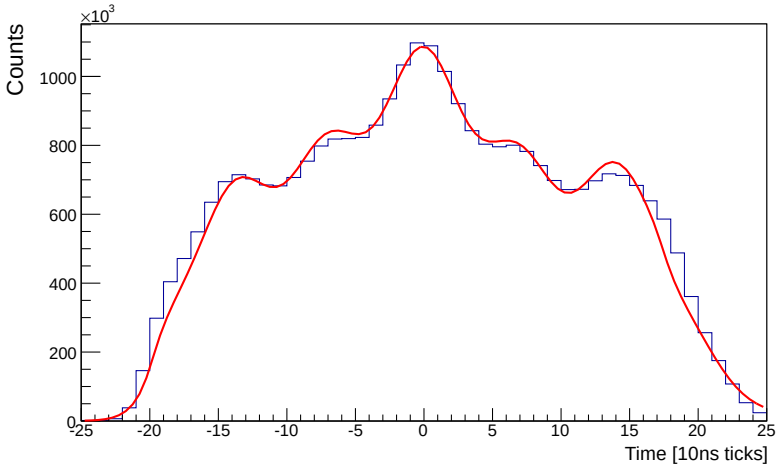

Figure 4.17: $e^{-}\gamma$ coincidence timing spectrum from beam data, with a fit with the deconvolved components described in the text. Limited to events with E_γ corresponding to ^{152}Sm $4_1^+ \rightarrow 2_1^+$.

4.4.4 Time-Gated Subtraction

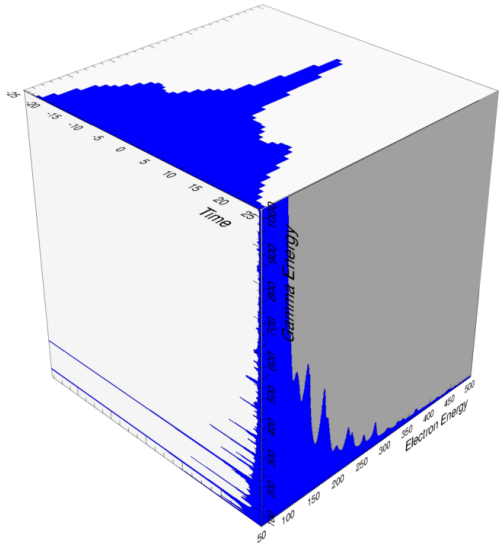

Figure 4.18: Graphic illustration of the sort of data cube one might be considering when performing the subtraction described in the text. Constructed using 3 data from each event: electron energy, γ ray energy and $e^{-}\gamma$ coincidence time. A gate on one of the three data reduces the cube to a matrix of the other two.

One may construct a data cube of E_{e^-}, E_γ and t_{co} for all $e^{-}\gamma$ events, graphically demonstrated in Figure 4.18. By placing a timing gate on the region of the genuine coincidence peak one produces a matrix $S_t(i,j)$ containing both genuine coincidence and

background false coincidence events. Figure 4.19 serves to illustrate the difficulties in setting the width of this gate to optimise statistics and minimise peak to background.

To determine the background fraction b_g, timing spectra were fitted with a piecemeal function combining the different contributions $S_{time}(t) = [S_{Genuine}(t) + S_{PromptFalse}(t) + S_{RandomFalse}(t)] \cdot F_{EventShaping}(t)$. Fitting to calibration data, in which only genuine and a small amount of random false coincidence are present, was performed first in order to constrain fit parameters. The blur at the edge of the event windows was trialled as a cosine function, but found to be fit best with a high-order polynomial in four parts, with the two parts at the upper boundary naturally being the inverse of the two at the lower. Slight differences are to be expected with beam data due to differences in relative intensities between detector elements. The timing peak was found to be asymmetric, having a long exponential tail. This was found to be associated with low-energy electrons and assumed to be a result from slower rise times or longer time of flight through the SAGE solenoid. The shape of the prompt background was kept as a series of simple Gaussian peaks and following initial testing the separation was fixed to the known cyclotron pulse period of 70 ns. The relative heights of the genuine peak, prompt and random backgrounds and the size of the prompt peak tail were then left as the free fitting parameters. Following on from this fitting, b_g can be determined from the area of the genuine peak inside the gate and N_t as for γ-gated backgrounds.

A further timing gate (or gates), placed away from the genuine coincidence, produces a matrix $S_b(i, j)$ containing only the false coincidence background events. Ideally the event width should be wide enough so that the background gate (gates) can be placed away from the genuine peak and that the fitting to determine b_g can ignore the blur at the ends of the event window, but this is not always possible. Due to the oscillations of the prompt false background, the ratio of prompt and random background in $S_t(i, j)$ is sensitive to the placement of the first time gate and this should be considered when selecting the background gate position. When either of the two background contributions dominates this becomes a smaller effect, however it was found that the ratio of the two contributions could not be unambiguously determined from the fitting of the timing spectrum alone.

From $S_b(i, j)$ one defines $B(i, j)$, which is subtracted from $S_t(i, j)$ to produce a background subtracted $S_p(i, j)$ in the same way as for one-dimensional histograms. By using this procedure we produce $e^-\gamma$ matrices free of false coincidences (and by an analogous process, $\gamma\gamma$ matrices).

Following this timing subtraction, normal γ-ray gating and background subtraction, as described in Section 4.4.2, may be performed on the matrices to produce final 1D spectra. If a target peak is obscured by a contaminant peak, which appears very nearby along both axis of the matrix, it may be beneficial to forgo γ-ray gating and instead fit the matrix directly. Such a fit is shown in Figure 4.20 for an isolated peak.

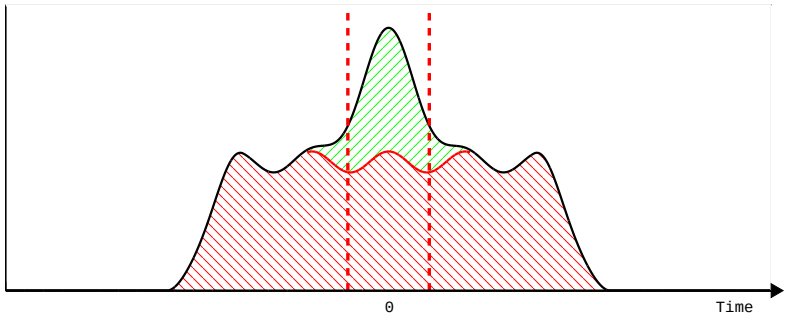

Figure 4.19: $e^{-}\gamma$ coincidence timing spectrum peak-to-background illustration. The Gaussian true coincidence timing peak (green) is revealed by deconvolution of the random cyclotron frequency background (red). The deconvolution shows that the peak tails extend beyond the indicated gate, but including them would significantly worsen the gated peak-to-background ratio.

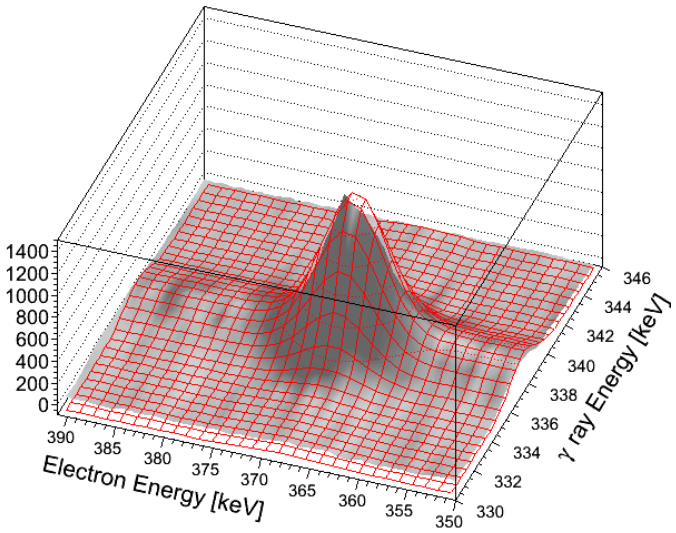

Figure 4.20: Experimental 2D fit to peaks in the $e\gamma$ matrix, following a row by row subtraction for Compton background along the γ axis.

4.5 Low Statistics Fitting

When the size of the peaks to be measured are on the scale of or smaller than the variance of the background the idealised fitting presented in Section 4.1.2 becomes unsuitable. Instead, confidence levels are considered on a simple normalised-Gaussian-plus-background fit. An example of such data and fit is given in Figure 4.21.

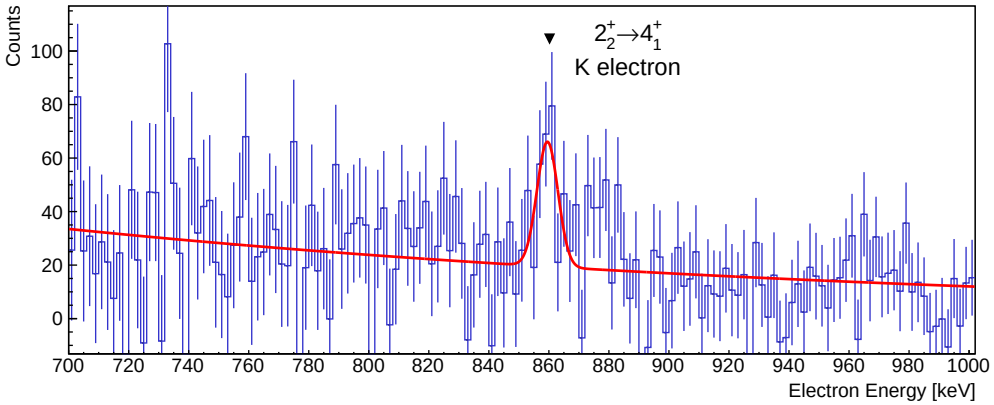

Figure 4.21: Low statistics spectrum example showing a fit to the ^{154}Sm $2_2^+ \rightarrow 4_1^+$ K electron.

To extract a measurement of the smallest peak areas in this work, normalised-Gaussian-plus-background fits were performed. The use of a normalised Gaussian contains the peak area, not height, as a fitting parameter, simplifying error analysis. Due to the appropriately propagated bin errors the background can be fit consistently with a simple second order polynomial or an exponential. Background fits were performed to a few hundred keV above and below target peaks. Exponential and polynomial backgrounds were found to be relatively insensitive to the inclusion of one or two peaks of the scale discussed in this section or to exclusion of the peak area. In all low statistics fits of this work both exponential and polynomial background functions were trialled with minimal difference.

4.5.1 Confidence Limit Calculations

For the smallest peaks presenting the fit area with a one sigma error is inappropriate. Instead, calculated confidence limits on the measurement are presented.

In order to define such confidence limits one must establish a probability distribution $P(x|\mu)$ for the measurement of counts x for given true mean value μ. Recall that the probability of the measurement depends on the unknown fixed value of μ and measurement error σ_x and not the reverse.

Ideally one might choose to measure the counts in the peak region and define this as peak plus known background $x = p + b$, where both are Poissonian quantities and hence :

$$P(x|\mu) = (\mu + b)^x e^{-\frac{\mu + b}{x!}} . \tag{4.28}$$

However, in the situation presented in this work the uncertainties in the spectral counts

are significantly larger than Poissonian, following the combination (subtraction) of several sets of initially Poissonian data. Hence the Central Limit Theorem is applied and the subtracted data are assumed to follow a Normal distribution. $P(x|\mu)$ is then given by a Normal distribution with some variance to be determined. The individual data bins are taken each to be normally distributed values with variance given by their error bars (which have been properly propagated throughout any subtractions).

Fitting of a sensibly chosen function using a Pearson's χ^2 test remains the best choice to extract a measurement of peak area, the χ^2-distribution being directly related to the probability distribution of Normal random variables [85],[86].

χ^2 Distribution Limits

For Normally distributed random variables, the values of the χ^2 distributions are clearly defined in terms of the variable's probability. For example: for one degree of freedom, if $\chi^2(x) = 3.84$ then the probability that a measurement x_0 would be as far, or further, from the mean $\hat{x}$ is only 5 %, $P(|x - \hat{x}| \leq |x_0 - \hat{x}|) = 0.05$, and of course the inverse is also true $P(|x - \hat{x}| > |x_0 - \hat{x}|) = 0.95$. Alternatively, if one finds the value of x for which $\chi^2(x) = 1$ then $P(|x - \hat{x}| > |x_0 - \hat{x}|) = 68.2\,\%$ hence $|x - \hat{x}| = \sigma$. This stated relation between confidence interval and standard deviation σ is only for the Normal distribution.

Following fitting of presented experimental data, an area is measured for the peak in consideration. This area may be zero or even negative due to fluctuations in background, this is allowed and does not stop a confidence limit calculation. It has been reasoned that the measurement of the peak area x will be Normally distributed ($P(x|\mu)$ will be Gaussian) and so the properties of the χ^2 distribution may be used to establish the spread of the distribution.

By fixing the value of x to successive values around the χ^2 fit minimum value $\hat{x}$ and performing a further fit minimisation to any free parameters at each step, a map is produced of the function $\chi^2(x)$; this distribution may be shifted such that $\chi^2(\hat{x}) = 0$, which represents the χ^2 distribution for the single degree of freedom x, shown in Figure 4.22. Then σ is determined for the Normally distributed measurement of peak area x by finding the values of x for which $\chi^2(x) = 1$. This procedure can be performed automatically by the MINOS routine [87], but the manual derivation of these quantities is explained here to aid understanding of the concepts on which the experimental method rests.

One could now proceed to find the values of x for which $\chi^2(x)$ equates to the appropriate confidence level and state these x as the confidence interval. But here $\chi^2(x)$ is used only to determine the variance of the normally distributed measurement x. The reason for doing so is to avoid underestimation when the measurement of a quantity, whose real (unknown) value must be positive, approaches zero or is found to be negative.

FC Confidence Interval

The method that will be followed is detailed by Feldman and Cousins [88]. The reason for the approach and an outline of the method will be presented.

In general one may write that for a given physical value μ the probability of a measure-

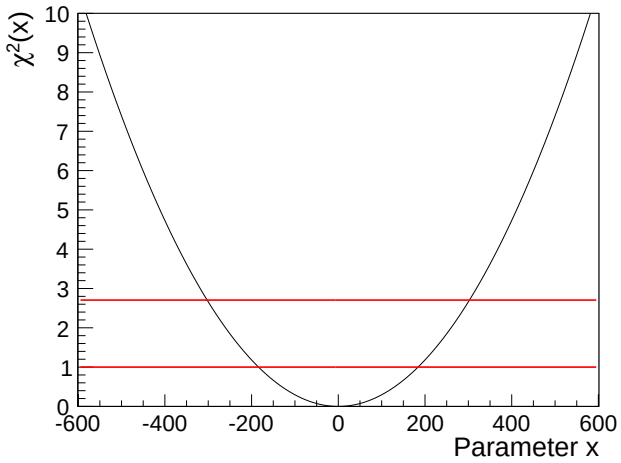

Figure 4.22: χ^2 distribution for a single parameter, the data corresponds to measurement of the peak area from Figure 4.21. Horizontal bands mark the 68% and 90% confidence intervals.

ment yielding the result x is given by $P(x|\mu)$. Hence one defines the confidence interval $[x_1, x_2]$ such that $P(x \in [x_1, x_2]|\mu) = \alpha$ where α is the confidence level. One then defines a measurement confidence interval $[x_1, x_2]$ for all possible values of the real parameter μ, producing a confidence band such as the one shown in Figure 4.23. Next, the line that intersects the measurement x_0 is taken and the points at which this crosses the bands give the μ confidence interval of $[\mu_1, \mu_2]$. In other words, the confidence region is all values of μ for which the measurement x_0 falls within the confidence level α. Hence for μ_t, the unknown true value, we have $P(\mu_t \in [\mu_1, \mu_2]) = \alpha$.

Consider a large number N of x measurements for the true unknown value μ_t. By definition the fraction in the range $P(x \in [x_1, x_2]|\mu_t) = \alpha$. For x values in the range $x_1 \leq x \leq x_2$, μ_t will fall within all confidence intervals $([\mu_1, \mu_2]|x)$. Hence the fraction of the N measurements x for which μ_t will be within the confidence intervals $([\mu_1, \mu_2]|x) = \alpha$.

The particular problem Feldman and Cousins [88] address appears when confidence bands are used near a physical boundary. For instance, when the real parameter μ cannot be negative but the measurement may be. If a value is measured for x lower than the bottom of the band $(x_1|\mu = 0)$ then one must say the confidence interval is the empty interval, it contains no physically allowed values of μ. A valid confidence belt should not yield any empty intervals [89].

Feldman and Cousins introduce an ordering principle based on likelihood ratios for the construction of the interval $(x \in [x_1, x_2]|\mu)$. For each value of μ it is still required that $P(x \in [x_1, x_2]|\mu) = \alpha$, which leaves the inversion of the confidence bands to determine confidence on $\hat{\mu}$ untouched. However, we do not require that $[x_1, x_2]$ be symmetric about $x = \mu$. Instead, for each given value of μ each element $x + dx$ is considered for addition to the range based on the ratio of likelihoods R. The elements are added to the range in order of descending R until $P(x \in [x_1, x_2]|\mu) = \alpha$ (the range is not required to be continuous). The ratio of likelihoods is given by $R = P(x|\mu)/P(x|\mu_{best})$ where μ_{best} is the value of μ which maximises the probability of $P(x|\mu)$ for each value of x.

For a Gaussian-distributed measurement x with measurement error σ_x :

$$P(x|\mu) = \frac{1}{\sigma_x\sqrt{2\pi}} e^{-\frac{(x-\mu)^2}{2\sigma_x^2}}, \tag{4.29}$$

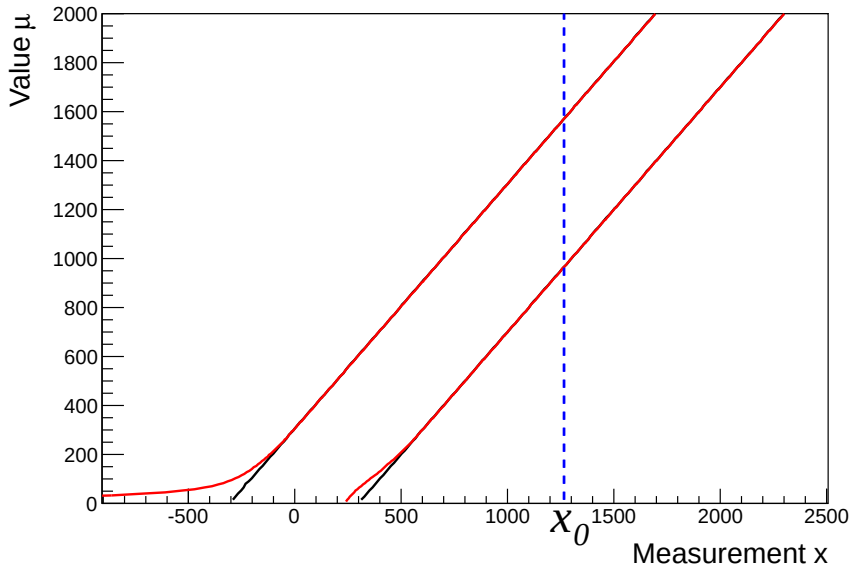

Figure 4.23: Confidence bands for Gaussian measurement x, the data corresponds to the 90% confidence level for measurement of the peak area from Figure 4.21. Red lines show the FC confidence bands deviating at small and negative values of x. This measurement x_0 is large on the scale in discussion and in the range where the FC confidence band converges with classical confidence band and the χ^2 estimates.

then $\mu_{best} = x$ for $x \geq 0$ and $\mu_{best} = 0$ for $x < 0$. The likelihood ratio then R is then :

$$R = \begin{cases} exp(-(x-\mu)^2/2\sigma_x^2), & \text{for } x \geq 0 \text{ and} \\ exp((2x\mu - \mu^2)/2\sigma_x^2), & \text{for } x < 0\,. \end{cases} \tag{4.30}$$

The use of this confidence interval construction ensures that for all values of x a valid interval is generated at the required confidence. Under-coverage is avoided and as $\mu \to 0$, $x_1 \to -\infty$.

As μ and x move away from the physical boundary the standard form of the confidence interval is returned and one expects the confidence limits to converge with that of χ^2.

The FC method also removes problems introduced by arbitrarily switching between upper limit and central confidence bands, which are not discussed here. A desired percentage central confidence limit is given far from the boundary and this smoothly transitions to an upper confidence limit at the desired percentage as the lower limit approaches the boundary.

"As in the Poisson case, particular caution is necessary when interpreting limits obtained from measured values of x which are unlikely for all physical μ."[88].

4.6 Conversion Coefficient Calculation

The conversion coefficient for a measured transition Γ is given by

$$\alpha_{K,exp} = \frac{I_{e,K,exp}}{I_{\gamma,exp}}\,, \tag{4.31}$$

where the subscript K indicated the measurement for the K electron and may be replaced with another electron shell or total conversion across all shell.

When intensities are from a γ-gated $e\gamma$ and $\gamma\gamma$ the experimental data, γ and electron transition intensities I_{exp} are calculated from the measured peak areas A_{exp} by :

$$I_{\gamma,exp} = \frac{A_{\gamma,exp}}{\varepsilon(E_\gamma)\cdot\Theta_{\gamma\gamma}(L_1,L_2)\cdot\tau_\gamma\cdot\Delta_{\gamma\gamma}} \text{ and} \tag{4.32}$$

$$I_{e,exp} = \frac{A_{e,exp}}{\varepsilon(E_e)\cdot\Theta_{e\gamma}(L_1,L_2)\cdot\tau_e\cdot\Delta_{e\gamma}}\,, \tag{4.33}$$

where ε is the calibrated detector efficiency at the peak energy, Θ_{AB} is the correction for a non-isotropic angular distributions, τ is the detector live time and Δ is the fraction of events within the timing window.

Efficiency and live time for detection of the gating γ ray are omitted as an identical gate is used for $e\gamma$ and $\gamma\gamma$ and the decay mode of the following (or prefacing) transition Γ has no influence on the isotropic detection efficiency of the gating γ, which cancel in the calculation of α_{exp}.

Combining Equations 4.31, 4.32 and 4.33 gives :

$$\alpha_{exp} = \frac{A_{e,exp}\cdot\varepsilon(E_\gamma)}{A_{\gamma,exp}\cdot\varepsilon(E_e)}\cdot\Lambda\cdot\Theta\,, \tag{4.34}$$

where the normalisation factors Λ and Θ defined as :

$$\Lambda = \frac{\tau_\gamma\cdot\Delta_{\gamma\gamma}}{\tau_e\cdot\Delta_{e\gamma}} \text{ and } \Theta = \frac{\Theta_{\gamma\gamma}(L_1,L_2)}{\Theta_{e\gamma}(L_1,L_2)}\,. \tag{4.35}$$

4.6.1 Angular Correction Factor

The correction factor Θ is needed to correct for increase or decrease in detection efficiency caused by any angular distribution of emitted radiation. In this work it is an effect we wish to remove for *known* multi-polarity transition, not one that is to be measured. Investigations revealed the importance of the Θ factor to be minimal and so an overview is given in lieu of the full mathematical formalism. A cut through of the detector setup is provided in Figure 4.24 for reference.

For an isotropic emission distribution there is a probability $P_A(iso)$ that a quanta of radiation is emitted towards the detector A. For a distribution given by the emission of an L quanta from an ensemble with average initial alignment i, the probability radiation is emitted towards the detector is $P_A(L|i)$. The factor $\Theta_{AB}(L_1,L_2)$ may then be defined for the detection of the first emitted quanta L_1 in detector A followed by detection of the

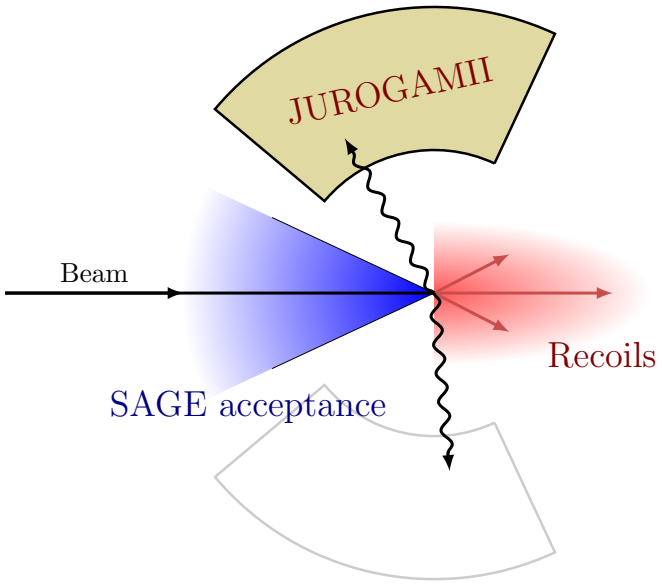

Figure 4.24: Cut through illustration of the experimental geometry showing detector acceptance angles. JUROGAMII spans $65 \leq \theta \leq 140$. The SAGE acceptance angle is energy dependant, $\theta \geq 155$ is shown.

second quanta L_2 in detector B, given as

$$\Theta_{AB}(L_1, L_2) = \frac{P_A(L_1|i)}{P_A(iso)} \cdot \frac{P_B(L_2|j)}{P_B(iso)}\,, \tag{4.36}$$

where j is the intermediate state ensemble before the emission of L_2, defined by the detection of L_1 in detector A. The definition has been kept general such that the two quanta may be electrons or γ rays and detectors A and B may be the same or different. Importantly, L_1 and L_2 are defined by the order of emission (which transition is used for gating is of no relevance here).

If the initial state ensemble i is uniformly oriented the following simplifications can be made: Subsequently $P_A(L_1|i) \equiv P_A(iso)$ for all L_1 and subsequently Equation 4.36 reduces to

$$\Theta_{AB}(L_1, L_2) = \frac{P_B(L_2|j)}{P_B(iso)}\,. \tag{4.37}$$

If either of L_1 or L_2 are an $E0$ quanta then $P_B(L_2|j) \equiv P_B(iso)$ and $\Theta_{AB} = 1$.

If L_1 and L_2 are known ($M1, E2$ etc) and the quanta are emitted consecutively, $P_B(L_2|j)$ can be calculated from Reference [90, Eq. 12.204]. This calculation was performed in Reference [91] and a summary of the conclusions is presented here.

When detector A is defined as the entire JUROGAMII array one finds that the angular acceptance ($65 \leq \theta \leq 140$) is sufficiently large that $j \approx uniform$ and hence $\Theta_{\gamma\gamma} \approx 1$ independently of the second quanta or detector B.

If detector A is taken to be SAGE, the angular acceptance (E_e dependant $\sim \theta > 130$) results in a poorly defined, but non-zero, orientation of the sub-states of j. Sub-states have sufficiently broad population distribution that when detector B is JUROGAMII the wide acceptance results in $P_B(L_2|j) \approx P_B(iso)$ and then $\Theta_{e\gamma} \approx 1$.

If L_1 and L_2 are *not* sequential and there are one or more undetected transitions between them, for example $L_1 = \Gamma_4$ and $L_2 = \Gamma_1$, then the alignment of j becomes more uniformly oriented and the approximation $\Theta_{AB} \approx 1$ becomes more accurate.

It has been shown that for a uniformly oriented initial state, $\Theta_{\gamma\gamma} \approx 1$ and $\Theta_{e\gamma} \approx 1$ is a valid assumption, resulting in $\Theta \approx 1$. However, for work where an initial orientation of the ensemble is defined or higher precision is required, a more rigorous approach to this factor must be taken.

Subsequently only the timing normalisation factor, Λ, is needed to calculate experimental conversion coefficients. This can be determined experimentally.

4.6.2 $\rho(E0)$ Calculation

General Definition

We wish to calculate the quantity $\rho(E0)$, the dimensionless monopole transition strength. $\rho(E0)$ contains all the information about the nuclear structure from the monopole matrix element [13] related by:

$$\rho(E0) = \frac{\langle\psi_f|\hat{T}(E0)|\psi_i\rangle}{eR^2}\,. \tag{4.38}$$

The square of $\rho(E0)$ can be directly calculated from the partial mean lifetime $\tau(E0)$:

$$\rho^2(E0) = \frac{1}{[\Omega_{ic}(E0) + \Omega_{\pi}(E0) + \Omega_{\gamma\gamma}(E0)] \cdot \tau(E0)}\,, \tag{4.39}$$

where Ω are the electronic factors. $\Omega_{ic}(E0)$ is the electronic factor for internal conversion and $\Omega_{\pi}(E0)$ is the electronic factor for internal pair production. $\Omega_{ic}(E0)$ is equal to the sum of the individual shell electronic factors $[\Omega_K(E0) + \Omega_{L1}(E0) + ...]$. These electronic factors are functions of the atomic number and transition energy, and may be calculated independently of nuclear properties. The higher order $\Omega_{\gamma\gamma}$ term for two photon emission is usually omitted from the sum as the strength of the 2γ transition is typically 10^{-3} that of internal conversion and pair production [92].

The partial lifetime, τ, is related to the $E0$ transition probability by $W(E0) = 1/\tau(E0)$ where $W(E0) = [W_{ic}(E0) + W_{\pi}(E0) + W_{\gamma\gamma}(E0)]$. The component transition probabilities are related to the total by the ratio of electronic factors, $(W(E0)/\sum_i \Omega_i) \cdot \Omega_j = W_j$. When the partial mean lifetime is not known $\rho^2(E0)$ can be calculated directly from the individual component transition probabilities:

$$\rho^2(E0) = \frac{W_K(E0)}{\Omega_K(E0)}\,. \tag{4.40}$$

This is perhaps the more useful form for the calculation of $\rho^2(E0)$ in electron spectroscopy, as one may indirectly measure the transition probability $W_K(E0)$. It is often easier to extract (or calculate from other quantities) the the ratio q_k^2 :

$$q_K^2(E0/E2) = \frac{W_K(E0)}{W_K(E2)}\,. \tag{4.41}$$

When the γ-ray transition probability $W_\gamma(E2)$ is known, either from lifetime or B(E2) measurements, the definition $W_K(E2) = W_\gamma(E2) \cdot \alpha_K(E2)$ can be used and Equation 4.40 can be written as :

$$\rho^2(E0) = q_K^2 \cdot \frac{\alpha_K(E2)}{\Omega_K(E0)} \cdot W_\gamma(E2)\,. \tag{4.42}$$

In the case of $0_i^+ \rightarrow 0_f^+$ E0 measurements the $W_K(E2)$ and $W_\gamma(E2)$ may refer to any arbitrary E2 transition from the initial state and $q_K^2(E0/E2)$ may be determined directly from a ratio of electron peaks.

E0+M1+E2

For a mixed (E0+M1+E2) $J_i \rightarrow J_f$ transition, the conversion coefficient is defined by [93] :

$$\alpha_{exp} = \frac{W_e(E0) + W_e(M1) + W_e(E2)}{W_\gamma(M1) + W_\gamma(E2)}\,. \tag{4.43}$$

When the mixing ratio $\delta^2 = W_\gamma(E2)/W_\gamma(M1)$ is known from angular correlations q^2 may be calculated. By use of the definitions of $\alpha(E2)$, $\alpha(M1)$, $q^2(E2/E0)$ and $\delta^2(E2/M1)$ Equation 4.43 may be rewritten as [94] :

$$\alpha_{exp} = \frac{1}{1+\delta^2}[\delta^2(1+q^2)\alpha(E2) + \alpha(M1)] \tag{4.44}$$

and hence rearrange to give q_K^2 :

$$q_K^2 = \frac{\alpha_{K,exp}(1+\delta^2) - \alpha_K(M1)}{\delta^2 \alpha_K(E2)} - 1\,, \tag{4.45}$$

which in turn can be used with Equations 4.42 to determine $\rho^2(E0)$.

5

^{154}Sm Experimental Details

5.1 Motivation

The even-even rare-earth nuclei show rapid changes in deformation across their isotopic chains. Particularly the N∼90 isotones in which a change from spherical ground state nuclei, through transitional nuclei, to deformed ground state nuclei is seen with the addition of just a few neutrons [95]. There is much controversy over the understanding of the low lying excited states in these nuclei. Most notably understanding of the nature of the low-lying 0^+ states is not complete [96, 97].

5.1.1 Bohr and Mottelson Beta-Vibrational States

The first excited 0^+ state has traditionally been interpreted as a collective excitation of the ground state [98]. As introduced in Section 2.2.2, the surface of quadrupole deformed can be described

$$R(\theta,\phi) = R_0\left\{1 + (\beta_0+\eta)Y_{20}(\theta,\phi) + \zeta[Y_{22}(\theta,\phi) + Y_{2-2}(\theta,\phi)]\right\}, \tag{5.1}$$

where β_0 is a constant of the equilibrium deformation and η and ζ are dynamic variables describing the change of the nuclear shape around the equilibrium static deformation. Subsequently, the solutions of the the Bohr-Mottelson Hamiltonian include harmonic oscillations in the β and γ degrees of freedom. Bohr and Mottelson then described low-lying 0^+ and 2^+ excitations as "one-phonon" β-vibrational and γ-vibrational modes [17]. Rotational bands are then built on the deformed ground state and each of these one-phonon collective shape oscillations, producing a rotational-vibrational spectrum.

These rotational-vibrational bands are characterised by large, collective, E2 transitions to the ground band. Using the collective quadrupole operator [99]

$$\hat{Q}^{\text{coll}}_{2\mu} = \frac{3Z}{4\pi R_0^3}\int r^4 Y^*_{2\mu}\mathrm{d}r\mathrm{d}\Omega\,, \tag{5.2}$$

the following $B(E2)$ strengths are calculated in the model [19] :

$$B(E2; I_\beta \to I_{1,f}) = K^2\beta_0^2\langle I_\beta 020|I_f 0\rangle^2 y^2(1+2\alpha)^2 \tag{5.3}$$

$$B(E2; I_\gamma \to I_{1,f}) = K^2\beta_0^2\langle I_\gamma 222|I_f 0\rangle^2 x^2(1-2\alpha)^2 \tag{5.4}$$

$$B(E2; I_{1,i} \to I_{1,f}) = K^2\beta_0^2\langle I_i 020|I_f 0\rangle^2(1+\alpha)^2 \tag{5.5}$$

where

$$K = \frac{3ZR_0^2}{4\pi} \quad \alpha = \frac{2}{7}\sqrt{\frac{5}{\pi}}\beta_0 \quad y = \sqrt{\frac{3\varepsilon}{2E_\beta}} \quad x = \sqrt{\frac{3\varepsilon}{E_\gamma}}\,. \tag{5.6}$$

The static deformation (β_0), vibrational energies (E_β, E_γ) and moment of inertia ($\hbar^2/\varepsilon$) can be determined experimentally. Using typical values[1], transition strengths $B(E2; I_\beta \rightarrow I_1)$ of the order ~ 10 W.u. are expected from a β band (see Section 2.1.1 for explanation of W.u.).

The intrinsic matrix element can provide a better measure of collectivity than the absolute $B(E2)$ strength as this removes the dependence on the Clebsch-Gordan coefficient for spin coupling. One expect similar $E2$ collectivity for β and γ bands as both are quadrupole vibrations which merely differ in projection on to the symmetry axis [97]. Very small $B(E2; 0^+_\beta \rightarrow 2^+_\gamma)$ should be observed as this transition is forbidden due to the simultaneous creation of a γ excitation quanta and annihilation of a β excitation quanta [15]. Due to their collective nature, these vibrational states should have little quasi-particle structure and hence should have small cross sections for population by particle-transfer reactions.

Finally, for transitions from the β-band the collective monopole operator, given in Section 2.2.2, predicts large monopole transition strengths, $\rho^2(E0; I_\beta \rightarrow I_1) \approx 100 \times 10^{-3}$, given by

$$\begin{aligned}\rho^2(E0; I_\beta \rightarrow I_1) &= \frac{9}{8\pi^2} Z^2 \beta_0^4 \frac{E(2^+_1)}{E(0^+_\beta)} \\ &= \frac{B(E2; 0^+_1 \rightarrow 2^+_\beta) 4\beta_0^2}{e^2 r_0^4 A^{4/3}}\,.\end{aligned} \tag{5.7}$$

The collective $E0$ operator does not allow γ-band to ground-band transitions; this follows logically as the γ band has projection $K^\pi = 2^+$ which an $E0$ transition cannot couple to the ground band projection $K^\pi = 0^+$.

Whereas γ vibrational states have been identified systematically in a range of deformed nuclei, clear experimental identification of β vibrations has proven elusive [100]. The first excited 0^+ state in a quadrupole deformed nucleus may not be the β-vibrational state, and should not be considered so by default [97]. The lowest excited 0^+ state in a nucleus may be a phase-coexisting collective state [101], a non-collective quasi-particle state dominated by $K^\pi = 0^+$ particle pairs [102] or even a shape-coexisting particle-hole state from excitation to intruder orbitals [103]. Rather than a pure β-vibrational state, the 0^+_β state may mix with another 0^+ state, or many 0^+ states, to form the observed 0^+_2 state in a nucleus. Strong mixing may degrade the characteristics of the 0^+_β state to the point where the label is no longer appropriate [97].

5.1.2 IBM in the Rare-Earth Region

It is desirable to have a model that spans the rare-earth region and is capable of explaining the various behaviours the nuclei exhibit. The IBA-1 has proved particularly effective

[1] Typical values can be seen in the calculation for ^{154}Sm on page 93

in this regard [104]. By use of a simplified Hamiltonian with two control parameters ζ and χ, the IBA can reproduce the properties of low-lying, collective, positive-parity excitations. Including producing β-like and γ-like collective excited states. The IBA control parameters, ζ and χ, can be adjusted to match the calculated states and transitions with those observed experimentally and these parameters tracked across an isotopic chain [105]. For matching of observed and model-predicted states, the first excited 0^+ is generally assumed to be collective in nature. The model-predicted γ-like 2^+ state is compared to the band head for the γ band in rotational nuclei, and is observed to transition to a member of the 2-phonon multiplet as one moves towards spherical nuclei.

IBA trajectories for several rare-earth isotope chains, calculated in Reference [104], are shown in Figure 5.1. In the referenced work, emphasis was placed on adjusting control parameters to match observables in the ground, 0_2^+ and 2_γ^+ bands, deemed to be the most important in the region. Emphasis was placed on the energy ratios $R_{4/2} \equiv E(4_1^+)/E(2_1^+)$, $E(0_2^+)/E(2_1^+)$ and $E(2_\gamma^+)/E(2_1^+)$, and on the transition ratios
$B_{2\gamma} = B(E2; 2_\gamma^+ \rightarrow 0_1^+)/B(E2; 2_1^+ \rightarrow 0_1^+)$ and $R_{2\gamma} = B(E2; 2_\gamma^+ \rightarrow 0_1^+)/B(E2; 2_\gamma^+ \rightarrow 2_1^+)$.
The results of Reference [104] differ from previous calculations in which less importance was given to the 0_2^+ state [106]. Furthermore, very different trajectories are observed for the heavy isotopes of ytterbium and hafnium where $E(0_2^+) < E(2_\gamma^+)$, smoother trends are produced for $N \geq 100$ if it is assumed that the 0_3^+ state is the first excited IBA collective 0^+ state, suggesting the 0_2^+ state belongs to an intruder structure.

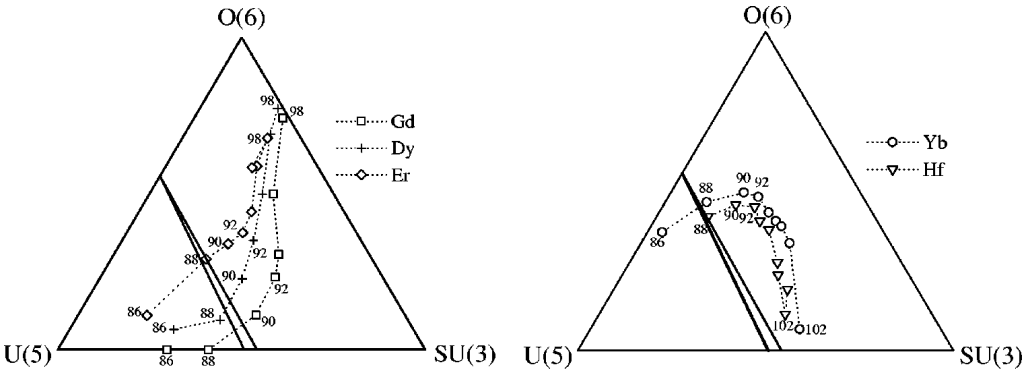

Figure 5.1: Calculated trajectories of rare-earth isotope chains on the IBA symmetry triangle [104].

Transition Critical Point

Nuclei are particularly difficult to describe where they fall in the phase transitional region, as deformation moves between spherical $U(5)$ and deformed $SU(3)$. This region is highlighted in Figure 5.2. In this small critical region of the IBA control parameter ζ the phenomena of phase coexistence is predicted, as the potential energy surface $\mathrm{E}(\beta, \gamma)$ has two minima [107]. Physically observed states in this region may be described by mixing between the two coexisting collective phases [101].

Nuclei which fall within this region may be described by the $X(5)$ dynamic symmetry model [108]; an analytical solution which decouples the β-and γ-deformation degrees of

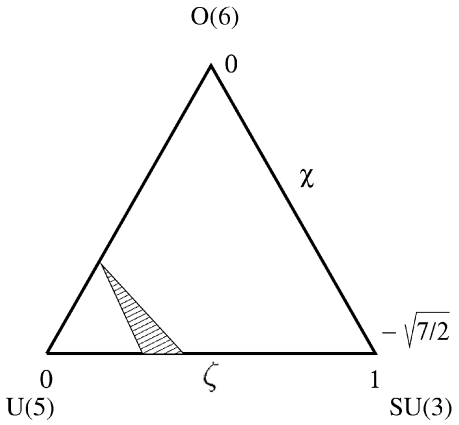

Figure 5.2: IBM symmetry triangle showing the schematic critical region in which phase coexistence is predicted [107].

freedom.[2]X(5) nuclei are easily identified by the characteristic observables of $R_{4/2} = 2.91$, $E(0_2^+)/E(2_1^+) = 5.67$ and ground state band $B(E2)$ value intermediate between vibrator and rotor [110]. There is limited application of this description, as nuclei are integer system and few land exactly at the critical point. The N=90 isotones ^{156}Dy, ^{154}Gd, ^{152}Sm and ^{150}Nd have been suggested as possible X(5) nuclei as the energy of 0_2^+ states are correctly predicted, however the model fails to fit the energy spacing of the excited states or the B(E2) transition strengths [111].

Clearly in this region, further development of models and the measurement of critical observables is paramount. Particularly measurement of the sparsely measured monopole transition strengths $\rho^2(E0)$ which are sensitive to both changes in nuclear shape and state mixing.

5.1.3 The Nature of ^{152}Sm and ^{154}Sm

Historically, the 0_2^+ states in ^{152}Sm and ^{154}Sm have viewed as ideal examples of β-vibrational one-phonon states, as described by Bohr and Mottelson [112, 113, 114]. However many measurements have challenged this assignment and suggest either one or both of these nuclei do not represent pure β-vibrators or that this assignment is entirely spurious. No single model has uniquely explained the behaviour of the nuclear states to a satisfactory level. The nature of the 0_2^+ states in ^{152}Sm and its neighbour ^{154}Sm remain unclear.

^{152}Sm Interpretations

The transitional nucleus ^{152}Sm, sitting between spherical ^{150}Sm and well-deformed ^{154}Sm (β=0.339), is a subject of continued debate. In the IBA the nucleus is found to sit close to the transition critical point in which coexisting collective phases are expected. It has been suggested that the 0_2^+ state in ^{152}Sm should be described as a near spherical phase coexisting state [115]. Consequently higher-lying excited states would be reordered as multiphonon vibrational states built on the phase coexisting 0_2^+ state, this is shown in Figure 5.3. In Reference [116] it was shown that the experimental data are explained at

[2]For the $U(5)$ to $O(6)$ transitional region the $E(5)$ model may be used[109]; in which the potential at the critical point is replaced by a five-dimensional square well.

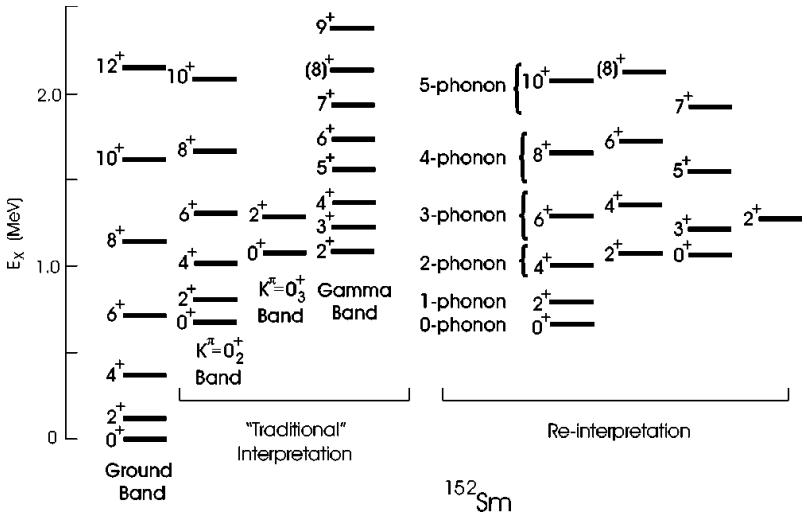

Figure 5.3: Positive-parity levels are of ^{152}Sm are shown with the traditional interpretation (left) and the reordering corresponding to a phase coexisting 0_2^+ state (right) [116].

least as successfully in the traditional picture. The 2_2^+ to 0_2^+ spacing is only 126 keV, which is significantly closer to the 122 keV rotation of the ground band than to the ∼300 keV multiphonon prediction or the ∼334 keV 2^+ phonon energy in spherical ^{150}Sm [117]. The $B(E2 : 2_2^+ \rightarrow 0_2^+)$ value of ∼111 W.u. is comparable to rotational values and larger than expected vibration excitations. The $R_{4/2}^{(2)}$ value, defined as $[E(4_2^+) - E(0_2^+)]/[E(2_2^+) - E(0_2^+)]$, of 2.69 is well above the 2.0 pure vibrator limit, though equally below the 3.33 rigid rotor limit. Finally, population of the suggested multiphonon states by one-and two-nucleon transfer reactions is observed to be far stronger than should be possible for such a forbidden transition.

A following interpretation (Reference [118]) showed that energy spacings and $B(E2)$ from the 0_2^+ band in ^{152}Sm could be described by the mixing of two coexisting $K^\pi = 0^+$ rotational bands of similar deformation. Using the prescription of Reference [17] the mixing amplitude for a $\Delta K = 0$ coupling between two rotational bands may be given as $b \approx V/\Delta E$ where ΔE is the energy difference between unperturbed states $|0_1\rangle$ and $|0_2\rangle$. The interaction matrix element V may subsequently be expanded as $V \approx h_1 I(I+1)$, where h_1 is the intrinsic mixing matrix element between bands. If a small amount of mixing occurs between the two rotational bands (perturbative case) this leads to the resultant states

$$|\tilde{I_1}\rangle \approx |I_1\rangle - \epsilon_0 I(I+1)|I_2\rangle \quad \text{and} \tag{5.8}$$

$$|\tilde{I_2}\rangle \approx |I_2\rangle + \epsilon_0 I(I+1)|I_1\rangle\,, \tag{5.9}$$

where the coefficient $\epsilon_0 = h_1/\Delta E$. Interband $B(E2)$ transitions strengths are then given by

$$B(E2; I_i \rightarrow I_f) = \langle I_i 020|I_f 0\rangle^2 \times \{M_1 + M_2[I_i(I_i+1) - I_f(I_f+1)]\}^2\,, \tag{5.10}$$

where M_1 is intrinsic matrix element between unperturbed states and M_2 is the contribution due to mixing. Assuming two unperturbed bands of approximately equal intrinsic

quadrupole moment, $\overline{Q}_0$, the rigid-rotor value for in-band transitions [2]

$$\langle I \pm 2||\hat{\mathfrak{M}}(E2)||I\rangle = \sqrt{\frac{5}{16\pi}}e\overline{Q}_0 \tag{5.11}$$

can be used for both unperturbed bands. Hence, M_2 is given by:

$$M_2 = \epsilon_0\sqrt{\frac{5}{16\pi}}e\overline{Q}_0\,. \tag{5.12}$$

Using $\overline{Q}_0 = 5.90\,\mathrm{b}$, the 0_2^+ band to 0_1^+ band $B(E2)$ values in ^{152}Sm were found to fit this model well, for a mixing coefficient $\epsilon_0 = -0.007$.

Other work [119], investigating negative parity states in ^{152}Sm, suggested a series of rotational bands built on the 0_2^+ indicating a complex example of shape coexistence. It is also highlighted that the large two-neutron transfer cross section of the 0_2^+ state indicates a significant, or even dominant, pairing component. Combined with the absence of candidates for the 2-phonon β-vibrational state, this seems to show that the 0_2^+ state in ^{152}Sm is a state of limited collectivity that should not be interpreted as the 0_β^+ state.

^{154}Sm Interpretations

The nucleus ^{154}Sm, which has value of $R_{4/2} = 3.25$, is further from the IBA critical point than ^{152}Sm, sitting towards the $SU(3)$ rigid rotor limit, at which one expects $R_{4/2} = 3.33$. As a result, a simpler level structure with reduced or negligible contribution from coexisting collective phases is expected. The 0_2^+ state in ^{154}Sm remains a prime candidate for a pure 0_β^+ β-vibrational band head.

The 0_2^+ state in ^{154}Sm at 1099 keV is significantly higher in energy than the 0_2^+ state in ^{152}Sm at 685 keV and so negligible mixing with the ground band is expected compared with that described for ^{152}Sm. However, the third 0_3^+ state in ^{154}Sm is located at 1202 keV and significant mixing between this and the 0_2^+ could be possible. From the results of a CoulEx experiment [114] values of $B(E2; 0_2^+ \rightarrow 2_1^+) = 12\,\mathrm{W.u.}$ and $B(E2; 0_3^+ \rightarrow 2_1^+) = 0.3\,\mathrm{W.u.}$ were determined for ^{154}Sm. The large difference indicates a significant mixing of the two 0^+ excited states can be excluded, despite their proximity. An upper limit on the mixing amplitude yields the $B(E2)$ of the two unmixed states differ by at a factor of 24. This shows the 0_3^+ state has no collective transition to ground, whereas the strong $B(E2; 0_2^+ \rightarrow 2_1^+)$ is consistent with an assignment of the 0_2^+ state as the β-vibrational band head. This can be shown by combining Equations (5.3) and (5.5) to give:

$$\frac{B(E2; I_\beta \rightarrow I_{1,f})}{B(E2; 2_1^+ \rightarrow 0_1^+)} = 5\langle I_\beta 020|I_f 0\rangle^2\frac{y^2(1+2\alpha)^2}{(1+\alpha)^2}\,. \tag{5.13}$$

Using the values for ^{154}Sm of $E_\beta = 1099\,\mathrm{keV}$, $\hbar^2/\mathfrak{J} = \varepsilon = 27.3\,\mathrm{keV}$, $B(E2; 2_1^+ \rightarrow 0_1^+) = 176\,\mathrm{W.u.}$ and β=0.339, one expects $B(E2; 0_\beta^+ \rightarrow 2_1^+) \approx 40\,\mathrm{W.u.}$, compared to which the experimentally measured value is of the correct magnitude.

Reduced parameter space IBA calculations, also presented in Reference [114], correctly place the energy of the 0_2^+ state and reproduce the large $B(E2)$, the comparison is shown

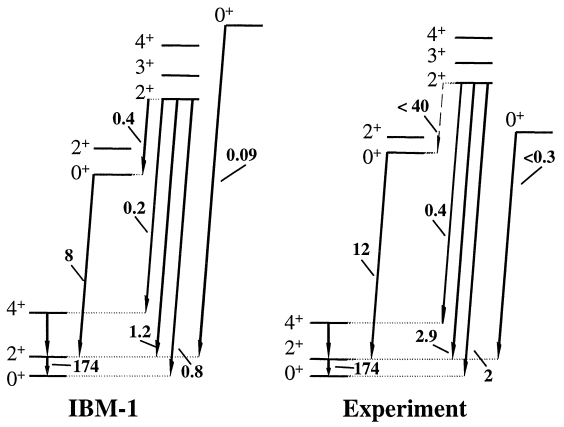

Figure 5.4: Experimental results and model predictions from Reference [114]. Excited states are assigned in the reference as the 2^+_γ band, 0^+_β band and 0^+_3 coexisting spherical state. Transition strengths are indicated in W.u..

in Figure 5.4. In the IBA, a very broad distribution of wave function amplitude as a function of the number of d bosons, n_d, is observed, consistent with a β-like state. The 0^+_3 state is found to be dominated by $n_d = 0$, leading to the interpretation as a phase coexisting spherical state which has moved up in energy for deformed ^{154}Sm (towards the $SU(3)$ limit) compared to its position in ^{152}Sm and ^{150}Sm.

Further CoulEx studies [120] measured $B(E2)$ values for ^{154}Sm of $B(E2; 2^+_2 \rightarrow 0^+_1) = 0.32$, $B(E2; 2^+_2 \rightarrow 2^+_1) = 0.72$ and $B(E2; 2^+_2 \rightarrow 4^+_1) = 1.32$ W.u.. From Equation (5.13) the expected β-band values should be of the order 8, 11.5 and 20.7 W.u. respectively. The values are smaller but not inconsistent with a β-band interpretation, due to the possibility of mixing between the 2^+_β and 2^+_γ states [97].

Identifying the two-phonon β-vibrational band of ^{154}Sm, which would decay more strongly to the one-phonon band than the ground band, would be a desirable step in confirming such an assignment for the 0^+_2 band.

Further information can be gained from the $\rho^2(E0)$ monopole transitions strengths from the band. From the first form of Equation (5.7) a value of $\rho^2(E0; 0^+_\beta \rightarrow 0^+_1) \approx 400 \times 10^{-3}$ is predicted for a pure β-vibrational band in the Bohr-Mottelson model.[3,4] In the Bohr-Mottelson model there is no angular momentum dependence for the monopole transition strength and hence $\rho^2(E0; 0^+_\beta \rightarrow 0^+_1) \equiv \rho^2(E0; 2^+_\beta \rightarrow 2^+_1)$[15].

In the IBA $\rho^2(E0)$ strengths can be approached in a more general way, such that the strengths in neighbouring ^{150}Sm, ^{152}Sm and ^{154}Sm may be related in a cohesive picture [28, 27]. In this approach the rapidly rising $\rho^2(E0)$ between ^{150}Sm $\rho^2(E0; 0^+_2 \rightarrow 0^+_1) = 18 \times 10^{-3}$ and ^{152}Sm $\rho^2(E0; 0^+_2 \rightarrow 0^+_1) = 58 \times 10^{-3}$ is explained by a move away from the $U(5)$ limit and more fluctuation of n_d in the wave function of transitional ^{152}Sm. This assumes a collective picture without the need for mixing of intruder states. As ζ further increases for ^{154}Sm, strengths of $\rho^2(E0; 0^+_2 \rightarrow 0^+_1) \approx 100 \times 10^{-3}$ are predicted for the 0^+_2 β-like collective state [28], this is shown in Figure 5.5.

A more recent IBA parametrisation predicts $\rho^2(E0; 0^+_2 \rightarrow 0^+_1) = 41$ and $\rho^2(E0; 2^+_2 \rightarrow 2^+_1) = 39$ [27, 121].

[3]The values of $\rho^2(E0)$ are presented in the format $\times 10^{-3}$ by convention.

[4]Using the form of Equation (5.7) which depends on $B(E2; 0^+_1 \rightarrow 2^+_\beta)$, measured value $78.4\, e^2 fm^4$, a value of $\rho^2(E0; 0^+_\beta \rightarrow 0^+_1) \approx 20 \times 10^{-3}$ is predicted. For a perfect β-band these two forms should match.

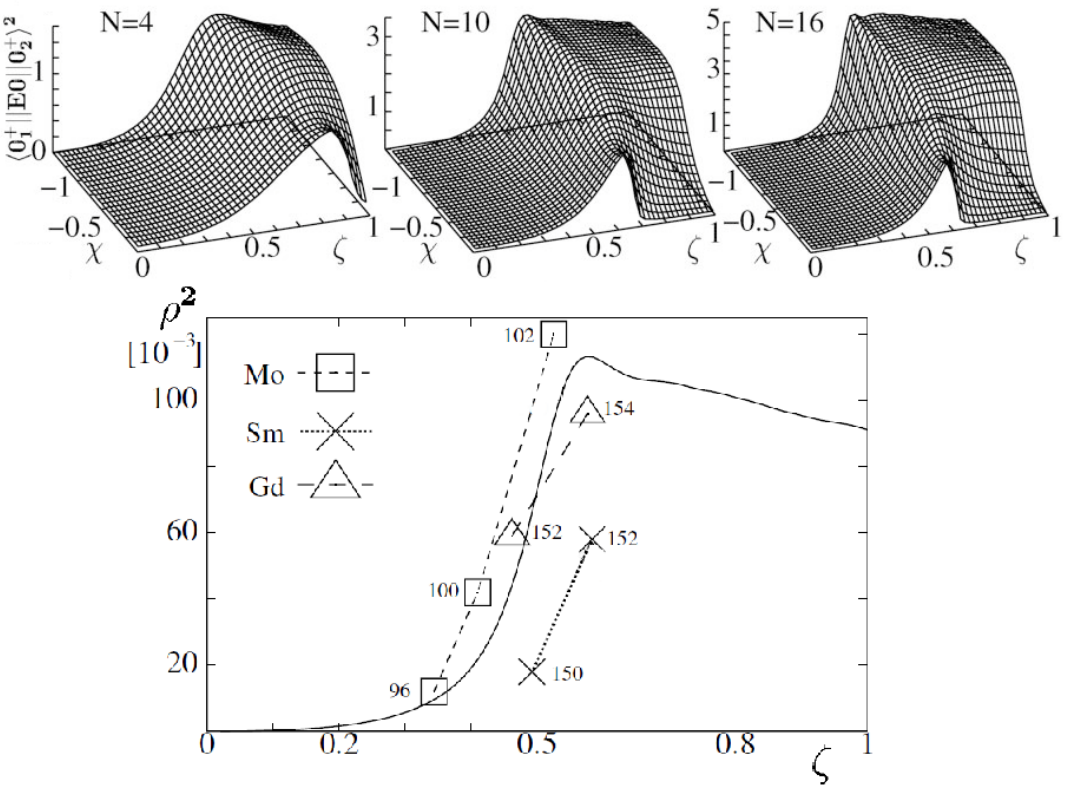

Figure 5.5: IBM monopole transition calculations from Reference [28]. The top three images demonstrate that there is little change with boson number N. The main image shows measured values (dashed lines) alongside IBM prediction (solid line) for N=10 and $\chi = -\sqrt{7}/2$.

5.1.4 Summary

Low-lying states in deformed even-even nuclei, particularly the 0_2^+ states, are not fully understood. Traditionally these 0_2^+ states were interpreted as a pure β-vibrational collective states in a geometrical picture. However a rich variety of excitation modes may mix with or displace the 0_β^+ state to form the 0_2^+ state in such nuclei.

For the β-vibrator candidate ^{154}Sm, a monopole transition strength, $\rho^2(E0; 0_2^+ \rightarrow 0_1^+)$, between the 0_2^+ and ground 0_1^+ states of the order 100×10^{-3} is expected for $0_2^+ = 0_\beta^+$. IBA calculations, which span the range of rare-earth nuclei, predict for ^{154}Sm, a 0_2^+ β-like collective state and expect $\rho^2(E0; 0_2^+ \rightarrow 0_1^+)$ values of $\sim 100 \times 10^{-3}$ [28] and 41×10^{-3} [27].

Measurement of $\rho^2(E0)$ values in ^{154}Sm will provide a crucial piece of evidence as to whether the nucleus can be described as a Bohr-Mottelson vibrating-rotor, or if the IBA can describe the low level structure of ^{154}Sm and its neighbour ^{152}Sm.

5.2 Aim and Setup

5.2.1 Experimental Aim

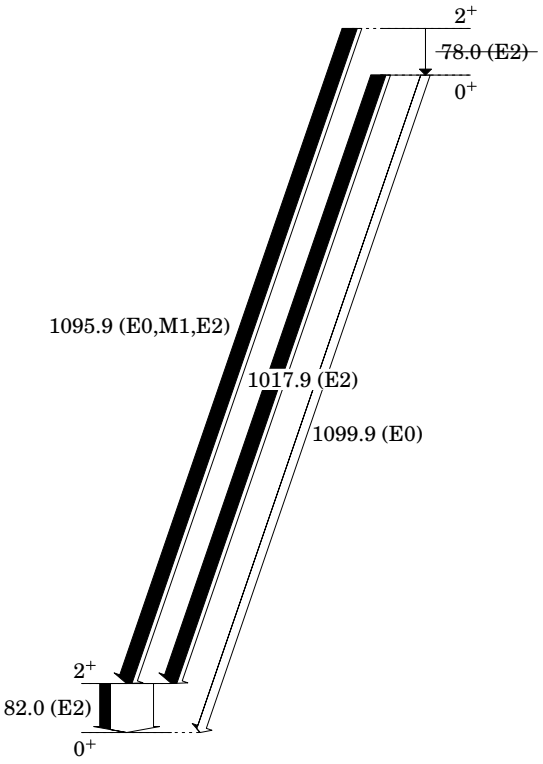

Figure 5.6: ^{154}Sm level scheme showing just the levels and transitions of importance to this work. Intensities (relative arrow widths) and conversion coefficients (fraction of arrow that is white) have been exaggerated for illustrative purposes.

The principal experimental aim was to determine if electric monopole transition strengths, $\rho(E0)$, in the isotope ^{154}Sm can be measured using the SAGE spectrometer and determine the feasibility of this method for further measurements in this region. Doing so involves measuring high-energy electrons ($\sim$1 MeV), for which SAGE is not optimised, and performing $e^-\gamma$-coincidence measurements for which SAGE is a particularly well-designed piece of equipment.

The electric monopole transition strengths, $\rho(E0)$, between the first excited 0_2^+ state and the ground 0_1^+ state can be determined from the ratio of the different decay branches of the 0_2^+ state. A measurement must be made of the ratio between the two internal-conversion branches, the intensity of electrons from the 1099 keV $0_2^+ \rightarrow 0_1^+$ transition, $I_e(E0)$, and the intensity of electrons from the 1017 keV $0_2^+ \rightarrow 2_1^+$ transition, $I_e(E2)$. This, combined with the known γ-ray transition probability $W_\gamma(E2)$ for the $0_2^+ \rightarrow 2_1^+$ transition, can be used to calculate $\rho(E0)$.

However the $2_2^+ \rightarrow 2_1^+$ and $0_2^+ \rightarrow 0_1^+$ transitions differ in energy by only 4 keV, as shown in Figure 5.6. As a result, electron peaks from the two transitions in a raw electron singles spectrum are too close together to be confidently separated, due to limitations of the detector resolution. Hence the experimentally measured electron intensity $I_{e,exp}$ is a sum of both transitions $I_{e,exp} = I_e(E0)_{0_2^+ \rightarrow 0_1^+} + I_e(E2+M1+E0)_{2_2^+ \rightarrow 2_1^+}$. The two intensities may be separated by performing an $e^-\gamma$-coincidence measurement. Measurement of electrons coincident with the 82 keV $2_1^+ \rightarrow 0_1^+$ γ ray allows clean determination of $I_e(E2 + M1 +$

$E0)_{2_2^+ \to 2_1^+}$ and hence separation of $I_e(E0)_{0_2^+ \to 0_1^+}$. Also, the conversion coefficient $\alpha_{2_2^+ \to 2_1^+}$ for the mixed E2+M1+E0 transition may be determined.

Although the $2_1^+ \to 0_1^+$ and $2_2^+ \to 0_2^+$ transitions also differ in energy by only 4 keV, the intensity of the $2_2^+ \to 0_2^+$ branch from the 2_2^+ state is so small it has not be observed, and so the $2_2^+ \to 0_2^+ \to 0_1^+$ decay path may be ignored.

Similar attempts to make $\rho(E0)$ measurements using mini-orange detectors coupled to germanium clovers have been attempted [122, 123]. However the good transport efficiency over a broad energy range of the electron spectrometer component of SAGE coupled to the nearly 4π coverage of JUROGAMII allows a sufficient $e^-\gamma$ yield to decouple the $2_2^+ \to 2_1^+$ and $0_2^+ \to 0_1^+$ in the manner described.

5.2.2 Initial Setup

Three 99% enriched targets of ^{154}Sm, each of thickness 1.5 mg/cm^2, were mounted on the target wheel at the centre of JUROGAMII, an aliuminium backing on one target was discover after the experiment. An ^{16}O beam was used to CoulEx the target over a beam spot of ~ 4 millimetres. The beam was chosen because of the ease with which it could be obtained from the accelerator, its high excitation threshold of 6 MeV avoids additional γ rays from beam excitations and a Z of 8 provides a moderate cross-section for multi-step CoulEx but is not dominated by many step reactions rising high up the yrast band.

The 1099 keV 0_2^+ level is predominantly populated by two-step CoulEx via the 82 keV 2_1^+ level; one-step excitation is not possible. The 1178 keV 2_2^+ level is predominantly populated by one-step and two-step excitations. An initial beam energy of 55 MeV was selected; this corresponds to a centre-of-mass energy of 49.82 MeV, which is significantly below the Coulomb barrier height of 60.97 MeV (as given by fusion-evaporation code PACE4 [124]). As such, only 'safe' CoulEx reactions are expected and the CoulEx code CLX [125] can be used to calculate the expected populations of states.[5] Following population of the excited states electron and γ-ray emission from de-excitation were detected in SAGE and JUROGAMII. No separator or particle detectors were used to measure the recoiling target nuclei or inelastically scattered beam particles. An initially low beam intensity of 1 particles nano Amp (pnA) or 6.2×10^9 particles per second (pps) corresponding to 3 electrical nano Amps as a +3 charge state for the ^{16}O beam was selected from the ion source. The system ran in its standard triggerless mode recording every individual detector event to disk with a time stamp, with higher multiplicity events being reconstructed from that data stream offline.

5.2.3 Expected Rates

In order to calculate the CoulEx population of states the spin, parity and energy of the states must be known. In addition the set of transition matrix elements between pairs of states are needed. The electromagnetic transition matrix elements can be calculated using

[5] 'safe' CoulEx refers to a reaction in which the centre-of-mass energy is sufficiently below the mutual Coulomb barrier of beam and target nuclei as to ensure that penetrability is low and the nuclear force may be neglected.

the reduced transition rate, $B(\sigma L)$, given by

$$\frac{1}{\tau_\gamma(\sigma L)} = \frac{2(L+1)}{\hbar\varepsilon_0 L[(2L+1)!!]^2}\left(\frac{E_\gamma}{\hbar c}\right)^{2L+1} B(\sigma L) \tag{5.14}$$

and using following form of the reduced matrix element

$$B(\sigma L) = \frac{1}{2J_i+1}\left|M_{fi}(\sigma L)\right|^2 . \tag{5.15}$$

Hence, the partial lifetimes of the individual γ-ray transitions (and components in the case of mixed transitions) are needed for these calculations.

The 0_2^+ and 2_2^+ state lifetimes were measured using the Doppler-shift Attenuation Method (DSAM) in Reference [114] to be 1.3(3)ps and >3.5ps respectively. The lifetimes are calculated from $\tau_\gamma = \tau(1+\alpha)$ where for both states it has been assumed $\rho(E0) = 0$ for the calculation of the conversion coefficient α. While this is an over-simplification, it is estimated to be at most a 10% error [114] on the lifetimes.

For states such as the 2_2^+, where there are multiple γ branches, the partial lifetimes for one γ-ray transition is related to the total state lifetime τ by $\tau/I_{\gamma_{2_2\to4_1}} = \tau_{\gamma_{2_2\to4_1}}$, where $I_{\gamma_{2_2\to4_1}}$ is the fractional intensity of the transition. The $2_2 \to 2_1$ γ-ray transition is a mixed E2,M1 transition where the mixing ratio, δ, is determined from measurement of γ-ray angular distributions to be $+60^{+130}_{-30}$ (an alternative -0.42±2 is also reported [126]), where I(E2)=$\frac{\delta^2}{1+\delta^2}$ and I(M1)=$\frac{1}{1+\delta^2}$, indicating a predominantly $E2$ transition in this case. From these data the following magnitudes of the transition matrix elements for particular electric or magnetic multipole orders are calculated:

$$\begin{aligned}
&|M(E2)_{0_2\to2_1}| = 0.108 \text{ eb},\\
&|M(E2)_{2_2\to0_1}| < 0.266 \text{ eb},\\
&|M(E2)_{2_2\to4_1}| < 0.181 \text{ eb},\\
&|M(E2)_{2_2\to2_1}| < 0.179 \text{ eb and}\\
&|M(M1)_{2_2\to2_1}| < 6.5E-5 \text{ eb}^{0.5}.
\end{aligned}$$

The limit $\delta = 60$ has been taken to caculate $|M(E2)_{2_2\to2_1}|$ and $|M(M1)_{2_2\to2_1}|$. The code CLX was used to determine initial nuclear state populations by CoulEx. For these calculations, the differential cross section was integrated over all possible centre-of-mass scattering angles because of the absence of recoil particle detectors and the selectivity this imposes on a measurement. Matrix elements from known B(E2)s for the yrast band in ^{154}Sm were included up to the 10_1^+ state. Matrix elements for reorientation were not included. A change of matrix element sign between bands had minimal effect on populations.

The resulting population cross sections for the 0_2^+ and 2_2^+ states were estimated to be $\sigma_{g\to0_2^+}$ =0.9 mb and $\sigma_{g\to20_2^+}$ =4.7 mb respectively. Assuming a similar $X(E0;0_2^+ \to 0_1^+$ /E2;$0_2^+ \to 2_1^+$) to ^{152}Sm of $\sim 6\,\%$ for the $0_2^+ \to 0_1^+$ transition $\sim 1.7\times10^5$ electrons/day are expected, and for the $2_2^+ \to 2_1^+$ transition $\sim 3.7\times10^5$ electrons/day are expected, assuming a beam current of 1 pnA.

Efficiency

The absolute isotropic efficiency of SAGE was calculated per the definition in Section 4.2, using calibration source data obtained at the beginning and end of the experiment. Three sources were used; a mixed ^{152}Eu and ^{133}Ba γ-ray only source, a $e^{-}\gamma$ ^{207}Bi source, producing electron peaks from 480 to 1050 keV and an open $e^{-}\gamma$ ^{133}Ba source provided a high density of electron peaks from 40 to 380 keV. JUROGAMII was initially calibrated without the open ^{133}Ba source, which unfortunately had a poorly calibrated intensity. The $e^{-}\gamma$ ^{133}Ba source was then scaled to match the γ intensities and subsequently included in γ and e^{-} calibrations. Further details of the sources and calibration peaks used, as well as spectral fits and resultant efficiency curves, are given in Appendix C.

An additional correction was required to get the true experimental efficiency, as the high voltage potential barrier of SAGE was not active during calibration.[6] This only has an effect on the lowest energy electrons, as shown in Figure 3.10, outside the primary region of interest.

Detailed simulations have previously been performed for field efficiency effects in SAGE, as detailed in Section 4.2. Effects from the electronics meant that the simulated efficiencies differ from that which was measured experimentally. However, it is reasonable to assume that when only the field is changed, the ratio of efficiency between the two field settings is accurately recreated by the simulation, which focuses on these effects. Hence the experimental field change can be determined by the ratio of the simulated efficiencies: $\varepsilon_{exp}(E) = \varepsilon_{cal}(E)\rho(E)$ where ρ is the ratio between simulations for the two field settings. The uncertainty in ρ is a combination of the simulation uncertainties for both field settings at the given energy. This unavoidably adds a large additional uncertainty even as ρ approaches 1. Above 500 keV, the scaling and its associated error may be neglected as the potential barrier has no effect. The calibrated efficiency curve and the result of the scaling to account for the potential barrier is shown in Figure 5.7.

Using the measured peak efficiency, the total isotropic detection efficiency for the $2_2^+ \rightarrow 2_1^+$ 1049 keV K-electron of ^{154}Sm is 0.14%. For the combined K-electron peak for both transitions of interest, which cannot be experimentally resolved, ∼800 counts/day were expected in the raw spectrum.

5.2.4 Preliminary Run

Twelve hours of data were collected using the initial settings. Based on the online analysis of this run, revised beam and DAQ settings were selected to optimise the experiment. These settings were then fixed for the remainder of the experiment due to operator constraints. An electron spectrum from this preliminary data is shown in Figure 5.8, here a ^{154}Sm conversion-electron spectrum is the dominant feature at low energies. K-shell electron peaks and L+M shell peaks are visible for the $2_1^+ \rightarrow 0_1^+$, $4_1^+ \rightarrow 2_1^+$ and $6_1^+ \rightarrow 4_1^+$ transitions. L-shell and M-shell electrons from samarium are not separable as they differ in energy by only 5 keV; typical L:M conversion ratio for such E2 are in the region of 4:1.

[6] This was an experimental oversight. The high voltage barrier is not required for an energy calibration that is most often required, it is only needed for the absolute efficiency calibration.

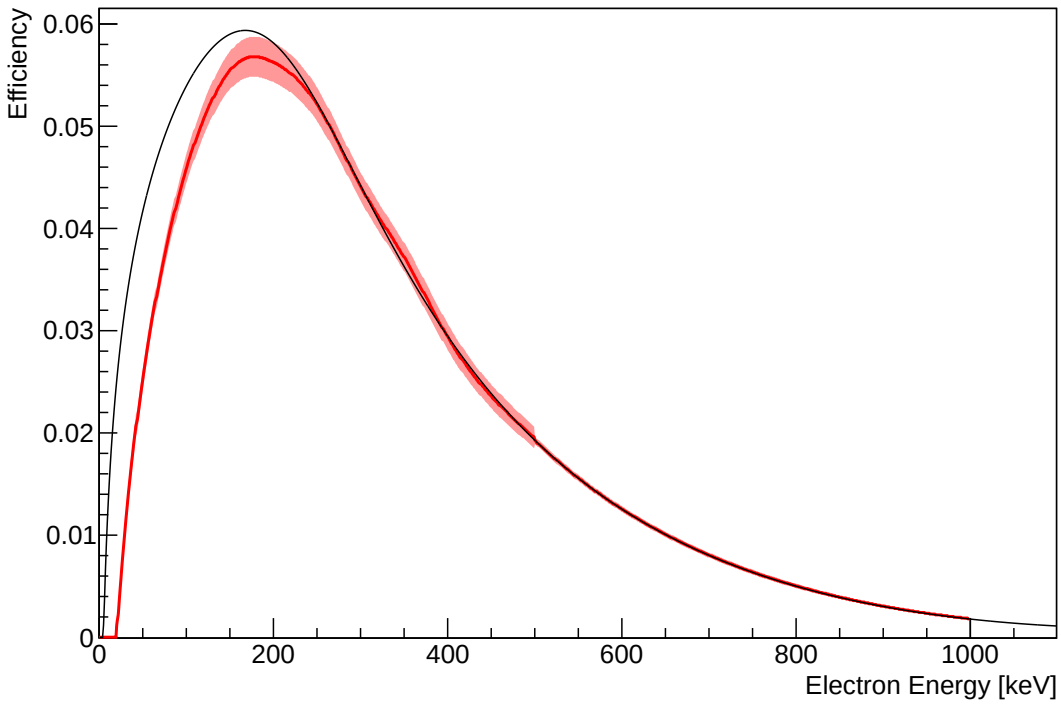

Figure 5.7: Scaling of electron efficiency curve to account for field change. Shown are the curves from calibration data (black) and the experimental curve (red) simulation scaled from 0 to 20 kV barrier with associated error.

The lowest energy K-shell electron sits at 35 keV and is sufficiently low in energy that this peak is dominated by the scattering background step and is also swamped by δ electrons.

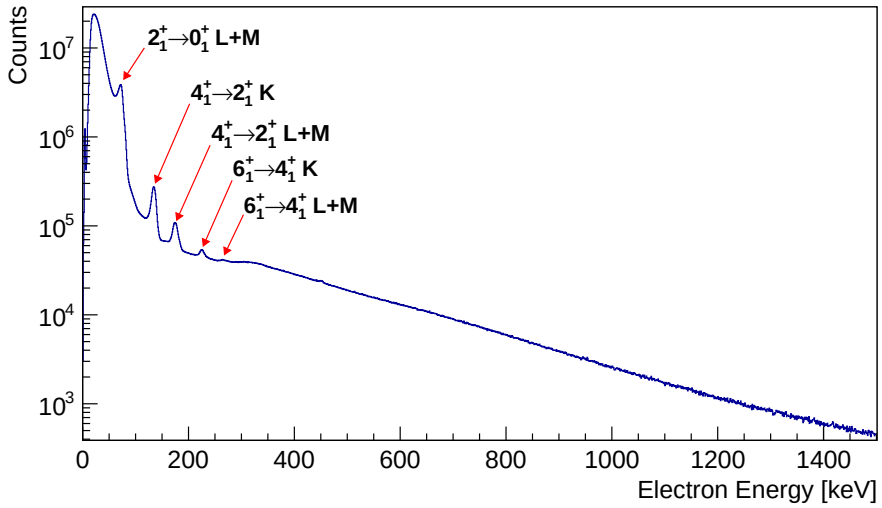

Figure 5.8: Raw electron spectrum from the preliminary run showing clear peaks for the ^{154}Sm yrast band transitions. An exponential tail is observed at high energies, see text for details.

At higher energies an abnormal distribution is seen. An exponential slope is observed, not in keeping with scatter from higher-energy electron peaks as seen from the ^{207}Bi calibration source (Figure 5.9). This distribution was shown to result from the presence

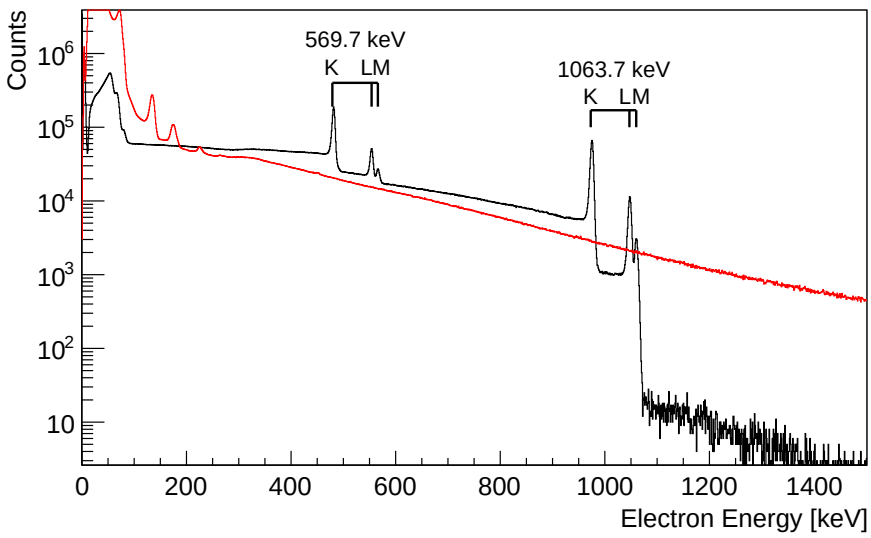

Figure 5.9: Raw electron spectrum from the preliminary run (red) against ^{207}Bi calibration data (black).

of β particles. Both β^+ and β^- emitted at the target position will be detected in SAGE identically to conversion electrons, with the exception that β^+ particles will be unhindered by the potential barrier. Coincident pairs of 511 keV γ rays were observed in JUROGAMII indicating the presence of β^+ particles either from radioactive decay in the target chamber or pair production from high-energy γ transitions, neither of which should be produced by the CoulEx reaction of ^{154}Sm.

Aluminium Contamination

It was determined that fusion evaporation on an aluminium backing to the first target was responsible for the large β background; Figure 5.10 shows production cross sections for the reaction. Amongst the products the β^+ emitters ^{34}Cl and ^{38}K were produced, which were confirmed in the γ spectrum.

The strength of cascades in the light products go predominately to the ground state through high-energy γ transitions (> 2 MeV) outside the region of interest. The light products ^{37,38}Ar, ^{37,40}K and ^{41}Ca were all produced in such an abundance that a few low-energy γ transitions in their cascades were observed even more strongly than those of samarium. Furthermore, the ^{41}Ca K-shell conversion electron of the 460 keV transition from the 3830 keV $15/2^+$ state can be seen in the raw electron spectra, despite a low Z resulting in small conversion coefficients. Performing γ coincidence gating on 168 keV, 1389 keV and 1607 keV coincident transitions produced a clear electron peak, as shown in Figure 5.11.

In the preliminary run, no electron peaks were visible for the transitions from the 0_2^+ and 2_2^+ states of interest in ^{154}Sm. Population of these was verified by detection of their γ-ray decays. Raw γ-ray spectra yield ambiguous results due to contamination. Gating on the 82 keV $2_1^+ \rightarrow 0_1^+$ ^{154}Sm γ ray yields a coincidence spectrum in which the 911 keV $2_2^+ \rightarrow 4_1^+$, 1096 keV $2_2^+ \rightarrow 2_1^+$ and 1017 keV $0_2^+ \rightarrow 2_1^+$ transitions are identifiable, as shown in Figure 5.12.

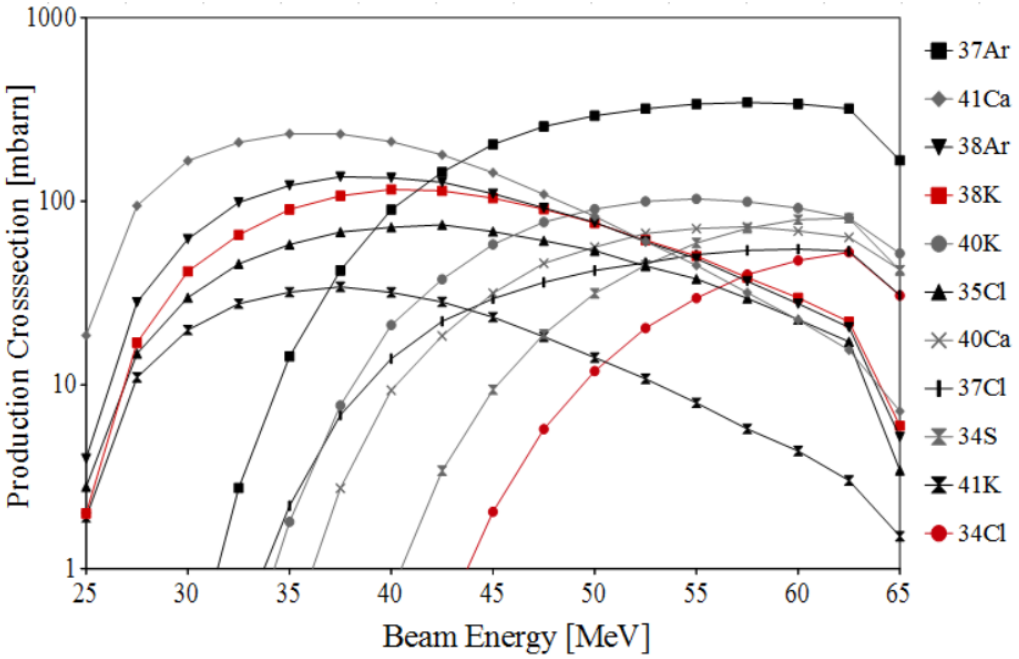

Figure 5.10: PACE4 [124] calculation results for fusion evaporation of ^{16}O beam impacting on ^{27}Al. Two β^+ emitters are highlighted in red.

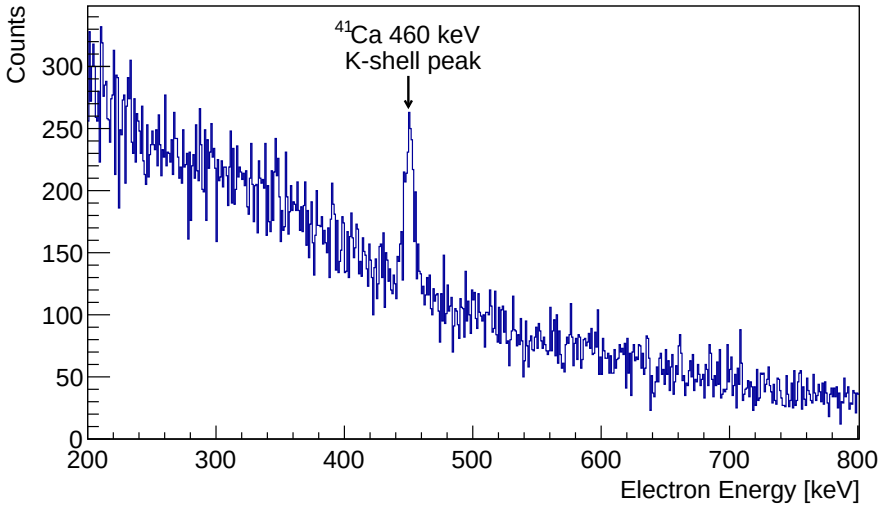

Figure 5.11: Conversion-electron peak from ^{41}Ca is clearly seen in this γ-gated electron spectrum. This spectrum is produced by gating on the coincident 168 keV, 1389 keV and 1607 keV γ rays from ^{41}Ca.

From this preliminary run it was established that the states of interest were being populated, but insufficiently. Furthermore, it was clear that experimental complications, which contribute to the high-energy electron background, would make observing the anticipated small electron peaks in a raw spectrum infeasible.

5.2.5 Revised Setup

The $E0$ transition of interest between $0_2^+ \rightarrow 0_1^+$ has no coincident γ transitions and appears only as a single SAGE event. From the preliminary run it was clear that such a weak transition would not be visible in the raw SAGE spectrum against the experimental

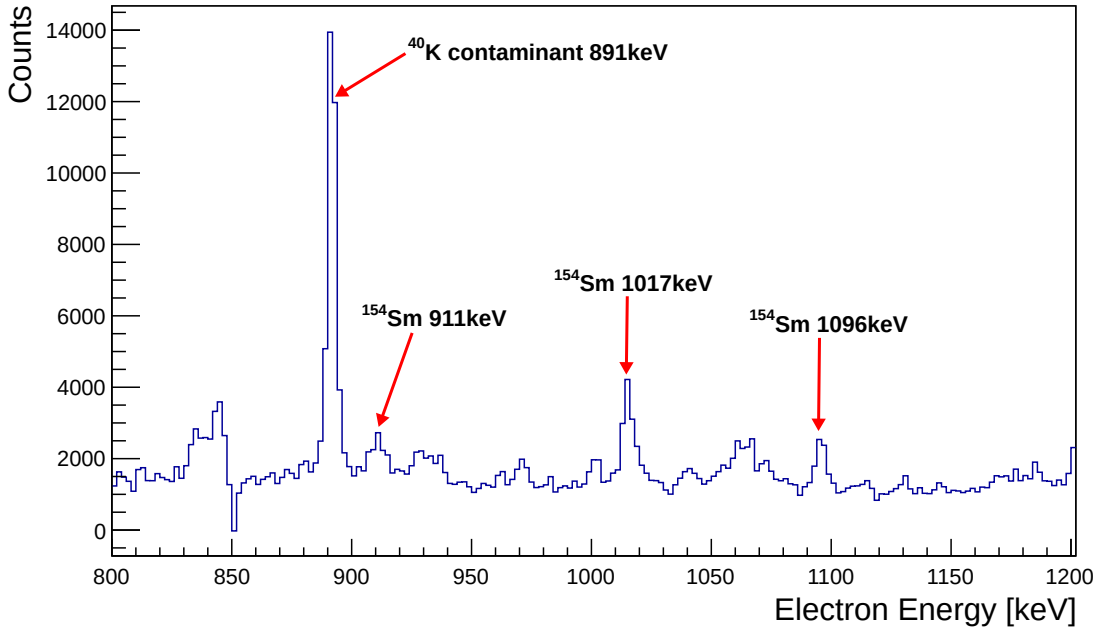

Figure 5.12: Transitions from the 0_2^+ band, gated on the energy of the 82 keV $2_1^+ \rightarrow 0_1^+$ ^{154}Sm transition. The gate contains some ^{40}K contamination.

noise. With no particle (beam/recoil) gate in the experiment and no beam signal there is no possible way to produce a clean spectrum for these events. It was decided to focus on $e^-\gamma$ events and hence the $2_2^+ \rightarrow 2_1^+$ transition which has the coincident $2_1^+ \rightarrow 0_1^+$ transition.

The beam current was increased to 20 pnA, which was at the limit for both target heating and data recording. In order to accommodate the increased data rate the DAQ was moved to a multiplicity fold two trigger, so only events in which 2 or more detectors/elements trigger within 200 ns of each other were recorded to disk. This setting reduced the data rate to a level which the disk write speed could accommodate. This trigger condition limits the available data to $e^-\gamma$, $\gamma\gamma$ and e^-e^- coincidences (as well as higher multiplicities). No true raw spectra are available for individual detectors, they can only be inferred. There is of course no requirement in the data stream for the coincidence to be genuine, thus this must be determined offline. Indeed, due to the high data rate of the experiment, false coincidences are found to be abundant, as will be shown.

In order to maximise the population of the states-of-interest, the energy of the beam was increased to 65 MeV. This corresponds to a centre of mass energy of 58.88 MeV, which is sufficiently close to the predicted barrier height that a significant nuclear contribution to the reaction is anticipated. Thus a pure CoulEx calculation is not valid and optical model calculations would be needed. However, the experiment is insensitive to the means of excitation as we do not attempt to extract information from the population process. (Hence such calculations are beyond our requirements, simple CoulEx calculations are sufficient to estimate the magnitude of the population increase.) Using CLX an increased cross section for the 2_2^+ state of $\sigma_{g\rightarrow 2_2^+}$ =7.2 mb for pure electromagnetic excitation is calculated.

The target wheel was rotated to use a target of the same specification with no backing, produced by Daresbury Laboratory, UK. The initial target had been one available at JYFL used because of concerns of oxidation of the Daresbury targets. The aluminium backing of the JYFL target was not identified until after the experiment. Data from the aluminium backed first target were not used in further analysis due to the very large β background and will not be included beyond this point.

5.3 Experimental Results

Beam data were collected for 2.7 days at beam energy 65 MeV and beam current between 10 and 20 pnA. A multiplicity two trigger was in effect for the data written to disk. The data were sorted into e^{-}-γ-*time* and γ-γ-*time* data cubes in the manner described in Section 4.4.4. Data selection to discard events associated with scattering in the SAGE silicon detector, as described in Section 3.2.2, was applied, as were vetoes by the BGO Compton suppression shields in JUROGAMII.

First, discussion of the content of the data will be presented, what states were populated, which decays can be observed and what background is present. This is predominantly achieved using $\gamma\gamma$ data in conjunction with data tables and level schemes. Electron data are shown in the context of background identification but is less useful when identifying state population. Discussion of the gating and subtractions used to tackle the background, particularly in electron data where there is still a β-decay background problem, will be discussed in Section 6.1. Although background subtraction and identification of states are fundamentally linked, indeed it will be shown that low intensity transition from some states can only be seen following background removal. The order of presentation is intended to guide the reader through what was actually an iterative process. Following these discussions a review of the conversion-electron measurements and analysis will be presented.

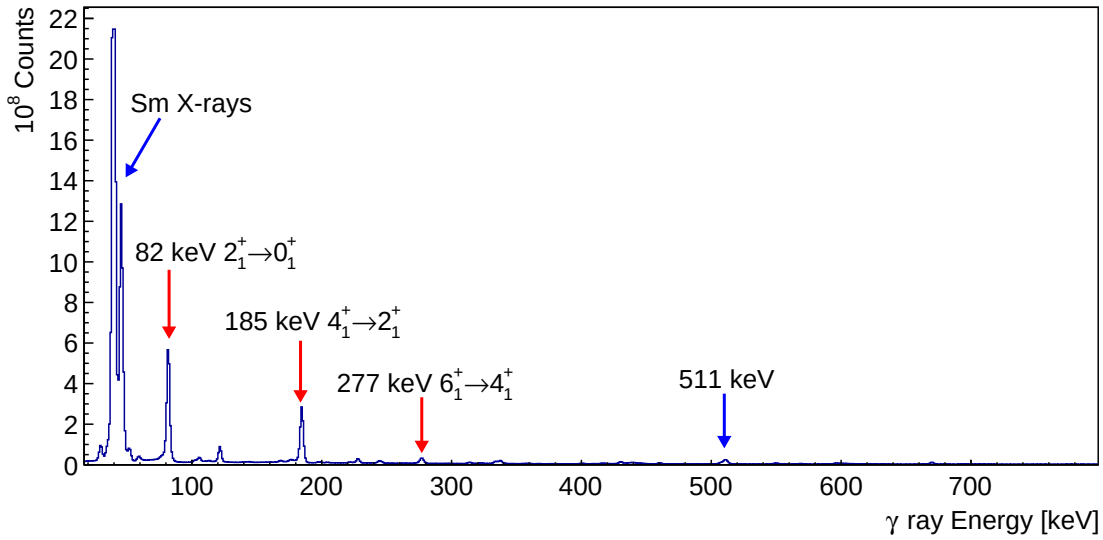

Figure 5.13: Projection of γ rays from the raw $\gamma\gamma$ cube. The highest intensity ^{154}Sm γ rays are highlighted as well as the 511 keV annihilation peak.

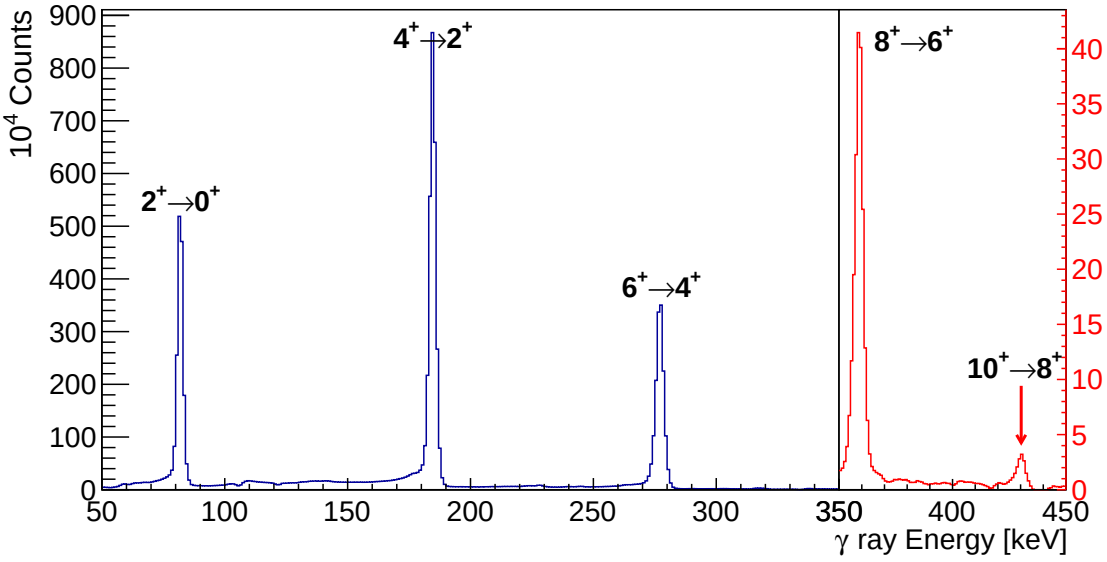

Figure 5.14: The first five ^{154}Sm yrast γ rays. The spectrum is a composite image of background subtracted $\gamma\gamma$-spectra gated on 82 keV $2_1^+ \rightarrow 0_1^+$, 185 keV $4_1^+ \rightarrow 2_1^+$ and 277 keV $6_1^+ \rightarrow 4_1^+$ transitions. The right side of the spectrum is on an increased vertical scale showing the weaker observed 359 keV $8_1^+ \rightarrow 6_1^+$ and 430 keV $10_1^+ \rightarrow 8_1^+$ transitions.

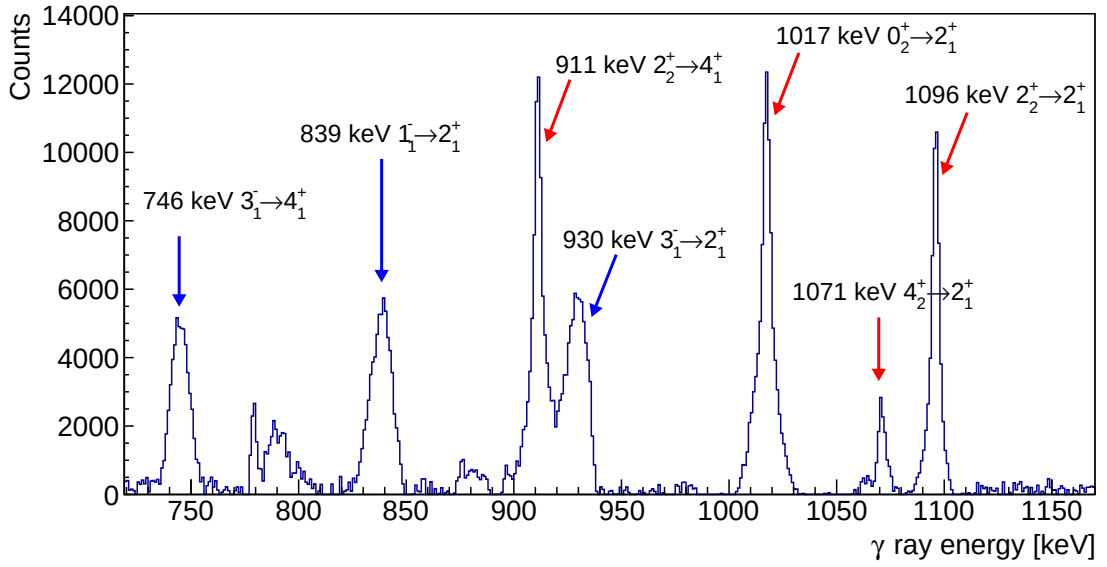

Figure 5.15: High-energy ^{154}Sm γ rays, in coincidence with $2_1^+ \rightarrow 0_1^+$ γ ray. This spectrum is produced following background subtraction.

5.3.1 ^{154}Sm State Population

Population of the yrast band of ^{154}Sm up to the 8^+ state at 902.8 keV can be identified in the raw projection of the $\gamma\gamma$-data (Figure 5.13). With careful gating on $\gamma\gamma$-data, a transition from the yrast 10^+ state at 1333.0 keV can be identified, as shown in Figure 5.14.

The additional beam energy increases population of the first-excited even-parity band states of interest. The γ decays from these states are seen in Figure 5.15, which shows $\gamma\gamma$-data gated on the 82.0 keV $2_1^+ \rightarrow 0_1^+$ transition. Present are the 1017.2 keV $0_2^+ \rightarrow 2_1^+$

transition from the 1099.3 keV 0_2^+ state, 911.0 keV $2_2^+ \rightarrow 4_1^+$ and 1095.9 keV $2_2^+ \rightarrow 2_1^+$ transitions from the 1177.8 keV 2_2^+ state and the 1070.7 keV $4_2^+ \rightarrow 4_1^+$ transition from the 1337.6 keV 4_2^+ state. The 794.9 keV $4_2^+ \rightarrow 6_1^+$ and 1255.6 keV $4_2^+ \rightarrow 2_1^+$ transitions from the 1337.6 keV 4_2^+ state are observed but not shown in the figure.

Also seen in Figure 5.15 are transitions from negative-parity band states. The 839.4 keV $1_1^- \rightarrow 2_1^+$ transition from the 921.4 keV 1_1^- state, 745.5 keV $3_1^- \rightarrow 4_1^+$ and 930.4 keV $3_1^- \rightarrow 2_1^+$ transitions from the 1012.4 keV 3_1^- state are shown. Further gating on the 184.8 keV $4_1^+ \rightarrow 2_1^+$ and 277.3 keV $4_1^+ \rightarrow 2_1^+$ transitions yield transitions from the 5_1^- and 7_1^- states at 1181.26 and 1430.9 keV respectively. Using the data-table lifetime of 21 fs for the 1_1^- state [127], matrix elements for population of the state were added to the earlier CoulEx calculation. From the calculated CoulEx cross section, relative population of the 1_1^- state to the 0_2^+ state of 0.38 is predicted. However, from the γ rays shown in Figure 5.15, assuming no feeding from higher states and accounting for relative efficiencies and branching ratios, an experimentally measured population ratio $1_1^- : 0_2^+$ of 0.95 was found. This enhanced population of the negative-parity band is perhaps a signature of the fact that the beam energy is in the region of unsafe CoulEx where the nuclear force comes into play in the reaction. The transitions from this negative-parity band are exclusively of E1 type and have small electron conversion coefficients, these are not negligible however and must be accounted for where there is overlap with other states.

Population of the 1440.0 keV 2_4^+ band head was observed from the 1173.1 keV $2_4^+ \rightarrow 4_1^+$ and 1358.0 keV $4_4^+ \rightarrow 2_1^+$ transitions. The 3^+ and 4^+ states in this band were also tentatively observed. The energies of the transitions from this band are sufficiently high that they are of no interest to this work, being well beyond the limit that is to be tested for the effectiveness of SAGE.

A negligible population was seen for the 0_3^+ and 2_3^+ levels at 1202.44 and 1286.3 keV, this is to be expected as seen from other work [114]. These states will not be investigated further in this work. A complete set of ^{154}Sm levels and γ transitions that can be observed in the data set is indicated in the reduced level scheme in Figure 5.16.

5.3.2 ^{152}Sm Contaminant

The enriched samarium target still included $\lesssim 1\,\%$ of ^{152}Sm, the exact fraction is unknown. This is sufficiently large that a measurable quantity of γ rays and electrons resulting from the excitation of ^{152}Sm were observed, shown in Figure 5.17.

As a result, a parallel analysis of ^{152}Sm can be performed to provide a direct source of comparison with the ^{154}Sm measurements. Owing to a significantly smaller amount of data, only a small fraction of the ^{152}Sm level scheme can be discerned. The 0_2^+ and 2_2^+ levels sit significantly lower in energy for ^{152}Sm at 684.7 and 810.5 keV respectively, as a result significant population of each is observed.

The 121.8 keV $2_1^+ \rightarrow 0_1^+$ and 244.7 keV $4_1^+ \rightarrow 2_1^+$ transitions from the 121.8 keV 2_1^+ and 366.5 keV 4_1^+ levels are both clearly visible in the raw $\gamma\gamma$ projection. The 340.4 keV $6_1^+ \rightarrow 4_1^+$ transition from the 684.7 keV 6_1^+ state is not visible in the raw projection due to a large ^{166}Yb contaminant peak at the same energy, higher lying transitions cannot be discerned from background. Gating on the $2_1^+ \rightarrow 0_1^+$ and $4_1^+ \rightarrow 2_1^+$ transitions yields the

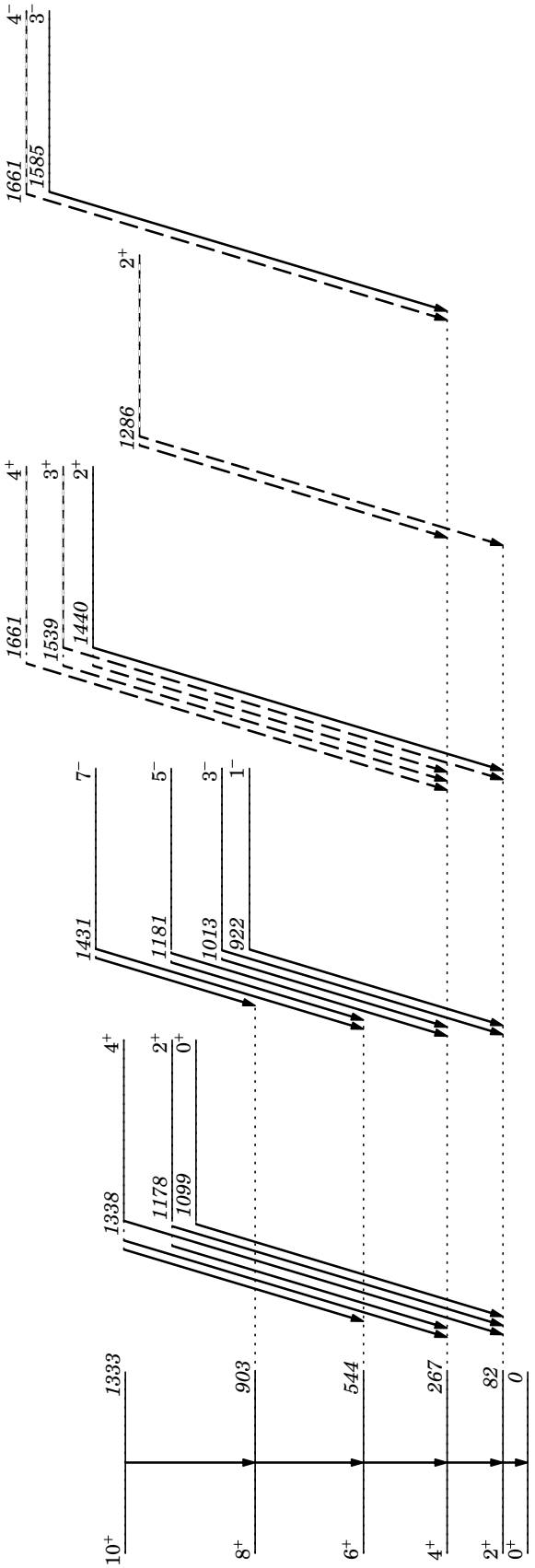

Figure 5.16: ^{154}Sm level scheme showing the levels for which population was observed and the γ-ray transitions that can be observed in $\gamma\gamma$ data. Energies are in keV. Original level scheme data obtained from Reference [127].

spectrum shown in Figure 5.18. The 340.4 keV $6_1^+ \rightarrow 4_1^+$, 562.9 keV $0_2^+ \rightarrow 2_1^+$, 444.0 keV $2_2^+ \rightarrow 4_1^+$ and 688.7 keV $2_2^+ \rightarrow 2_1^+$ transitions are clearly identifiable. The resolution of the spectra is sufficient that the 125.7 keV $2_2^+ \rightarrow 0_2^+$ and 121.8 keV $2_1^+ \rightarrow 0_1^+$ γ-ray transitions would be separable. However, the $2_2^+ \rightarrow 0_2^+$ transition, which would allow observation of the 684.9 keV $0_2^+ \rightarrow 0_1^+$ E0 electron transition, is not observed as the $2_2^+ \rightarrow 0_2^+$ transition takes only 1.1% of the decay strength from the 2_2^+ state.

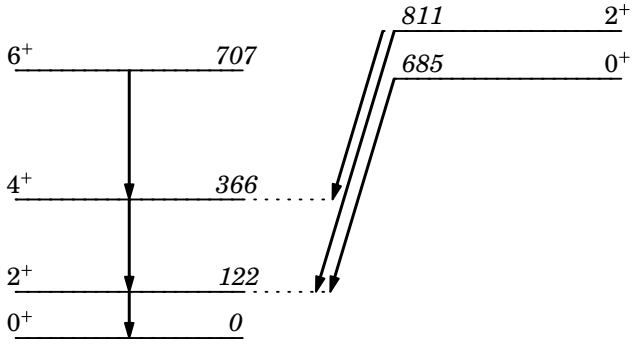

Figure 5.17: ^{152}Sm level scheme showing the levels for which population was observed and the γ transitions that can be seen in $\gamma\gamma$ data. Energies are in keV. Original level scheme data obtained from Reference [127].

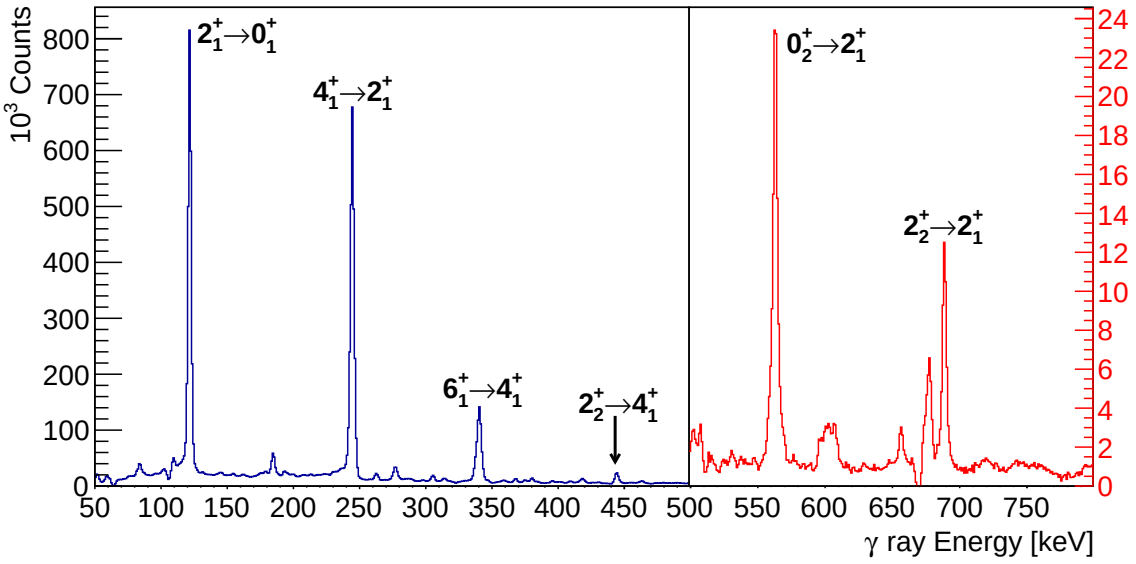

Figure 5.18: Composite ^{152}Sm γ-ray spectrum from $\gamma\gamma$ gated on $2_1^+ \rightarrow 0_1^+$ and $4_1^+ \rightarrow 2_1^+$ transitions, background subtracted. The first three yrast-band transitions are seen as well as three transitions from the first excited positive-parity band. The right side of the spectrum is on an increased vertical scale.

5.3.3 Sub-Barrier Fusion

Figure 5.19 shows the electron projection of the $e^-\gamma$ data cube. In addition to the β tail, that is still present, there are numerous extra peaks compared with the raw electron spectrum from the preliminary data, in which only ^{154}Sm electron peaks were observed. The additional electron peaks come from ^{166,167}Yb isotopes. With a beam energy of 65 MeV to boost 2_2^+ state population in ^{154}Sm, there is sufficient energy for a significant sub-barrier fusion cross section. ^{166,167}Yb are produced through the 4n and 3n fusion evaporation channels from ^{16}O+^{154}Sm (in which the compound nucleus is ^{170}Yb).

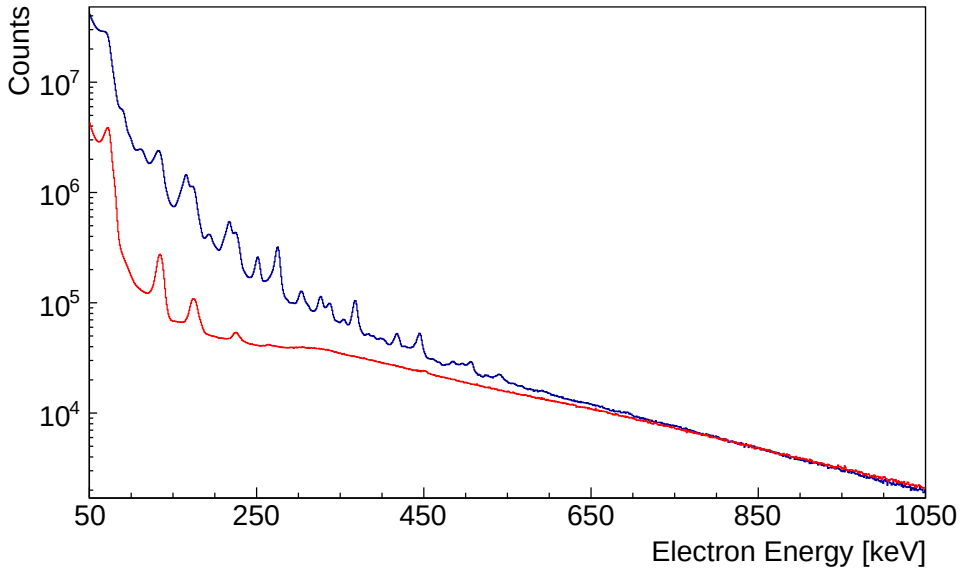

Figure 5.19: Electron projection of the $e^{-}\gamma$ data cube. Preliminary run electron data are shown beneath in red.

The two ytterbium isotopes are produced with a maximum excitation of 40 MeV and maximum spin of 80 $\hbar$, although the actual production state in each case will have values significantly less than these. In both cases, decays to the ground state occur by multi-step processes through many intermediate levels. The important result of this high event multiplicity is that the experimental trigger actually preferentially selects the ytterbium events. The trigger used requires the detection of two emitted particles to record an event. Assuming a uniform efficiency for particle detection ε, then the trigger probability is given by:

$$P_{trig}(N;2) = 1 - \left[N(\varepsilon(1-\varepsilon)^{N-1}) + (1-\varepsilon)^{N}\right] , \tag{5.16}$$

where N is the multiplicity of the event. For a realistic $\varepsilon = 0.05$, one finds $P(2) = 0.0025$ and $P(5) = 0.0226$, which is nine times larger. For a general m fold trigger, the probability is given by:

$$P_{trig}(N,m) = 1 - \sum_{i=0}^{m-1} \frac{N!}{i!(N-i)!} \cdot \varepsilon^{i} \cdot (1-\varepsilon)^{N-i} . \tag{5.17}$$

The additional protons in ytterbium mean it has larger conversion coefficients than samarium further increasing the relative presence of ytterbium in the $e^{-}\gamma$ data.

The higher-lying states in ^{166}Yb strongly feed the yrast band. As a result, the yrast band is strongly observable up to the 2779.5 keV 14^{+}_{1} state, as shown in Figure 5.20. The feeding of the yrast band, from the initially fragmented strength of fusion-evaporation population, produce sufficient conversion electrons that the yrast transitions may be used as another source of normalisation for the conversion-coefficient measurements. The strength through the non-yrast states is sufficiently fragmented to be of little benefit or interest, a few exceptions are highlighted in Section 6.4.2.

The even-odd nucleus ^{167}Yb has a significantly fragmented decay scheme, the levels observable through gating of the $\gamma\gamma$ data are shown in Figure 5.21. Population of states is

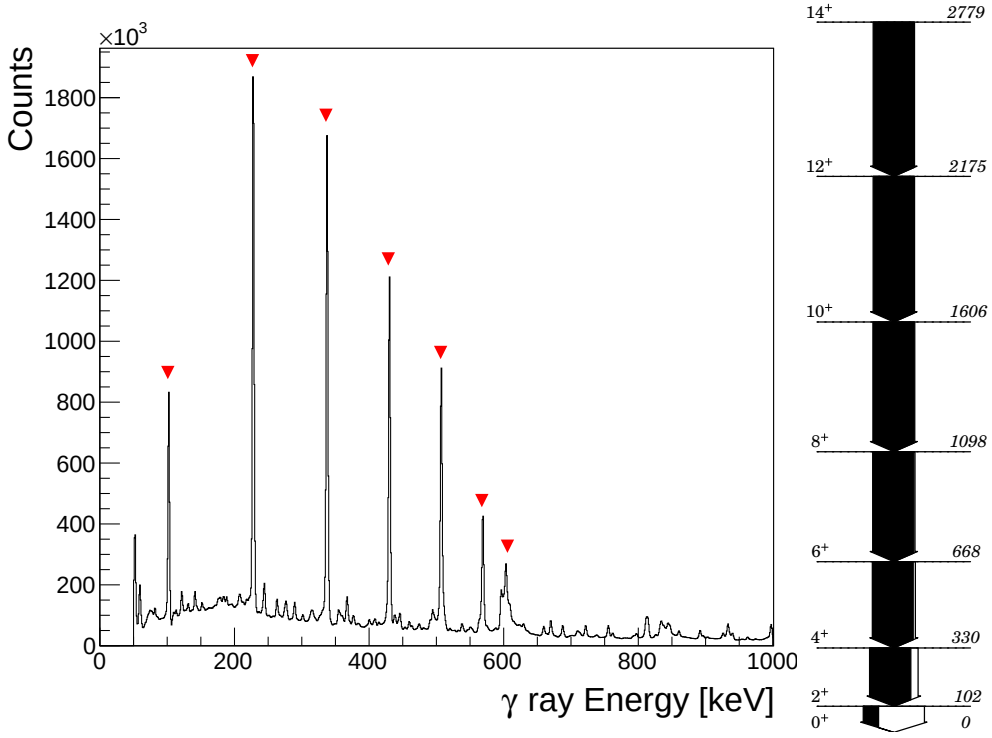

Figure 5.20: ^{166}Yb yrast spectrum from gated $\gamma\gamma$ data and the corresponding section of the ^{166}Yb level scheme. Energies are in keV

observed across bands up to energies of 4 MeV, an example of a band observable in the data is shown in Figure 5.22. These bands decay predominately down by in-band transitions, inter-band transitions are more frequent at lower energies and a large amount of mixing is present near the ground state. The division of strength through many transitions makes ^{167}Yb unprofitable for normalisation, however in Section 6.3 further investigation of ^{167}Yb contamination is conducted to use SAGE to confirm some uncertain spin-parity assignments.

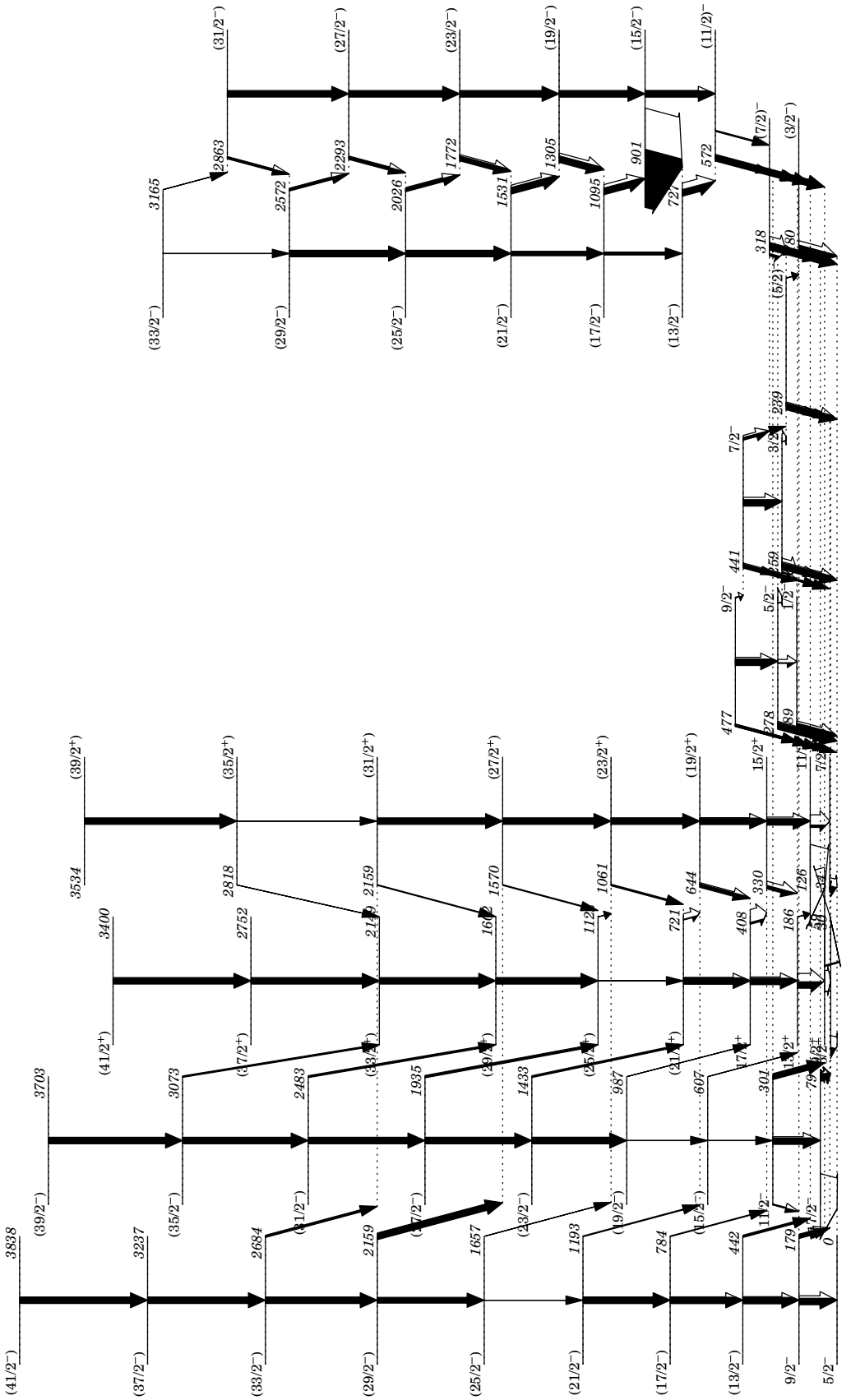

Figure 5.21: ^{167}Yb observable levels and γ transitions from $\gamma\gamma$ data. Expanded views of portions of this level scheme are shown in Section 6.3. Full level scheme from Reference [78] and original assignments taken from Reference [127].

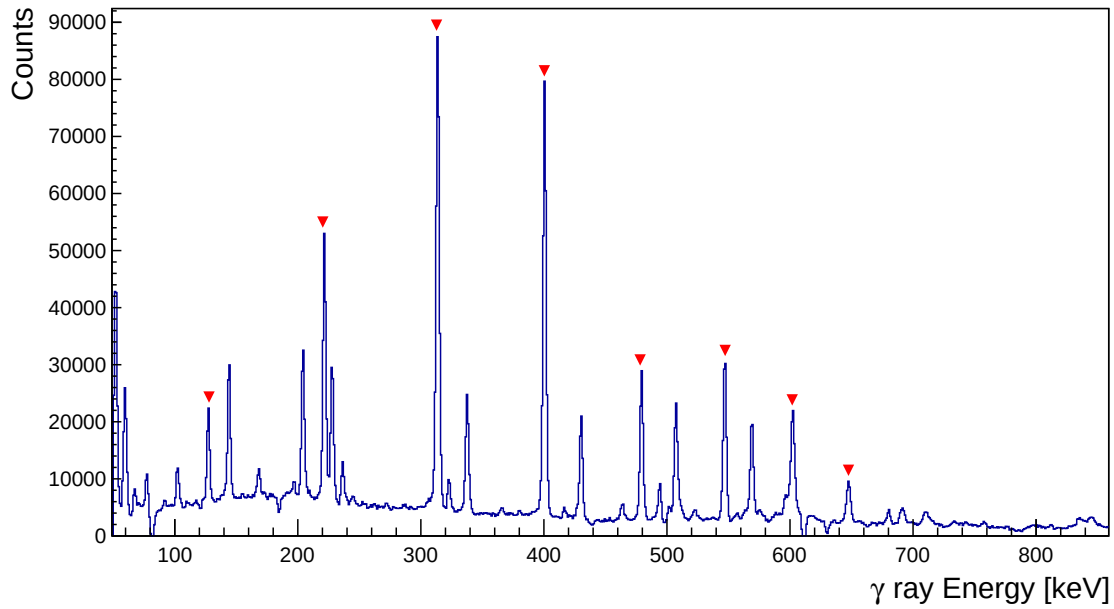

Figure 5.22: ^{167}Yb spectrum gated on transitions in the positive-parity band below the 3400 keV $(41/2^+)$ state. Peaks corresponding to the in-band transitions are marked.

5.3.4 Target Decay

Ytterbium

Both isotopes of ytterbium are radioactive with half-lives shorter than the experiment run time. The decay chain to stable ^{166,167}Er is shown in Figure 5.23. From the relative half-lives it can be seen that the ^{167}Yb→^{167}Tm decay rate will quickly equilibrate with the production rate of ^{167}Yb, the ^{167}Tm→^{167}Er decay will be small and a build-up of ^{167}Tm will occur. Conversely the ^{166}Yb→^{166}Tm decay rate will not equilibrate due to ^{166}Yb's longer half-life and the ^{166}Tm→^{166}Er decay will be of similar rate with little build-up of ^{166}Tm. Calculated decay rates and build up of the daughter nuclei is shown in Figure 5.24. The decay cascades are low-multiplicity events and as such will be less prevalent in the multiplicity triggered beam data, as described in Equation (5.16). Four hours of decay data were collected immediately following the experimental beam time and the expected γ transitions following ytterbium decays were clearly observed.[7]

Of particular importance are the β branches of ^{166}Tm and ^{167}Yb, as the β background is a serious point of concern for the electron measurement. The endpoint energy of the ^{167}Yb decay is 639 keV, so while it may contribute to the background at lower energies it is of no concern in the region of interest. The ^{166}Tm β-endpoint energy is sufficiently high at 1935 keV. Figure 5.25 shows an electron spectrum from the decaying target; the conversion-electron peaks from the ^{166}Tm decay are significantly smaller than expected relative to the β background (after accounting for detection efficiency), indicating a significant additional β contribution.[8]

[7] The first ninety minutes used the same multiplicity trigger as the experiment and raw data were collected following this.

[8] The shape of the β background was found to be dominated by the SAGE efficiency function.

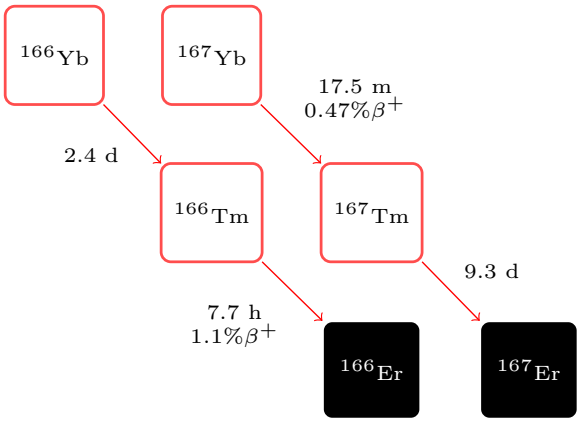

Figure 5.23: Decay chain for the fusion-evaporation products ^{166,167}Yb, $t_{1/2}$ and β branches are shown.

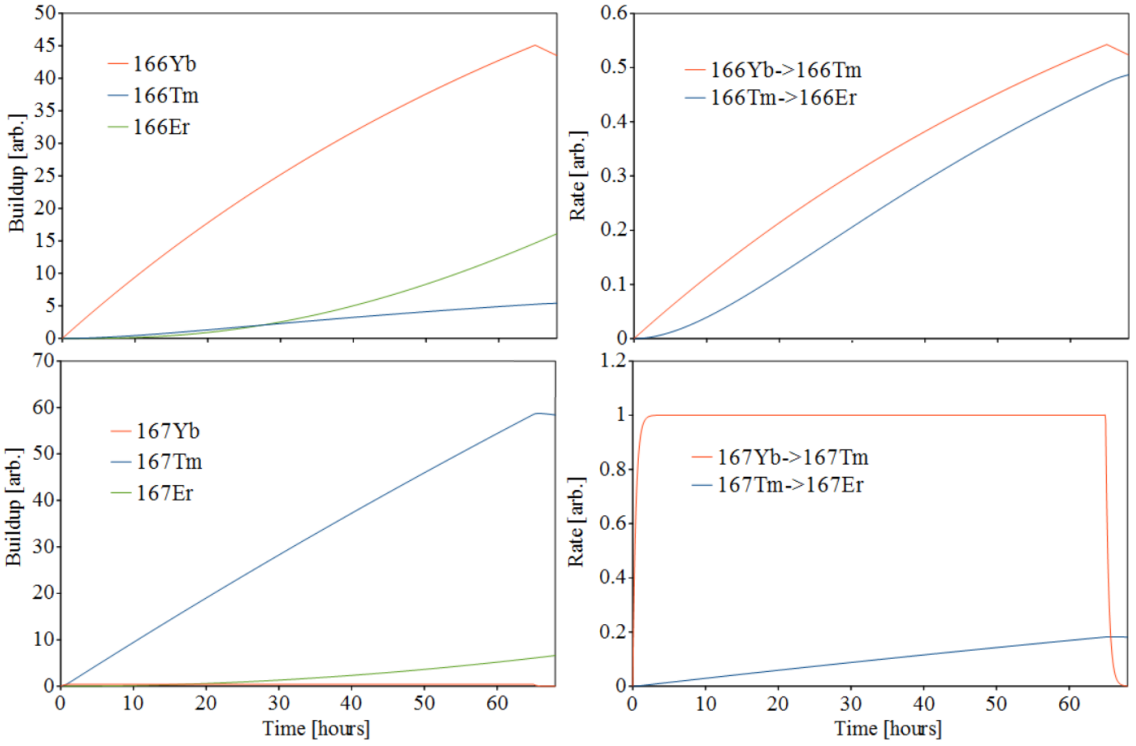

Figure 5.24: Build-up and decay rates for ^{166,167}Yb isotopes and decay products assuming constant beam current for 65 hours. Rates are relative to Yb fusion evaporation production rate.

Light β Emitters

The light products from the fusion-evaporation reaction of ^{16}O+^{27}Al, listed in Figure 5.10, remain present in the experimental data following the change of target, with a heavily-reduced relative intensity. The continued presence is explained by a small beam halo clipping the aluminium target frame. Although only a small fraction of the beam intensity impinges on the frame, the reaction benefits from a large amount of target material relative to the samarium target foil. Figure 5.10 shows the cross section as a function of energy as the beam particles will be fully stopped in the frame and have the entire stopping length ($\sim$ 46 μm) in which to interact. The light products are predominantly observed more

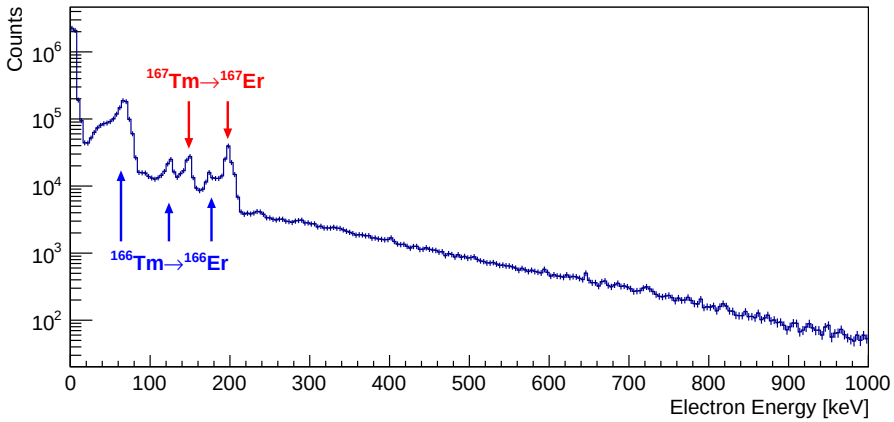

Figure 5.25: Raw electron spectrum of 4 hours of target decay data. Conversion-electron peaks expected from the decay chains of ^{166,167}Yb are highlighted.

weakly than the samarium in $\gamma\gamma$ data and are negligible in $e^-\gamma$. However the β^+ emitters ^{34}Cl and ^{38}K are of concern.

Gating on the 511 keV positron annihilation γ rays in the target decay spectrum produces a coincident spectrum of the β^+ decaying nuclei, shown in Figure 5.27. The most intense γ rays associated with the β^+ decay branches of ^{166}Tm and ^{167}Yb, 80.6 keV and 113.3 keV respectively, are barely present. The γ rays 1176.7, 2127.5 and 3304.0 keV from the β^+ decay of the 3^+ isomer in ^{34}Cl, along with 2167.5 keV γ ray from the β^+ decay of ^{38}K, are observed to be the strongest peaks in spectrum (aside from the other 511 keV annihilation γ ray). The origin of these peaks is confirmed by fitting their decay lifetimes, Figure 5.28, yielding 32.0 minutes for the ^{34}Cl isomer (data table value 31.99 m) and 7.9 minutes for ^{38}K (data table value 7.636 m). Furthermore both a 0^+ isomer in ^{38}K and the ground state of ^{34}Cl β decay directly to the ground states of their respective daughters with half-lives of 924.0 ms and 1.5266 s, their contribution cannot be determined from the decay data.

Also present in the $\gamma\gamma$ decay data were coincident 2754 and 1368 keV γ rays from the β^- emitter ^{24}Na, the source of which is unknown but is only present in small quantities. A 1461 keV line from the known lab background ^{40}K was also visible.

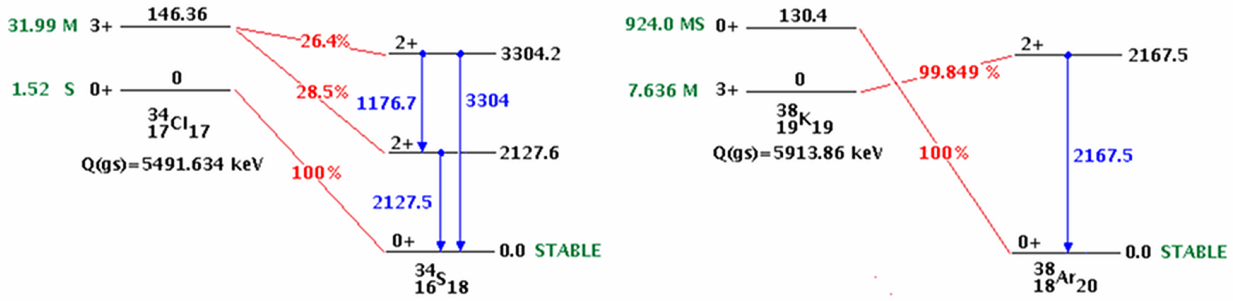

Figure 5.26: Predominant β decay branches and associated γ rays for ^{34}Cl and ^{38}K ground state and isomers. The energies of the daughter nuclei are not relatively aligned.

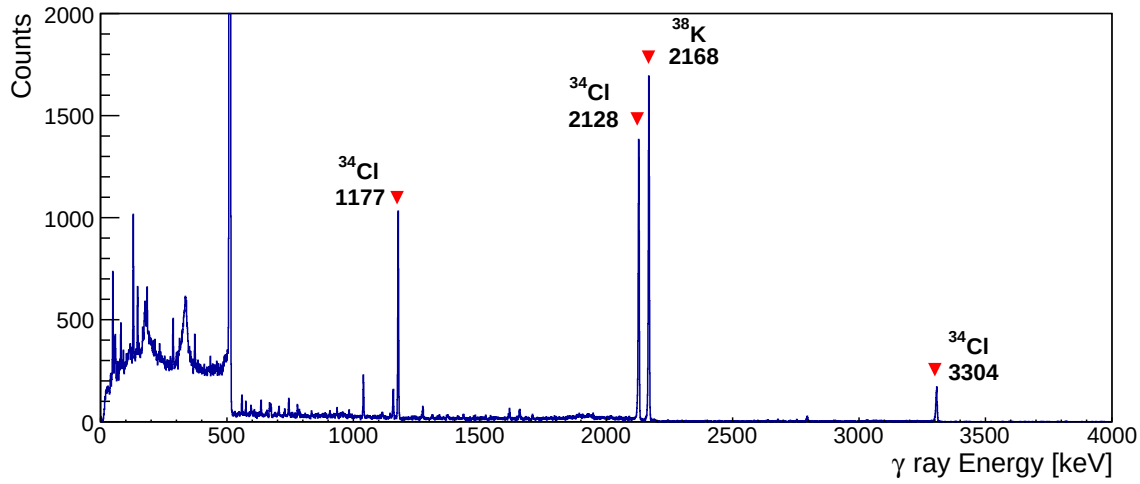

Figure 5.27: Decay γ spectrum, 511 keV coincidence gated.^{34}Cl and ^{38}K decay γ rays are indicated.

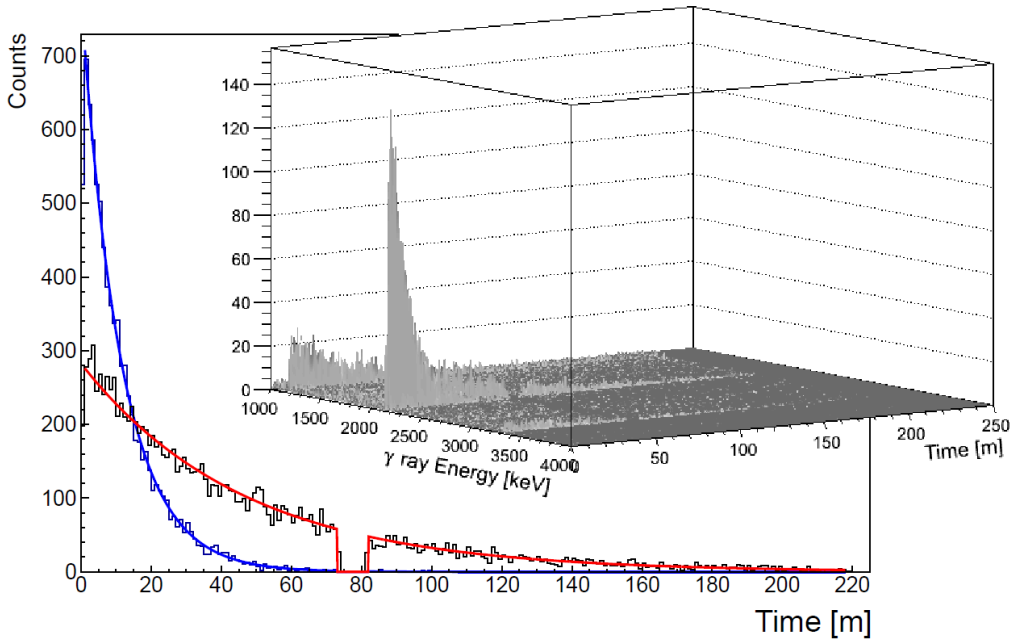

Figure 5.28: Decay γ spectrum with time, 511 keV coincidence gated. γ rays from ^{34}Cl and ^{38}K are confirmed with lifetime fits.

5.3.5 Experimental Summary

In summary, considerable population of the states of interest in ^{154}Sm was observed as well as analogous states in the ^{152}Sm target contaminant. Additionally a large amount of ^{166,167}Yb were produced, the electron conversions from which may also be studied. The high-energy electron transitions of interest were not observed and remain hindered by a large β background in SAGE. The majority of the β background can be confidently attributed to result from activation of the target frame producing ^{34}Cl and ^{38}K, both of which decay 100% by β^+ emission with endpoint energies >1 MeV. The precise contribution from decays from the ground state or isomer of each cannot be established.

6

^{154}Sm Analysis and Results

In this analysis, methods of background suppression and subtraction are applied, as discussed in Section 4.4.4, in order to produce clean data sets for fitting. Fitting is then performed on the strong yrast transitions, these easily measured and well-known E2 transitions allow normalisation of the conversion coefficient calculations. The chosen confidence limit calculations, used where there is less data, will be explained and the effectiveness when applied to non-yrast E2 transitions demonstrated. Following on from this the precision of the method will be shown on known E0 transitions, before finally calculating an upper limit measurement for the target E0 transition in ^{154}Sm.

6.1 Background Subtraction

From the preliminary data it was established there is a need to clean raw spectra using coincidence measurements and additional information to remove background. Firstly, a coincidence timing gate is placed on both data cubes ($e\gamma t$ and $\gamma\gamma t$) collapsing each cube to a matrix, and then a γ-gate is placed on the resultant matrix to produce a final spectra. Identical γ-gates are placed on both $e\gamma$ and $\gamma\gamma$ data. Following each gate a background subtraction is performed as detailed in Section 4.4.4. An example of the effectiveness of the subtraction is given in Figure 6.1.

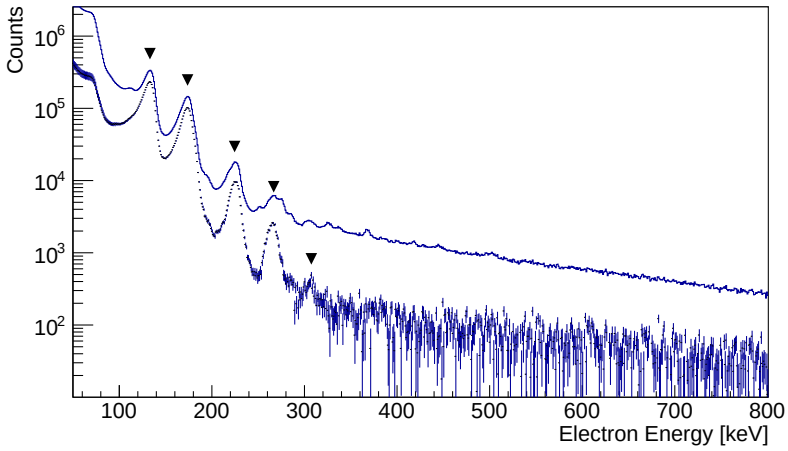

Figure 6.1: Electron spectrum from $e\gamma t$ data cube gated on prompt time (170 ns gate) and ^{154}Sm $2_1^+ \rightarrow 0_1^+$ 82 keV γ-ray transition. Shown before (top) and after (bottom) background subtraction. Markers indicate ^{154}Sm electron peaks.

6.1.1 Time Gate

The time gate is intended to focus on only genuine coincidence events. It is understood that some false coincidences fall within the gate time. The time background subtraction is designed to remove these counts, and the nature of false coincidences in the experiment must be understood in order to understand the importance of the subtraction. A false coincidence is any count in our $\gamma\gamma$ or $e\gamma$ matrix in which the two data did not originate from the same physical process. The cause of this is that one datum or both of the data are from an intense process in the experiment and so the probability of it randomly occurring alongside a different process is high. False coincidences should in fact simply be a reflection of the raw singles spectrum, however due to the multiplicity-two trigger used in the experiment, this information is lost to us and must be inferred. The strongest examples of these intense processes are X-rays and δ electrons.

X-Rays

Every beam pulse produces X-rays and δ electrons from the electromagnetic interaction with the target atoms independent of any nuclear process. In addition to the beam interaction, X-rays also accompany every internal conversion or electron capture and can even be produced by the ionisation of β particles. With the attenuation plates removed

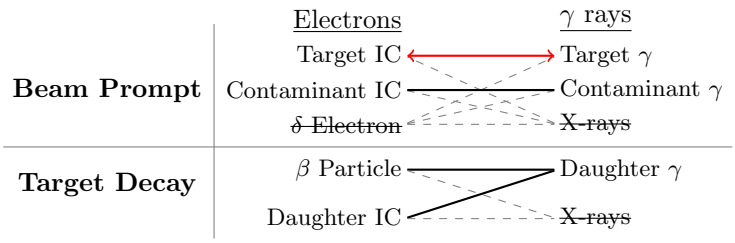

Figure 6.2: This map shows all genuine $e^{-}\gamma$ coincides events. The line in red represents the events of interest and the dashed lines indicate those suppressed by the threshold discussed in the text.

from JUROGAMII, to increase detection efficiency at low energy for the ^{154}Sm $2_1^+ \rightarrow 0_1^+$ γ transition, X-rays account for $\frac{2}{3}$ of all 'γ rays' (both random and genuine) in the $e\gamma t$ data cube, see Figure 5.13. Shown in Figure 6.3 is the effect on the timing spectrum of placing a 50 keV threshold on both electron and γ energies to suppress X-rays and δ electrons. From the figure it is clear that both of these processes contribute more to random coincidences than to the genuine coincidence peak. The removal of these events notably improves the background fraction in the timing gate, making separation of genuine events using timing data more tenable. Because each of these processes are at the bottom of the energy range, a threshold is sufficient to suppress them (one need not be concerned with scatter contributions). The thresholds also suppress events which are genuine coincidences but not of interest, as shown in Figure 6.2.

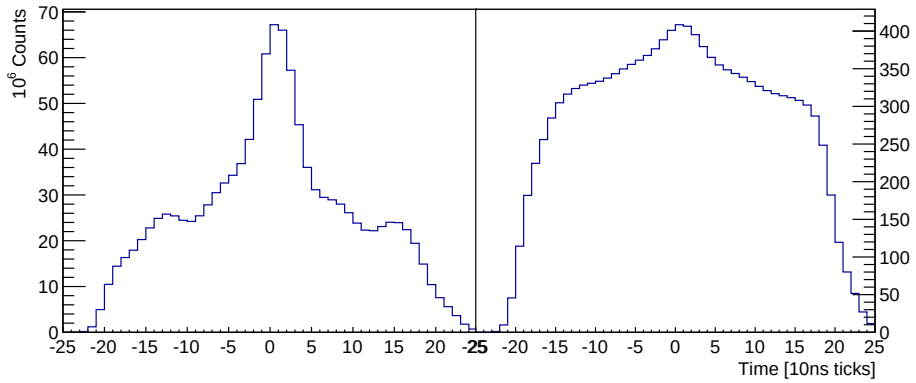

Figure 6.3: γ electron coincidence time with (left) and without (right) application of 50 keV thresholds on both electron and γ rays to suppress the large flux of X-rays and δ electrons.

Beta Particles

In the previous chapter it was established that the main sources of the β particles obscuring the high energy electron measurement were ^{34}Cl and ^{38}K. The decay of which are low multiplicity events accompanied by one, two or zero γ rays. As a result, it was deduced that their presence in γ gated electron spectra are mainly the result of false coincidence and not contamination of the γ gate by an identical energy γ transition or Compton background. Figure 6.4 serves to illustrated this point and the importance of time subtraction for β background suppression.

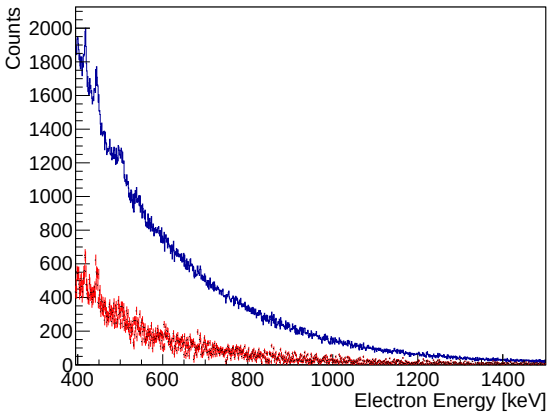

Figure 6.4: Effect of time subtraction on β background. An electron spectra time gated and γ gated on ^{154}Sm $2_1^+ \rightarrow 0_1^+$ is shown with no subtraction (blue) and with time randoms subtracted (red).

Gating Gamma Transition

It is crucial to acknowledge that the γ-ray transition on which one gates may also be the high intensity process producing false coincidence. This is the very situation faced with ^{154}Sm. The 82 keV $2_1^+ \rightarrow 0_1^+$ in ^{154}Sm on which gating must be done in order to perform the target measurement is a poor choice of gating transition.[1] In addition to the major deficiency that the transition is 83% electron converted, it is also massively weighted towards multiplicity one events. The cross section for direct population of the 2_1^+ state resulting in a multiplicity one event of just the $2_1^+ \rightarrow 0_1^+$ transition is the largest

[1] This is not a choice, we are forced to use this transition by the aim of the experiment.

of any process in the experiment at approximately 7.8 barns. The next most intense process is population of the 4_1^+ state at approximately 1.0 barns. Further processes are at least an order of magnitude smaller. Hence, real physical processes involving the 82 keV $2_1^+ \rightarrow 0_1^+$ γ ray are very likely for any given beam pulse and also most likely a multiplicity one event. Figure 6.5 shows the change in the γ projection of the $e\gamma$ matrix with time random subtraction. The large reduction of the 82 keV $2_1^+ \rightarrow 0_1^+$ γ ray is immediately obvious. Following the subtraction the 185 keV $4_1^+ \rightarrow 2_1^+$ γ ray has become the most prominent peak. This logically follows from the knowledge that a genuine coincidence event containing either of the transitions is most likely to be the $4_1^+ \rightarrow 2_1^+ \rightarrow 0_1^+$ process containing both transition, in which the 82 keV is more heavily converted. The ^{152}Sm 122 keV $2_1^+ \rightarrow 0_1^+$ γ ray is also suppressed for the same reason as that of ^{154}Sm.

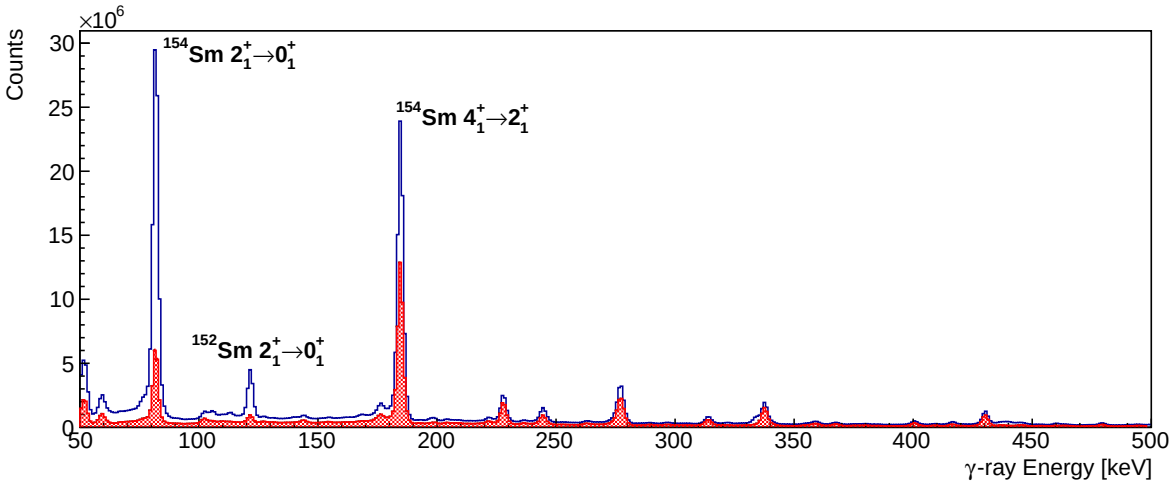

Figure 6.5: Time gated $e\gamma$-matrix γ projection, shown with (red) and without (black) background subtraction.

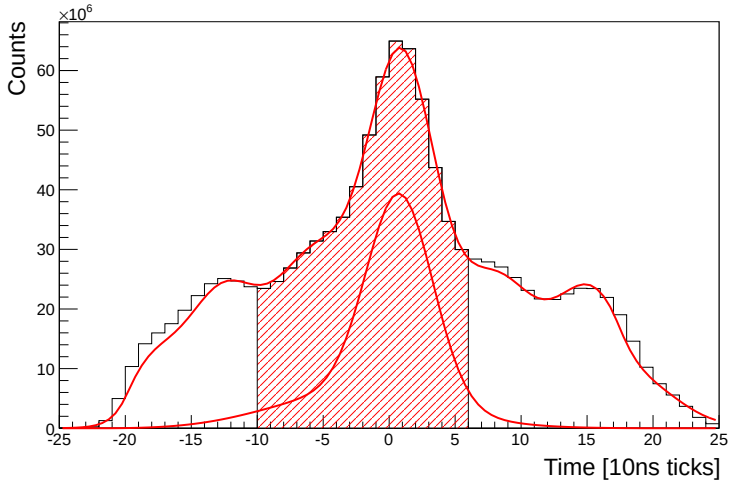

Figure 6.6: Time spectrum for $e^-\gamma$ coincidence, with time gate, time fit and extracted genuine coincidence peak shown.

Time Gate and Background Fraction

The selection of a time gate to define spectra S_t and S_b is discussed in Section 4.4.4, where it is noted that the timing gate should be optimised to minimise the background fraction, b_g, while maximising counts and that the background gate should ideally be placed away from the timing peak. However, in this experiment the event window was set to only 200 ns, limiting the selection of both gates. In order that the background spectrum, S_b, be a good representative sample of the background, the data used in its construction should be maximised, and to this end it was necessary to set the background gate as the inverse of the genuine gate. The placement of the gate, shown for $e\gamma$ in Figure 6.6, was then a compromise between minimising b_g (by narrowing the gate) and reducing the amount of the genuine peak that lies outside of the gate to improve S_b (by widening the gate).

Time gates were set at $-60 < t_{co} < 60$ ns for $\gamma\gamma$ data and $-110 < t_{co} < 60$ ns for $e\gamma$ data to accommodate the asymmetric timing peak observed in $e\gamma$ coincidences, see Section 4.4.4.

In order to determine the background fraction, b_g, an initial estimate was obtained from the time fit function. Spectra were produced, gated and subtracted on coincidence time and γ-ray energy for each observable yrast transition in ^{152,154}Sm and ^{166}Yb. These spectra were created for consecutive values of the timing b_g, an exampled is show in Figure 6.7. The optimum value of b_g was determined by observing the reduction of the 82 and 185 keV transitions in ^{154}Sm and the 122 keV transition in ^{152}Sm, each of which was identified as highly random. The value of b_g was set to that which removed the peaks from spectra in which each transition should not be genuinely coincident but did not over-subtraction them. The uncertainty on b_g was defined as the minimum step size at which difference could be discerned. The value of b_g for the $\gamma\gamma$ time gate was found to be 0.15 ± 0.01 and for the $e\gamma$ time gate 0.55 ± 0.02. The uncertainty on b_g translates to slightly larger bin errors in the subtracted spectra rather than directly affecting any measurement.

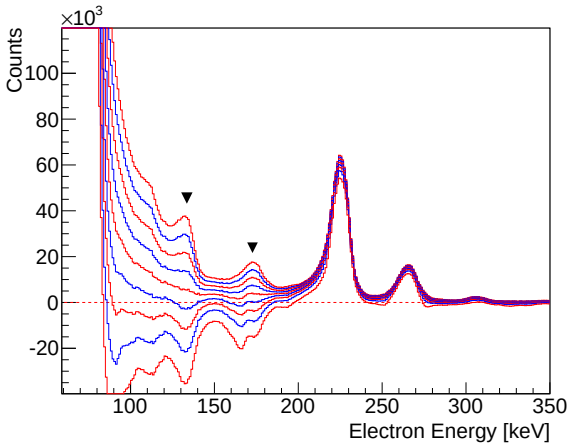

Figure 6.7: Electron spectra gated on the ^{154}Sm 185 keV $4_1^+ \rightarrow 2_1^+$ γ transition and background subtracted with values of time b_g from 0.1 to 0.9. The falsely coincident K and L electron peaks from the ^{154}Sm $4_1^+ \rightarrow 2_1^+$ transition change from present to over-subtracted.

6.1.2 Resultant Spectra

Following time background subtraction both data cubes were reduced to matrices, with individual bin errors $> \sqrt{N}$, free of random coincidences, shown in Figure 6.9. Upon these matrices identical γ gates were placed to produce pairs of electron spectra and γ spectra for conversion coefficient calculations. The background subtraction for the individual γ gates follow the procedure of Section 4.4.2. The cumulative effect of both subtractions is shown in Figure 6.8.

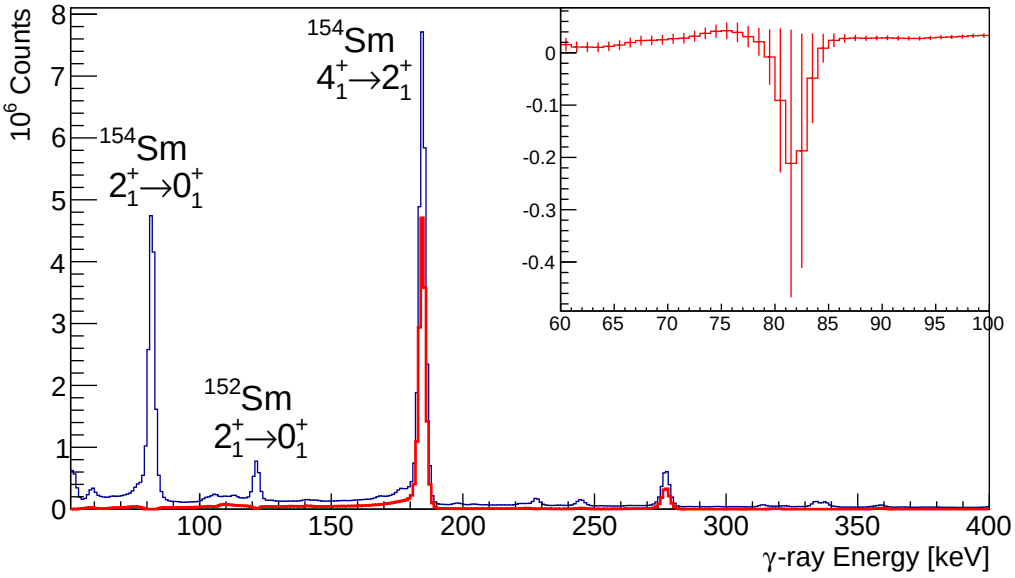

Figure 6.8: Gamma spectrum from $\gamma\gamma t$ data cube gated on prompt time and ^{154}Sm $2_1^+ \rightarrow 0_1^+$ γ transition. Shown with and without background subtraction. The inset shows the importance of the propagated error bars for the most heavily subtracted part of the spectrum. Error bars include a contribution to account for the unknown systematic error added by background subtraction, as well as random counting errors.

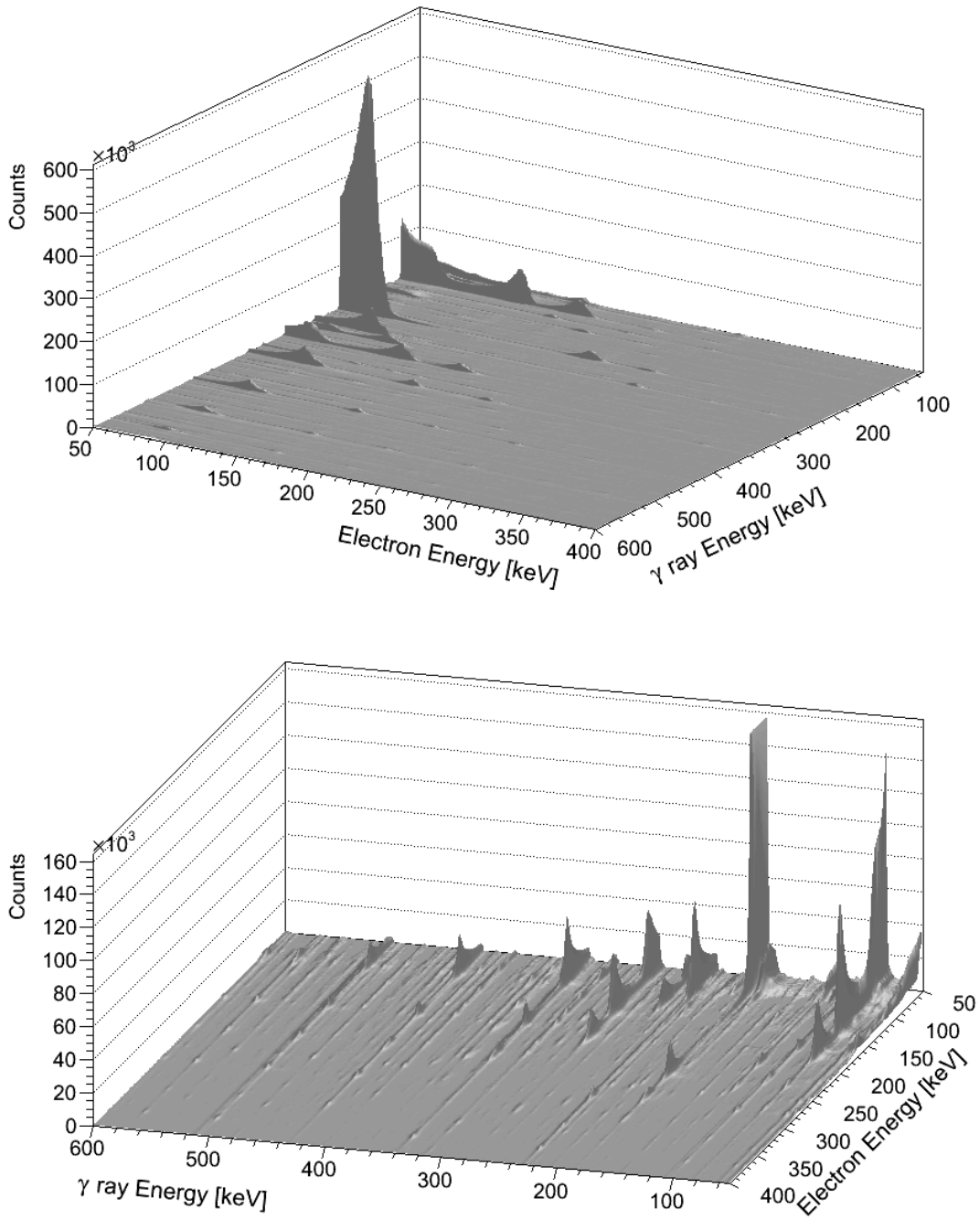

Figure 6.9: Projection of the $e\gamma$ matrix following subtraction of random coincidence background. The large tails from scattering below each electron peak mark clear lines of their coincident γ rays.

6.2 Yrast Conversion Coefficients

The in-band yrast transition for ^{152,154}Sm and ^{166}Yb are well known, unmixed, E2 transitions. As such the conversion coefficients can be calculated with BRICC to a reasonable degree of certainty. Following gating, the full energy peaks from these transitions can be clearly identified and peak area measured for both electron and γ spectra. When com-

bined with the known detector efficiencies the measured areas can be used to calculate experimental conversion coefficients and these α_{exp} can then be compared to calculations in order to normalise any remaining factors. For convenience the in-band yrast transitions will be refereed to as follows : $\Gamma_1 = 2_1^+ \rightarrow 0_1^+$, $\Gamma_2 = 4_1^+ \rightarrow 2_1^+$, etc.

6.2.1 Kinematic Shifts

Particles emitted from a recoiling nucleus can suffer a kinematic energy shift when measured in the lab frame, as discussed in Section 4.3. An understanding of the factors involved is needed for use in the non-trivial low statistics fits that follow in Section 6.4. As both JUROGAMII and SAGE are (approximately) cylindrically symmetric only β_z is of concern for kinematic peak shifts. The bulk of JUROGAMII is situated either side of 90° resulting in only Doppler centroid shifts but a large Doppler broadening. SAGE is an axial detector and as such is maximally sensitive to kinematic centroid shift but minimal broadening is anticipated.

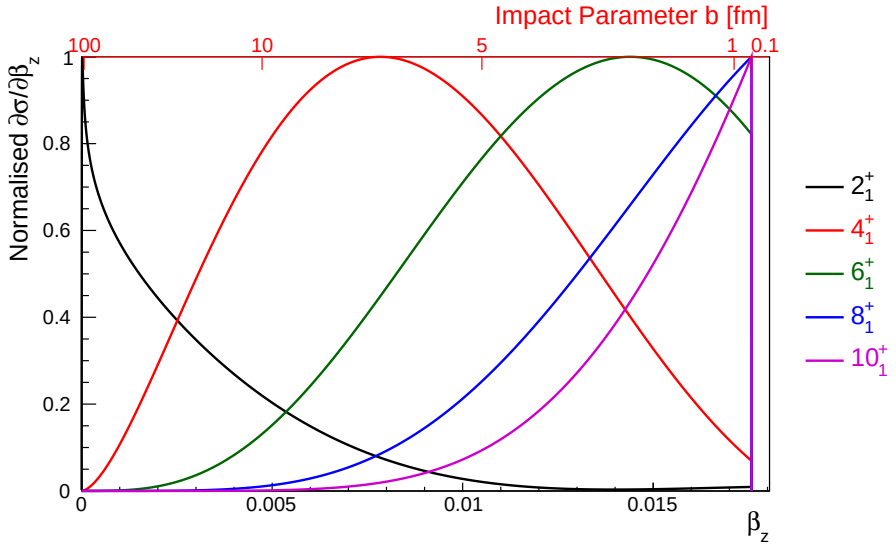

Figure 6.10: Coulex population cross section for yrast states in ^{154}Sm, shown as a function of recoil beam axis velocity β_z. For context a secondary axis denoting values of impact parameter b is shown (red).

The target was a 1.5 mg/cm^2 (2.1 μm) thick samarium foil. The 65 MeV ^{16}O beam will lose 3.2 MeV passing through the target. Subsequently, Sub-barrier fusion producing ytterbium will be heavily weighted towards the front of the target. The compound nucleus will be produced with $\beta \equiv \beta_z = 0.0088$ and subsequent evaporation of neutrons produce only a small perturbation. The stopping range for the product ytterbium isotopes is 1.05 μm and the majority of ytterbium stops within the target, coming to rest in ~ 0.8 ps.

Conversely the maximum momentum that can be imparted to a target samarium nucleus, given by a head-on elastic collision, is $\beta_z \leq 0.0176$.[2] At this maximal β_z the stopping range for the recoil is 4.07 μm and a recoil would punch-through through the target in $\lesssim 0.5$ ps. However the CoulEx cross-section for the maximal momentum transfer

[2]The small excitation energies seen in samarium $E < 2$ MeV are only a small perturbation on the elastic case.

is small, as shown in Figure 6.10, The increased geometric cross-section at large impact parameters results in a lower average $\beta_z << 0.0176$, except for high momentum transfer (multi-step) CoulEx transitions need to reach high spin states.

For both reactions mechanisms longer lived states will decay while moving at reduced velocities or stationary. To perform a full kinematic correction for the data set is both impractical and uninformative, as there is no consistent β_z, as a result one is not performed. This poses no problem for the fitting of yrast states, the lifetimes of which are given in Table 6.1. For the presented yrast states kinematic shifts are small because of long lifetimes

J^π	τ ^{166}Yb	τ ^{154}Sm	τ ^{152}Sm
2^+	1.79 ns	4.36 ns	1.403 ns
4^+	76.3 ps	148 ps	57.7 ps
6^+	11.3 ps	32.8 ps	10.29 ps
8^+	3.09 ps	8.51 ps	3.06 ps
10^+	1.44 ps	3.53 ps	
12^+	0.74 ps		

Table 6.1: Yrast state lifetimes for the three nuclei under discussion.

and present no challenge to the identification and fitting of individual peaks.

The observed kinematic shifts of yrast electrons are shown in Figure 6.11 and are much lower than that resulting from maximal β_z. Even when emitted from a stationary nucleus the measured energy of electrons have some shift due to energy loss through the target (energy loss of electrons was discussed in Sections 3.2.1 and 4.1.4). This effect is minimal at 1 MeV and increases for lower or higher energies.

For the measured yrast transitions no notable shift or broadening was seen in γ spectra. It is only in decays from the very short lived negative parity states in ^{154}Sm where Doppler effects in γ rays are observed. Lifetimes of around 20 fs lead to clearly Doppler broadened peaks in JUROGAMII.

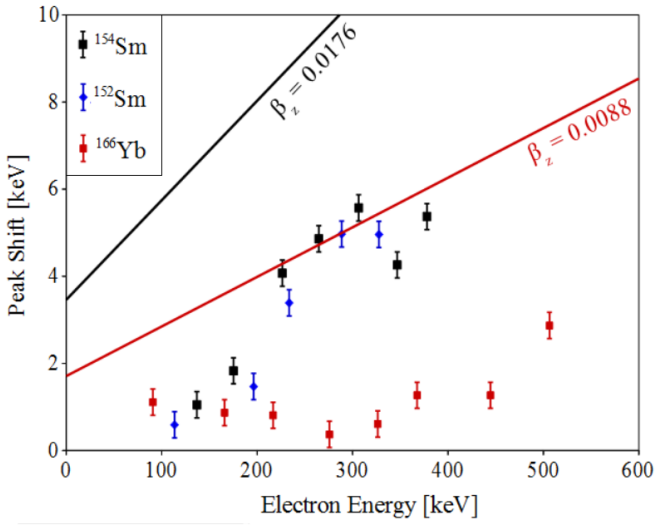

Figure 6.11: Observed peak shifts for the conversion electron of in-band yrast transitions for ^{152,154}Sm and ^{166}Yb. Lines show the maximum possible kinematic shift for the two population mechanism involved. See text for additional detail.

6.2.2 Fitting

Individual spectra were produced by gating on the Γ_1, Γ_2 and Γ_3 transitions of ^{154}Sm, Γ_1,Γ_2,Γ_3 and Γ_4 of ^{166}Yb and the Γ_1 and Γ_2 of ^{152}Sm.[3]

Initially, fitting was performed for the individual spectra, producing multiple measurements for each $\alpha(\Gamma)_{exp}$. However, it was decided that using the combined spectra from multiple gates to produce a single measurement for each $\alpha(\Gamma)_{exp}$ produced the optimum results. This minimised background fluctuation, maximised counts for small peaks at high energy and reduced systematic errors from gate contamination.

Fitting was performed following the methods outlined in Section 4.1. The full set of fits are shown in Figures 6.12 - 6.14. Where significant overlap of peaks was observed, they were fitted together and the individual areas extracted. K electron peaks were predominately isolated, but L, M and higher order electron peaks are nearly degenerate. For samarium the L-M energy difference is 5.7 keV, for ytterbium it is 7.6 keV at which point the M electron peak becomes discernible as a shoulder on the larger L electron peak. In both cases L and M peak areas cannot be disentangled with confidence and so the total area of both is used to calculate a combined α_{L+M}. N, O and higher order electron contributions were found to be smaller than the measurement error ($\alpha_{L+M} \approx \alpha_{L+M+N+O}$) and so their contributions were neglected.

[3] A gate on the Γ_3^{152} was not used as it was dominated by the tail of Γ_3^{166}.

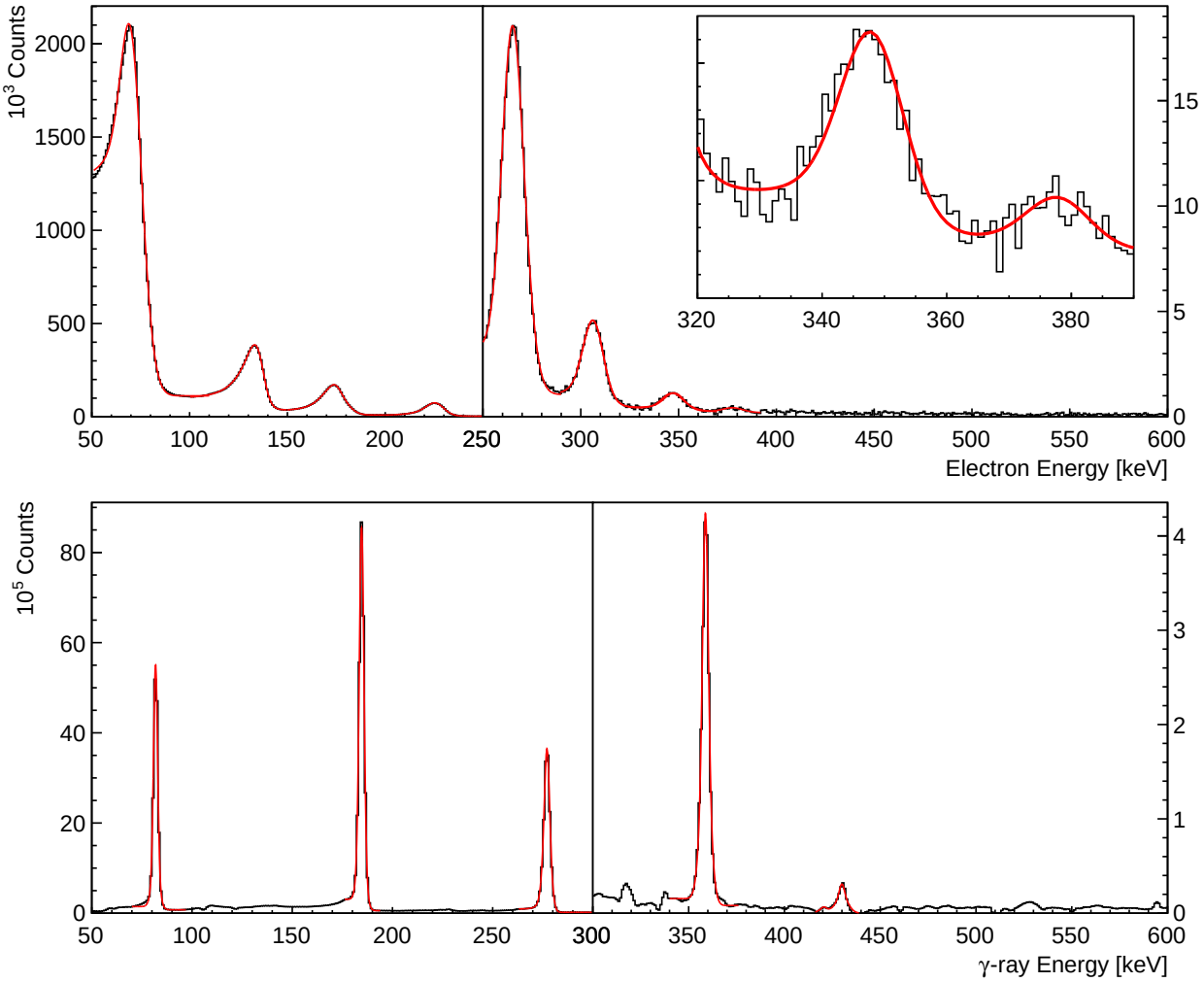

Figure 6.12: ^{154}Sm yrast electron spectrum (above) and γ-ray spectrum (below). Produced following time-gated background subtraction and gating on the ^{154}Sm Γ_1, Γ_2 and Γ_3 γ-ray transitions. Data is shown in black with fits overlain in red. The inset expands the fit on the lowest intensity electron peaks.

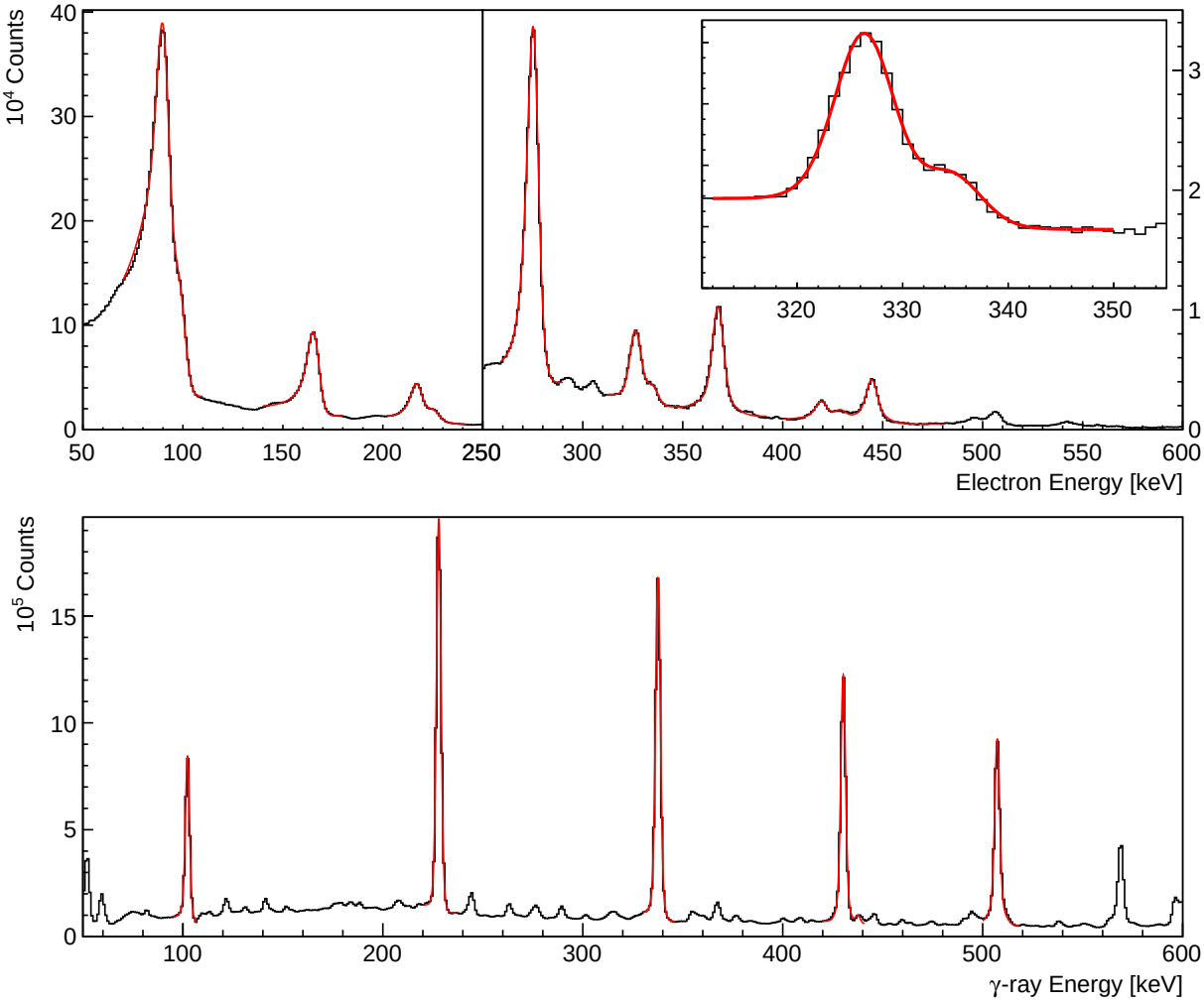

Figure 6.13: ^{166}Yb yrast electron spectrum (above) and γ-ray spectrum (below). Produced following time-gated background subtraction and gating on the ^{166}Yb Γ_1, Γ_2, Γ_3 and Γ_4 γ-ray transitions. Data is shown in black with fits overlain in red. The inset expands the $6_1^+ \rightarrow 4_1^+$ L electron peak, a clear M electron shoulder can be seen and the displayed fit account for both components.

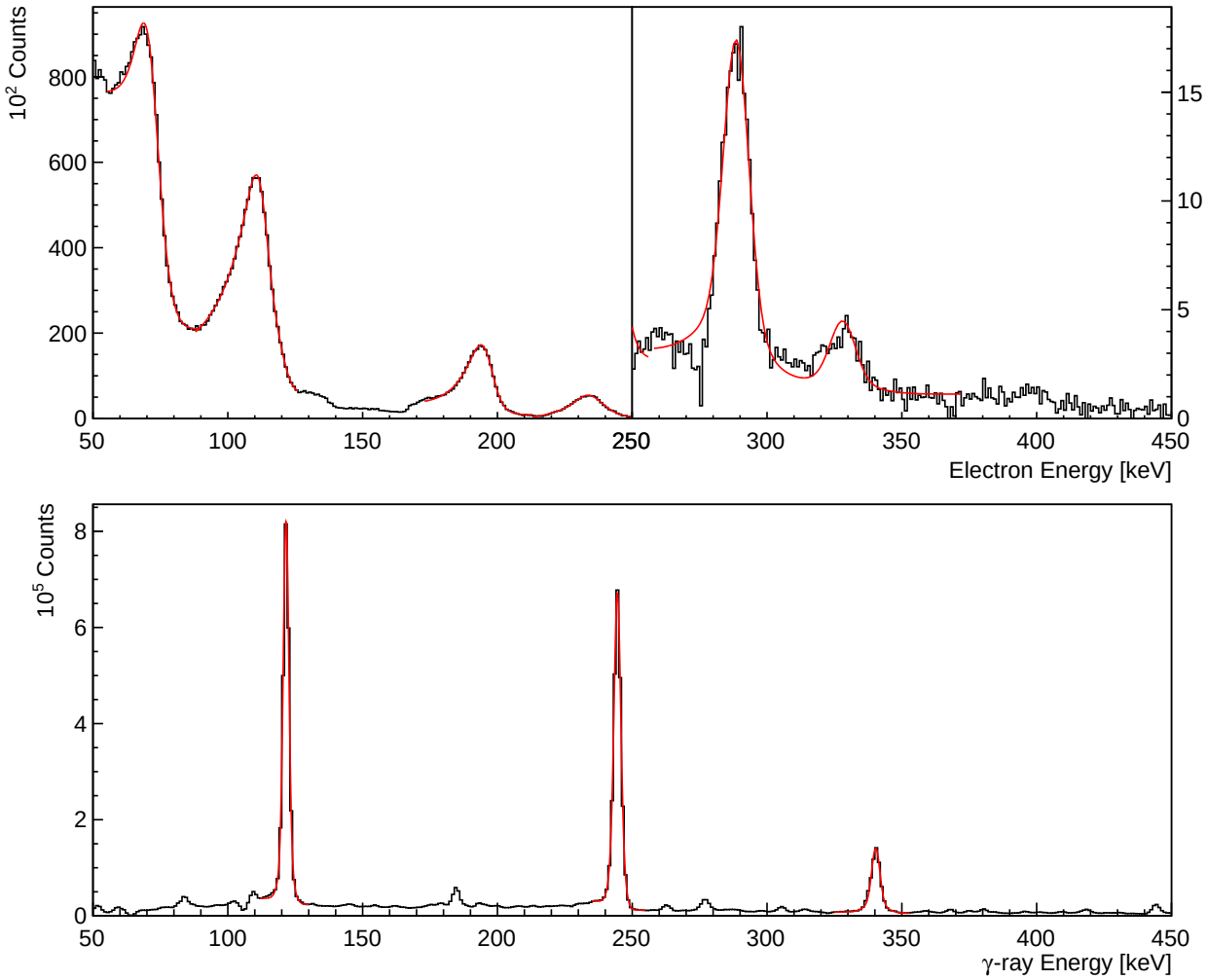

Figure 6.14: ^{152}Sm yrast electron spectrum (above) and γ-ray spectrum (below). Produced following time-gated background subtraction and gating on the ^{152}Sm Γ_1 and Γ_2 γ-ray transitions. Data is shown in black with fits overlain in red.

6.2.3 Normalisation Factors

Recall from Section 4.6 that experimental conversion coefficients are calculated using:

$$\alpha_{exp} = \frac{A_{e,exp} \cdot \varepsilon(E_\gamma)}{A_{\gamma,exp} \cdot \varepsilon(E_e)} \cdot \Lambda \cdot \Theta \,, \tag{6.1}$$

where ε is the calibrated detector efficiency at the peak energy, A_{exp} is the measured peak area and Λ and Θ are timing and angular normalisation factors respectively.

In this work the observed ytterbium states are predominately fed from higher lying states via unobserved transitions. Conversely states in samarium are populated directly, but neither the direction of the beam or recoil is detected, resulting in an averaged ensemble being observed and not a selected subset. As a result there are insufficient restrictions to confer a preferential alignment of the magnetic sub-states in either case and initial state ensemble is assumed to be uniformly oriented. As a result the simplification $\Theta \approx 1$ is valid.

The timing normalisation factors Λ is defined as

$$\Lambda = \frac{\tau_\gamma \cdot \Delta_{\gamma\gamma}}{\tau_e \cdot \Delta_{e\gamma}} \,, \tag{6.2}$$

where τ is the detector live time and Δ is the fraction of events within the timing window. $\Delta_{e\gamma}$ and $\Delta_{\gamma\gamma}$ are estimated from timing spectra to be ~ 0.93 and ~ 0.91. τ_γ and τ_e are unmeasured.

The Λ factor is determined from the yrast data by requiring $\alpha_{BRICC} \equiv \alpha_{exp}$, where the transitions are known to be purely E2 type. Figure 6.15 shows a plot of $\alpha_{exp}/\alpha_{BRICC}$ for the yrast measurements before normalisation ($\Lambda = 1$), from which Λ is then extracted to normalise later results. One observes consistency across the different nuclei and, crucially, no energy dependence. Consistent results are obtained for α_K and α_{L+M}. The main source of error comes from the objective choice when setting the range of an electron fit, especially when there are background features that are unclear or hidden by peaks. Peaks in which there were background peculiarities, preventing confident fits, were not used.

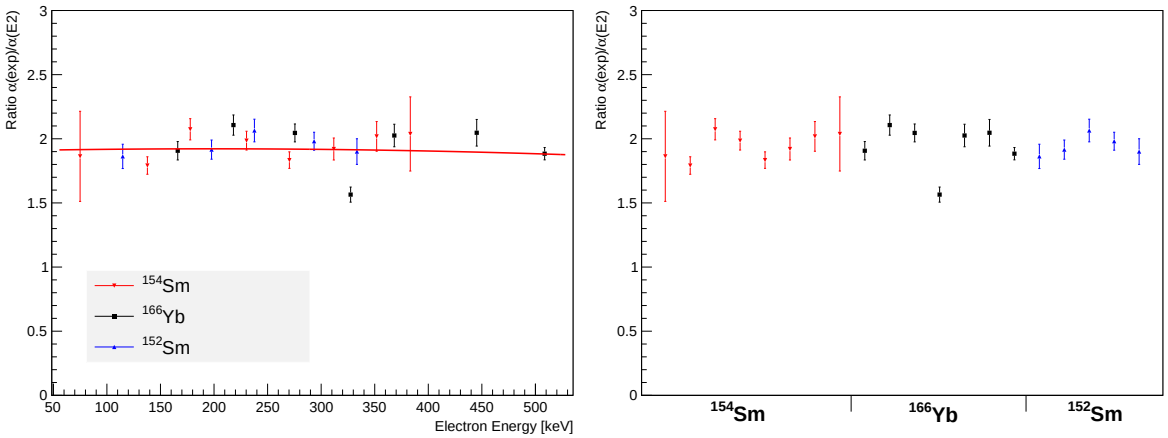

Figure 6.15: Yrast α normalisation $\alpha_{exp}/\alpha_{BRICC}$. On the left the points are ordered by energy and on the right by isotope. As a constant is expected, a second order polynomial fit is shown to demonstrate linearity, yielding the result $y = 1.91 + 1.7 \times 10^{-4}x - 4.2 \times 10^{-7}x^2$.

The weighted mean of the set of $\alpha_{exp}/\alpha_{BRICC}$ was taken to determine Λ and the variance from the mean taken to give the error on Λ. From this a value of $\Lambda = 0.52 \pm 0.04$ was found. This indicates $\tau_\gamma \ll 1$, which can be attributed to high beam rate producing a large X-ray flux coupled with the removal of the attenuators from JUROGAMII.

From the yrast data consistent α calculations across a wide energy range have been shown, and the normalisation constant Λ needed for further experimental measurements has been calculated.

6.3 ^{167}Yb Triple Coincidence Investigation

At this point in the analysis it is useful to demonstrate the effectiveness of the electron peak fitting and conversion coefficient calculations on the fusion evaporation product ^{167}Yb. In doing so the strengths of SAGE not deonstrated in the primary experiment shall be shown and useful physical quantities are extracted.

As well as its coupling to the RITU separator SAGE benefits from far higher γ-ray detection efficiency than has been available in previous $e^-\gamma$ experiments, in which single germanium detectors were coupled with mini-orange spectrometers [122, 128], thanks to JUROGAMII. In the principal experimental measurement of this thesis, this γ-ray detection efficiency is utilised extensively. However, the fundamental difference between experiments using a single germanium detector or a full germanium array, is the ability to measure multiple γ rays simultaneously in coincidence with an electron. This was not applicable in the primary results, where the decay cascades of interest were primarily only two-step processes. This advantage of SAGE can however be shown with the high multiplicity events relating to the ytterbium contaminants.

6.3.1 ^{167}Yb Transitions of Interest

The states that were populated in the even-odd nucleus ^{167}Yb are shown in Figure 5.22. Highlighted selections of the populated level scheme with highlighted transitions of interest are shown in Figures 6.17 and 6.16, of particular interest are the 263 keV, 314 keV and 175 keV transitions.

The (E2) 263 keV transition joins the 179 keV $9/2^-$ and the 442 keV $(13/2^-)$ states. These states are identified as members of the $(\pi, \alpha) = (-, +\frac{1}{2})$ rotational band in cranked-Nilsson model built on the unpaired valance neutron in the $[523]\frac{5}{2}^-$ orbital [129, 130]. The spin and parity of the 442 keV state remains tentative as the multipolarity of the 263 keV transition, determined from γ-ray angular distributions in Reference [131], is also tentative. Measurement of the conversion coefficient for 263 keV the transition can confirm the assignment of the transition and the state above. This will, by extension, confirm the J^π assignments of the following three states in the band at 784 keV, 1193 keV and 1657 keV, which are linked by confirmed E2 transitions.

The (E2) 314 keV transition joins the 330 keV $15/2^+$ and the 644 keV $(15/2^+)$ states. These states are identified as part of the $(\pi, \alpha) = (+, -\frac{1}{2})$ rotational band built on the $[642]\frac{5}{2}^+$ orbital [129, 130]. The spin and parity of the 644 keV state remains tentative as the multipolarity of the 314 keV transition, also measured in Reference [131], is tentative.

Measurement of the conversion coefficient for 314 keV the transition can confirm the assignment of the transition and the state above. This will, by extension, confirm the J^π assignments of the following 1061 keV state in the band which is linked by a confirmed E2 transition.

An additional example will be provided by measurement of the, as yet unassigned, multipolarity of the 175 keV transition between the 902 keV $(15/2^-)$ and 727 keV $(13/2^-)$ states identified as members of the $(\pi, \alpha) = (-, -\frac{1}{2})$ and $(-, +\frac{1}{2})$ bands respectively built one valance neutron in the $[505]\frac{11}{2}^-$ orbital [132].

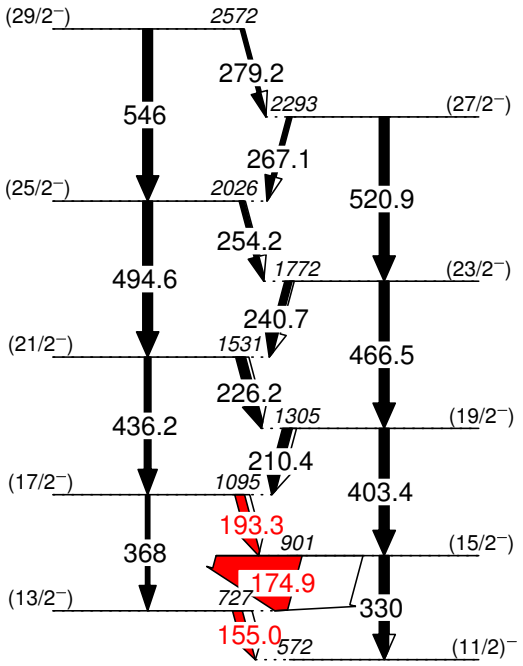

Figure 6.16: Highlighted section of the ^{167}Yb level scheme for states populated in the experiment. The inter-band transition highlighted in red are discussed in the text.

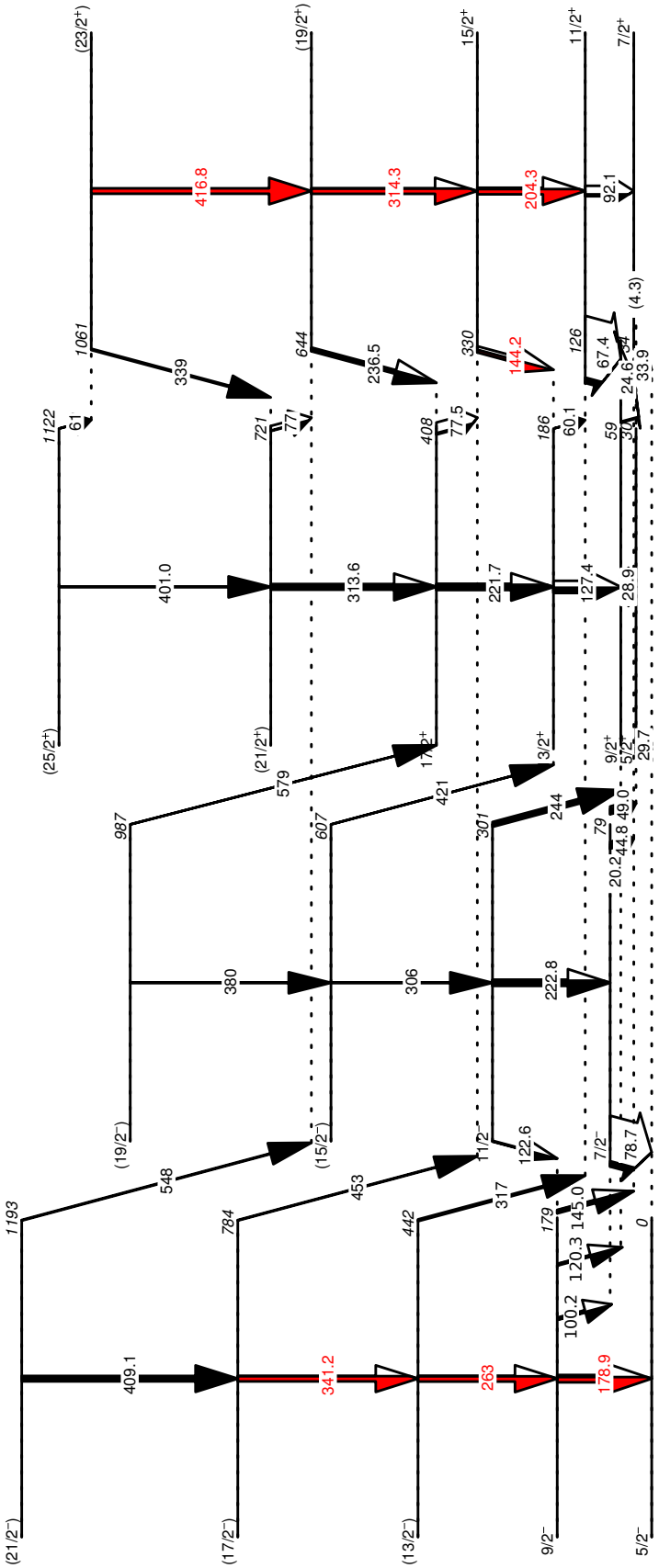

Figure 6.17: Highlighted section of the ^{167}Yb level scheme for states populated in the experiment. The transition highlighted in red are discussed in the text.

6.3.2 ^{167}Yb Analysis Method

From the main experimental data, sets of triple coincidence events were constructed for $\gamma\gamma\gamma$ and $e^-\gamma\gamma$. The same coincidence time requirement as used in Section 6.1.1 was required between each $e^-\gamma$ and $\gamma\gamma$ permutation in order to suppress background. The previously discussed background subtraction was not applied as triple coincidence data were found to be sufficiently clean (large peak to total ratio) for the peaks of interest to be easily resolved. Furthermore, background subtraction with high-fold gates is a more involved process as it must account for correlations and thus the subtraction from Section 4.4 would be insufficient [81].

A pair of γ-ray gates are applied to both $\gamma\gamma\gamma$ and $e^-\gamma\gamma$ data sets to produce double-gated electron and double-gated γ-ray spectra. Identical gates are used for $\gamma\gamma\gamma$ and $e^-\gamma\gamma$. By requiring two γ-ray coincidences in same cascade as the target transition, clean resultant spectra with little background are produced. Other transitions in the cascade of the two gating transitions also appear in the resultant spectra but random background is heavily suppressed. If either gate is heavily contaminated, the contaminant is suppressed in the final spectra, unless it is coincident with a transition in the second gate as well. In this section, gates directly above and below the transition of interest are used; this preferentially selects the target transition over any other part of the cascade coincident with the gates.

Peak fits as described in Section 4.1 were performed on the gated spectra to calculate electron and γ full energy peak areas. The conversion coefficients were then determined by using

$$\alpha_{exp} = \frac{A_{e,exp} \cdot \varepsilon(E_\gamma)}{A_{\gamma,exp} \cdot \varepsilon(E_e)} \cdot \Lambda_3 \,, \tag{6.3}$$

where the triple timing factor Λ_3 is defined here as

$$\Lambda_3 = \frac{\tau_\gamma \cdot \Delta_{\gamma\gamma} \cdot \Delta_{\gamma\gamma} \cdot \Delta_{\gamma\gamma}}{\tau_e \cdot \Delta_{e\gamma} \cdot \Delta_{e\gamma} \cdot \Delta_{\gamma\gamma}} \,. \tag{6.4}$$

The additional Δ terms result from the three coincidence timing gates used for the possible pairs in a triple event. This may be a slight overestimation if there are correlations between the three Δ terms from the timing of physical processes. The constant Λ_3 is related to the timing constant experimentally determined in Section 6.2.3 by

$$\Lambda_3 = \Lambda \cdot \frac{\Delta_{\gamma\gamma}}{\Delta_{e\gamma}} \,. \tag{6.5}$$

In Section 6.2.3 $\Delta_{e\gamma}$ and $\Delta_{\gamma\gamma}$ were estimated to be 0.926 and 0.909 respectively. Combining these Δ values, with an assumed 5 % error, with the measured $\Lambda = 0.522 \pm 0.040$ gives a value of $\Lambda_3 = 0.512 \pm 0.053$, with which α_{exp} may be determined. As discussed in Section 6.2.2, L and M electron peak areas were summed to calculate a combined α_{L+M}, resulting in improved accuracy.

6.3.3 ^{167}Yb Results

To isolate the 263 keV transition, coincidence gates were placed on the 341 keV and 179 keV in-band transitions directly above and below, highlighted in Figure 6.17. Double-gated electron and γ-ray spectra for the 263 keV transition are shown in Figure 6.18. The K, L and M electron features relating to the 263 keV transition are clearly observed, as is the corresponding γ ray. There is notable contamination from the 227 keV $4_1^+ \rightarrow 2_1^+$ transition of ^{166}Yb, which has a genuine coincidence with the upper gate and is of sufficient intensity that Compton continuum in the lower gate results in the false triple coincidence observed. The L and M electrons peaks of the contaminant were included in the fit of the gated electron spectrum to improve accuracy. Values of $\alpha_{K,exp} = 0.057 \pm 0.011$ and $\alpha_{L+M,exp} = 0.032 \pm 0.016$ were measured for the 263 keV transition.

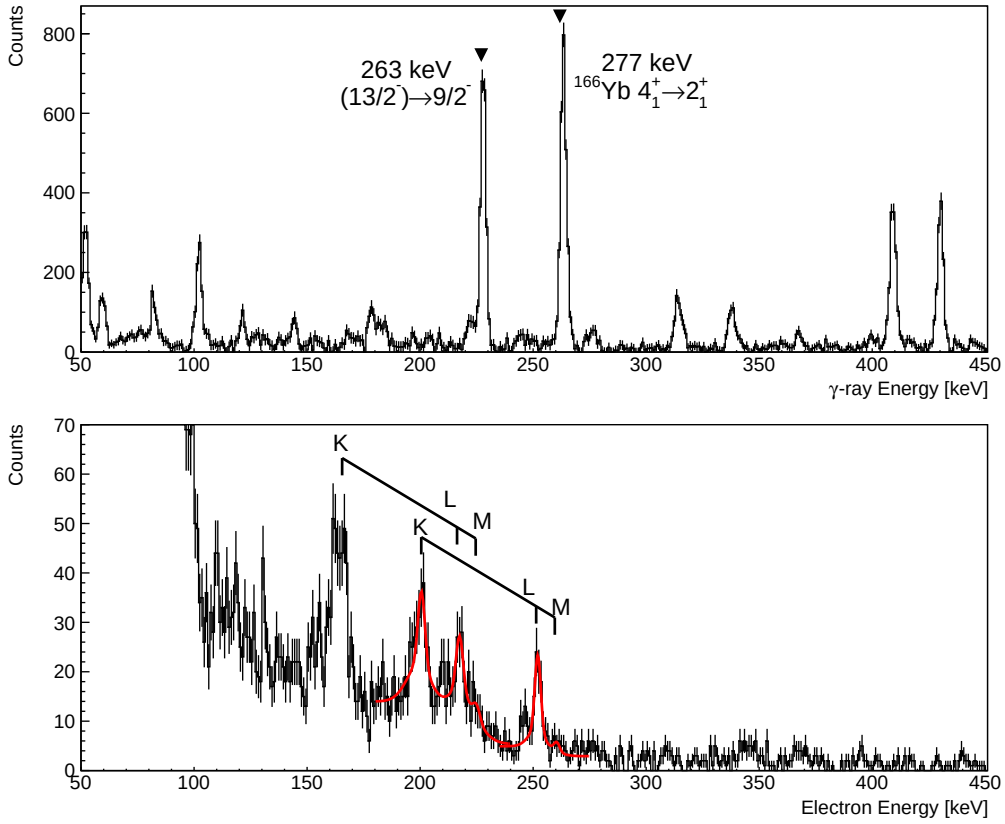

Figure 6.18: Double-gated electron and γ-ray spectra highlighting the ^{167}Yb 263 keV transition. The 227 keV $4_1^+ \rightarrow 2_1^+$ transition of ^{166}Yb is also prominent.

For the 314 keV a sum of data from two sets of γ-ray coincidence gates was used. Firstly a coincidence with the 417 keV in-band transitions directly above was required. Then a following second coincidence was required with either the 204 keV in-band transitions directly below, or the 144 keV inter-band transitions, also directly below, as highlighted in Figure 6.17. The resultant double-gated electron and γ-ray spectra are shown in Figure 6.19. The data are particularly clear and yields measurements of $\alpha_{K,exp} = 0.048 \pm 0.006$ and $\alpha_{L+M,exp} = 0.020 \pm 0.003$.

Finally, the 175 keV inter-band transitions was isolated by requiring coincidences with the 193 keV and 155 keV inter-band transitions directly above and below, shown in Fig-

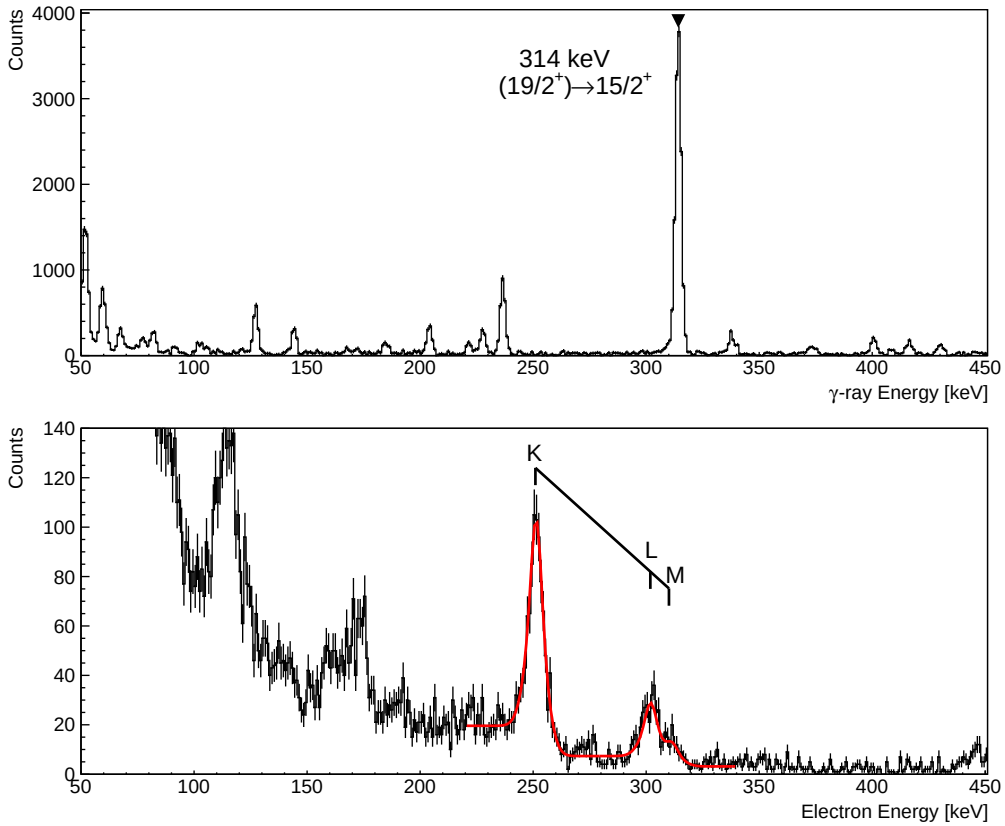

Figure 6.19: Double-gated electron and γ-ray spectra highlighting the ^{167}Yb 314 keV transition.

ure 6.16. Resultant electron and γ-ray spectra are shown in Figure 6.20. The 210 keV inter-band transitions directly above the upper gating transition, shown in Figure 6.16, is genuinely coincident with both gates and visible in the spectra. The K electron peak from the 210 keV transitions is included in the electron fit to improve accuracy. Resultant values of $\alpha_{K,exp} = 0.192 \pm 0.047$ and $\alpha_{L+M,exp} = 0.139 \pm 0.046$ were measured.

These three sets of conversion coefficient measurements are shown in Figure 6.21. The conversion coefficient measurements for each transition are plotted alongside the BRICC calculations for the different possible multipolarities of the transition. In all three cases a pure E2 transition is clearly established. In these three examples, the α_{L+M} measurements do not unambiguously identify the transition type, but limit it to E2 or M1. The α_K measurements constrain the transition to E2 with negligible mixing, if any. The clarity of these results, and the electron spectra shown, demonstrate the power of high-fold-gated electron spectroscopy possible with SAGE.

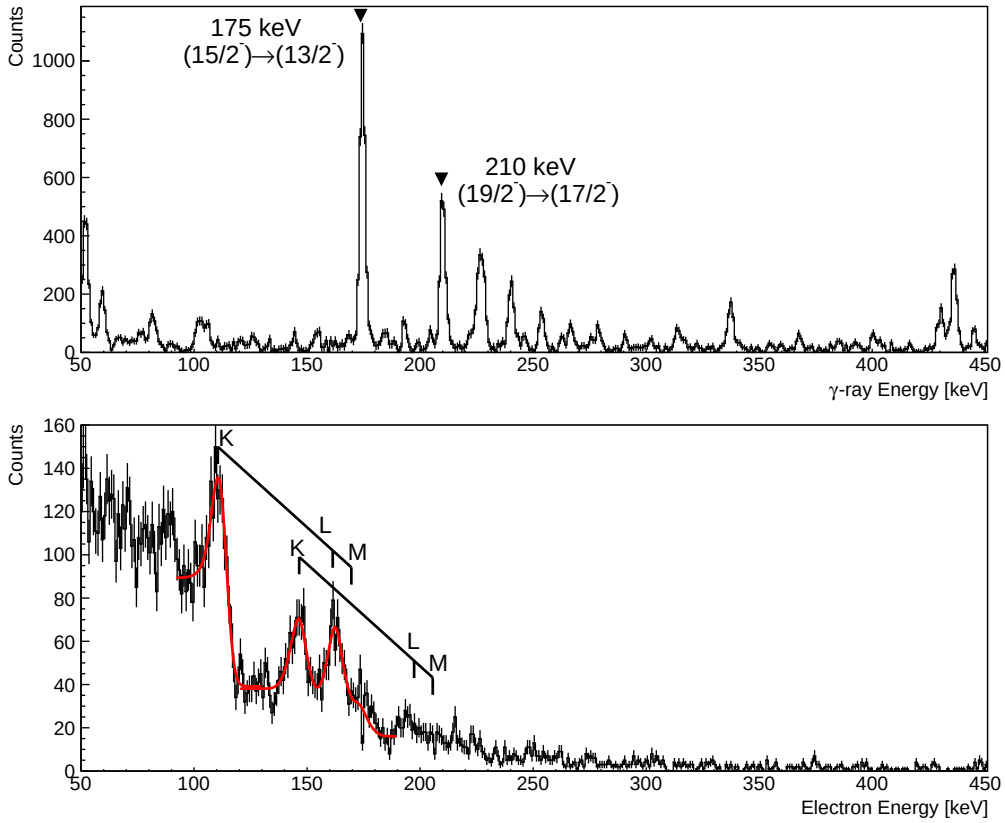

Figure 6.20: Double-gated electron and γ-ray spectra highlighting the ^{167}Yb 175 keV transition. The 210 keV transition is also prominent.

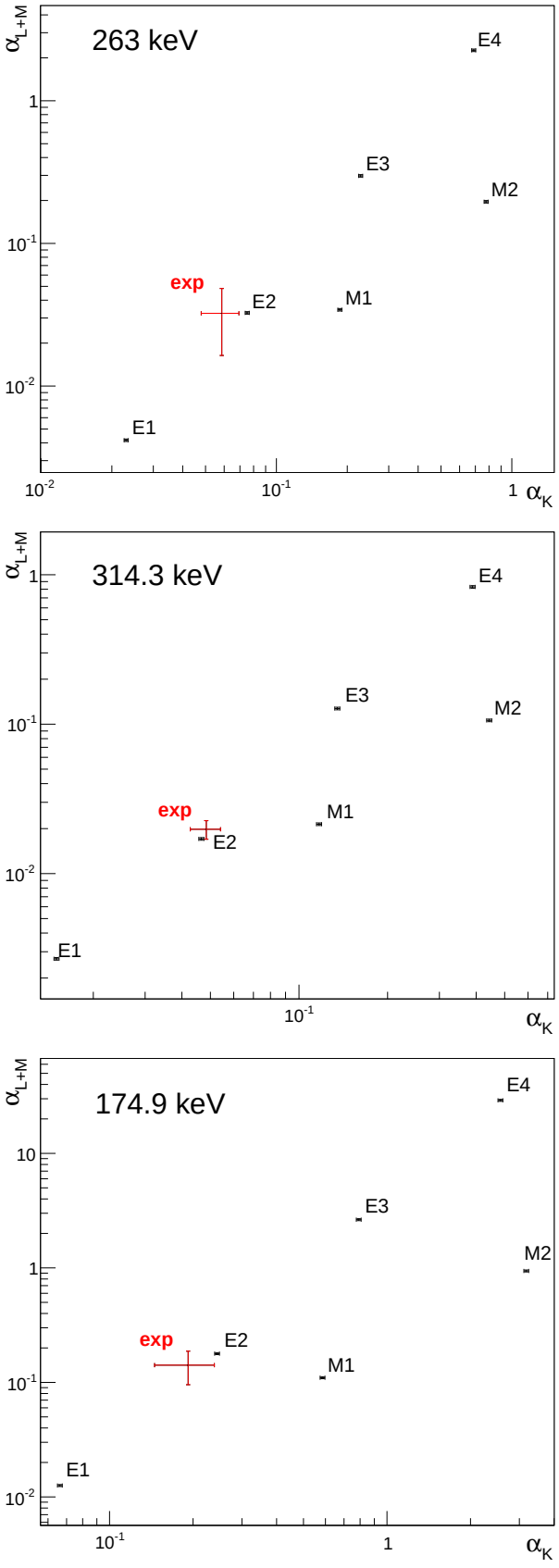

Figure 6.21: Measured conversion coefficients for the three transitions in ^{167}Yb, plotted against calculated multipolarities for the given transition energy.

6.4 Non-Yrast Transitions

Following normalisation of the conversion coefficient calculations using yrast data, we proceed to look at inter-band transitions from non-yrast states in which mixed multi-polarities and $E0$ enhancements can be observed. Transitions are observed in the energy range 500 - 1000 keV where the yrast structures do not dominate the electron spectra. Following the gating and background subtraction a greatly reduced background is presented at these higher energies. The remaining background is one which, while reduced, is not negligible and has a large variance and large cumulative bin errors.

For the electron peaks under consideration in this region the statistics are low, only those from the most intense transitions or from transitions with enhanced electron conversion can be distinguished. Several such transitions can be identified in the data for known transitions in the different nuclei ^{152,154}Sm and ^{166}Yb, conversion calculations are performed for each as a test of the method.

In this section the size of the electron peaks to be measured are on the scale of or smaller than the variance of the background, hence the idealised fitting presented in Section 4.1.2 is unsuitable and the confidence limit fits of Section 4.5 are used. When a clear peak could not be distinguished, peak centroid and width were fixed leaving only the area variable as a free parameter. Peak width and any kinematic centroid shifts were taken from the nearest measurable neighbour. In such cases fitting was repeated with width and centroid values varied around the 'optimum' value to check the measurement sensitivity to each parameter.

For fitting of the low statistics peaks, rebining of data between the initial 1 keV bins and a maximum of 5 keV bins was performed to aid identification of peaks and guide the eye during fitting. In each case attention was paid to any difference in results between different binning in order to avoid fit anomalies. 5 keV was selected as the maximum physical binning as peak σ in the range $\sim 4-7$ keV were expected, equating to FWHM $\sim 9-16$ keV and hence larger binning would result in a loss of peak information.

Using the above procedure we produce limits at the 95% confidence level, both from FC bands and χ^2. In each case the graphical representation of the confidence band is produced so it can clearly be seen if convergence is expected between the two and if the limit value x is accepted as a valid measurement.

Measurements of counterpart γ-peaks remain far simpler and are a negligible source of error.

6.4.1 ^{152}Sm Conversion Coefficients for $0_2^+ \rightarrow 2_1^+$ and $2_2^+ \rightarrow 2_1^+$

Both the $0_2^+ \rightarrow 2_1^+$ and $2_2^+ \rightarrow 2_1^+$ transitions of ^{152}Sm are sufficiently strong that they can be observed in the low statistics regime of the electron data, using data gated on the Γ_1 transition. Measurement of both conversion coefficients provides a test of the low statistics method that will be applied to the analogous states in ^{154}Sm, but at significantly lower energies where SAGE efficiency is significantly higher. The $2_2^+ \rightarrow 2_1^+$ transition is of particular interest as it is the equivalent transition to that to be measured in ^{154}Sm. In all following cases focus is on the K electron measurement.

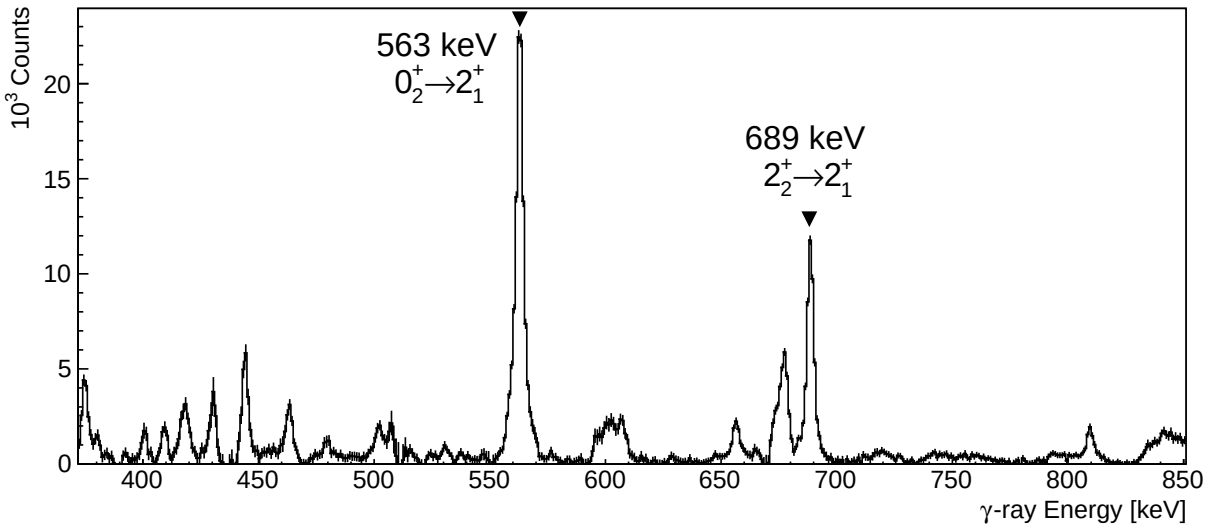

Figure 6.22: ^{152}Sm high energy γ spectrum. Relevant transitions are indicated.

Figure 6.22 shows the appropriate region of the γ spectrum, in which a smoothing algorithm has been applied to subtract Compton continuum. From the 562.9 keV $0_2^+ \rightarrow 2_1^+$ γ branch it can seen that the 0_2^+ has been well populated, which will allow observation of the conversion electrons. Just below the 688.7 keV $2_2^+ \rightarrow 2_1^+$ γ peak the 674.7 keV $3_1^- \rightarrow 4_1^+$ transition can be seen, this is a pure E1 transition and has a small conversion coefficient of 0.0019 which will not be observed.

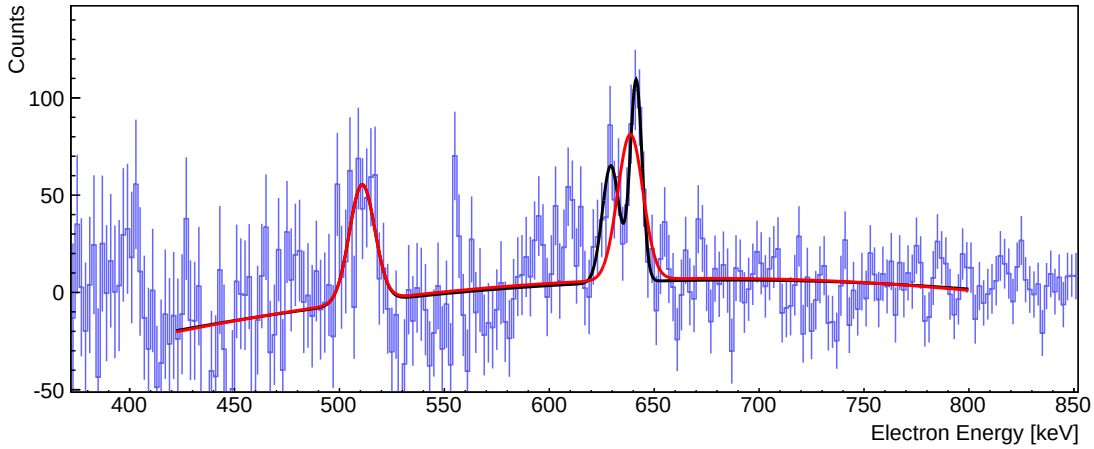

Figure 6.23: ^{152}Sm high energy electron spectrum. The peak fit used is shown (red) and additional fit is shown (black) for interest as described in the text.

Figure 6.23 shows the electron spectrum fit. The $0_2^+ \rightarrow 2_1^+$ transition is a pure E2 transition but is sufficiently low in energy that it is suitably converted for observation. For the $0_2^+ \rightarrow 2_1^+$ K electron peak a good fit minimum is reached without constraints. A centroid shift of -5.9 keV is measured, in-keeping with a smaller impact parameter and larger β_z, which is expected as the 0_2^+ state cannot be populated by a single step CoulEx reaction. A peak area of 453(218) is measured at the 95% confidence level, the confidence bands sit just in the convergent region away from the boundary, as shown in Figure 6.24. Then peak area given is taken from Figure 6.23 where a 2 keV binning has been used.

This is consistent with the mean across all considered binnings of 454(217). Using this electron peak area and the measured γ peak area of $1.14(1) \times 10^5$ an α_{exp} was calculated using Equation (6.1), where the peak efficiency for electrons is 1.84(4) % and for γs it is 6.15(2) %. It is found that the smaller 1σ uncertainties on efficiencies and γ peak are negligible and only the 7.6% error on the measured value of Λ is of some small significance. A final value of $\alpha_{K,exp} = 0.0069(34)$ is determined for the ^{152}Sm $0_2^+ \rightarrow 2_1^+$ transition. This value is in very good agreement with the accepted data table value of $\alpha_K(E2) = 0.0078(1)$, upon which only a 1σ uncertainty is quoted.

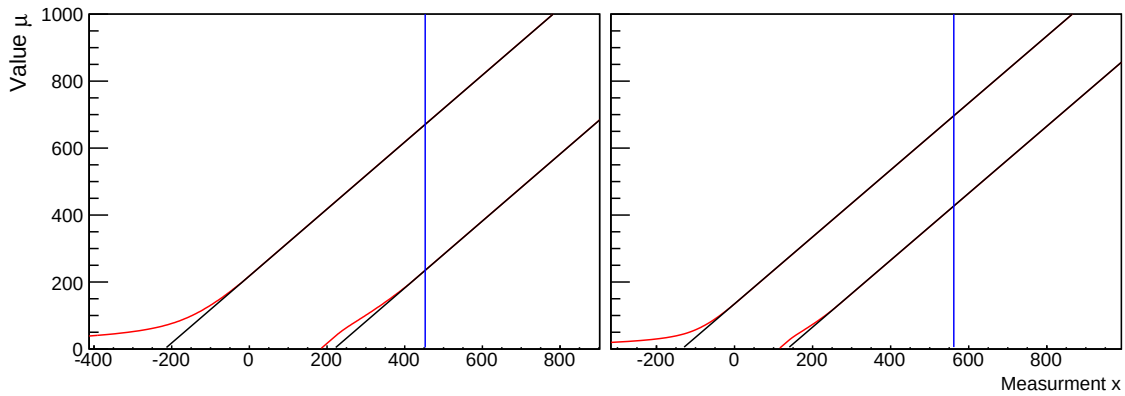

Figure 6.24: ^{152}Sm electron peak area measurement confidence bands. K electron peak areas for $0_2^+ \rightarrow 2_1^+$ (left) and $2_2^+ \rightarrow 2_1^+$ (right).

The $2_2^+ \rightarrow 2_1^+$ transition is $J_i^\pi = J_f^\pi$ and benefits from enhanced electron conversion from M1 and E0 contributions. In the electron spectrum the $2_2^+ \rightarrow 2_1^+$ K electron peak is prominent, but less distinct than that of the $0_2^+ \rightarrow 2_1^+$. An unconstrained fit leads to a peak that is too broad ($\sigma > 10$ keV) and pulled down notably in energy. The peak width was fixed to $\sigma = 6$ keV based on the neighbouring peaks, while the centroid was left free. As a result, a good fit minimum was reached at an acceptable centroid, leading to a peak shift of -3.3 keV. The 2_2^+ K peak can in fact be fit well by a pair of peaks, perhaps corresponding to an un-boosted component from CoulEx population and a separable component from heavily Doppler shifted nuclear population. Such a fit is unjustified at these levels of statistics and background fluctuations and is performed for interest only. Using the single Gaussian fit a peak area of 562(135) is measured at the 95% confidence level. The confidence bands, shown in Figure 6.24, are in the region where FC and classical χ^2 estimations converge. This area is taken at the 2 keV binning level and is consistent with the mean value of 561(135). Combining this with the measured γ peak area of $5.11(9) \times 10^4$ and using electrons and γ peak efficiency of 1.06(3)% and 5.49(2)% respectively, a value of $\alpha_{K,exp} = 0.0297(75)$ is measured for the ^{152}Sm $2_2^+ \rightarrow 2_1^+$ mixed E0+M1+E2 transition. This value is in remarkable agreement with the data table value $\alpha_K(E0 + M1 + E2) = 0.0359(13)$ as measured by several ^{152}Eu decay experiments, most recently in Reference [133].

It is worth noting this is considerably larger than either of $\alpha_K(E2) = 0.0048$ or $\alpha_K(M1) = 0.0083$. The E0 enhancement $W_e(E0)$ can be extracted if the mixing ratio $\delta(E2/M1)$ is known (as it is for this transition) from angular correlations. Such analysis

is applied to the later ^{154}Sm measurement.

6.4.2 ^{166}Yb Conversion Coefficients for $8_3^+ \rightarrow 8_1^+$ and $(6)_2^+ \rightarrow 6_1^+$

In the low statistics region, above the well-populated yrast transitions (>600 keV) and below the maximum measurable electron energy (<1000 keV), there are many observable ^{166}Yb γ rays belonging to yrast feeding transitions from states in higher lying bands, the observable levels are shown in the scheme of Figure 6.25. The upper graph in Figure 6.26 shows the γ spectrum gated on ^{166}Yb Γ_2 and Γ_3. Measurements of conversion coefficients are performed as a test of the measurement method at yet higher energies than ^{152}Sm and for an entirely different population method. Of the transitions observed

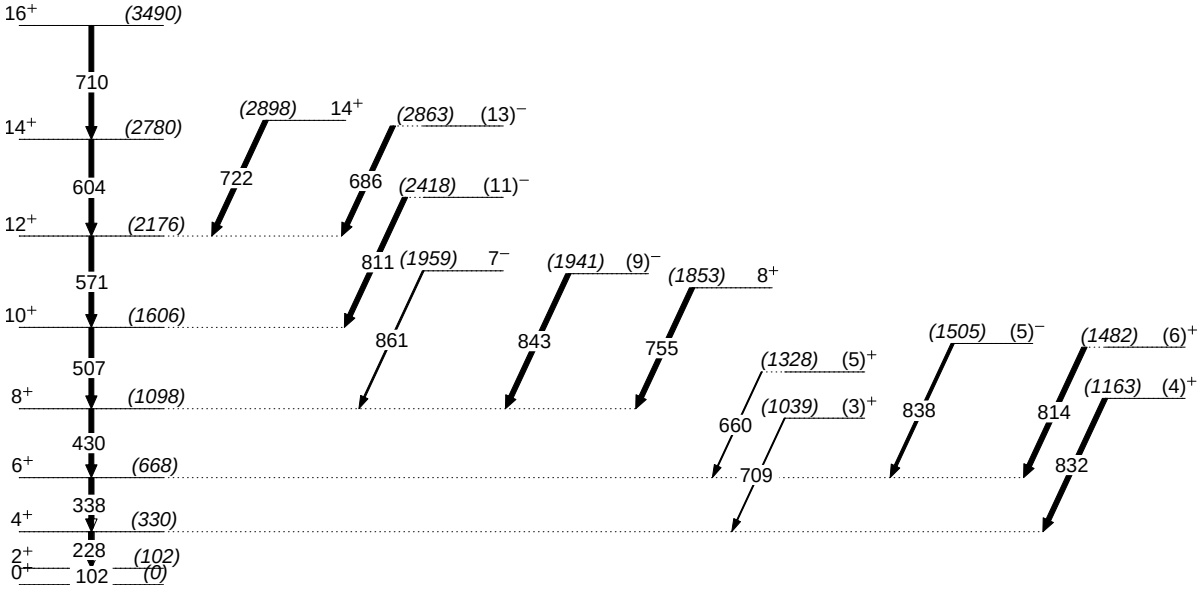

Figure 6.25: ^{166}Yb observable levels and γ transitions from $\gamma\gamma$ data. Full level scheme from Reference [78] and original assignments taken from Reference [127].

only a few are sufficiently intense or sufficiently converted that they have observable electron peaks. The small E1 and E2 transitions are negligible as none are seen strongly enough to outweigh their smaller conversion coefficients. Measurements are focused on the 754.8 keV E0+M1+E2 transition between the 1853 keV 8^+ and 1098 keV 8_1^+ states, and the 814.5 keV M1 transition between the 1482 keV $(6)^+$ and 668 keV 6_1^+ states. Data from the Γ_4 gate is included for fitting of the $8 \rightarrow 8$ peaks as this gains a few vital counts. The Γ_1 gate however is not used, it is heavily converted ($\alpha = 2.97$) and what little γ peak remains is heavily contaminated by ^{38}Ar; its peak to noise ratio makes its inclusion unprofitable.

The 832.2 keV $(4)^+ \rightarrow 4_1^+$ has a sizeable conversion coefficient, but the γ ray is poorly distinguishable from adjacent peaks and an α_{exp} calculation is not attempted. A peak for the K electron of the transition is included to improve the electron fit as it is not negligible for calculation of the neighbouring $6 \rightarrow 6$. The lower graph of Figure 6.26 shows the electron data fit for the $6 \rightarrow 6$ K electron. A suitable fit minimum is reached without constraint. Narrower peak widths in the range $\sigma = 3.4 - 4.8$ keV are measured from fitting of the ytterbium electron peaks, this is in-keeping with the lower Doppler broadening for

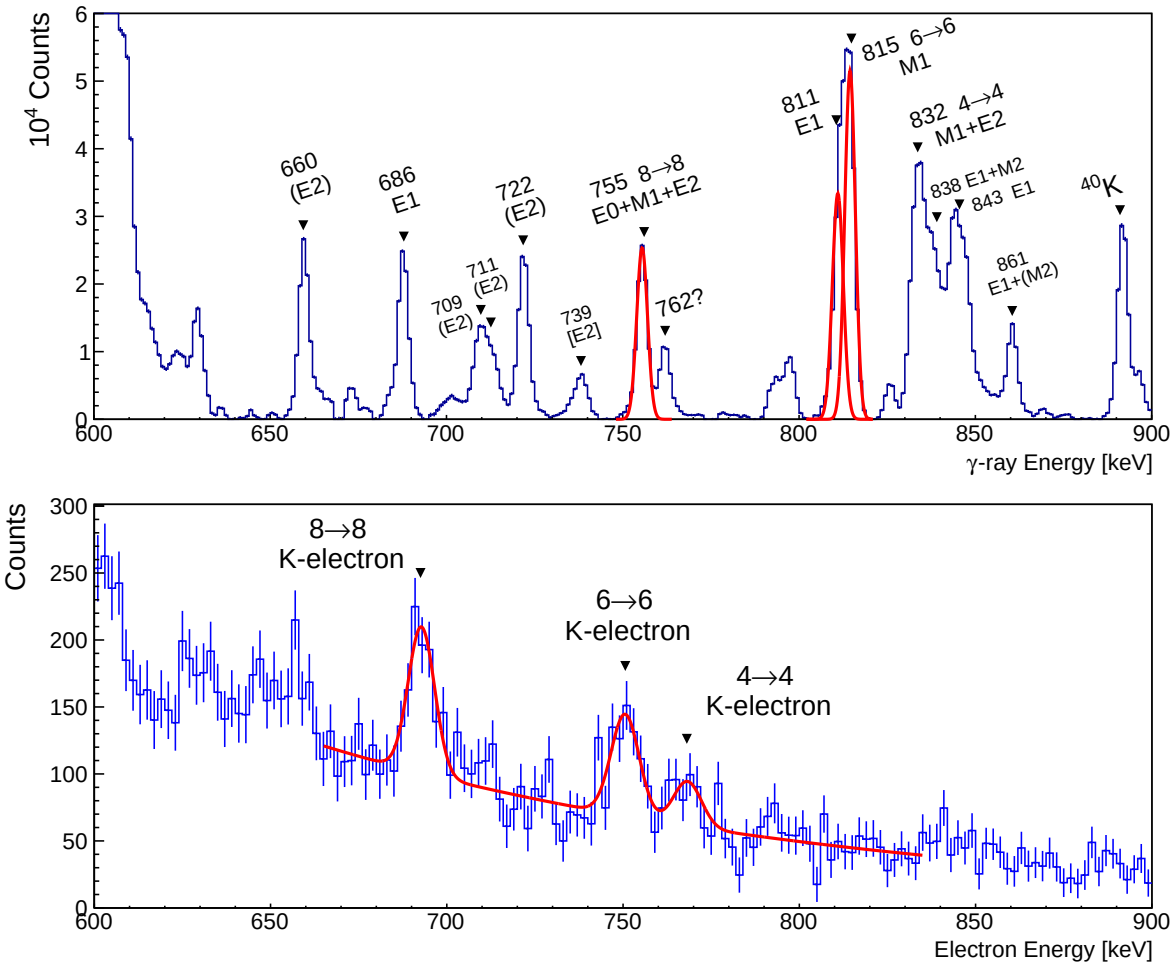

Figure 6.26: ^{166}Yb high energy spectra for γ-ray transitions (above) and electrons (below), gated on Γ_2 and Γ_3. Fits shown in red are detailed in the text.

the slower ytterbium nuclei and the higher energy electrons being closer to the energy straggling minimum at ∼1 MeV.

Peak shifts of -2.5 keV and -0.8 keV are measured for the $6 \rightarrow 6$ and $8 \rightarrow 8$ K electron peaks respectively. From the discussion in Section 6.2.1 this indicates a lifetime for the 1853 keV 8^+ state of $>>$ 1 ps, however the certainty on the centroids of the low statistics peaks are insufficient to certify such a claim.

The 814.5 keV $6 \rightarrow 6$ transition's K electron peak area is measured at the 95% confidence level to be 385(129) using a 2 keV binning (average over all levels of binning 375(134)), shown in Figure 6.27. This peak includes a contribution from the K electron of the inseparable smaller 811.0 keV $(11)^- \rightarrow 10^+_1$ E1 transition. For the counterpart γ peaks, negligible Doppler shift or broadening of the peaks allows a simple two Gaussian fit with fixed centroids to deconvolve the two peak areas, giving $1.93(1) \times 10^5$ counts from the 815 γ and $1.30(1) \times 10^5$ counts from the 811 γ. Using peak efficiencies of 0.63(2) % and 4.97(2) % for electrons and γs respectively, and taking $\alpha_K(E1) = 0.00188$ as known for the 811 transition, the E1 contribution to the electron peak is calculated to be 60(5). Hence using an electron count of 325(129) a conversion coefficient is calculated of $\alpha_{K,exp}(815) = 0.0069(28)$. This is slightly lower than the previously measured value by

Fields *et al.* of $\alpha_{K,exp}(815) = 0.010(1)$ [128] on which the pure M1 assignment to the transition is based ($\alpha_K(M1) = 0.0100$, $\alpha_K(E2) = 0.0047$). This slightly lower measurements hints at a possible E2 component [4]. However, some underestimation in the measurement is possible due to the the smaller, indistinguishable from background, electron peaks. These were ignored and may have marginally driven the background fit up and hence electron peak area measurement down.

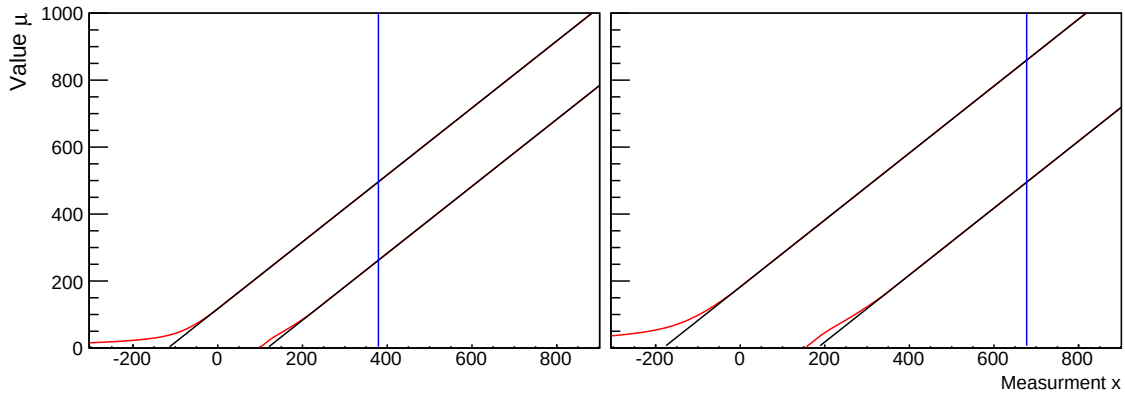

Figure 6.27: ^{166}Yb electron peak area measurement confidence bands. K electron peak areas for $(6)^+_2 \rightarrow 6^+_1$ (left) and $8^+_3 \rightarrow 8^+_1$ (right).

For the calculation of α_K for 754.8 keV $8 \rightarrow 8$ transition, a K electron peak area is measured at the 95% confidence level to be 669(181) using a 2 keV binning (average over all levels of binning 656(180)), shown in Figure 6.27. A γ peak area of $1.38(1) \times 10^5$ is measured, this is easily separated from the neighbouring 761.9 keV peak. The neighbour γ peak is unidentified. It is coincident with ^{166}Yb $\Gamma_{1,2,3,4,5}$, indicating an unknown higher lying yrast feeding transition, but no states at matching energies are known. The 761.9 keV neighbour is sufficiently separated that if any notable electron peak were produced it would be separably identifiable, and such an electron peak is not seen. Peak efficiencies of 0.83(3)% and 5.20(2)% for electrons and γs are used. The result is a conversion coefficient measurement of $\alpha_{K,exp} = 0.0158(45)$. This is in good agreement with the Fields *et al.* measurement of $\alpha_{K,exp} = 0.017(3)$ [128], from which multi-polarity and α assignments to the transition are taken, and is within error of the previous Fields *et al.* measurement of $\alpha_{K,exp} = 0.020(1)$ [134]. The E0 component is clearly confirmed as $\alpha_K(M1) = 0.0121$ and $\alpha_K(E2) = 0.0055$ are both $<< \alpha_{K,exp}$.

Both of these measurements support the effectiveness of the method, but the high density of smaller transitions merging with background fluctuations cast doubt on the small differences to previous measurements that might contain interesting physics.

6.4.3 ^{154}Sm Conversion Coefficients for $2^+_2 \rightarrow 4^+_1$

The K electron of the 911 keV $2^+_2 \rightarrow 4^+_1$ transition in ^{154}Sm is the highest energy discernible electron peak in the experimental data set. The electron peak appears just above the level of the background fluctuation in the region. Measuring the pure E2 conversion coefficient for this transition against the calculated BRICC E2 value provides the final test of the

[4] Without a δ measurement an E0 contribution cannot be ruled out for a $J^\pi \rightarrow J^\pi$ transition.

method at the highest energy for which data are available, while also constraining the properties of the population of 2_2^+ state, which will allow for constraint of the behaviour of the $2_2^+ \rightarrow 2_1^+$ decay branch from the state.

For the measurement of the $2_2^+ \rightarrow 4_1^+$ transition data from the Γ_2 gate is used alone as it offers far better peak to noise than the inclusion of the Γ_1 gate otherwise would.

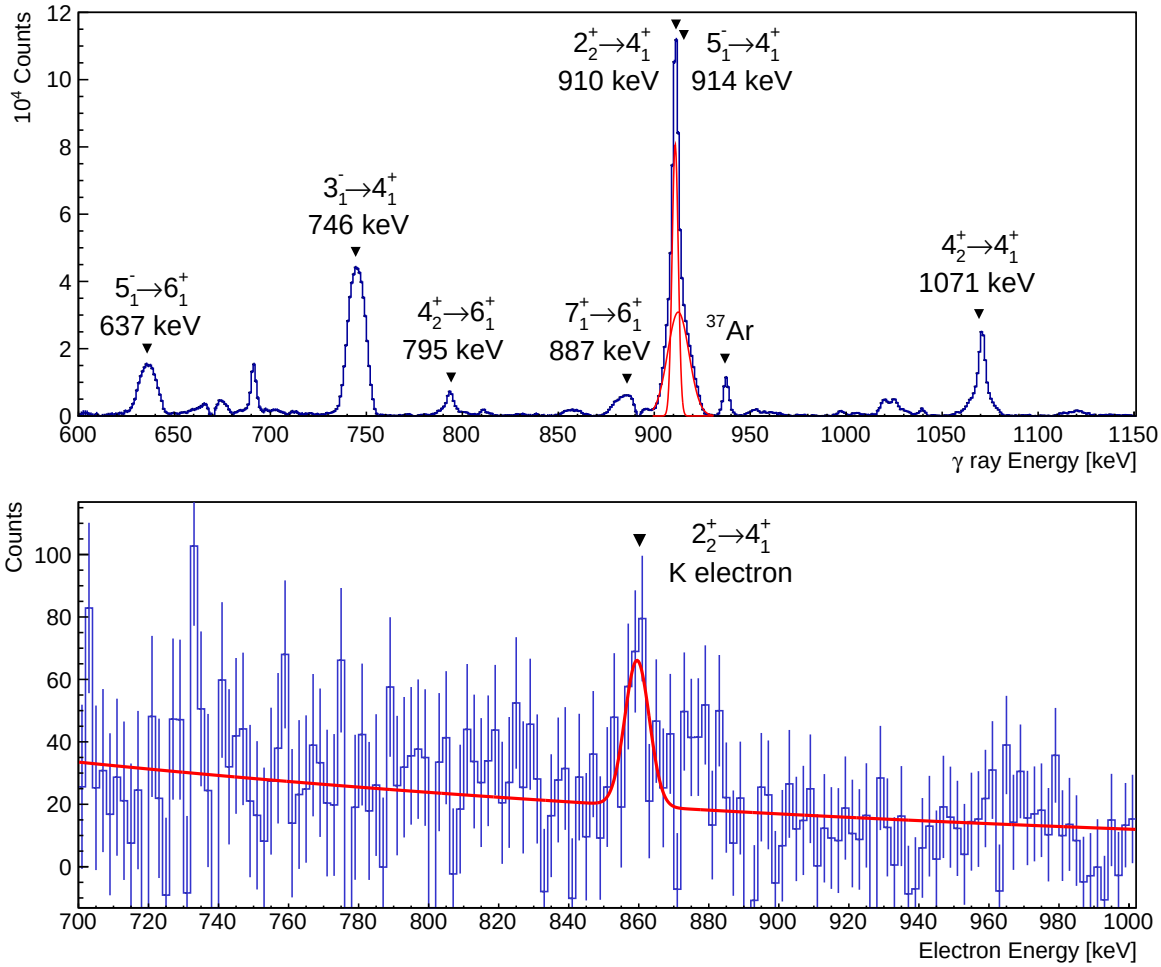

Figure 6.28: ^{154}Sm high energy spectra for γs (above) and electrons (below), gated on Γ_2. Fits shown in red are detailed in the text.

The gated γ ray spectrum is shown in the upper graph of Figure 6.28. The γ peak of interest is heavily convoluted with the Doppler-broadened 914 keV $5_1^- \rightarrow 4_1^+$ transition. Because the E1 transition from the negative parity states are broadened to non-Gaussian shapes, and have very small centroid shifts, separation by peak fitting is ineffective. The integrated area of the two convoluted peaks is measured to be $8.10(2) \times 10^5$ counts. The smaller decay branch of the 5_1 state is clearly visible in the γ spectrum at 637 keV. This $5_1^- \rightarrow 6_1^+$ transition has 35.0(7) % of the intensity of the dominant $5_1^- \rightarrow 4_1^+$ branch. Decay cascades following both the $5_1^- \rightarrow 6_1^+$ and $5_1^- \rightarrow 4_1^+$ decays pass Γ_2 100 % and hence the peaks in Figure 6.28 must have the relative intensities of the branching ratios, with scaling for the efficiencies at the two energies. A peak area of $1.79(2) \times 10^5$ is measured for the $5_1^- \rightarrow 6_1^+$. JUROGAMII peak efficiencies at corresponding energy to the high and low peaks are 4.64(2)% and 5.75(2)% respectively.

Total corrected counts are of $8.90(21) \times 10^6$ and $8.54(23) \times 10^6$ are calculated for the $5_1^- \rightarrow 4_1^+$ and $2_2^+ \rightarrow 4_1^+$ transitions respectively.

From the Doppler broadening observed in the negative parity state γ rays, Section 6.2.1, the electrons corresponding to the $5_1^- \rightarrow 4_1^+$ K electron peak will have a Doppler shift of approximately -20 keV. The peak will also be broader and contain fewer electrons as a result of being an $E1$ transition. For these reasons it is not necessary to include contributions from the $5_1^- \rightarrow 4_1^+$ transition when measuring the $2_2^+ \rightarrow 4_1^+$ electron peak.

The gated electron spectrum is shown in the lower graph of Figure 6.28. An unconstrained fit fails to minimise to a physically acceptable minimum. The χ^2 surface, shown on the left in Figure 6.29, is found to be extremely flat in the direction of peak σ across the range of reasonable values. The width minimum is driven towards broader peaks by the large positive background fluctuation to the right of the peak. This particular fluctuation is confirmed to be random and not some component of the peak, or another transition, as it is at the incorrect energy for either.

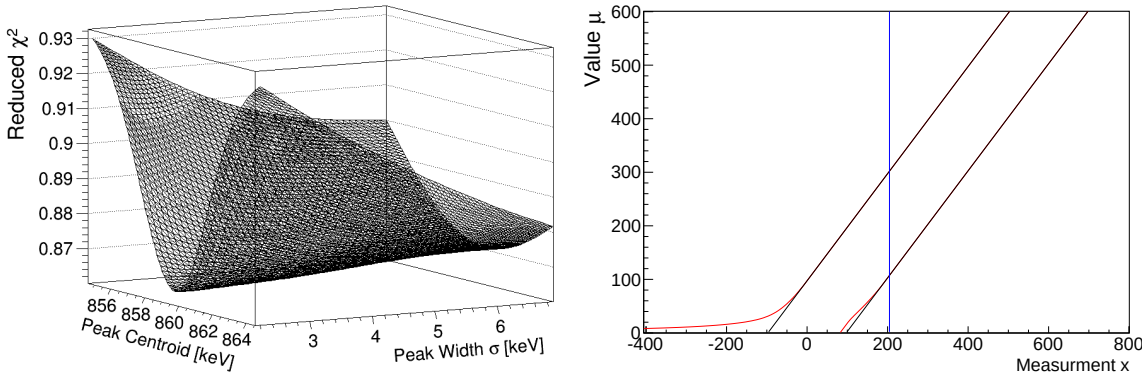

Figure 6.29: Parameter χ^2 surface for the ^{154}Sm $2_2^+ \rightarrow 4_1^+$ K electron fit, goodness of fit is plotted as a function of peak width σ and peak centroid x_0 (left). Confidence bands for the peak measurement area of the final fit are also show (right).

From the ^{207}Bi calibration source the intrinsic detector resolution at an equivalent energy with no experimental broadening gives $\sigma = 2.8$ keV. The nearest experimental peaks are the ytterbium 693 and 753 keV peaks with widths measured in the range $\sigma = 3.4 - 4.8$. The 864.1 keV ^{154}Sm K electrons are closer to the energy straggling minimum than the referenced ytterbium peaks, but may have some small Doppler broadening. A peak width of $\sigma = 3.5$ keV was selected as a suitable value with which to proceed. Using this value a peak area of 205(97) is measured at the 95% confidence level and a peak centroid shift of -4.8 keV equivalent to $\beta_z = 0.0037$. It is worth taking note that the fit minimum is very broad with respect to centroid position, $\sigma(x_0) = 1.4$ keV for the chosen peak width.

Using an electron peak efficiency of 0.37(2)% the conversion is calculated as $\alpha_{K,exp} = 0.0034(16)$. This is within error of the data table value $\alpha_K(E2) = 0.00257(4)$, confirming the validity of the method and estimations therein.

This is the smallest electron peak measured thus far in a region with the highest relative background. A 45% uncertainty is quoted on the measurement and Figure 6.29 shows this is at the limit of convergence with the classic confidence estimator. At this level

of uncertainty caution is needed, as it is the limits that become the physical measurement and one should not extrapolate undue physical meaning from the modal value.

6.5 $2_2^+ \rightarrow 2_1^+$ E0 Measurement

Following confirmation of the method by trial at lower energies, the primary experimental measurement of the E0 strength in the 1096 keV $2_2^+ \rightarrow 2_1^+$ mixed E0+M1+E2 transition of ^{154}Sm is performed. Background subtracted data gated on the Γ_1 transition is used as it is the only observable coincident γ transition. Γ_1 gated data are heavily background-subtracted due to large levels of false coincidences, resulting in large uncertainties in the resultant electron and γ spectra.

Figure 6.30 shows the gated γ spectrum with highlighted transitions. The surrounding transitions are predominantly of type E1 or E2 and of lower intensity than the $2_2^+ \rightarrow 2_1^+$ transition of interest. As a result no notable conversion electron peaks corresponding to the transitions would be expected to interfere with the $2_2^+ \rightarrow 2_1^+$ measurements. Decays from the 2_3^+ state can be seen indicating very strong population of the state. However, the energy of the transitions down from the 2_3^+ state are at higher energies than those of the 2_2^+, in a region where electron efficiency is $< 0.1\%$ and hence beyond the scope of this investigation. The $2_2^+ \rightarrow 2_1^+$ γ peak area in Figure 6.30 is measured to be $1.07(4) \times 10^5$. The JUROGAMII γ peak efficiency at this energy is 4.14(2)%.

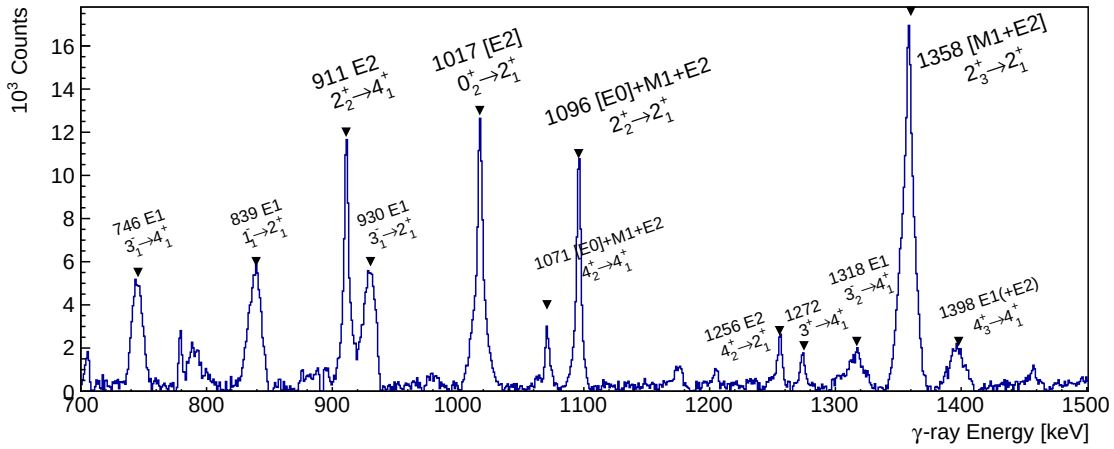

Figure 6.30: ^{154}Sm high energy γ spectrum gated on Γ_1 transition. Relevant transitions are indicated.

For the counterpart K electron peak, shown in Figure 6.31, no peak can be identified in the gated spectrum. The level of background fluctuations are high and a small peak can be easily obscured. A fit with constrained parameters for the peak under investigation can yield a useful upper limit. The peak centroid shift and peak width are functions of the transition energy and the population of the initial state. The $2_2^+ \rightarrow 4_1^+$ transition originates from the same initial state and so the parameters obtained from the fit of that transitions K electron can be used to constrain the $2_2^+ \rightarrow 2_1^+$. The two states are sufficiently close in energy that peak width σ is expected to be unchanged and centroid shift should be the same to within 1 keV. Hence, a fit with fixed centroid shift -5 keV and fixed peak width

$\sigma = 3.5$ keV was conducted for the $2_2^+ \rightarrow 2_1^+$ K electron.

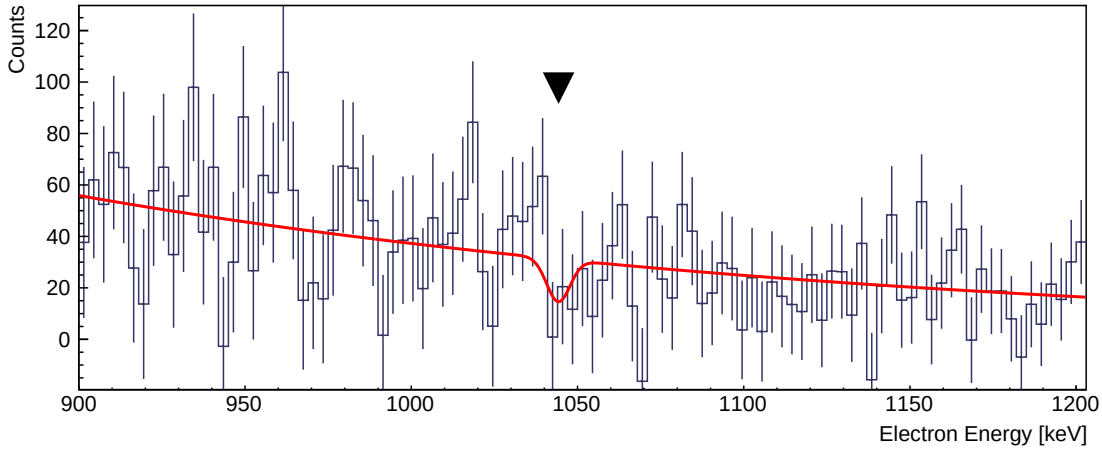

Figure 6.31: ^{154}Sm high energy electron spectrum gated on Γ_1 transition. The peak fit is shown in red, giving a non-physical negative area due to large background fluctuations resulting from heavy background subtraction. Marker shows expected peak location.

Figure 6.31 shows the electron fit at the 3 keV binning level. The figure shows that the fit yields a non-physical peak area of -48.4 counts, this gives an electron measurement of $0_{+48.4}$ counts at the 95% confidence level, as shown in Figure 6.32.[5] Clearly a measurement of $\bar{\mu} = 0$ will result in $\alpha_{K,exp} = 0$, which is known to be incorrect as a clear γ peak is measured and the smallest value of α is given by $\alpha_{K,exp} \geq \alpha_K(E2) = 0.00174$.

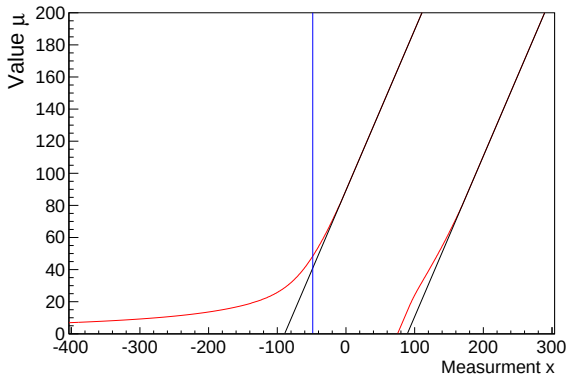

Figure 6.32: ^{154}Sm electron peak area measurement confidence bands for the $2_2^+ \rightarrow 2_1^+$ K electron fit. Note the measurement is in the region FC differs from classic bands and where the 95% confidence level has become an upper confidence limit and not a central confidence band.

With such a large uncertainty it is reasonable to consider the full range of the confidence interval and not the modal value. The upper confidence bound +48.4 is taken as the electron area to calculate an upper confidence limit for α and the quantities that follow. Hence using an electron peak efficiency of 0.143(5)% an upper limit is calculated of $\alpha_{K,exp}$ =0.00672, where one may include a cumulative error from the other factors of +9.2%. Adding the additional uncertainty from these factors to give an upper-upper limit is valid but would be considered an over-cautious upper limit and so here the central value will be calculated and the cumulative error from additional factors quoted separately.

[5]The identical numerical value is coincidental, the upper limit is properly computed.

6.5.1 $\rho^2(E0)$ Calculation

Recall from Section 4.6.2 that a $\rho^2(E0)$ can be calculated using

$$\rho^2(E0) = q_K^2 \cdot \frac{\alpha_K(E2)}{\Omega_K(E0)} \cdot W_\gamma(E2)\,. \tag{6.6}$$

For a a mixed (E0+M1+E2) $J_i \rightarrow J_f$ transition the q_K^2 is given by

$$q_K^2 = \frac{\alpha_{K,exp}(1+\delta^2) - \alpha_K(M1)}{\delta^2 \alpha_K(E2)} - 1\,, \tag{6.7}$$

For the calculations of transition strength for the $2_2^+ \rightarrow 2_1^+$ decay, the latest published values are used of δ and $B(E2)$, taken from T. Möller *et al.* [120]. These values are calculated from angular correlations and CoulEx yields, offer an improvement over the data table value taken from [114], which offers only an upper limit on $B(E2)$ from lifetime measurements.

A value of $\delta = -30(21)$ and $B(E2) = 0.72(9)$ W.u. is reported [120], equating to $W_\gamma(E2) = 68.5(86)$ ns^{-1}. An alternative 'disfavoured' solution to the angular distribution gives $\delta = -0.48(2)$, $B(E2) = 0.15(2)$ W.u. hence $W_\gamma(E2) = 14.3(19)$ ns^{-1}, for which calculations of $\rho^2(E0)$ are also performed.

Using the upper limit value of $\alpha_{K,exp} = 0.00672(62)$ and the BRICC values of $\alpha_K(E2) = 0.001746(25)$ and $\alpha_K(M1) = 0.00271(4)$, values are calculated for q^2. The large error on δ has only a small effect, clarified by use of the rearranged form of Equation 6.7 :

$$q_K^2 = \frac{1}{\alpha_K(E2)} \left(\frac{\alpha_{exp} - \alpha_K(M1)}{\delta^2} + \alpha_{exp} \right) - 1\,. \tag{6.8}$$

The result is a value of $q^2 = 2.85(27)$ (disfavoured alternative $q^2 = 12.8(19)$).

Finally, using an electronic factor of $\Omega_K(E0) = 3.654 \times 10^{10}$ s^{-1} and Equation 6.6 values of $\rho^2(E0)$ are calculated. The result is an upper limit of $\rho^2(E0) \leq 9.4(15) \times 10^{-3}$ and an alternative value of $\rho^2(E0) \leq 8.8(18) \times 10^{-3}$ relating to the disfavoured δ value.[6] This is a particularly weak transition, the implications of which are discussed below.

6.6 Discussion

6.6.1 Measurement

A summary of results is presented in Table 6.2. Good agreement is observed between the measured $\alpha_{K,exp}$ and accepted values for the three nuclei across the energy range measured. For comparison, the $\rho^2(E0)$ value of the ^{152}Sm $2_2^+ \rightarrow 2_1^+$ transition was calculated using the measured $\alpha_{K,exp}$ to be $56(14) \times 10^{-3}$. The result agrees with the accepted value of $69(6) \times 10^{-3}$, as it should given the agreement of $\alpha_{K,exp}$.

Due to the lack of observation of an electron peak for the ^{154}Sm $2_2^+ \rightarrow 2_1^+$ transition, the result is highly sensitive to the fit constraints that were used, which were determined from

[6] The values of $\rho^2(E0)$ are presented in the format $\times 10^{-3}$ by convention.

Nucleus	Transition Energy [keV]	ML	$\alpha_{K,exp}$	Accepted Value
^{152}Sm	562.9	$E2$	0.0069(34)	0.0078(1)
^{152}Sm	688.7	$E0+M1+E2$	0.0297(75)	0.0359(13)
^{166}Yb	754.8	$E0+M1+E2$	0.0158(45)	0.017(3)
^{166}Yb	814.5	$M1$	0.0069(28)	0.010(1)
^{154}Sm	911.0	$E2$	0.0034(16)	0.00257(4)
^{154}Sm	1095.9	$E0+M1+E2$	$\leq$0.00672(62)	-

Nucleus	Transition	$\rho^2(E0)_{exp}$ $\times10^{-3}$	Accepted Value
^{152}Sm	$2_2^+ \rightarrow 2_1^+$	56(14)	69(6)
^{154}Sm	$2_2^+ \rightarrow 2_1^+$	$\leq$ 9.4(15)	-

Table 6.2: Summary table of results from Sections 6.4 and 6.5.

the $2_2^+ \rightarrow 4_1^+$ K electron peak. The dependence of the upper limit electron measurement on the two fit constraints is shown in Figure 6.33. The maximum value in Figure 6.33 is approaching 200 counts, for a centroid shift of -14 keV and peak width σ 6.5 keV, both of which are significantly higher than would be expected. Using the calculation from Section 6.5, with the favoured $B(E2)$ and δ values and an upper limit of 200 electrons taken from Figure 6.33, a value of $\rho^2(E0) \leq 49.5 \times 10^{-3}$ is computed.

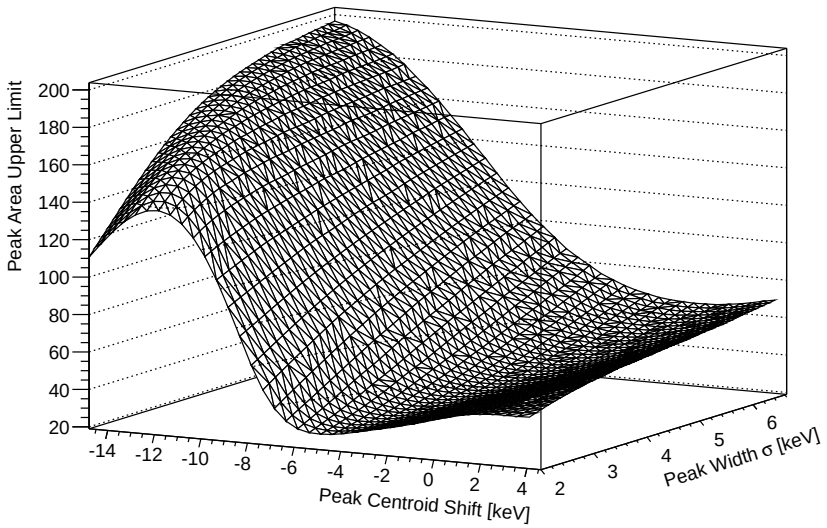

Figure 6.33: Electron fit area parameter surface. Shown is the upper limit of the electron peak area, for the fit of the ^{154}Sm $2_2^+ \rightarrow 2_1^+$ K electron, plotted as a function of the two constrained parameters, peak width σ and peak shift (centroid).

The justification given for selection of the fit constraints, and the consistent result obtained for $\alpha_{K,exp}$ of the $2_2^+ \rightarrow 4_1^+$ transition, are sufficient to give confidence in the parameters selected and the upper limit presented in Table 6.2. From the behaviour of the surface, shown in Figure 6.33, as a function of centroid shift, it is apparent that the upper limit is heavily dependant on local fluctuations of the background. Effectively,

the upper limit is the answer to the question *"What is the largest peak that could be obscured by background variation at the location specified?"* Understanding this is crucial in establishing confidence in the present measurement, which is significantly smaller than Bohr-Mottelson and IBA predictions given in Section 5.1. To further illustrate this point the following example is given: assuming the Bohr-Mottelson collective prediction for a β-band of $\rho^2(E0) = 100 \times 10^{-3}$, and using the peak efficiencies and clearly measured γ-peak area given in Section 6.5, an electron peak area of 391 counts would be expected. Randomly generated Gaussian peaks with an area of 391 and peak width $\sigma = 3.5\,\text{keV}$ and $\sigma = 5\,\text{keV}$ are shown, in Figures 6.34 and 6.35 respectively, against the measured electron spectra. In both cases the likelihood that a peak of the size shown could be obscured by the background in the data is small, even with the large uncertainties in the background.

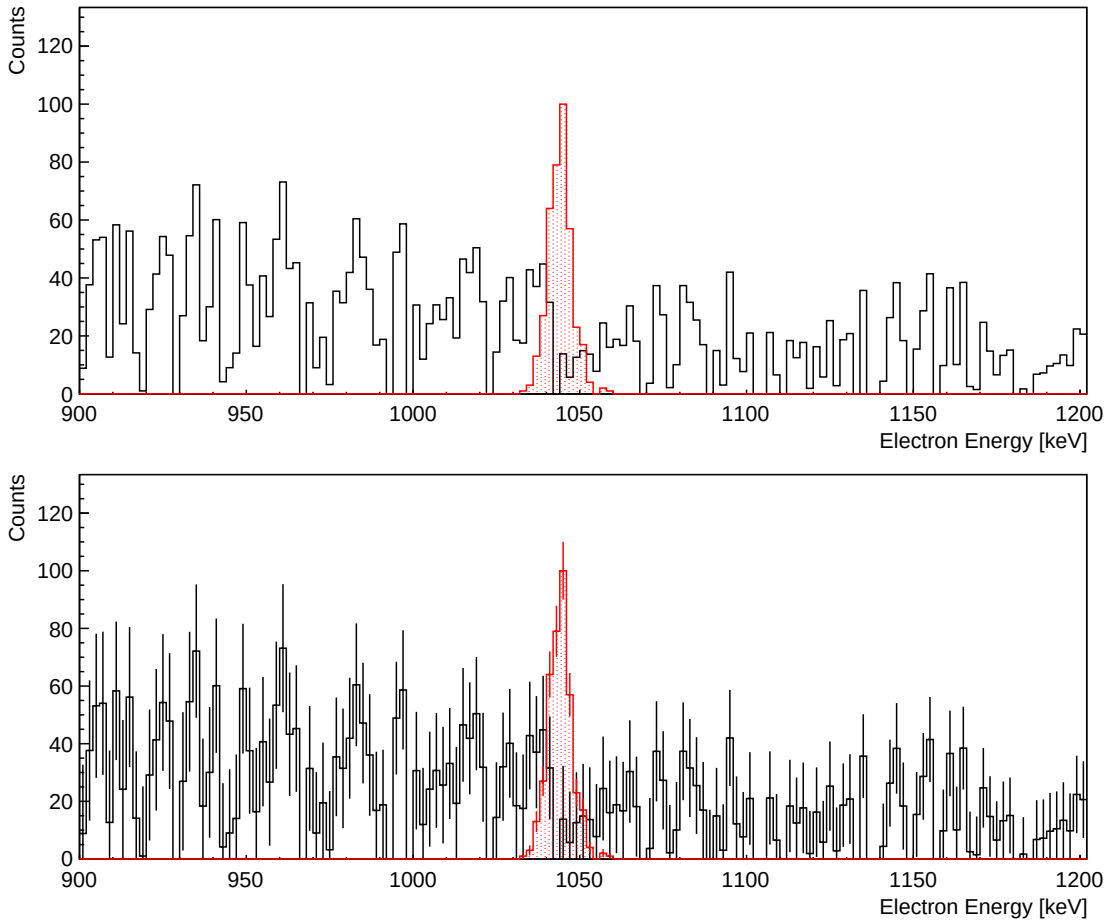

Figure 6.34: ^{154}Sm high energy electron spectrum gated on Γ_1 transition, alongside Gaussian peak with area as expected from $\rho^2(E0) = 100 \times 10^{-3}$ prediction and observed γ intensity. Overlain peak is of width $\sigma = 3.5$ keV and centroid shift -5 keV, as expected from the $2_2^+ \rightarrow 4_1^+$ peak. Image is shown with and without error bars as the information they provide is important but their presence hinders visual assessment.

6.6.2 Interpretation

Without a measurement of $\rho^2(E0; 0_2^+ \rightarrow 0_1^+)$ it is difficult to make overarching claims regarding the nature of the 0_2^+ band in ^{154}Sm. However, the result obtained for $\rho^2(E0; 2_2^+ \rightarrow 2_1^+)$ presents an interesting challenge for the interpretation of the 2_2^+ state and comparison

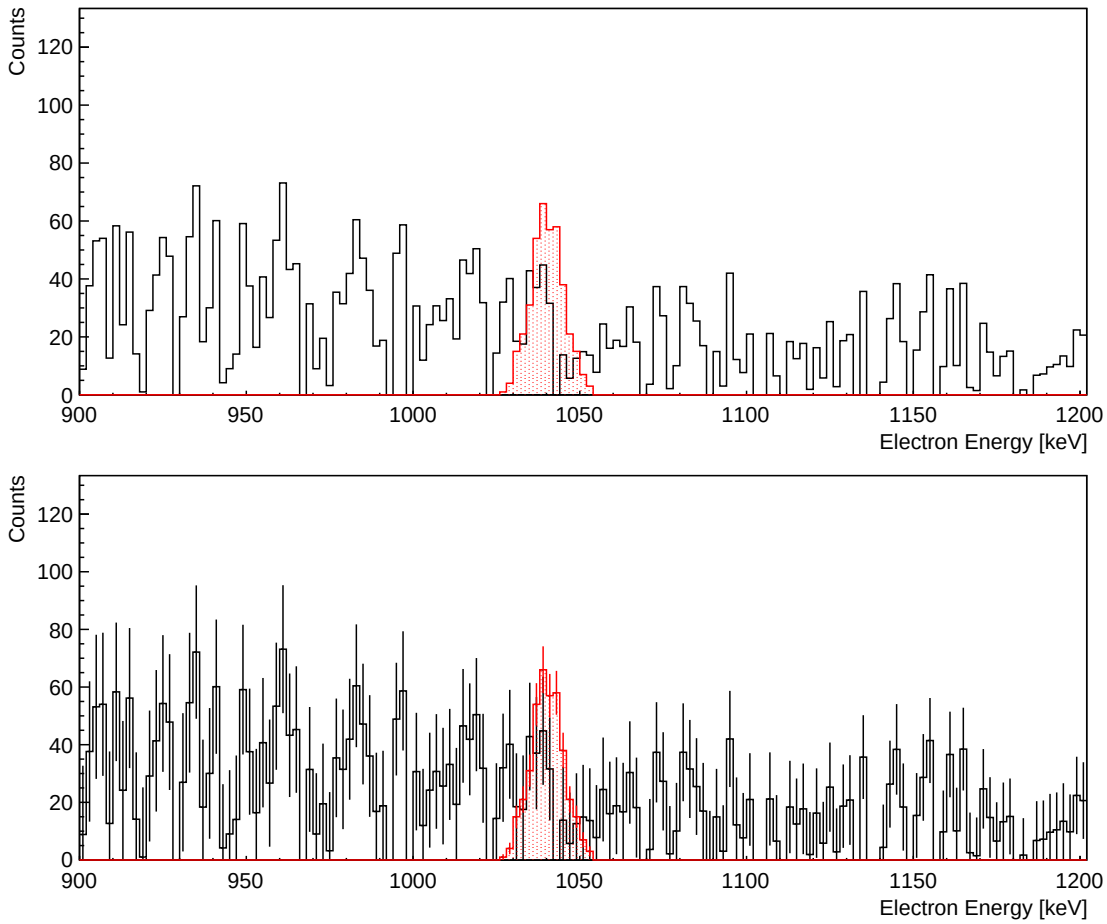

Figure 6.35: As Figure 6.34 but with peak width $\sigma = 5$ keV and centroid shift -9 keV to demonstrate the more extreme case.

of the measured value to predictions made by various models can give useful evidence in support or opposition of the models.

For a pure β-vibrational band of the Bohr-Mottelson picture, $\rho^2(E0; I_\beta^+ \rightarrow I_1^+)$ should have a value of the order 100×10^{-3} and there should be no I dependence [15]. This is far larger than the measured upper limit $\rho^2(E0; 2_2^+ \rightarrow 2_1^+) \leq 9.39(1.47) \times 10^{-3}$. Figures 6.34 and 6.35 serves to illustrate that such a large value is outside of reasonable possibility. Hence, it must be concluded that the 2_2^+ state in ^{154}Sm cannot be described as the 2_β^+ state of the Bohr-Mottelson macroscopic collective interpretation.

Calculations performed by P. Van Isacker [27, 121], in the more general collective picture of the IBA, predict $\rho^2(E0; 2_2^+ \rightarrow 2_1^+) = 39$. This value lies between the measured upper limit and the Bohr-Mottelson prediction, but is still notably larger than the upper limit presented in this work. This IBA prediction is within the experimental limit that would be given in this work if less stringent constraints were placed on the electron fit parameter, as illustrated in Figure 6.33. As explained in the previous section, the consistency of the results obtained for the other α_K measurements across ^{152}Sm, ^{166}Yb and ^{154}Sm leads to the conclusion that such large values are not to be expected and the presented upper limit should be accepted. Consequently it must be concluded that the IBA fails to reproduce the behaviour of the the 2_2^+ state with regards to $E0$ transitions.

Having concluded that neither of the models considered here adequately describe the

observed 2_2^+ state of ^{154}Sm state mixing should be considered: Could mixing between a 2^+ β-like collective state, as described by either model, and another 2^+ state could produce the observed result? Band mixing of ^{154}Sm was discussed in Section 5.1. In Reference [114] it was suggested that little mixing between the 0_1^+ and 0_2^+ bands should be expected. The measured $\rho^2(E0)$ value would appear to support this assertion as mixing between bands should strengthen the $E0$ transitions between the mixed bands [15]. Mixing between the 0_2^+ state and 0_3^+ state, believed to be a spherical coexisting configuration, was also discussed in Reference [114]. It was shown that there is a maximum mixing amplitude of 4% between the two excited 0^+ states. It would be unlikely that there would be significantly higher mixing between the 2_2^+ and 2_3^+ states [122] despite their proximity, being located at 1177.8 keV and 1286.3 keV respectively. Mixing with the 2_γ^+ state at 1440 keV by a $\Delta K = 2$ coupling of the two rotational bands might also be possible. This would naturally only mix the states with $I \geq 2$ of the 0_2^+ band.

Here it is worth considering the mixing amplitude required in a simple two-state mixing solution in order to justify the observed $E0$ strength. Assuming an initial unperturbed β-like 2_β^+, as considered in the two comparison models, mixing with an unspecified state 2_x^+ resulting in the observed states:

$$|2_2^+\rangle = a|2_\beta^+\rangle - b|2_x^+\rangle \quad \text{and} \tag{6.9}$$

$$|2_X^+\rangle = a|2_x^+\rangle + b|2_\beta^+\rangle\,, \tag{6.10}$$

where $a^2 + b^2 = 1$. By definition the measured $\rho^2(E0)$ limit is given by

$$\rho^2(E0; 2_2^+ \to 2_1^+)_{exp} \geq \left| \frac{\langle 2_1^+|\hat{T}(E0)|2_2^+\rangle}{eR_0^2} \right|^2 . \tag{6.11}$$

Hence by manipulation of the relation:

$$\langle 2_1^+|\hat{T}(E0)|2_2^+\rangle = a\langle 2_1^+|\hat{T}(E0)|2_\beta^+\rangle - b\langle 2_1^+|\hat{T}(E0)|2_x^+\rangle\,, \tag{6.12}$$

one may write:

$$\rho^2(E0; 2_2^+ \to 2_1^+)_{exp} \geq \left| \pm a\sqrt{\rho^2(E0; 2_\beta^+ \to 2_1^+)} \mp b\sqrt{\rho^2(E0; 2_x^+ \to 2_1^+)} \right|^2 . \tag{6.13}$$

In this final equation there are sign ambiguities, as the signs of the unperturbed $\hat{T}(E0)$ matrix elements are not known and the state mixing potential is not specified as attractive or repulsive (sign of b). However, if one assumes $\rho^2(E0; 2_x^+ \to 2_1^+) \to 0$, as is the case for the 2_γ^+ band or for a coexisting or quasi-particle state with no mixing with the ground state band, then Equation (6.13) simplifies. For the maximum mixing amplitude, $a = b = 1/\sqrt{2}$, the measured upper limit gives the relation

$$\rho^2(E0; 2_\beta^+ \to 2_1^+) \leq 17.8(2.9) \times 10^{-3}\,, \tag{6.14}$$

which is still significantly smaller than either of the two collective models presented here

predict. This shows that simple mixing, with either of the near-energy candidate 2^+_x states, is insufficient to support either interpretation of a collective β-like 2^+_2 state.

It must be concluded that a different interpretation of the 2^+_2 state is required, potentially a more complex sum of many 2^+ states with negative interference of non-zero $\hat{T}(E0)$ matrix elements. In the IBA the total $E0$ strength depends on the sum of many n_d components, even small changes of admixtures from other states may decisively change the n_d distribution, reducing $E0$ strength [28]. Alternatively, it may be concluded that the very small $E0$ strength, inconsistent with either collective model, indicates that the 2^+_2 state is largely quasi-particle in nature with little collective contribution. Such an interpretation is supported by the $B(E2; 2^+_2 \rightarrow I^+_1)$ values measured in Reference [120] and discussed in Section 5.1, which are smaller than predicted by collective models. In support of such an interpretation, experiments using the ^{152}Sm$(t,p)^{154}$Sm reaction to populate states in ^{154}Sm, could be performed to investigate the neutron-pairing component of state wave-functions. Previous (t,p) work failed to populated the 2^+_2 state [135].

Finally, it should be remarked that the $\rho^2(E0; 2^+_2 \rightarrow 2^+_1)$ upper limit measured in this work agrees with an unconfirmed measurement reported in References [123, 122]. Importantly, in the same work a value of $\rho^2(E0; 0^+_2 \rightarrow 0^+_1) \approx 100 \times 10^{-3}$ was reported, which is consistent with a collective interpretation of the 0^+_2 state. The energy spacing of the 0^+_2, 2^+_2, 4^+_2 and $6^+_{(3)}$ states is indicative of a rotational band. As such, any interpretation of the nature of the 2^+_2 state as having a majority component incompatible with the interpretation of the 0^+_2 state, should be approached with caution.

7

Conclusions

In this thesis, an overview of techniques for performing electron spectroscopy experiments with the SAGE spectrometer was presented. Unique contributions found in this work are the peak-fitting methods introduced in Section 4.1 and implemented throughout the work, and the background suppression techniques introduced in Section 4.4 and used to great effect with main experimental dataset in Section 6.1. The motivation for this work was the measurement of sparsely-known monopole transitions strengths in rare-earth nuclei. In Section 2.2, the relation of $E0$ transitions strength to key behaviours inside the nucleus was explained. Results were presented for the test case of ^{154}Sm, in which the $E0$ measurement acts as a probe of β-vibrational collective behaviour.

7.1 Experimental Summary

The primary experimental aims were to measure the monopole transitions strengths $\rho^2(E0; 0_2^+ \to 0_1^+)$ and $\rho^2(E0; 2_2^+ \to 2_1^+)$ in ^{154}Sm and to determine the feasibility of the experimental method for further measurements in the region.

Large β-particle background, from fusion-evaporation reactions with the target frame, rendered measurement of the electron peaks of interest in singles spectra impossible. As a result, focus was placed on background suppression in $\gamma\gamma$ and γe^- events. This meant a loss of ability to measure the $0_2^+ \to 0_1^+$ transition, which would only be observed as a one-step de-excitation. Following development of time-random and Compton-scattering background subtraction of the data set, clean γ-gated electron spectra and γ-gated γ-ray spectra were produced, from which conversion coefficients could be calculated.

Conversion coefficient calculations were normalised to 20 yrast transitions across 3 nuclei and 2 populations methods, shown in Figure 6.15. The resulting normalisation factor $\Lambda = 0.522 \pm 0.040$ indicated a particularly large effective dead-time of JUROGAMII, approaching 50%. High incident particle rates can increase effective dead time in JUROGAMII due to genuine pile up in the detector elements and false coincidence in BGO suppression shields, leading to overzealous event vetoing. Despite this, the number appears large, indicating some factor unaccounted for in the normalisation. This cements the need for a comprehensive normalisation, such as the one performed. Subsequently, using this normalisation coefficient, six conversion coefficients of known transitions were correctly measured in the $E_e > 500\,\text{keV}$ low statistics region. Furthermore, in Section 6.3 consistent results are obtained using the same normalisation extended to $\gamma\gamma\gamma$ and $\gamma\gamma e^-$ triple coincidences.

For the $2_2^+ \to 2_1^+$ transition of ^{154}Sm, a final result for the conversion coefficient was

obtained of $\alpha_K(E0; 2_2^+ \rightarrow 2_1^+) \leq 0.00672(62)$. This value equates to a monopole transition strength of $\rho^2(E0; 2_2^+ \rightarrow 2_1^+) \leq 9.39(1.47) \times 10^{-3}$. The calculated transition strength contradicts both of the collective models considered in this work, showing a clear need for further investigation.

7.2 Improvements for Future Work

The main deficiency of this work was the inability to measure the $0_2^+ \rightarrow 0_1^+$ electron transition. Before attempting to repeat the measurement for ^{154}Sm, or extend the method to investigate $E0$ transitions in other rare-earth nuclei, improvements must be made.

The energy of the collective states of interest, and subsequently of the $E0$ transitions from them, are at energies where the efficiency of SAGE is low. In order to optimise SAGE for detection of the high-energy electrons of interest ($E_e > 500\,\text{keV}$), several alterations can be made from the experimental setup used in this work. For electrons with energy greater than $\sim 200\,\text{keV}$, the main limitation on transport efficiency results from their orbital radii being greater than the target chamber aperture, as shown in Figure 3.10. Increasing the current in the solenoid coils, in order to maximise the axial magnetic field, will increase the transport efficiency for high-energy electrons by reducing their orbital radii. Full-energy peak efficiency is then further affected by detector interactions. At high electron energies, punch through of the detector becomes likely, as shown in Figure 3.11. Increasing the thickness of the SAGE silicon detector will reduce this effect. Scattering within the detector is also a major effect for high-energy electrons requiring further development of addback techniques, as discussed in Section 3.2.2. Finally, if the detection of only high-energy electrons are of interest, operating the potential barrier at its highest setting will maximise suppression of low-energy electrons with little effect on detection efficiency for high-energy electrons. Doing this will enable running at higher rates without being paralysed by δ-electrons and low-energy conversion electrons, which have large conversion coefficients.

Owing to the high energy of the transitions under consideration, the electron conversion branch is always small and, even with improved efficiency, background suppression will still be imperative. The background subtraction, which was shown to be particularly effective in this work, can be further improved for future experiments. The γe^- coincidence timing gate used in this work was 170 ns wide compared to a total event width of 400 ns. Ideally the event width should be made wider, at the cost of a reduction in experimental rate. Doing so improves the sample size for the time-random background spectrum and allows for greater separation between the genuine coincidence peak and the selection for the time-random background. Together these changes produce a cleaner time-random background subtraction. Careful beam tuning, to reduce the amount of random contaminant present to begin with, is also advisable.

The inclusion of more coincident data handles would increase the degree of suppression that can be achieved. One advantage of SAGE is the ability to perform high-fold γ-coincidence measurements with JUROGAMII. The effectiveness of high-fold γ-gating is demonstrated in Section 6.3 for ^{167}Yb. However, for the target $0_2^+ \rightarrow 0_1^+$ transitions in

the even-even rare-earth nuclei, coincidence with high-fold γ-ray cascades, or even a single γ ray, may not be available. The 0_2^+ state in ^{154}Sm is fed by a 20% branch from the 2069 keV (2^+) state, a 33% branch from the 2131 keV (2^+) state and a 100% branch from the 2196 keV ($1, 2^+$) state; none of which can be discerned in the current data set.

Recoil detection is the fundamental element needed in such a situation and absent from the present work. Detection of a recoiling nucleus provides an additional data handle for all genuine beam-target interactions, even those which result in emission of only a single quanta of radiation, such as the $0_2^+ \rightarrow 0_1^+$ electron conversion in ^{154}Sm following direct population of the 0_2^+ state. The presented time-random background subtraction can then be performed using the coincidence time between detection of the emitted quanta and detection of the recoiling nucleus. By requiring recoil detection, coincidence decay events in the target chamber, which may include genuine $\gamma\gamma$ and γe^- events, are heavily suppressed.

Furthermore, in this work kinematic shifts of electrons were found to be particularly challenging as there were many unknowns. This was discussed in Section 6.2.1. Kinematic shift of electron peaks are particularly problematic when dealing with low statistics data, in which peak identification is difficult, or when performing spectroscopy of transitions with previously unmeasured energy, not performed in this work. By detecting a recoiling target, beam or product nucleus, the kinematic solutions are dramatically simplified, allowing for a full correction to be performed.

In the calculations of conversion coefficients, the angular correlations were discussed in Section 4.6.1 and taken to have have negligible effect. In the case of recoil detection, the alignment of the initial ensemble becomes constrained and the approximations made in this work are no longer correct. For future work involving recoil detection further investigation of angular correlations should be performed.

SAGE is designed to work with the RITU separator, which can detect recoiling products from fusion-evaporation reactions. It is not optimised for detection of recoiling target or beam nuclei in a CoulEx experiment, such as the one presented in this work. Some small fraction of the recoiling beam nuclei will be backscattered and detected in SAGE silicon detector. As nuclei are less easily constrained than electrons, this will occur in a negligible fraction of events. If recoil detection is to be used for future work, one must consider if a different reaction method is viable or if different apparatus is more appropriate.

7.3 Future Work

Using the experimental and analysis techniques outlined in this work, further measurements of monopole transition strength should be performed in the rare-earth region alongside development of theoretical models, including both collective and quasi-particle behaviour.

Confirmation measurements of the $0_2^+ \rightarrow 0_1^+$ and $2_2^+ \rightarrow 2_1^+$ $E0$ strengths in ^{154}Sm should be performed. This investigation can be extended to measurement of the $4_2^+ \rightarrow 4_1^+$ $E0$ strength if the required sensitivity can be achieved. The $4_2^+ \rightarrow 4_1^+$ measurement has the benefit of an additional coincident γ-ray transition in the yrast band, which can be used either to increase γe^- efficiency, or used for improved selectivity in a triple-coincidence $\gamma\gamma e^-$ measurement.

Following on from this work, near-identical experiments can be performed with ^{148}Nd and ^{150}Nd, both of which have candidate even-parity rotational-like bands built on 0_2^+ states at 916.8 and 675.9 keV respectively. The lifetimes of the 0_2^+ are measured in both nuclei allowing for calculation of monopole strength $\rho^2(E0; 0_2^+ \rightarrow 0_1^+)$ using the previously defined method. The lifetimes of the 2_2^+ states in both nuclei are also known. However, the mixing ratio $\delta(E2/M1)$ for the $2_2^+ \rightarrow 2_1^+$ transition is not known for ^{150}Nd. As a result, a measurement of $\rho^2(E0; 2_2^+ \rightarrow 2_1^+)$ is possible for both neodymium isotopes but would have large uncertainty for ^{150}Nd, an uncertainty which would be smaller for larger values of $\rho^2(E0)$. For the three cases stated above, and the other stable rare-earth isotopes, a CoulEx reaction of the type used in this work offers the best cross section for population of the states of interest. However, this reaction method poses a problem for the inclusion of recoil detection in the SAGE setup. SAGE is coupled with the RITU separator, which can be used to detect the forward-scattered target nuclei, but does not have the capability to identify scattered beam nuclei. The most forward-scattered target nuclei, close to the beam axis, corresponding to a close distance of approach. Detecting these target nuclei preferentially select multi-step CoulEx interactions rather than the two-step and one-step interactions which are the dominant population processes for the 0_2^+ and 2_2^+ states. The widest acceptance of RITU is $\pm 4.8°$ from the beam axis in the horizontal direction. Figure 7.1 shows the CoulEx population cross section for the 0_2^+ and 2_2^+ states of ^{154}Sm in the 65 MeV ^{16}O(^{154}Sm,^{154}Sm*)^{16}O reaction used in this work. This figure serves to demonstrate that such an angular limitation on the recoiling target nuclei seriously limits the population intensity that will be observed, and hence longer run time will be needed to collect the required statistics. However, this is balanced by the improvements to selectivity that recoil detection brings.

Inverse kinematics can be used to improve upon geometric limitation. Use of a heavy beam and light target will forward focus the scattering nuclei. As a result, a greater fraction of the reaction cross section corresponds to events accepted by the separator. At very forward angles this has little effect with regards to target scattering direction; for an samarium beam impinging on a oxygen target and a 4.8° scattered target acceptance, this corresponds to 170.3° scattering in the centre-of-mass-frame, whereas for the reversed setup the same scattered target acceptance corresponds to 170.2°, resulting in a minimal

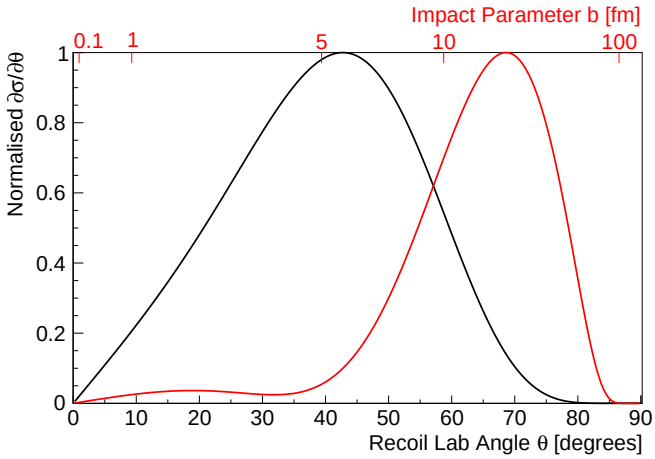

Figure 7.1: Coulex-population cross section for the excited 0_2^+ (black line) and 2_2^+ (red line) states in ^{154}Sm, shown as a function of target recoil angle θ. A secondary axis denoting values of impact parameter b is shown.

gain in cross section. Furthermore, neither samarium nor neodymium beams are currently available for use with SAGE setup, and ^{16}O is too light to be focused through RITU.

Prolonged beam runs with a CoulEx excitation from an ^{16}O beam (or similar Z nucleus) remains the preferred experimental method to investigate $E0$ transitions in the stable rare-earth nuclei with the SAGE and RITU setup.

For investigations beyond the stable isotopes of the region, fusion-evaporation or transfer reactions will be required. The SAGE and RITU setup is optimised for fusion-evaporation reactions. Such reactions will mainly produce neutron-rich nuclei and tend to produce nuclei in high-spin states. As a result, the 0_2^+ and 2_2^+ states of interest are unlikely to be populated directly and the intensity observed will be heavily dependent on feeding of these states.

To continue the investigation of the evolution of the samarium isotopes, a measurement should be made of $E0$ strength in radioactive ^{156}Sm ($t_{1/2} = 9.4\,\mathrm{h}$). This proton-deficient isotope could be produced by the ^{160}Gd(^{12}C,^{16}O)^{156}Sm α-transfer reaction. The reaction has a +6.159 MeV Q-value due to large binding energy of doubly-magic ^{16}O, which should result in suitable reaction cross sections. Furthermore, by detecting beam-like products at close to zero scattering angle, $L = 0$ transfer reactions will be preferentially selected, maximising observation of direct population of 0^+ states. However, caution is required as cross section for population in such reactions can be dependent on structural properties of the target states. There is a known excited 0^+ state in ^{156}Sm at 1068 keV, however the lifetime and branching ratios of the state, needed to calculate $\rho^2(E0)$, are unmeasured. As a result, continuing the investigation of the samarium isotopes to ^{156}Sm would require a two-part study.

Appendix A
JUROGAMII Angles

JUROGAM II Detector Angles

Array Position[(a)]	$\theta^{o(b)}$	$\phi^{o(c)}$
T01	157.6	0
T02	157.6	72
T03	157.6	144
T04	157.6	216
T05	157.6	288
T06	133.57	18
T07	133.57	54
T08	133.57	90
T09	133.57	126
T10	133.57	162
T11	133.57	198
T12	133.57	234
T13	133.57	270
T14	133.57	306
T15	133.57	342
Q01	104.5	15
Q02	104.5	45
Q03	104.5	75
Q04	104.5	105
Q05	104.5	135
Q06	104.5	165
Q07	104.5	195
Q08	104.5	225
Q09	104.5	255
Q10	104.5	285
Q11	104.5	315
Q12	104.5	345
Q13	75.5	15
Q14	75.5	45
Q15	75.5	75
Q16	75.5	105
Q17	75.5	135
Q18	75.5	165
Q19	75.5	195
Q20	75.5	225
Q21	75.5	255
Q22	75.5	285
Q23	75.5	315
Q24	75.5	345

Table 1: The JUROGAM II array specifications. [(a)] T is tapered detector, Q is Clover detector. [(b)] defined with respect to the beam direction. [(c)] ϕ=0^o is defined as vertically upwards, ϕ increases in a clockwise direction when the array is viewed from a position upstream. All angles are midpoint angles. Each Clover detector has four crystals - *a,b,c,d* (blue, black, green, and red respectively) arranged in a clockwise fashion when viewed from the Dewar side of the detector. The detectors are mounted such that *c & d* crystals are closest to θ=90^o. Each of the four crystals' midpoint angles subtend 4.5^o

.

Appendix B

Radius Energy Relations in SAGE

In this section the formulation for the minimum energy electron expected in each element of the SAGE detector shall be explained. Following this, the effectiveness of using this information to identify scattering events shall be shown. Details from Sections 3.1.1 and 3.2.1 will be assumed.

An electron emitted at the target position follows a helical path, the radius of which is given by:

$$r = \frac{P_\perp}{eB} \tag{B.1}$$

Where $P_\perp$ is the component of the electron's relativistic momentum perpendicular to the magnetic field. The SAGE detector is perpendicular to the field axis and centred to it. An unperturbed electron will remain tangential to the field axis. Hence the furthest radial point on the detector an unperturbed electron can reach will be given by twice this orbital radius. Therefore the minimum value $p_\perp$ required to reach a given detector element can be written in terms of the inner radius of the element r_{min}:

$$P_\perp = \frac{Br_{min}c}{2 \cdot 10^9} = 0.1499 \cdot Br_{min} \tag{B.2}$$

Where B is measured in Tesla, r_{min} in mm and $P_\perp$ has been converted to $^{MeV}/_c$. $P_\perp$ and $P_\parallel$ can be related to the total P_e by:

$$P_e^2 = P_\perp^2 + P_\parallel^2 \tag{B.3}$$

and with the usual trigonometric identities. The momenta may be related to the relevant kinetic energy by:

$$T_e = \sqrt{P_e^2 + 0.511^2} - 0.511 \tag{B.4}$$

$$P_e = \sqrt{T_e^2 + 2 \cdot T_e \cdot 0.511} \tag{B.5}$$

where the rest mass of the electron $m_e = 0.511^{MeV}/c^2$ has been substituded.

In order to pass the potential barrier an electron must have kinetic energy with respect to motion along the field $T_\parallel$ axis greater than $V \cdot q$. As an electron has a charge of one this gives $T_\parallel \geq V$ where the units are MeV and MV respectively, from which the minimum value of $P_\parallel$ can be given. For elements at larger radii $P_\parallel$ may be greater than this as the angle θ an electron makes with field axis must be below the value at which electrons are reflected by the magnetic field.

$$Tan^{-1}\left(\frac{P_\perp}{P_\parallel}\right) < \theta_{max}\,. \tag{B.6}$$

Hence the minimum energy an electron can have for in any given detector element is given by whichever is the larger of the following two equations:

$$T_{Barriermin} = \left((0.1499 \cdot Br_{min})^2 + V^2 + V \cdot 1.022 + 0.511^2\right)^{1/2} - 0.511 \tag{B.7}$$

$$T_{Anglemax} = \left(\left(\frac{0.1499 \cdot Br_{min}}{sin(\theta_{max})}\right)^2 + 0.511^2\right)^{1/2} - 0.511 \tag{B.8}$$

Any electron recorded with energy below the minimum for the detector element in which it was measured can be concluded to be the result of a scattering event.

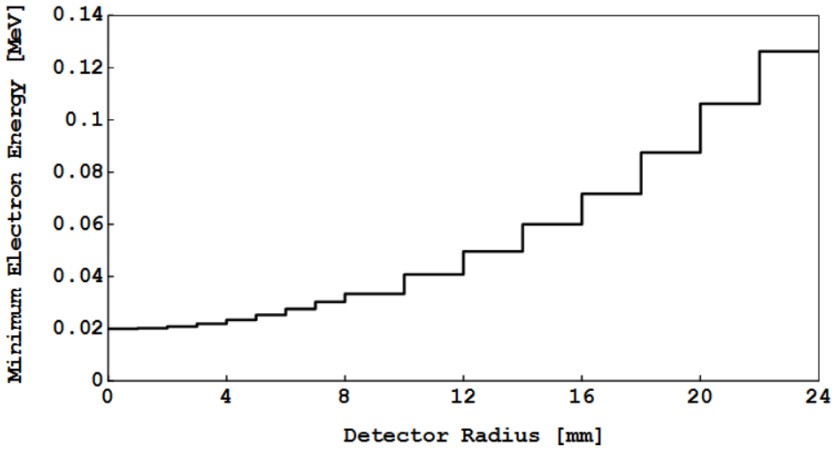

Figure B.1: This graph shows the minimum energy for unperturbed electron events across the radius of the SAGE detector. Values shown correspond to B=0.1T, θ_{max}=65°and V=0.02MV. Steps mark the start of new ring of detector elements.

Some additional uncertainty comes from B, θ_{max} and detector alignment. Following this only electrons in the region below 100 keV will be notably effected. Additionally because of the discreet nature of the element spacing an artificial step pattern is introduced to electron spectra in this region. Although the removal of the excluded events is legitimate, introducing an irregular shape to the background makes the fitting of genuine features more challenging. For both of these reasons the benefit from the exclusion of scattering events by this method is minimal.

Appendix C
Calibration Data

C.1 Sources

^{207}Bi γe^- source.[JYFL-91]
Experiment intensity 350±10 kBq.
Run time 4019±2 sec.

EuBa ^{154}Eu^{133}Ba γ source.[JYFL-80-81]
Eu experiment intensity 25.6±0.3 kBq
Ba experiment intensity 23.8±0.3 kBq
Run time 58302±2 sec.

^{133}Ba γe^- source.[JYFL-90]
Experiment intensity 307±3 kBq
Run time 6155±2 sec
^{133}Ba γe^- source did not match the stated calibration intensity. Source intensity renormalised using calibration fit from other sources.

E_γ	$\varepsilon_{oldcalib}$	ε_{fit}	Ratio
30.8	0.0048 (2)	0.0150 (4)	0.324(11)
35.1	0.0104 (2)	0.0294 (2)	0.350(8)
53.1	0.0412 (8)	0.0728 (6)	0.567(11)
80.89	0.0510 (6)	0.1020 (8)	0.450(8)
160.6	0.0522 (6)	0.1060 (6)	0.492(7)
223.2	0.0494 (6)	0.0970 (4)	0.508(7)
276.4	0.0460 (6)	0.0900 (4)	0.511(7)
302.9	0.0438 (6)	0.0868 (4)	0.505(7)
356	0.0396 (4)	0.0812 (4)	0.487(5)
383.8	0.0382 (4)	0.0786 (2)	0.485(6)

Table C.1: ^{133}Ba source adjustment data points.

Weighted mean calculated using:

$$\bar{x} = \frac{\sum x_i/\sigma_i^2}{\sum 1/\sigma_i^2} \qquad V(\bar{x}) = \frac{1}{\sum 1/\sigma_i^2} \tag{C.1}$$

Giving $\bar{S} = 0.480 \pm 0.003$ and hence an intensity of 147 ± 2kBq.

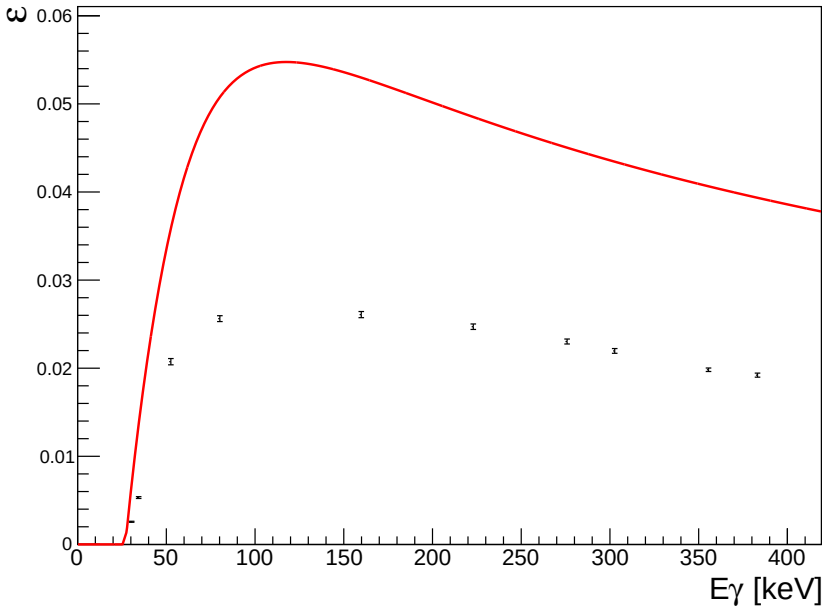

Figure C.1: ^{133}Ba source scaling.

C.2 Gamma rays

Neighbouring transitions with energy seperation significantly less than peak σ were fitted as a single peak with summed intensity.

Energy [KeV]	Source	Branch Intensity [%]	Calculated Efficiency [%]
30.8	^{133}Ba	96.1(21)	1.008(26)
30.9	EuBa ^{133}Ba	96.1(21)	1.458(34)
35.1	^{133}Ba	20.8(4)	2.14(4)
35.1	EuBa ^{133}Ba	20.8(4)	3.16(6)
39.9	EuBa ^{152}Eu	58.9(8)	4.16(8)
45.6	EuBa ^{152}Eu	13.5(2)	4.76(8)
53.2	EuBa ^{133}Ba	2.14(3)	6.96 (12)
53.2	^{133}Ba	2.14(3)	8.42 (16)
80.9	^{133}Ba	35.5(7)	9.88 (14)
80.9	EuBa ^{133}Ba	35.5(7)	10.18 (14)
121.8	EuBa ^{152}Eu	28.7(2)	10.5 (1)
160.6	^{133}Ba	0.638(5)	11.2 (2)
160.6	EuBa ^{133}Ba	0.638(5)	10.52 (14)
223.2	^{133}Ba	0.453(3)	10.3 (2)
223.2	EuBa ^{133}Ba	0.453(3)	9.82 (12)
244.7	EuBa ^{152}Eu	7.61(4)	8.94 (10)
276.4	^{133}Ba	7.16(5)	9.40 (14)
276.4	EuBa ^{133}Ba	7.16(5)	9.34 (12)
295.9	EuBa ^{152}Eu	0.448(6)	8.46 (14)
302.9	^{133}Ba	18.3(1)	8.90 (12)
302.9	EuBa ^{133}Ba	18.3(1)	8.0 (1)
344.3	EuBa ^{152}Eu	26.6(5)	7.74 (16)
356.0	^{133}Ba	62.05(1)	8.18 (10)

356.0	EuBa ^{133}Ba	62.05(1)	7.9 (1)
367.8	EuBa ^{152}Eu	0.862(1)	7.48 (12)
383.8	^{133}Ba	8.94(6)	7.84 (10)
383.8	EuBa ^{133}Ba	8.94(6)	7.58 (10)
411.1	EuBa ^{152}Eu	2.24(3)	7.52 (12)
444.0	EuBa ^{152}Eu	3.16(3)	6.58 (8)
534.2	EuBa ^{152}Eu	0.0428(12)	6.1 (4)
569.7	^{207}Bi	97.75(3)	5.7 (2)
656.5	EuBa ^{152}Eu	0.145(2)	5.86 (18)
688.6 *	EuBa ^{152}Eu	0.878(11)	5.46 (10)
778.9	EuBa ^{152}Eu	13.0(1)	4.94 (8)
867.4	EuBa ^{152}Eu	4.26(3)	4.8 (6)
897.8	^{207}Bi	0.128(5)	4.58 (24)
922.8 *	EuBa ^{152}Eu	0.779(13)	4.34 (8)
964.1	EuBa ^{152}Eu	14.65(7)	4.46 (4)
990.2	EuBa ^{152}Eu	0.0313(14)	4.14 (48)
1005.3	EuBa ^{152}Eu	0.648(5)	4.76 (6)
1063.7	^{207}Bi	74.5(3)	4.14 (12)
1086.3 *	EuBa ^{152}Eu	12.0(1)	4.20 (4)
1111.9 *	EuBa ^{152}Eu	13.9(1)	4.06 (04)
1213.0	EuBa ^{152}Eu	1.43(1)	3.92 (04)
1249.9	EuBa ^{152}Eu	0.189(4)	4.02 (12)
1261.3	EuBa ^{152}Eu	0.0335(14)	3.94 (26)
1299.1	EuBa ^{152}Eu	1.62(1)	3.40 (6)
1408.0	EuBa ^{152}Eu	21.1(1)	3.46 (4)
1442.2	^{207}Bi	0.131(2)	3.62 (12)
1528.1	EuBa ^{152}Eu	0.282(5)	3.64 (8)
1771.2	^{207}Bi	6.87(3)	2.84 (8)

Table C.2: γ Efficiency calibration points.

* Multiple peaks with significant overlap were intensity summed following fitting.

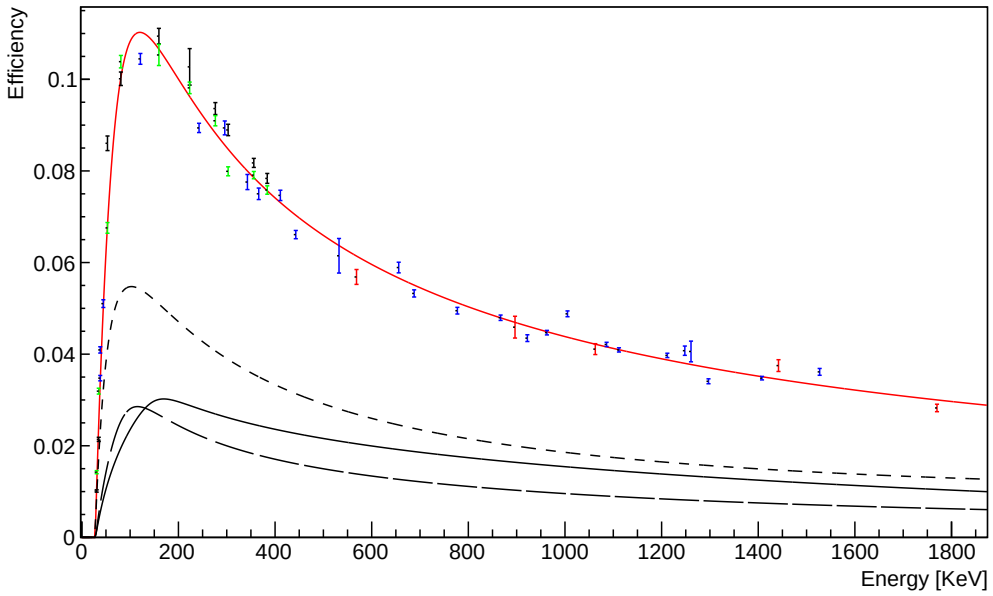

Figure C.2: γ efficiency data and line of fit for the complete array. Below the data are shown curves from the individual detector rings, 75.5°clover ring (solid line), 104.5°clover ring (dashed line) and 133.57°phase-one ring (dotted line). Differences between the two symmetric clover rings are attributed to attenuation by the target mount.

C.3 Electrons

Neighbouring transitions with energy separation significantly less than peak σ were fitted as a single peak with summed intensity.

Energy [KeV]	Source	Branch Intensity [%]	Calculated Efficiency [%]
41.9	^{133}Ba	51(2)	4.07(18)
74.7	^{133}Ba	9.66(15)	4.70(12)
124.6	^{133}Ba	0.149(3)	5.75(17)
155.9 *	^{133}Ba	0.0378(11)	6.8(5)
187.3	^{133}Ba	0.0379(6)	6.27(28)
240.4	^{133}Ba	0.329(5)	5.43(14)
267.1 *	^{133}Ba	0.760(13)	5.10(13)
297.7 *	^{133}Ba	0.111(2)	4.11(11)
320.0	^{133}Ba	1.31(1)	4.05(0.08)
349.9 *	^{133}Ba	0.421(3)	3.67(8)
378.9 *	^{133}Ba	0.0303(5)	3.19(18)
481.7	^{207}Bi	1.54(2)	2.11(0.07)
556.7 *	^{207}Bi	0.553(1)	1.62(5)
975.7	^{207}Bi	7.08(17)	0.194(7)
1050.5 *	^{207}Bi	2.28(8)	0.143(5)

Table C.3: e^- Efficiency calibration points.
* Multiple peaks with significant overlap were intensity summed following fitting.

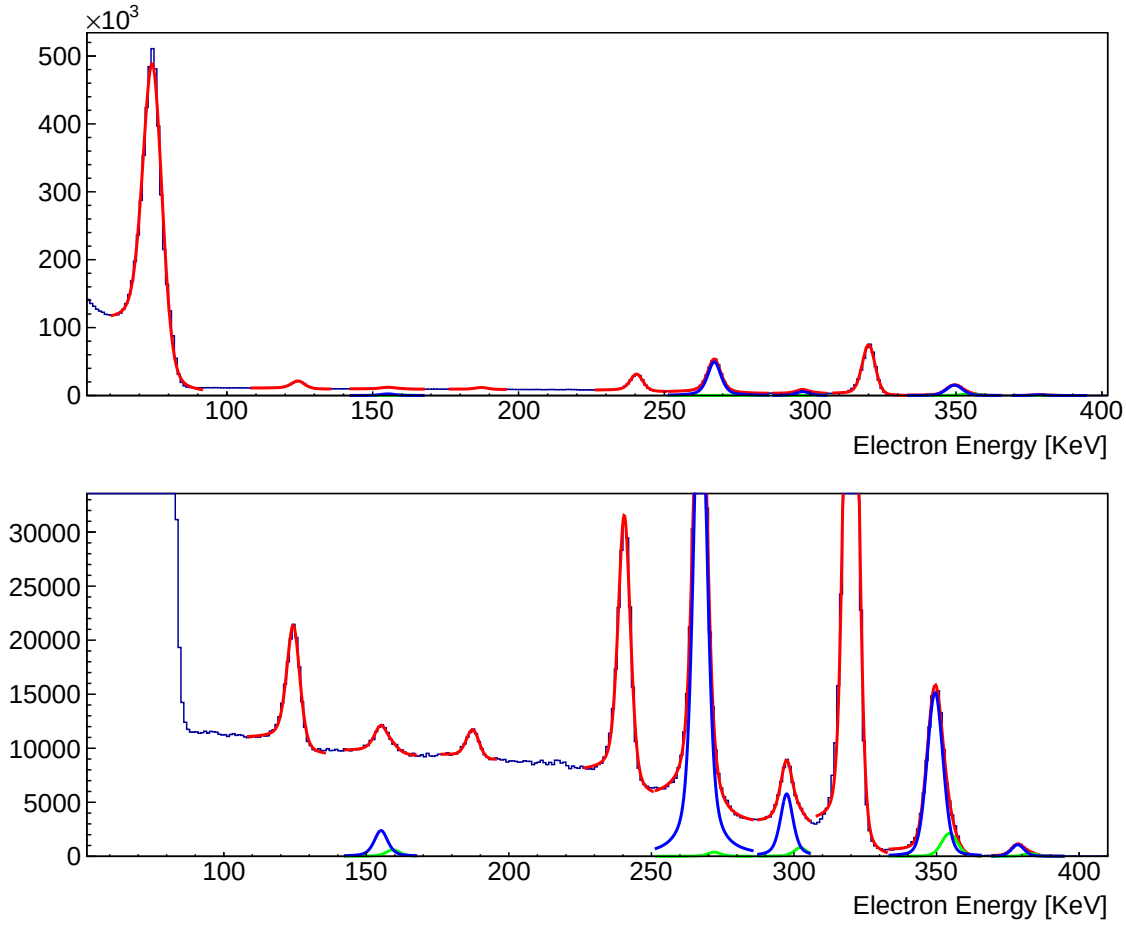

Figure C.3: ^{133}Ba e^- calibration data, peak fits shown in red. Blue and green peaks indicate decomposition of a multi-peak fit.

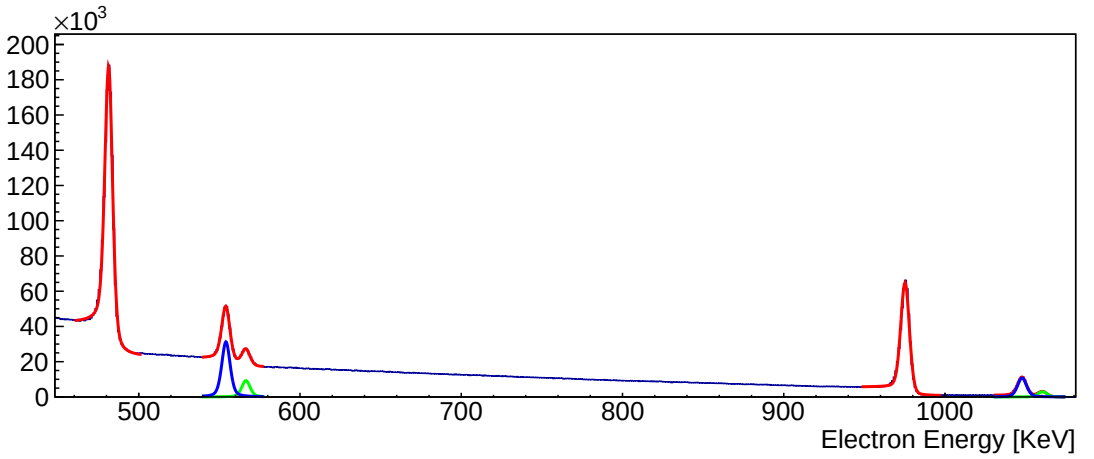

Figure C.4: ^{207}Bi e^- calibration data, peak fits shown in red. Blue and green peaks indicate decomposition of a multi-peak fit.

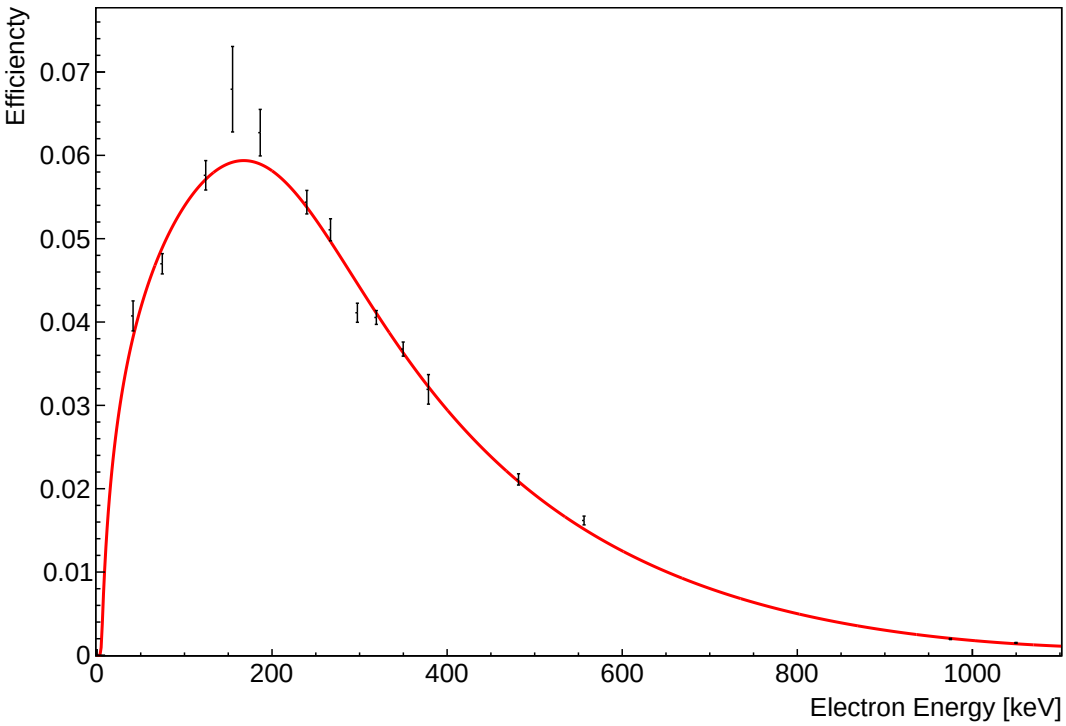

Figure C.5: Efficiency data and line of fit for the SAGE electron detector array.

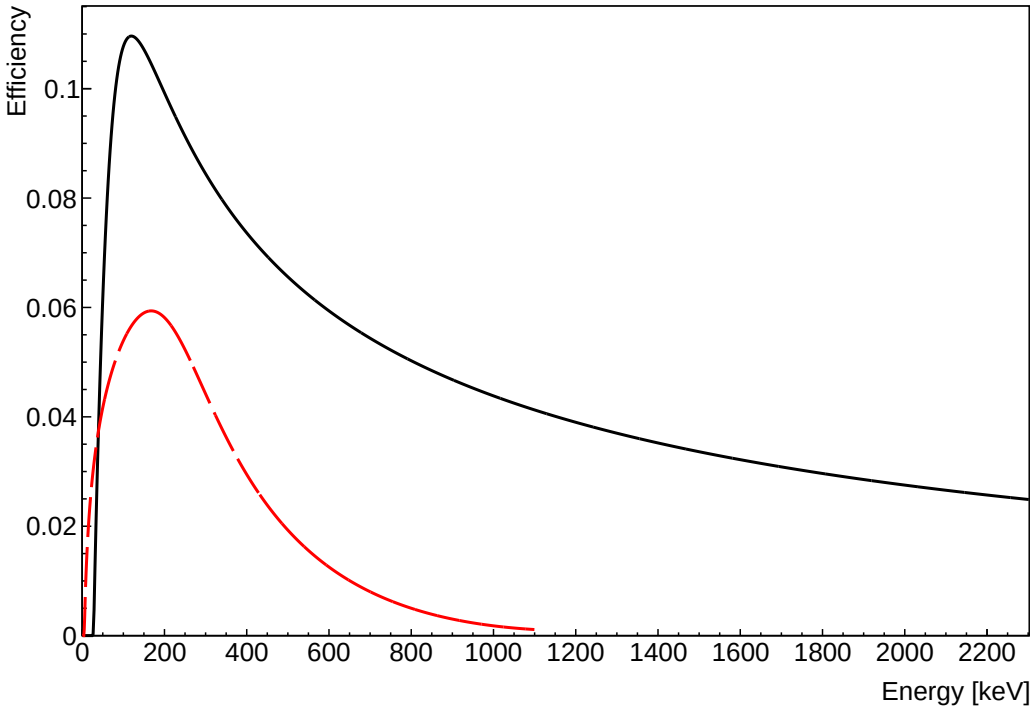

Figure C.6: Calibrated γ-efficiency curve for all of JUROGAMII (solid black) shown along side electron-efficiency curve of SAGE (dashed red).

List of Abbreviations

JYFL University of Jyväskylä

SAGE Silicon And GErmanium array

GREAT Gamma Recoil Electron Alpha Tagging focal plane spectrometer

RITU Recoil Ion Transport Unit

HPGe High Purity Germanium

BGO Bismuth Germanium Oxide

DSSSD Double Sided Silicon Strip Detector

MWPC Multi Wire Proportional Counter

ToF Time of Flight

PMT Photo Miltiplier Tube

TDR Total Data Readout

TDREB TDR Event Builder

CoulEx Coulomb excitation

DAQ Data Acquisition system

CDF Cumulative Distribution Function

pps particles per second

pnA particles nano Amp

IBA Interacting Boson Approximation

GCM Geometrical Collective Model

References

[1] J. M. Blatt and V. F. Weisskopf. *Theoretical Nuclear Physics*. Dover Publications Inc, 1979.

[2] D.J. Rowe and J.L. Wood. *Fundamentals of Nuclear Models: Foundational Models*. World Scientific, 2010.

[3] K. Heyde. *Basic Ideas and Concepts in Nuclear Physics: An Introductory Approach, Third Edition*. Fundamental and applied nuclear physics series. Taylor & Francis, 2004.

[4] W. Greiner, J.A. Maruhn, and D.A. Bromley. *Nuclear Models*. Springer London, Limited, 1997.

[5] K.S. Krane. *Introductory Nuclear Physics*. Wiley, 1987.

[6] L. Meitner. In: *Z. Phys.* 29 (1924), p. 169.

[7] H.R. Hulme. In: *Proc. R. Soc. Lond. A* 138 (1932), p. 643.

[8] H.M. Taylor and N.F. Mott. In: *Proc. R. Soc. Lond. A* 138 (1932), p. 665.

[9] I.M. BAND et al. In: *At. Data Nucl. Data Tables* 81.12 (2002), pp. 1 –334.

[10] F. Rosel et al. In: *At. Data Nucl. Data Tables* 21.45 (1978), pp. 291 –514.

[11] J. Gerl et al. In: *At. Data Nucl. Data Tables* 94.5 (2008), pp. 701 –738.

[12] T. Kibedi et al. In: *Nuc. Inst. Meth. A* 589.2 (2008), pp. 202 –229.

[13] T. Kibdi and R.H. Spear. In: *At. Data Nucl. Data Tables* 89.1 (2005), pp. 77 –100.

[14] A. De Shalit and I. Talmi. *Nuclear Shell Theory*. Dover Books on Physics. Dover Publications, Incorporated, 2004.

[15] J.L. Wood et al. In: *Nuclear Physics A* 651.4 (1999), pp. 323 –368.

[16] A.S. Reiner. In: *Nuclear Physics* 27.1 (1961), pp. 115 –133.

[17] A. Bohr and B.R. Mottelson. *Nuclear Structure*. v. 2. W. A. Benjamin, 1975.

[18] L. Fortunato. English. In: *Eur. Phys. J. A* 26.1 (2005), pp. 1–30.

[19] Amand Faessler, Walter Greiner, and Raymond K. Sheline. In: *Nuclear Physics* 70.1 (1965), pp. 33 –88.

[20] John O. Rasmussen. In: *Nuclear Physics* 19.0 (1960), pp. 85 –93.

[21] A. Arima and F. Iachello. In: *Phys. Rev. Lett.* 35 (16 Oct. 1975), pp. 1069–1072.

[22] R. F. Casten and D. D. Warner. In: *Rev. Mod. Phys.* 60 (2 Apr. 1988), pp. 389–469.

[23] D. D. Warner and R. F. Casten. In: *Phys. Rev. C* 28 (4 Oct. 1983), pp. 1798–1806.

[24] R. Gilmore, C. M. Bowden, and L. M. Narducci. In: *Phys. Rev. A* 12 (3 Sept. 1975), pp. 1019–1031.

[25] R. Gilmore. In: *J. Math.Phys.* 20.5 (1979), pp. 891–893.

[26] A. E. L. Dieperink, O. Scholten, and F. Iachello. In: *Phys. Rev. Lett.* 44 (26 June 1980), pp. 1747–1750.

[27] S. Zerguine, P. Van Isacker, and A. Bouldjedri. In: *Phys. Rev. C* 85 (3 Mar. 2012), p. 034331.

[28] P. von Brentano et al. In: *Phys. Rev. Lett.* 93 (15 Oct. 2004), p. 152502.

[29] P. Papadakis. "AIP Conference Proceedings". In: vol. 1090. pp. 14-20. 2009.

[30] J. F. Krizmanica, M. L. Cherryc, and R. E. Streitmatter. In: *Nuc. Inst. Meth. A* 563 (2006), pp. 303–305.

[31] Y. Asano and et al. S. Mori. In: *Nuc. Inst. Meth. A* 259 (1987), pp. 438–446.

[32] B. Klank and R.A. Ristinen. "Proc. Int. Conf. on Radioactivity in Nuclear Spectroscopy". In: 1969.

[33] N. Laulainent and H. Bichsel. In: *Nuc. Inst. Meth. A* 104 (1972), 531539.

[34] F. Bell et al. In: *Nuc. Inst. Meth. A* 194 (1982), pp. 423–427.

[35] P. Papadakis. "Combining in-beam γ-ray and conversion electron spectroscopy, The sage spectrometer". PhD thesis. University of Liverpool Oliver Lodge Laboratory, 2010.

[36] Glenn F. Knoll. *Radiation Detection and Measurement*. 3rd. John Wiley & Sons, 1999.

[37] G. Duchne et al. In: *Nuc. Inst. Meth. A* 432.1 (1999), pp. 90 –110.

[38] C.W. Beausang et al. In: *Nuc. Inst. Meth. A* 313 (1992), pp. 37 –49.

[39] R. D. Evans. *The Atomic Nucleus*. McGraw-Hill Book Company, 1955.

[40] K. Alder and A. Winther. *Electronmagnetic Excitation*. North-Holland publishing Company, 1975.

[41] A. Ghiorso et al. In: *Nuc. Inst. Meth. A* 269.1 (1988), pp. 192 –201.

[42] Willis E. Lamb. In: *Phys. Rev.* 58 (8 Oct. 1940), pp. 696–702.

[43] M. Leino. In: *Nuc. Inst. Meth. B* 204.0 (2003), pp. 129 –137.

[44] M. Leino. In: *Nuc. Inst. Meth. B* 126 (1997), pp. 320 –328.

[45] N. Bohr. In: *Phys. Rev.* 59 (3 Feb. 1941), pp. 270–275.

[46] M. Paul. In: *Nuc. Inst. Meth. B* 52.34 (1990), pp. 315 –321.

[47] P. Armbruster et al. In: *Nuc. Inst. Meth.* 91.3 (1971), pp. 499 –507.

[48] T. Enqvist et al. In: *Nuc. Inst. Meth. B* 204.0 (2003), pp. 138 –140.

[49] J. Sarn et al. In: *Nuc. Inst. Meth. A* 654.1 (2011), pp. 508 –521.

[50] H. Kankaanp et al. In: *Nuc. Inst. Meth. A* 534.3 (2004), pp. 503 –510.

[51] R.D. Page et al. In: *Nuc. Inst. Meth. B* 204.0 (2003), pp. 634 –637.

[52] W.R. Leo. *Techniques for Nuclear and Particle Physics Experiments: A How-To Approach*. Springer-Verlag, 1994.

[53] D.H. Wilkinson. *Ionization chambers and counters*. Cambridge monographs on physics. University Press, 1950.

[54] A.H. Snell. *Nuclear Instruments and Their Uses: Ionization detectors, scintillators, Cerenkov counters, amplifiers: assay, dosimetry, health physics*. v. 1. John Wiley & Sons, 1962.

[55] P.P. Skakkeeb et al. In: *Nuc. Inst. Meth. A* 366.23 (1995), pp. 320 –324.

[56] D. Fabris et al. In: *Nuc. Inst. Meth.* 216.12 (1983), pp. 167 –170.

[57] A.E. Smith et al. In: *Nuc. Inst. Meth. A* 289.12 (1990), pp. 231 –235.

[58] A. M. Rogers et al. In: *Phys. Rev. C* 84 (5 Nov. 2011), p. 051306.

[59] R. D. Page et al. In: *Phys. Rev. C* 75 (6 June 2007), p. 061302.

[60] H. I. Park et al. In: *Phys. Rev. C* 85 (3 Mar. 2012), p. 035501.

[61] James F. Ziegler. *SRIM/TRIM software*. 2013. URL: `http://www.srim.org/` (visited on 07/31/2013).

[62] S. J. Steer et al. In: *Phys. Rev. C* 84 (4 Oct. 2011), p. 044313.

[63] B. Voss et al. In: *Nuc. Inst. Meth. A* 364.1 (1995), pp. 150 –158.

[64] S. Nishimura et al. In: *Nuc. Inst. Meth. A* 510.3 (2003), pp. 377 –388.

[65] C. R. Gruhn. In: *Nucl. Inst. and Meth.* 196 (1982), p. 33.

[66] R.W.P. McWhirter, P. Palit, and E.H. Bellamy. In: *Nuclear Instruments* 3.2 (1958), pp. 80 –84.

[67] J. Smallcombe. "Study of the ^{11}B(^{3}He,d)^{12}C reaction on the MC40 cyclotron". MA thesis. University of Birminhham, 2009.

[68] Philippos Papadakis. Personal communication. 2012.

[69] John David Jackson. *Classical Electrondynamics*. John Wiley & Sons, 1962.

[70] NIST Physical Measurement Laboratory. *estar*. 2013. URL: `http://physics.nist.gov/PhysRefData/Star/Text/ESTAR.html` (visited on 01/04/2013).

[71] University of Liverpool. *Matter: materials, e-learning ,resources*. 2013. URL: `http://www.matter.org.uk/tem/electron_scattering.htm` (visited on 01/04/2013).

[72] A.H. Wuosmaa et al. In: *Nuc. Inst. Meth. A* 345.3 (1994), pp. 482 –491.

[73] P. Rahkila. In: *Nuc. Inst. Meth. A* 595.3 (2008), pp. 637 –642.

[74] Yuyan Liu et al. In: *J. Opt. Soc. Am. B* 18.5 (May 2001), pp. 666–672.

[75] R. Brun. *Basic concepts of MINUIT*. 2013. URL: `http://root.cern.ch/root/html/TMinuit.html` (visited on 04/24/2013).

[76] J. E. Gaiser. "Harmonium Spectroscopy from Radiative Decays of the J/Psi and Psi-Prime". PhD thesis. SLAC, 1982, p. 178.

[77] Daniel M Cox. Personal communication. 2013.

[78] D. Radford. *Radware Peak*. 2013. URL: `http://radware.phy.ornl.gov/gf3/#1.` (visited on 04/25/2013).

[79] D. Radford. *Radware Efficiency*. 2013. URL: `http://radware.phy.ornl.gov/gf3/gf3.html#5.3.` (visited on 02/27/2013).

[80] J. Konki. "Geant4 simulations and measurements of the performance of the SAGE spectrometer". PhD thesis. University of Jyvaskyla, 2011.

[81] K. Starosta et al. In: *Nuc. Inst. Meth. A* 515.3 (2003), pp. 771 –781.

[82] G. Hackman and J.C. Waddington. In: *Nuc. Inst. Meth. A* 357.23 (1995), pp. 559 –566.

[83] B. Crowell et al. In: *Nuc. Inst. Meth. A* 355.23 (1995), pp. 575 –581.

[84] J. Robin. In: *Nuc. Inst. Meth. A* 555.12 (2005), pp. 282 –287.

[85] W.T. Eadie and F. James. *Statistical Methods in Experimental Physics*. World Scientific Publishing Company Incorporated, 2006.

[86] R.J. Barlow. *Statistics: A Guide to the Use of Statistical Methods in the Physical Sciences*. Manchester Physics Series. Wiley, 1989.

[87] F. James and M. Roos. In: *Comp. Phys. Commun.* 10.6 (1975), pp. 343 –367.

[88] Gary J. Feldman and Robert D. Cousins. In: *Phys. Rev. D* 57 (7 Apr. 1998), pp. 3873–3889.

[89] J. Neyman. In: *Philos. T. Roy. Soc. A* 236.767 (1937), pp. 333–380.

[90] W.D. Hamilton. *The Electromagnetic interaction in nuclear spectroscopy*. North-Holland, 1975.

[91] Stephen Gillespie. Personal communication. 2013.

[92] J. Kramp et al. In: *Nuclear Physics A* 474.2 (1987), pp. 412 –450.

[93] T. Kibdi et al. In: *Nuclear Physics A* 567.1 (1994), pp. 183 –236.

[94] A.V. Aldushchenkov and N.A. Voinova. In: *At. Data Nucl. Data Tables* 11.4 (1973), pp. 299 –325.

[95] W. D. Kulp et al. In: *Phys. Rev. C* 69 (6 June 2004), p. 064309.

[96] Fang-Qi Chen, Yang Sun, and Peter Ring. In: *Phys. Rev. C* 88 (1 July 2013), p. 014315.

[97] P E Garrett. In: *Journal of Physics G* 27.1 (2001), R1.

[98] F. Iachello. In: *Phys. Rev. Lett.* 53 (15 Oct. 1984), pp. 1427–1429.

[99] Eisenberg J M and Greiner W. *Nuclear Theory vol I*. Amsterdam: North-Holland, 1987.

[100] John L Wood. In: *Journal of Physics: Conference Series* 403.1 (2012), p. 012011.

[101] N. V. Zamfir et al. In: *Phys. Rev. C* 66 (2 Aug. 2002), p. 021304.

[102] V.G. Soloviev. In: *Nuclear Physics* 69.1 (1965), pp. 1 –36.

[103] Kris Heyde and John L. Wood. In: *Rev. Mod. Phys.* 83 (4 Nov. 2011), pp. 1467–1521.

[104] E. A. McCutchan, N. V. Zamfir, and R. F. Casten. In: *Phys. Rev. C* 69 (6 June 2004), p. 064306.

[105] V. Werner et al. In: *Physics Letters B* 527.12 (2002), pp. 55 –61.

[106] W.-T. Chou, N. V. Zamfir, and R. F. Casten. In: *Phys. Rev. C* 56 (2 Aug. 1997), pp. 829–838.

[107] F. Iachello, N. V. Zamfir, and R. F. Casten. In: *Phys. Rev. Lett.* 81 (6 Aug. 1998), pp. 1191–1194.

[108] F. Iachello. In: *Phys. Rev. Lett.* 87 (5 July 2001), p. 052502.

[109] F. Iachello. In: *Phys. Rev. Lett.* 85 (17 Oct. 2000), pp. 3580–3583.

[110] N. Blasi et al. In: *Phys. Rev. C* 88 (1 July 2013), p. 014318.

[111] R. M. Clark et al. In: *Phys. Rev. C* 68 (3 Sept. 2003), p. 037301.

[112] L. L. Riedinger, Noah R. Johnson, and J. H. Hamilton. In: *Phys. Rev.* 179 (4 Mar. 1969), pp. 1214–1229.

[113] R. F. Casten et al. In: *Phys. Rev. C* 57 (4 Apr. 1998), R1553–R1557.

[114] R. Krucken et al. In: *Physics Letters B* 454 (1999), pp. 15 –21.

[115] N. V. Zamfir et al. In: *Phys. Rev. C* 60 (5 Oct. 1999), p. 054312.

[116] D. G. Burke. In: *Phys. Rev. C* 66 (2 Aug. 2002), p. 024312.

[117] Jan Jolie, Pavel Cejnar, and Jan Dobes. In: *Phys. Rev. C* 60 (6 Nov. 1999), p. 061303.

[118] R. M. Clark et al. In: *Phys. Rev. C* 67 (4 Apr. 2003), p. 041302.

[119] P. E. Garrett et al. In: *Phys. Rev. Lett.* 103 (6 Aug. 2009), p. 062501.

[120] T. Möller et al. In: *Phys. Rev. C* 86 (3 Sept. 2012), p. 031305.

[121] P. Van Isacker. Personal communication. 2013.

[122] K. Wimmer et al. *First identification of large electric monopole strength in well-deformed rare earth nuclei*. 2008. URL: `arXiv:0802.2514` (visited on 07/25/2013).

[123] K. Wimmer et al. "Conf. Proc. AIP". In: 2009.

[124] O.B. Tarasov and D. Bazin. In: *Nuc. Inst. Meth. B* 204.0 (2003), pp. 174 –178.

[125] H. Ower. "Computer program CLX". Not published.

[126] A.M. Demidov et al. English. In: *Physics of Atomic Nuclei* 69.4 (2006), pp. 555–561.

[127] Brookhaven National Lab (BNL) National Nuclear Data Center (NNDC). *Evaluated Nuclear Structure Data Files (ENSDF)*. 2013. URL: `http://www.nndc.bnl.gov/ensdf/` (visited on 09/25/2013).

[128] C.A. Fields, K.H. Hicks, and R.J. Peterson. In: *Nuclear Physics A* 431.3 (1984), pp. 473 –485.

[129] J.C. Bacelar et al. In: *Nuclear Physics A* 442.3 (1985), pp. 509 –546.

[130] A. Fitzpatrick et al. In: *Nuclear Physics A* 582.12 (1995), pp. 335 –356.

[131] N. Roy et al. In: *Nuclear Physics A* 382.1 (1982), pp. 125 –158.

[132] D H Smalley et al. In: *Journal of Physics G* 22.10 (1996), p. 1411.

[133] Jatinder Goswamy et al. In: *Int. J. Rad. App. Inst. A* 42.11 (1991), pp. 1025 –1032.

[134] C.A. Fields et al. In: *Physics Letters B* 130.34 (1983), pp. 157 –160.

[135] J.H. Bjerregaard et al. In: *Nuclear Physics* 86.1 (1966), pp. 145 –166.